SOLUTION STRUCTURE, RHEOLOGY, AND NANOCOMPOSITES OF A LIQUID CRYSTALLINE POLYELECTROLYTE

Ryan John Fox

A dissertation submitted to the faculty at the University of North Carolina at Chapel Hill in partial fulfillment of the requirements for the degree of Doctor of Philosophy in Materials Science in the College of Arts & Sciences.

Chapel Hill
2020

Approved by:

Theo J. Dingemans

M. Gregory Forest

Sergei S. Sheiko

Ehssan Nazockdast

Frank A. Leibfarth

ABSTRACT

Ryan John Fox: Solution Structure, Rheology, and Nanocomposites of a Liquid Crystalline Polyelectrolyte
(Under the direction of Theo J. Dingemans)

High-performance polymers, most notably all-aromatic polyamides (aramids), enable the convergence of the disparate material properties, such as low density, high strength, high stiffness, and thermal stability. Sulfonated derivatives of aramids (sulfo-aramids) represent a unique class of materials that are a nexus between stiff and strong engineering materials and soft and dynamic biological matter. Specifically, sulfo-aramids are water soluble and often self-assemble into rodlike supramolecular structures in solution, similar to rodlike viruses or polypeptide helical assemblies. Such rodlike systems undergo spontaneous self-organization into a liquid crystalline (nematic) phase above a critical concentration, resulting in a high degree of local orientational order. Application of an external field, such as shear flow, can either increase or decrease the global orientational order of the nematic phase. Thus, understanding the solution structure and rheology of such phases has important implications for the fabrication of high-performance, sulfo-aramid nanocomposites.

In this Dissertation, we investigate aspects of the solution structure, rheology, and nanocomposites fabricated from helical, rodlike assemblies of the sulfo-aramid, poly(2,2'-benzidine-4,4'-disulfonyl terephthalamide) (PBDT). PBDT forms a fully nematic phase at low concentrations in water, evidencing its high aspect ratio, enabling environmentally-benign fabrication of advanced nanocomposites with liquid crystalline graphene oxide or

ionic liquids. Moreover, the low concentrations required for formation of a fully nematic phase enables direct interrogation of the rheological responses of the liquid crystalline rodlike assemblies. In contrast, the rheology of previously studied model LCPs are dominated by the nematic defect texture. In addition, the dynamic self-assembled nature of PBDT rodlike assemblies result in an unusual rheological behavior, known as irreversible shear-activated gelation, at high concentrations. Overall, our new insights on the solution structure and rheology of sulfo-aramids not only inform the design of advanced nanocomposites, but also provide a new platform for elucidating the flow behavior of high-aspect-ratio, charged rods.

To my love, Sofia.

ACKNOWLEDGMENTS

I have had the pleasure of working with many people who have made this Dissertation possible. My research advisor, **Prof. Theo Dingemans**, has provided me with the direction, resources, and opportunities that have enabled me to undertake this work and the freedom to explore my own interests. From my first meeting with Theo, I became convinced that his research direction was an exciting area with many opportunities, and I've enjoyed conducting the research presented in this Dissertation. I thank my doctoral committee, **Profs. Sergei Sheiko**, **Ehssan Nazockdast**, **Frank Leibfarth**, and especially my committee chair, **Prof. Greg Forest**, who have provided significant guidance and support in a variety of ways. Thanks to **Profs. Stephen Picken**, **Lou Madsen**, and **Ed Samulski** for elaborating many complex ideas in soft matter physics that I needed to integrate in order to complete this work. Many thanks to the members of the Dingemans Lab, **Drs. Maruti Hegde**, **Will Daniels**, **Shreya Choudhury**, and **Anna Fraser**, and all my other colleagues in the Applied Physical Sciences and Chemistry departments, and for their help over the years and making UNC a great place to work.

The foundation of my interests in polymers and soft matter began while I was a Chemical Engineering undergraduate at North Carolina State University. My undergraduate research advisor, **Prof. Orlin Velev**, gave me the opportunity to work in his laboratory on interesting research projects and taught me many things about soft matter, thermodynamics, and most importantly, scientific communication. The experience I had in the Velev group was invaluable and I want to especially thank **Drs. David Chang** and **Brittany Mertens** for

being excellent graduate research mentors, as well as **Drs. Koohee Han**, **Sangchul Roh**, **Alex Richter**, **Tim Shay**, **Sabina Islam**, **Dane Grismer**, and **Prof. Bhuvnesh Bharti** for making a great lab environment to work in as an undergraduate. I thank my academic advisors, **Profs. Michael Dickey** and **Lisa Bullard**, for providing a significant amount of support in my path through Chemical Engineering at NC State.

I want to especially thank **Matt Baker** and **Justin Whiteman**, who supervised me while as an intern at Stiefel, a GlaxoSmithKline company. As my first laboratory experience, I could not have asked for a better pair of Chemical Engineers to introduce me to soft matter research and process engineering. Their guidance and words of advice were one of the primary reasons that I pursued graduate research. In addition, I thank my supervisors during my internship with Novozymes, **Drs. Sarah Gould** and **Elizabeth DeFreese**, who introduced me to all things related to enzyme fermentation. They taught me many things about graduate school and industrial research at an important time in my undergraduate career.

During my time as a graduate student, I have been fortunate to have received training opportunities provided by the Department of Energy (DOE). First, I want to thank the staff and scientists at Argonne National Laboratory and Oak Ridge National Laboratory (ORNL) for sponsoring my attendance to the 20th National School on Neutron and X-Ray Scattering in 2018. The knowledge and skills I gained, in addition to the many scientists I met, provided an invaluable experience. That experience led to my application and acceptance to the DOE Office of Science Graduate Student Research (SCGSR) program working under **Dr. Wei-Ren Chen** at ORNL. The six months that I spent at ORNL was invaluable in terms of productivity and knowledge gained about small-angle scattering and rheology of liquid crystalline polymers. In addition, I also thank **Drs. Guan-Rong Huang**, **Changwoo Do**, and

William Heller for their help and support, in addition to the instrument staff, radiological control technicians, and instrument hall coordinators for their assistance during my experiments conducted at ORNL.

Finally, I want to thank my family, close friends, and my partner, **Dr. Sofia Garakyaraghi**, for their enduring love and support. I can unambiguously conclude that without Sofia, I would not have pursued graduate school. I can't overstate her contributions to not only my personal happiness, but also my professional and scientific development. She has undoubtably had the largest influence on my development in the context of scientific data presentation and writing. Her guidance and foresight were instrumental in my development and progress throughout graduate school. I would not know what to do without her love, kindness, and support in my life. I love you and can't wait to begin writing our next chapter together in our life.

TABLE OF CONTENTS

LIST OF TABLES ..... **xiv**

LIST OF FIGURES ..... **xv**

LIST OF ABBREVIATIONS AND SYMBOLS ..... **xxi**

CHAPTER 1: INTRODUCTION **1**

1.1. LIQUID CRYSTALS 1

1.2. LIQUID CRYSTALLINE POLYMERS 5

1.3. POLYELECTROLYTES 10

1.4. SULFONATED ALL-AROMATIC POLYAMIDES 12

1.5. POLYMER ELECTROLYTE MEMBRANES 23

1.6. GRAPHENE OXIDE NANOCOMPOSITES 27

1.7. DISSERTATION OUTLINE 31

CHAPTER 2: OBSERVATION OF TRANSITION CASCADES IN A SHEARED LIQUID CRYSTALLINE POLYELECTROLYTE **35**

2.1. INTRODUCTION 35

2.2. EXPERIMENTAL 38

2.3. RESULTS AND DISCUSSION 40

2.3.1. Nonlinear Transient and Steady-State Rheology 40

2.3.2. Assignment of Director State Transition Cascade 50

2.3.3. Transient Shear Step-Downs 52

2.4. CONCLUSIONS 60

CHAPTER 3: FINGERPRINTING THE NONLINEAR RHEOLOGY OF A LIQUID CRYSTALLINE POLYELECTROLYTE 62

3.1. INTRODUCTION 62

3.2. EXPERIMENTAL 65

3.3. RESULTS AND DISCUSSION 67

3.3.1. Nonlinear Rheology in the Isotropic Phase 67

3.3.2. Nonlinear Rheology in the Nematic Phase 75

3.3.3. Alignment under Nonlinear Shear from Rheo-SANS 83

3.3.4. Transient Rheology of the Nematic Phase 88

3.3.5. Construction of Dynamic Stress Paths 97

3.4. CONCLUSIONS 102

CHAPTER 4: IRREVERSIBLE SHEAR-ACTIVATED GELATION OF A LIQUID CRYSTALLINE POLYELECTROLYTE 103

4.1. INTRODUCTION 103

4.2. EXPERIMENTAL 104

4.3. RESULTS AND DISCUSSION 105

4.3.1. Rodlike Assemblies and Nematic Phase Diagram 105

4.3.2. Nonlinear Rheology and Irreversible Gelation 107

4.3.3. Linear Rheology and Structural Characterization 110

4.3.4. Shear Rate Dependence of the Induction Time 114

4.3.5. Mechanism of Gel Formation 116

4.4. CONCLUSIONS 117

CHAPTER 5: MECHANICAL REINFORCEMENT OF LIQUID CRYSTALLINE GRAPHENE OXIDE NANOCOMPOSITES 118

5.1. INTRODUCTION 118

5.2. EXPERIMENTAL 121

5.3. RESULTS AND DISCUSSION 127

5.3.1. Wide- and Small-Angle X-ray Scattering: Solid-State Nanocomposites 127

5.3.2. Nanocomposite Cross-section: SEM and AFM Modulus Mapping 132

5.3.3. Stress-Strain Behavior 134

5.3.4. Thermomechanical Analysis 137

5.4. CONCLUSIONS 141

CHAPTER 6: NANOFIBRILLAR IONIC POLYMER COMPOSITES ENABLE HIGH MODULUS ION-CONDUCTING MEMBRANES 143

6.1. INTRODUCTION 143

6.2. EXPERIMENTAL 145

6.3. RESULTS AND DISCUSSION 148

6.3.1. Polymer Electrolyte Membranes from PBDT and IL 148

6.3.2. Morphological Observations 153

6.3.3. Thermal Behavior 156

6.3.4. SAXS/WAXS Characterization 159

6.3.5. Thermo-Mechanical Characterization 165

6.3.6. Time-Temperature Superposition 172

6.3.7. Stress-Strain Behavior 175

6.4. CONCLUSIONS..... 176

APPENDIX A: CHAPTER 2 SUPPORTING INFORMATION 178

APPENDIX B: CHAPTER 3 SUPPORTING INFORMATION 180

APPENDIX C: CHAPTER 4 SUPPORTING INFORMATION 188

APPENDIX D: CHAPTER 5 SUPPORTING INFORMATION 196

APPENDIX E: CHAPTER 6 SUPPORTING INFORMATION 207

REFERENCES..... 212

LIST OF TABLES

Table 6.1. Tabulated peak positions of WAXS analysis of PBDT-IL composites. 164

Table D.1. Dilute solution viscometry results in concentrated (96%) sulfuric acid of commercial PPTA and synthesized PBDT. 206

LIST OF FIGURES

Figure 1.1. Schematic of the orientational and structural ordering found in liquid crystal phases. 3

Figure 1.2. Description of a rodlike nematic phase at the (a) microscopic and (b) mesoscopic length scales. 4

Figure 1.3. Concentration regimes of rodlike particles in solution. 6

Figure 1.4. Models for describing the molecular conformation of liquid crystalline polymers within the nematic phase. 10

Figure 1.5. Chemical structures of some commonly studied polyelectrolytes with flexible backbones. 11

Figure 1.6. Solution structure of polyelectrolytes in contrast to neutral polymers. 12

Figure 1.7. Chemical structures of the sulfonated derivatives of PPTA. 13

Figure 1.8. Synthetic route and chemical structure of the sulfo-aramid, poly(2,2'-disulfonyl-4,4'-benzidine terephthalamide) (PBDT). 14

Figure 1.9. Phase diagram of PBDT in water as a function of temperature and concentration. 15

Figure 1.10. Polarized optical micrographs of a neat PBDT solid-state film. 17

Figure 1.11. Morphological and structural differences between solid-state films of PBDT and PBDI, an isotropic structural isomer. 20

Figure 1.12. X-ray scattering data and analysis leading to the double helical structural model of PBDT self-assembly. 22

Figure 1.13. Liquid crystalline ion gels formed from PBDT and a room-temperature ionic liquid (IL). 24

Figure 1.14. Molecular dynamics (MD) simulations of PBDT-IL composite materials. 26

Figure 1.15. Characteristics of single layer graphene oxide (GO) sheets that form a phase of liquid crystalline graphene oxide (LCGO) in water. 28

Figure 1.16. Schematic of the perpendicular orientation of the polymer director (n_p) and GO director (n_{GO}) in the hybrid liquid crystalline phase. 30

Figure 2.1. Characterization of the transient and steady-state nonlinear rheology of nematic PBDT rodlike assemblies in water. 41

Figure 2.2. Steady-state flow curve of nematic PBDT in H_2O at $c = 1.9$ wt.%, with the assignment of director state transitions. 51

Figure 2.3. Steady-state flow curve (*top*) and normalized transient shear stress as a function of strain following shear step-down (*bottom*). 53

Figure 2.4. Correlation of the steady-state rheological properties with the stress transients following shear step-down. 56

Figure 2.5. Fourier transform power spectra of transient stress following shear step-downs at $c = 1.9$ wt.% 59

Figure 3.1. Nonlinear rheology of quiescently isotropic PBDT solutions in D_2O. 68

Figure 3.2. Concentration scaling of Cross model results from fitting the flow curves of quiescently isotropic PBDT solutions 71

Figure 3.3. Steady-state η and N_1 as a function of shear rate of quiescently isotropic and biphasic PBDT solutions under shear. 74

Figure 3.4. Steady-state η (top) and N_1 (bottom) of fully nematic PBDT solutions in D_2O at solution concentrations of 21, 23 and 30 g L^{-1}. 76

Figure 3.5. Semi-log representation of the steady-state η as a function of shear rate for nematic PBDT solutions in D_2O. 78

Figure 3.6. Steady-state η and N_1 of liquid crystalline PBDT in D_2O as a function of shear rate for 38 and 45 g L^{-1}. 82

Figure 3.7. Measurement of shear-induced alignment of nematic PBDT in D_2O using rheo-SANS. 84

Figure 3.8. Steady-state η and S_{13} as a function of shear rate for (a) 21, (b) 30, and (c) 45 g L^{-1}. 85

Figure 3.9. Analysis of shear flow reversal experiments for $c = 21$ g L^{-1}. 89

Figure 3.10. Normalized stress transient following shear step-down from 570 s^{-1} to the shear rate indicated in the figure for $c = 21$ g L^{-1}. 92

Figure 3.11. Normalized stress transients following step-down from an initial shear rate of 180 s^{-1} for $c = 30$ g L^{-1}. 95

Figure 3.12. Comparison of $\sigma(t)$ and $N_1(t)$ transients following shear step-down. 96

Figure 3.13. Transient stress paths following shear step-down for $c = 21$ g L^{-1} from an initial shear rate of 570 s^{-1}. 99

Figure 3.14. Transient stress paths following shear step-down for $c = 30$ g L^{-1} from an initial shear rate of 180 s^{-1}. 100

Figure 4.1. Structure and nematic phase behavior of PBDT in salt-free water. 106

Figure 4.2. Nonlinear rheology of nematic PBDT solutions. 108

Figure 4.3. Linear rheology of PBDT shear-activated gels. 111

Figure 4.4. Induction time prior to shear-activated gelation at $c = 30$ wt.%. 115

Figure 5.1. Overview of synthesis of PBDT-LCGO hybrid liquid crystalline nanocomposites. 120

Figure 5.2. 2D wide-angle X-ray scattering (WAXS) of PBDT-rGO nanocomposite films. 128

Figure 5.3. 2D small-angle X-ray scattering (SAXS) images of a 1.8 vol.% rGO nanocomposite. 131

Figure 5.4. Morphological analysis of PBDT-rGO nanocomposites via SEM and AFM. .. 133

Figure 5.5. Stress-strain behavior of PBDT-rGO nanocomposites from uniaxial tension measurements. 135

Figure 5.6. DMTA and time-temperature superposition (TTS) analysis of PBDT-rGO nanocomposites. 138

Figure 6.1. PBDT-IL composite membranes fabricated from the sulfonated all-aromatic polyamide, PBDT, and the IL [Emim][TfO]. 149

Figure 6.2. Comparison of PBDT-IL composites to a comprehensive literature compilation of PEMs and ion gels. 151

Figure 6.3. AFM of the PBDT-IL composite morphology. 154

Figure 6.4. AFM phase angle map of a 5 wt.% PBDT-IL composite and idealized representation of the two-phase morphology. 156

Figure 6.5. DSC characterization of PBDT-IL composites. 157

Figure 6.6. SAXS analysis of PBDT-IL composites. 159

Figure 6.7. WAXS spectra of neat PBDT, PBDT-IL composites, and neat IL measured in the perpendicular configuration. 163

Figure 6.8. Isochronal DMTA results of PBDT-IL composites. 166

Figure 6.9. Analysis of the thermo-mechanical relaxations of neat PBDT and PBDT-IL composites. 170

Figure 6.10. TTS analysis of PBDT-IL composites. 172

Figure 6.11. Stress-strain measurement in uniaxial tension for three samples of neat PBDT (*top*) and 20 wt.% PBDT-IL composite (*bottom*). 175

Figure A.1. Analysis of 1D scattering intensity of a nematic PBDT monodomain. 178

Figure A.2. Analysis of 2D scattering anisotropy of a nematic PBDT monodomain. 179

Figure B.1. Determination of the relaxation time by fitting the steady-state flow curve 180

Figure B.2. Linear oscillatory rheology frequency sweeps of G′ and G″ within the linear viscoelastic regime (strain amplitude = 10%) at 25 °C. 181

Figure B.3. Concentration scaling of G′ at 10 rad s^{-1} of quiescently isotropic PBDT solutions. 182

Figure B.4. Intensity as a function of azimuthal angle at various shear rates for $c = 21$ g L^{-1} PBDT solution. 183

Figure B.5. Intensity as a function of azimuthal angle at various shear rates for $c = 30$ g L^{-1} PBDT solution. 184

Figure B.6. Transient shear stress and N_1 following shear step-down from a flow aligned state for $c = 21$ g L^{-1} PBDT solution. 185

Figure B.7. Transient shear stress and N_1 following shear step-down from a flow aligned state for $c = 21$ g L^{-1} PBDT solution. 186

Figure B.8. Transient shear stress and N_1 following shear step-down from a flow aligned state for $c = 30$ g L^{-1} PBDT solution. 187

Figure C.1. Stop-start test during shear-activated gelation, and final shear-activated gel for $c = 18$ wt.%. 188

Figure C.2. TTS analysis of shear-activated PBDT gels. 188

Figure C.3. 1D SAXS intensity as a function of scattering vector of PBDT pre-shear, low-viscosity solutions and shear-activated gels. 190

Figure C.4. Correlation length for PBDT solutions and shear-induced gels versus concentration pre-shear and post-shear. 191

Figure C.5. 1D WAXS intensity for PBDT solutions and shear-induced gels at 18 and 20 wt.% pre-shear and post-shear. 192

Figure C.6. Scanning electron microscopy (SEM) images of the cross-section surface of a freeze-fractured 16 wt.% PBDT sample pre-shear and post-shear. 193

Figure C.7. Effect of salt on the structure and nonlinear rheology of PBDT solutions. 195

Figure D.1. Tapping mode AFM of neat PBDT film revealing slender nanofibers with cross-sectional dimension between 50 and 200 nm. 196

Figure D.2. Thermogravimetric analysis of GO. 197

Figure D.3. Flake size analysis of GO by SEM. 197

Figure D.4. Scanning TGA at 10 °C min^{-1} of PBDT-GO nanocomposite films after drying at 60 °C in air. 198

Figure D.5. Scanning TGA of a neat PBDT and 4 wt.% GO (2.4 vol.% rGO) nanocomposite film at 10 °C min^{-1}. 198

Figure D.6. 1D WAXS lineouts of a neat PBDT film (radially averaged) and a 1.8 vol.% rGO nanocomposite film with 30° sector averages. 199

Figure D.7. Representative 2D WAXS patterns of PBDT-rGO nanocomposite films in the perpendicular configuration. 200

Figure D.8. Loss tangent over the temperature range of −30 to 110 °C in 5 °C intervals from 0.1 to 10 Hz. 202

Figure D.9. Arrhenius plots over the β-relaxation temperature range. 203

Figure D.10. Fitting and residuals of the β-relaxation using the Havriliak-Negami function for the loss modulus master curves. 204

Figure D.11. Dilute solution viscometry of PBDT and PPTA in 96% sulfuric acid at 25 °C. 206

Figure E.1. ^{1}H NMR spectra of 0.1 wt.% PBDT in D_2O directly after synthesis and purification. 207

Figure E.2. TGA of neat PBDT and corresponding PBDT-IL composites. 208

Figure E.3. AFM 3D topological scans of a 5 (*left*) and 70 (*middle*) wt.% PBDT-IL composite compared to the 100 wt.% PBDT film (*right*). 208

Figure E.4. DSC 2nd heat thermograms at a rate of 2 °C min^{-1} for neat [Emim][TfO] and with 3.4 and 6.8 wt.% of [Na][TfO].. 209

Figure E.5. Differential scanning calorimetry thermograms of a 5 wt.% PBDT-IL composite at a heating rate of 2 °C min^{-1}. 209

Figure E.6. WAXS of neat [Emim][TfO] and with the addition of 3.4 and 6.8 wt.% [Na][TfO]. 210

Figure E.7. Decrease in E' from −50 to −10 °C as a function of IL crystallinity. 211

LIST OF ABBREVIATIONS AND SYMBOLS

Aramid	All-aromatic polyamide
AFM	Atomic force microscopy
k_B	Boltzmann constant
DSC	Differential scanning calorimetry
DMTA	Dynamic mechanical thermal analysis
E	Elastic modulus
S_{eq}	Equilibrium scalar order parameter
σ_∞	Equilibrium shear stress
N_1	First normal stress difference
T_g	Glass transition temperature
GO	Graphene oxide
LCGO	Liquid crystalline graphene oxide
LCP	Liquid crystalline polymer
E''	Loss modulus (tension)
G''	Loss modulus (shear)
T_m	Melting temperature
$\boldsymbol{n}$	Nematic director
para-aramid	*para*-substituted all-aromatic polyamide
PEM	Polymer electrolyte membrane

PBDT	Poly(2,2-benzidine-4,4'-disulfonyl terephthalamide)
PPTA	Poly(*p*-benzidine terephthalamide)
q	Magnitude of the scattering vector
rGO	Reduced graphene oxide
D_r^0	Rotational diffusivity in dilute solution
$\overline{D}_r$	Rotational diffusivity in semidilute solution
Sulfo-aramid	Sulfonated all-aromatic polyamide
T	Temperature
TGA	Thermogravimetric analysis
η	Viscosity
LCP	Liquid crystalline polymer
LCGO	Liquid crystalline graphene oxide
T_m	Melting temperature
S_{13}	Scalar order parameter in the 1—3 (flow—vorticity) plane
SANS	Small-angle neutron scattering
SAXS	Small-angle X-ray scattering
σ, σ_{xy}	Shear stress
E'	Storage modulus (tension)
G'	Storage modulus (shear)
$\sigma(t)$	Transient shear stress
WAXS	Wide-angle X-ray scattering

CHAPTER 1: INTRODUCTION

1.1. LIQUID CRYSTALS

Condensed phases of simple liquids, such as diatomic argon, have a relatively simple structure in comparison to crystalline solids, such as metals. Simple liquids have no long-range positional order, like a crystalline lattice, or orientational order, like magnetic dipole moments of ferromagnets. It is well-known that the mathematical form of the intermolecular potential energy dictates, to a large extent, the liquid structure and phase behavior.[1] For simple liquids, their structure arises from the well-known hard-core repulsion and van der Waals attraction, respectively, embodied in the classic Leonard-Jones potential energy

$$V_{LJ} = 4\varepsilon\left[\left(\frac{\sigma}{r}\right)^{12} - \left(\frac{\sigma}{r}\right)^{6}\right] \qquad \textbf{(Eqn. 1.1)}$$

where V_{LJ} is the potential energy, ε is the depth of the potential energy well, σ is the distance at which the pair-wise potential is zero, and r is the distance between the molecules.[2] The r^{-12} repulsive contribution arises from the Pauli exclusion principle, while the r^{-6} contribution describes long-range attractions. This mathematical form of the potential energy results in a characteristic distance of nearest neighbors, with a gradual reduction in the positional correlations of the radial distribution function as r tends towards infinity. Moreover, due to the spherical symmetry of simple molecular liquids, the fluids are isotropic. That is, their physical properties do not depend on their orientation in space.

However, Nature uses more complex forms of pair-wise interactions in concert with anisotropic (i.e., non-spherical) molecular architecture that it uses to construct life as we know it. Anisotropic molecular architectures are found in a variety of natural molecules, e.g., lipids and peptides, and biological systems, e.g., tobacco mosaic virus.[3,4] In the case of rodlike particles, shape anisotropy is present when the length L far exceeds the diameter D, meaning the aspect ratio p is much greater than unity. The ultimate function of these anisotropic molecules or biological systems strongly depends on their shape and chemical composition.

In a fluid of anisotropic molecules or particles, a first-order phase transition occurs above a critical concentration from the isotropic state to an anisotropic, or liquid crystalline, state.[5,6] Liquid crystals are intermediate states of matter that possess the fluidity of liquids, while possessing a variety of orientational and structural ordering (depending on the exact liquid crystal phase, see below) associated with solids. The liquid crystalline phase can be either lyotropic (containing solvent) or thermotropic (no solvent). A variety of anisotropic shapes, such as rods, disks, boomerangs, and hockey sticks can exhibit liquid crystalline phases.[7] The anisotropy of the properties of liquid crystalline phases has spawned a plethora of new technologies, from liquid crystal displays (LCDs) to high-strength body armor (e.g., Kevlar™), making them an extremely important class of functional and structural materials.

A variety of liquid crystalline phases can be obtained with increasing complexity, such as nematic, smectic, and columnar phases.[5] A schematic depiction of the organizational differences between liquid crystal phases is shown in **Figure 1.1**.[8] Nematic liquid crystals exhibit macroscopic orientational order without any positional ordering, and possess an axis of rotational symmetry. The constituent particles can either be rodlike (calamitic) or disklike (discotic). Here, we will focus on the case of calamitic nematic phases for the sake of simplicity. The direction of

average rod orientation is defined as the director, denoted by $\boldsymbol{n}$. The angular distribution function of individual rods and distribution of rod orientations with respect to the director is quantified through a scalar order parameter. For perfect rod alignment, the order parameter is unity, while for an isotropic distribution of rod orientations, it is zero. Higher order phases, such as the cholesteric phase, can exhibit helical trajectories of the director. In addition, the class of smectics, may exhibit positional ordering, and tilts of the molecular axis within smectics layers.

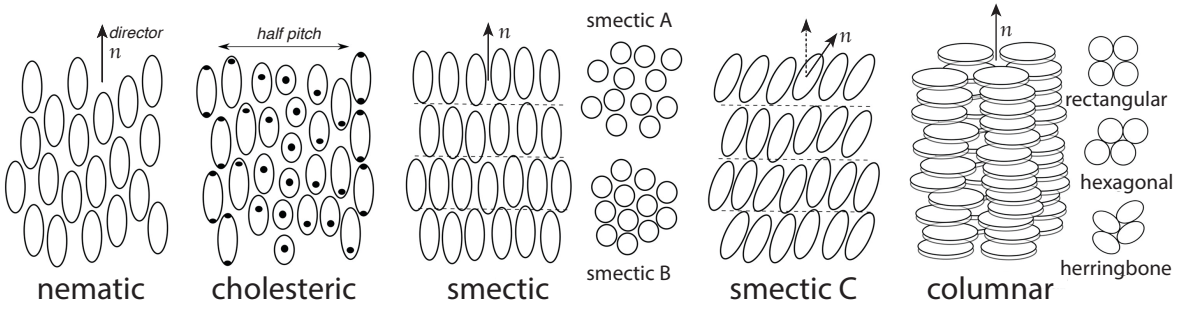

Figure 1.1. Schematic of the orientational and structural ordering found in liquid crystal phases. From left to right: nematic, cholesteric, smectic A and B, smectic C, columnar phases. The director ($\boldsymbol{n}$) denotes the average orientation of the constituent molecules/particles. The black dots for the cholesteric phase indicate the rotation of the director in a helical pattern, characterized by a pitch length. Smectic liquid crystals organize into layers, which can be positionally ordered or disordered, or feature a tilt axis. Columnar phases of disklike molecules/particles are characterized by a director oriented normal to the surface, which can be positionally ordered. Reprinted with permission under Creative Commons CC BY license from Elsevier, *Journal of Molecular Liquids*, Introduction to liquid crystals, Andrienko, D., 2018.

The first observations of liquid crystals were made on small molecules, but sufficiently rigid polymers also exhibit liquid crystallinity. The structure and properties of nematic liquid crystals composed of rodlike polymers is the focus of this Dissertation. Rodlike liquid crystal polymers (LCPs) have at least three important length scales that influence the bulk fluid properties. For the purposes of this work, we will focus our attention solely on lyotropic LCPs, more specifically, in the concentration regimes where the solvent makes up the large majority of the volume fraction.

At the molecular level, chemical bonds and the polymer-solvent friction coefficient dictate the inherent rigidity of the polymer and its' interactions with the surrounding solvent while undergoing translational or rotational motion. On microscopic length scales, the direction of average rod orientation is defined as the director, denoted by $\boldsymbol{n}$, shown in **Figure 1.2a**. The breadth of the molecular orientational distribution function with respect to the director, $\boldsymbol{\Psi(u)}$, where $\boldsymbol{u}$ is the orientation of a test molecule, is quantified through a scalar order parameter, S_m. For perfect rod alignment with respect to the director, S_m is unity, while it is zero for an isotropic distribution of rod orientations.

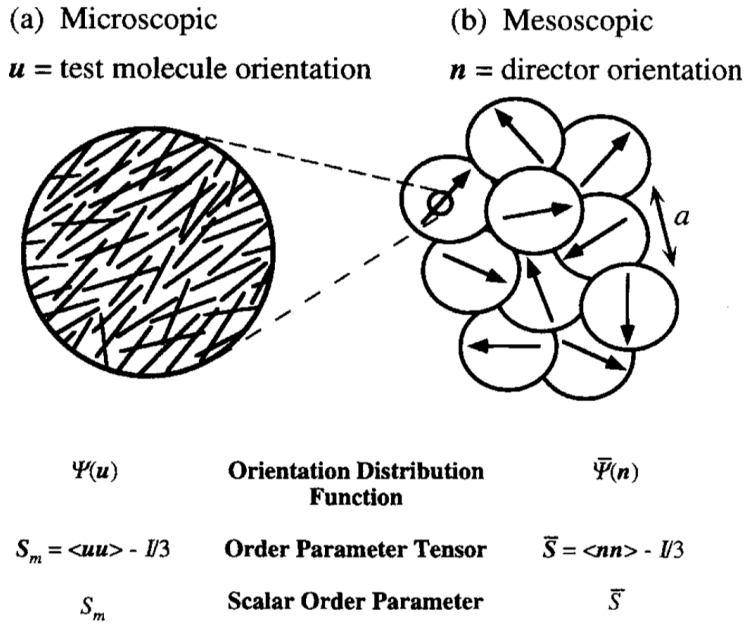

Figure 1.2. Description of a rodlike nematic phase at the (a) microscopic and (b) mesoscopic length scales. Above a critical concentration (c^*) the rods spontaneously self-organize along a common direction, termed the director ($\boldsymbol{n}$) whose orientational ordering is quantified through S_m. On mesoscopic length scales, nematic domains with size a may point in arbitrary directions, whose orientational order is characterized by the domain order parameter $\bar{S}$. Reprinted from *Macromol. Chem. Phys.*, 199, Burghardt, W. R., Molecular Orientation and Rheology in Sheared Lyotropic Liquid Crystalline Polymers, 471-488, Copyright 1998, with permission from John Wiley & Sons, Inc.[9]

On mesoscopic length scales, nematic domains are pointed in arbitrary directions separated by disclination lines, i.e., discontinuities in the director field, shown in **Figure 1.2b**. As a result, in the absence of an applied field, a spatially heterogeneous "polydomain" defect texture (or Schlieren texture) is generally observed. The domain orientational distribution function, $\bar{\boldsymbol{\Psi}}(\boldsymbol{n})$, is similarly quantified through a scalar order parameter $\bar{S}$, which similarly takes values from zero to unity for isotropic or perfect alignment, respectively. Generally, in the quiescent state, the presence of a polydomain defect texture results in LCPs having no global orientational order. This fact necessitates the use of external fields, such as electrical, magnetic, or shear, to produce macroscopic orientational order for fabrication of aligned materials, or to study the local degree of alignment. Due to the presence of interactions between neighboring nematic domains, the defect texture has a significant contribution to the stress tensor of LCPs. This elasticity that arises from the polydomain defect texture is one of the primary differences between LCPs and small-molecule LCs, and gives rise to some interesting rheological properties.

1.2. LIQUID CRYSTALLINE POLYMERS

Polymers that possess a high degree of intrinsic rigidity when dissolved in solution can be thought of as rodlike particles in a continuous medium. Prototypical examples of such polymers is the *para*-substituted all-aromatic polyamide (*para*-aramids), poly(*p*-phenylene terephthalamide) (PPTA, Kevlar®, Twaron®). The high rigidity of *para*-aramids requires strong mineral acids for dissolution but enable liquid crystalline phases to be obtained that can be used in the fabrication of highly oriented fibers. The use of *para*-aramids in the fabrication of high-strength fibers is undoubtably their most important industrial application. For example, these fibers are used in puncture resistant fuel tanks, tires, light-weight body armor, and cables. The high degree of molecular orientation that is achieved in the fiber spinning process enables the

rigid polymer chain, with a modulus of ca. 230 GPa, to bear the tensile load.[10] The molecular alignment necessary for fabricating stiff and strong *para*-aramid fibers can only be attained when spun from the liquid crystalline state.[11] However, it is well-known that LCP fibers are hierarchically assembled into micro-, meso-, and macroscopic fibrils, whose organization and local orientation of polymer within the fibrils dictate the final mechanical properties after fiber spinning.[12]

Four concentration regimes define the relevant solution structure of rodlike polymers, the (i) dilute, (ii) semidilute, (iii) concentrated isotropic, and (iv) liquid crystalline states, shown schematically in **Figure 1.3**.[6]

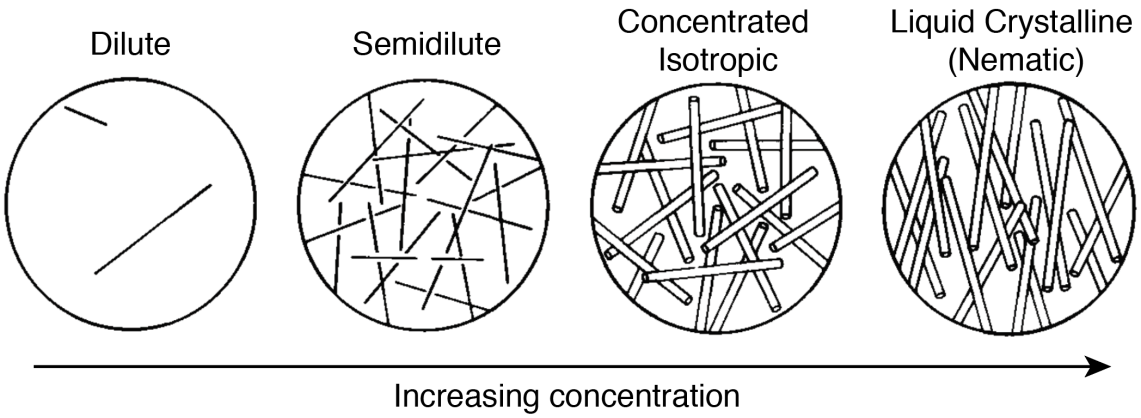

Figure 1.3. Concentration regimes of rodlike particles in solution. The dilute, semidilute, concentrated isotropic, and liquid crystalline phases are accessed by increasing the rod number density in solution. Reproduced with permission of the Licensor through PLSclear, Doi & Edwards 1986.[6]

In the dilute regime, the rodlike polymers do not overlap and can undergo unhindered rotational and translational motion. This solution concentration regime is defined as $v_1 < 1/L^3$, i.e., the swept volume of a single rod of length L undergoing rotational motion does not overlap with any

neighboring rods. The rods undergo rotational diffusion with a diffusion constant in dilute solution D_r^0 defined as

$$D_r^0 = \frac{k_B T}{\zeta_r} = \frac{3k_B T[ln(L/D)-\gamma]}{\pi \eta_s L^3} \quad \textbf{(Eqn. 1.2)}$$

where $k_B T$ is the thermal energy, ζ_r is the rod-solvent friction coefficient, L/D is the aspect ratio, γ is a geometrically specific constant, and η_s is the solvent viscosity. The relaxation time of the rotational motion is $\tau_r = 1/(2D_r^0)$, and thus scales as $\sim L^3$ in dilute solution. In comparison, the longest relaxation time τ_R in the Rouse model for flexible polymers exhibits a squared dependence on the degree of polymerization. Thus, the dynamics of rodlike polymers are more strongly dependent on the size of the polymer than in the case of flexible polymers. In this concentration regime, the viscosity increases linearly with concentration and the rodlike polymers do not interact.

Above a number density $v_1 \approx 1/L^3$, rods begin to overlap with one another and increasingly constrain their rotational motion. In this concentration regime, the solution is termed semidilute and the viscosity increases rapidly with concentration. Note that this definition is different than that used in defining the transition to semidilute solution for flexible polymers, where the overlap volume fraction is defined as $\phi^* = N v_{mon}/V$, where N is the degree of polymerization, v_{mon} is the volume of a monomer, and V is the volume of the polymer coil.[13] As the concentration is increased within the semidilute regime, the solution dynamics become strongly affected. In particular, the rotational diffusion coefficient in semidilute solution $\overline{D}_r$ is slowed down in comparison to D_r^0, calculated as

$$\overline{D}_r = \beta D_r^0 (vL^3)^{-2} \quad \textbf{(Eqn. 1.3)}$$

where v is the rod number density and β is a positive, numerical prefactor. The value of β is estimated to be on the order of 10^3—10^4. Recent experiments of rodlike *fd* virus particles in the semidilute concentration regime provide evidence that the value of β is near 1300.[14] This expression gives a very strong dependence of $\overline{D}_r$ on L, and thus on the molecular weight of the rodlike polymer, as $L \sim M$.

At concentrations near $v_2 \approx 1/DL^2$, excluded volume effects between rods become important and both the static and dynamical properties of the solution are affected. The rotational diffusivity is predicted to be hindered further with increasing concentration due to topological entanglements. Above a critical concentration, denoted v^*, c^*, or ϕ^*, the rodlike polymers spontaneously align with their neighbors into a liquid crystalline phase.[15, 16] In experimental systems, non-ideal effects such as length dispersity, flexibility, and electrostatic interactions play a role in the critical concentrations for formation of the nematic phase.[17-21] However, a widely used expression for the onset of liquid crystallinity for rods of diameter D and length L is the so-called Onsager relation[15, 16]

$$\phi^* = \frac{4D}{L} = \frac{4}{p} \qquad \textbf{(Eqn. 1.4)}$$

where $p = L/D$ is the aspect ratio, or axial rigidity ratio. That is, the higher the aspect ratio, the lower the critical concentration for formation of the nematic phase. An alternative expression is given by Flory[22]

$$\phi^* = \frac{8}{p}\left(1 - \frac{2}{p}\right) \qquad \textbf{(Eqn. 1.5)}$$

The difference between these two expressions can be illustrated, for example, when $p = 100$, ϕ^* is 0.04 and 0.078 for Onsager and Flory relations, respectively. For disklike particles, p is defined as the lateral dimension divided by the thickness.[23] For rodlike polymers, where the

length is proportional to the molecular weight, the onset of liquid crystallinity decreases inversely proportional with the molecular weight of the polymer.[24]

The solution conformation of LCPs is an important factor in their structure and rheology but has been largely neglected. Onsager and Flory both considered rigid rods and derived their theories for the nematic phase behavior using this model. Later work to describe the rheology of LCPs in the nematic phase assume rigid rods, which captures much of the salient features of LCP rheology.[25-33] However, this oversimplification was noted and theories that incorporate flexibility in the description of LCP rheology have been developed.[34-36] Theory developed by Odijk[37, 38] shows that even for polymers having a contour length much less than their persistence length, perfect rigidity is not realized. Small-angle neutron scattering (SANS) experiments on uniaxially aligned, contrast-matched solutions of PPTA in sulfuric acid by Picken et al. provided information on the single-chain conformation within the isotropic and nematic phases.[39] These authors found that the nematic environment had no effect on the persistence length of the PPTA chains, in contrast to the expectation that the nematic potential would extend the chain. Analysis of the radius of gyration parallel and perpendicular to the nematic director led these authors to conclude that hairpin defects must be present in the nematic. The significance of this work is that the confinement effect of the nematic potential does not completely prevent large angular excursions of the semirigid chain. Later work reported on the energies associated with such hairpins and their contribution to the physical properties of isotropic PPTA solutions.[40] As such, molecular nematic LCPs are characterized by a significant degree of flexibility that must be taken into consideration.

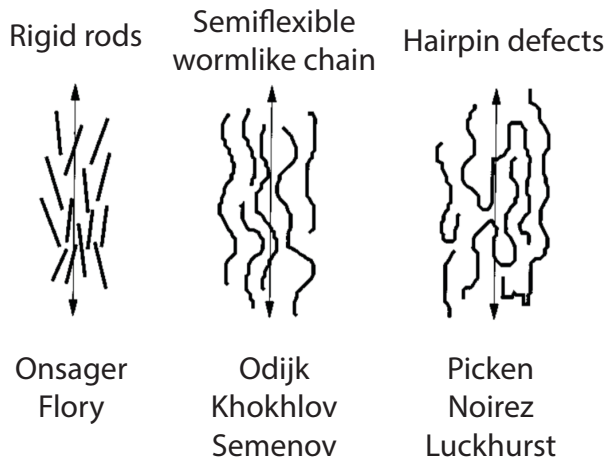

Figure 1.4. Models for describing the molecular conformation of liquid crystalline polymers within the nematic phase, ranging from idealized rigid rods (Onsager/Flory), semiflexible wormlike chains (Odijk, Khokhlov and Semenov), and wormlike chains with hairpin defects (Picken, Noirez, and Luckhurst). The arrows indicate the direction of the nematic director. Reprinted from Picken, S. J.; Noirez, L.; Luckhurst, G. R., Molecular conformation of a polyaramid in nematic solution from small angle neutron scattering and comparison with theory. *J. Chem. Phys.* **1998,** *109* (17), 7612-7617., with the permission of AIP Publishing.[39]

1.3. POLYELECTROLYTES

Polyelectrolytes are polymers that bear electrically charged groups along the backbone, also referred to as polyions (polyanions and polycations for negative and positive backbone charges, respectively). Some commonly studied synthetic polyanions with flexible backbones are shown in **Figure 1.5**, while some commonly studied polyelectrolytes of biological origin include deoxyribonucleic acid (DNA), alginates, carrageenan, and carboxymethyl cellulose. One of the most important features of polyelectrolytes is that they are, in general, water soluble, while most synthetic polymers are not. That is, the addition of charges to the polymer backbone is crucial for water solubility. Polyelectrolytes are found throughout Nature, such as deoxyribonucleic acid (DNA) and proteins, and are utilized in a variety of industrial applications, such as flocculants for water purification.[41] The effect of charges along the backbone has significant implications with respect to inter- and intra-molecular interactions, and thus the polyelectrolyte conformation,

solution structure and dynamics.[42-44] As such, a fundamental understanding of polyelectrolyte behavior is crucial from a scientific and technological perspective.

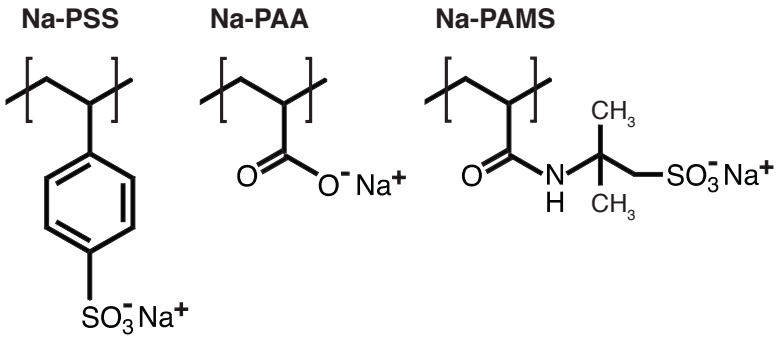

Figure 1.5. Chemical structures of some commonly studied polyelectrolytes with flexible backbones. Sodium poly(styrene sulfonate) (Na-PSS), sodium poly(acrylic acid) (Na-PAA), and sodium poly(2-acrylamido-2-methylpropanesulfonate) (Na-PAMS).

The electrostatic repulsion between chains gives rise to one of the most salient features of polyelectrolytes in comparison to neutral polymers. The high osmotic pressure of the counterions surrounding each chain prevents overlap of the correlation volumes, leading to a positional localization of the electrostatic correlation volumes, which contain the polyelectrolyte chains. This effect manifests itself as a peak in the small-angle scattering spectra for polyelectrolytes in contrast to neutral polymers, shown in **Figure 1.6a**.[45] The correlation length ξ between polyelectrolyte chains can be found by application of Bragg's law to the scattering peak, $\xi = 2\pi/q^*$, where q^* is the scattering vector of the peak. A schematic depiction of the structure of flexible polyelectrolytes is shown in **Figure 1.6b**, which show the correlation length between chains, and the electrostatic blob size, ξ_e. Within the electrostatic blob, electrostatic interactions are completely screened such that the chain conformation at length scales smaller than ξ_e is a self-avoiding random walk.[46] Significant differences between neutral and charged flexible

polymers are found, including the effect of concentration on the viscosity, terminal modulus, and longest relaxation time.[43]

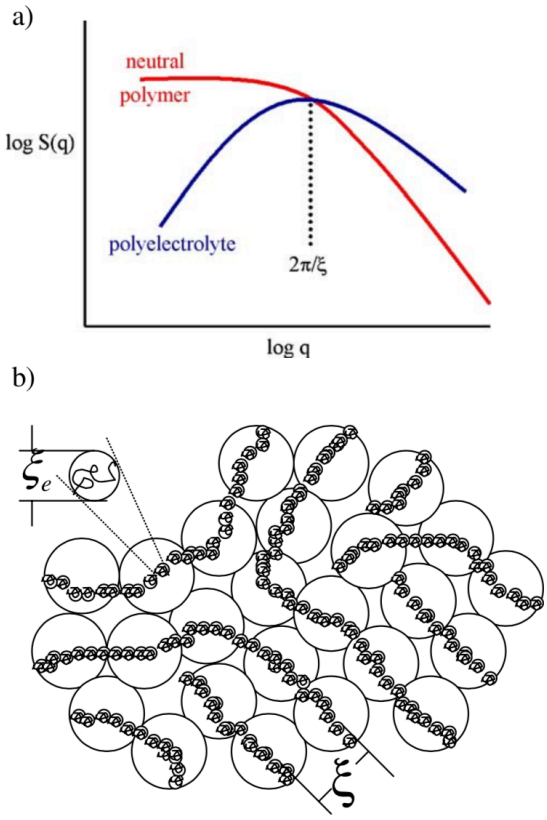

Figure 1.6. Solution structure of polyelectrolytes in contrast to neutral polymers. (a) Difference between the structure factors of neutral polymers (red) and polyelectrolytes (blue). (b) Electrostatic blob model of flexible polyelectrolytes. Reprinted by permission from Springer, Rheologica Acta, Structure and linear viscoelasticity of flexible polymer solutions: comparison of polyelectrolyte and neutral polymer solutions, Ralph H. Colby, 2010.[45]

1.4. SULFONATED ALL-AROMATIC POLYAMIDES

Many polyelectrolyte systems, such as double stranded DNA,[47] *fd* virus,[48] and sulfonated *para*-phenylenes,[49] exhibit a high degree of intrinsic rigidity in solution. Such macromolecules can form higher-order self-assembled structures in solution, such as supramolecular rods, and form liquid crystalline phases. Notable examples of synthetic, rigid polyelectrolytes are sulfonated

derivatives of all-aromatic polyamides (sulfo-aramids). Picken and coworkers investigated sulfonated derivatives of PPTA, namely S-PPTA,[50-52] S-invert-PPTA,[53] and S^2-PPTA,[54] shown in **Figure 1.7**, investigated for their envisioned use in proton exchange membranes. Picken and coworkers found that the location of the sulfonate strongly affected the solution properties and morphology of the resulting solid-state membranes.[55] In the case of S-PPTA and S-invert-PPTA, rodlike aggregates form in water with a diameter of ~30 Å and lengths on the order of 1 μm. In contrast, S^2-PPTA forms molecular solutions that require solution concentrations of ca. 40 wt.% to obtain a nematic phase. Thus, the self-assembly behavior of sulfo-aramids is apparently sensitive to the specific placement of charged groups along the polymer backbone. Moreover, the effect of either protonated or lithiated sulfonate groups was investigated using neutron scattering on S-PPTA. Mendes et al. found that increasing the fraction of sulfonates with Li^+ counterions enhanced the low-q scattering intensity, suggesting an enhancement of network formation of rodlike aggregates.

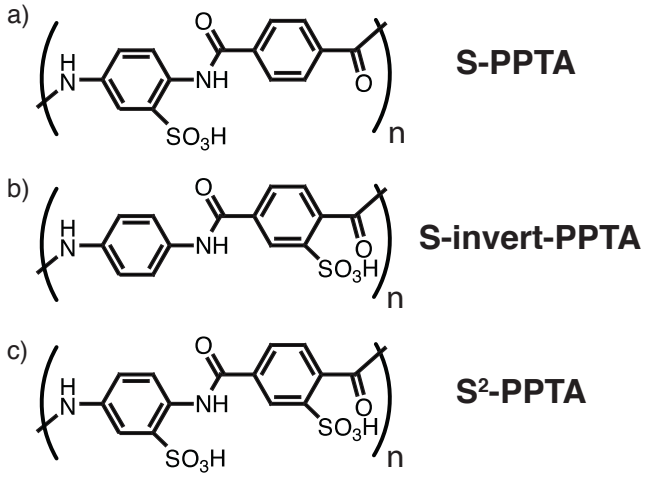

Figure 1.7. Chemical structures of the sulfonated derivatives of PPTA, (a) S-PPTA, (b) S-invert-PPTA, and (c) S^2-PPTA synthesized by Picken and coworkers.[50-54]

Sarkar and Kershner synthesized a variety of sulfo-aramids for their envisioned use as rheology modifiers in aqueous media, many of which were water soluble.[56] Interesting differences in the solution viscosities were observed depending on the particular chemical architecture that these authors suggested to arise from formation of higher-order assemblies, and possible helix formation. One such sulfo-aramid was the condensation product of 4,4'-diaminobiphenyl-2,2'-disulfonic acid (BDSA) and terephthaloyl chloride (TPC), poly(2,2'-disulfonyl-4,4'-benzidine terephthalamide) (PBDT), shown in **Figure 1.8**. An interfacial polymerization method was utilized with sodium carbonate acting as a base and polyethylene glycol (PEG300) as a phase-transfer catalyst. The viscosity dependence on the concentration of PBDT exhibited a maximum near 3 wt.% in salt-free water and decreased with increasing concentration, suggesting the formation of an anisotropic liquid crystalline phase.

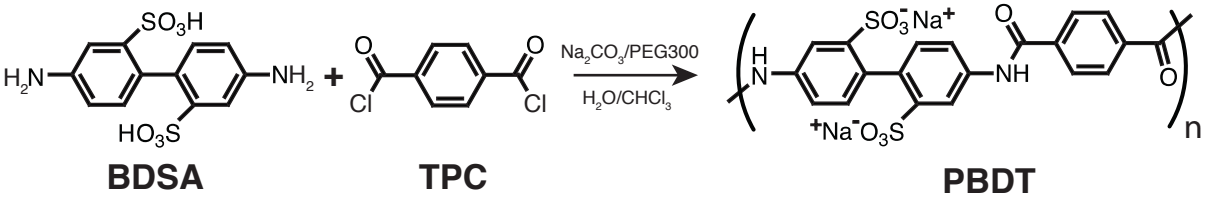

Figure 1.8. Synthetic route via low-temperature interfacial polycondensation and chemical structure of the sulfo-aramid, poly(2,2'-disulfonyl-4,4'-benzidine terephthalamide) (PBDT).[56]

Funaki et al. reported a phase map of PBDT that showed the onset of shear-induced birefringence at ca. 2 wt.% at room temperature, shown in **Figure 1.9**.[57] An equilibrium nematic phase was observed at a concentration of ca. 2.5 wt.%. The concentration regime where coexistence of isotropic and nematic phase exist was not reported in this publication, but a fully nematic polarized optical micrograph at 5 wt.% was presented. For solutions above 1 wt.%, the addition of monovalent salt, NaCl, was found to increase the viscosity of the solutions, while at a

solution of 0.1 wt.%, addition of salt reduced the viscosity. This result was interpreted by invoking the formation of a mesoscopic network structure upon the addition of NaCl above a critical concentration through hydrophobic and hydrogen bonding interactions. Later work by Yang et al. further studied the influence of salt on the solution structure of PBDT through dynamic light scattering, viscometry, and cryo-TEM.[58] These authors found a variety of unusual structures through TEM with increasing amounts of salt. However, the influence of the TEM sample preparation cannot be neglected in this case, as sample preparation in this work involved the use of a heavy metal staining agent and blotting polymer solutions to dry prior to TEM observations.

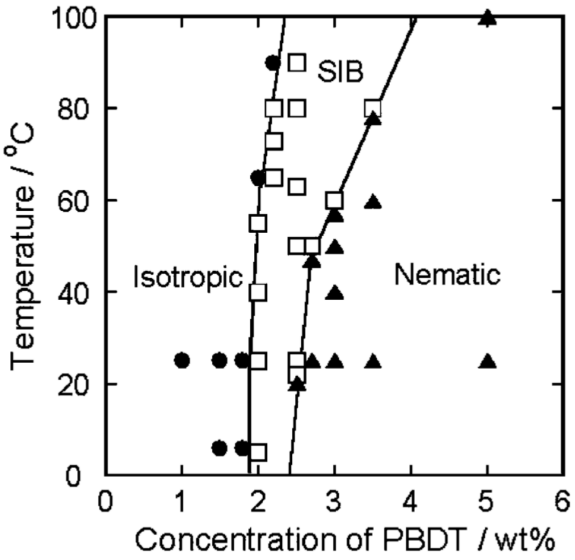

Figure 1.9. Phase diagram of PBDT in water as a function of temperature and concentration, showing isotropic, shear-induced birefringence (SIB), and nematic regimes. Reprinted with permission from Funaki, T.; Kaneko, T.; Yamaoka, K.; Ohsedo, Y.; Gong, J. P.; Osada, Y.; Shibasaki, Y.; Ueda, M., Shear-Induced Mesophase Organization of Polyanionic Rigid Rods in Aqueous Solution. *Langmuir* **2004,** *20*, 6518-6520. Copyright 2004 American Chemical Society.[57]

Later work by Wu et al. reported small-angle X-ray scattering and cryo-TEM measurements on PBDT solutions in salt-free water.[59] The onset of liquid crystallinity was reported at 2 wt.% and a biphasic regime up to 6 wt.%. Both isotropic and nematic solutions of PBDT in water exhibited a peak in their scattering function, typical of polyelectrolytes, corresponding to the lateral correlation length between rods. Above 2 wt.%, the scattering peak was anisotropic, evidencing the nematic orientational ordering of the solution. The scaling exponent for the concentration dependence of the correlation length, predicted as $c^{-1/2}$, was found as $c^{-0.35}$. The authors suggested that this discrepancy originated from the self-assembly of PBDT into rodlike aggregates, thus decreasing the effective concentration of particles. However, it is now known that deviations from the $c^{-1/2}$ to lower values originate from macromolecular clustering that arises from the solvation of counterions, resulting in long wavelength concentration fluctuations.[60] This clustering results in a decrease in the scaling exponent, as scaling theory of de Gennes assumed that the polyelectrolyte solutions were homogeneous.[61] Thus, it is evident that macromolecular clustering due to counterion solvation is present in PBDT solutions.

Wang et al. investigated the role of molecular orientation on the dynamics of water and counterions within isotropic and nematic PBDT solutions.[62] The authors combined polarized optical microscopy, pulsed-field-gradient (PFG) NMR diffusometry, ^{2}H NMR spectroscopy, and small-angle X-ray scattering to quantify the diffusion coefficients of Na^+, the orientation of probe D_2O solvent molecules, and quantify the orientational order of the nematic phase. Similar to the results of prior workers, they observed birefringence under POM consistent with a nematic phase above a critical concentration, which was further confirmed by splitting of the D_2O peaks of the ^{2}H NMR spectra. Here, an I-N transition concentration of 1.2 wt.% was reported with a fully nematic phase above 1.8 wt.%, in comparison with earlier reports of the onset concentration at

2.5—3 wt.%. These differences were attributed to variations in the polymer molecular weight that presumably have an influence on the self-assembled PBDT rod length. Solid-state films of PBDT exhibited Schlieren textures that are typical of nematic liquid crystals, indicating that the nematic order is maintained in the films, see **Figure 1.10**.

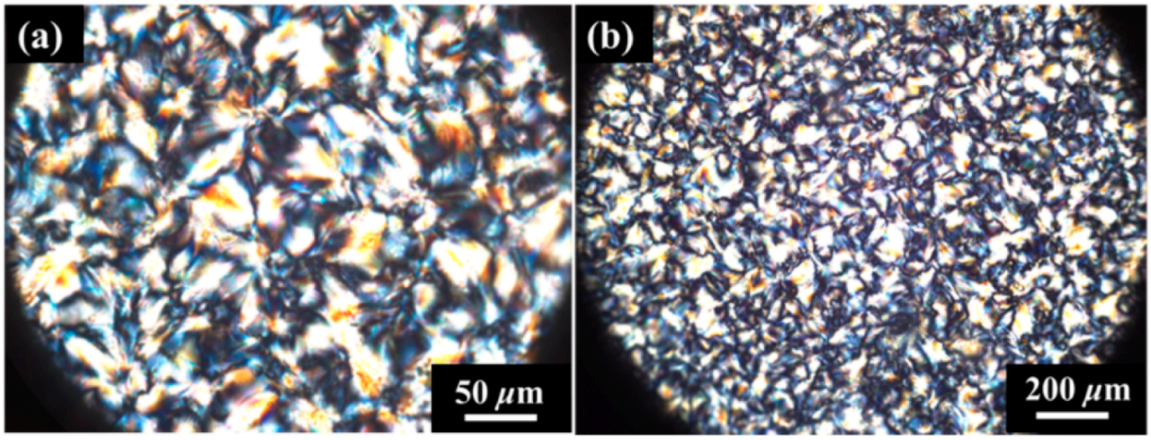

Figure 1.10. Optical micrographs under crossed polarizers of a neat PBDT solid-state film drop casted from a 6 wt.% PBDT solution at room temperature, exhibiting birefringent domains at (a) 40x and (b) 10x magnification. Reprinted with permission from Wang, Y.; Gao, J.; Dingemans, T. J.; Madsen, L. A., Molecular Alignment and Ion Transport in Rigid Rod Polyelectrolyte Solutions. *Macromolecules* **2014,** *47* (9), 2984-2992. Copyright 2014 American Chemical Society.[62]

In solution, the Na^+ counterions in PBDT solutions may either reside strongly localized, or condensed, near the charged groups or remain free to diffuse. Understanding the extent to which counterions are condensed along the polymer backbone is important for understanding the mechanisms controlling ion transport in PBDT solutions. In this context, Manning theory of counterion condensation[63] was used by Wang et al. to calculate whether or not the counterions localize along the backbone expressed through the charge parameter, ξ, given as

$$\xi = \frac{e^2 \alpha}{4\pi\varepsilon_0 \varepsilon k_B T l} \qquad \textbf{(Eqn. 1.6)}$$

where e is the elementary charge, ε_0 and ε are the absolute and relative dielectric constants, k_B is the Boltzmann constant, T is the temperature, l and α are the repeat unit length and the number of charges per repeat unit, respectively. In the case of $\xi < 1$, counterions are assumed to be subject to Brownian motion and are uncondensed, while for $\xi > 1$ a certain fraction of counterions become condensed along the chain. Their motion is not eliminated in the condensed case, but becomes restricted to be along the long axis of the chain. Note that ξ is independent of polymer concentration and thus is an intrinsic property of the polyelectrolyte in question. However, it is known that the fraction of condensed counterions on a solution of charged rigid-rods in fact depends on the separation distance.[64]

Regardless, from the consideration of a single PBDT chain, one can either treat the two sulfonates per repeat unit as one or two charges. These two considerations result in calculated charge parameters of 1.78 or 0.89, respectively. However, if a PBDT helical dimer is considered (see below for discussion on PBDT self-assembly), the results become 3.56 and 1.78, both values being above the critical value for the onset of counterion condensation. Thus, based on this theory, counterions are expected to condense along the backbone of PBDT rodlike assemblies. Experimentally, the lower values of the diffusion coefficient for Na^+ ions in PBDT solutions as measured by NMR, in comparison to pure NaCl solutions, is consistent with some fraction of counterions being condensed along the PBDT backbone that restricts their free diffusion.

The degree of orientational ordering of PBDT rods within the nematic phase was elucidated through a combination of ^2H NMR measurements and small-angle X-ray scattering (SAXS). After obtaining uniaxial alignment by application of a magnetic field to the nematic solution, the authors measured the molecular order parameter S_m by fitting the scattering anisotropy of the polyelectrolyte peak to calculate the scalar order parameter. The S_m within the biphasic regime

was 0.61 and plateaued at 0.79 at 4 wt.%. A deuterated version of PBDT, d-PBDT, was also synthesized and the quadrupolar splitting of the deuterons resulted in similar order parameters found through this independent method. The high order parameter of the PBDT nematic monodomain evidences the high aspect ratio of the rodlike particles.

Gao et al. investigated membranes fabricated from liquid crystalline PBDT and a structural isomer, poly(2,2'-disulfonyl-4,4'-benzidine isophthalamide) (PBDI) for application as proton exchange membranes.[65] The *meta*-linkage of the diacid chloride used in the synthesis of PBDI, in comparison to the *para*-linkage of the diacid chloride for PBDT, results in a kinked molecular geometry. This kinked molecular geometry prevents the formation of a nematic liquid crystalline phase and instead isotropic physical gels are formed at low concentrations.[65, 66] . The cross-sections of the two films after freeze fracturing are shown in **Figure 1.11**, where PBDT membranes possess high in-plane alignment, while PBDI films were isotropic as measured by X-ray scattering. These authors reported water diffusion coefficients for neat polymer membranes and membranes with increasing degrees of ionic crosslinking with the divalent cation, Ba^{2+}. The difference between the in-plane and through-plane diffusion coefficients were used as a measure of the anisotropy of water transport through the membrane. For the isotropic PBDI membranes, the water diffusion coefficients were isotropic in all three Cartesian coordinates. In contrast, PBDT membranes exhibited a diffusion anisotropy of 3 for the neat film and increased up to 4.6 for ionically crosslinked membranes. They suggested the formation of hydrophilic channels between rodlike assemblies of PBDT chains that were aligned in the plane of the film, and the presence of Ba^{2+} further restricted the diffusion of water to be along these channels.

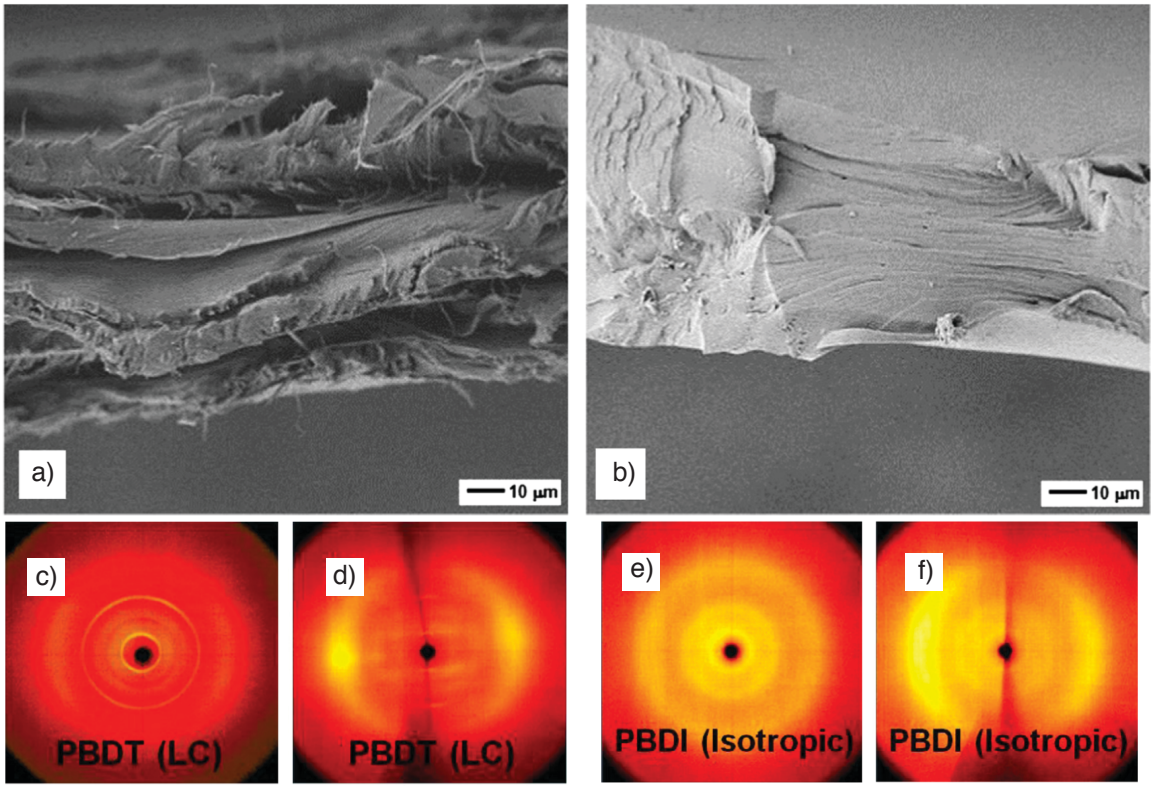

Figure 1.11. Morphological and structural differences between solid-state films of PBDT, a liquid crystalline (LC) sulfo-aramid, and PBDI, an isotropic structural isomer. Cross-sectional scanning electron micrographs of neat (a) PBDT and (b) PBDI. Wide-angle X-ray scattering (WAXS) in the (c) through-plane direction shows a low degree of anisotropy, while the (d) in-plane scattering exhibits high anisotropy. WAXS of PBDI films in the (e) through-plane and (f) in-plane directions are consistent with an isotropic polymer orientation distribution function. Reprinted from *J. Membr. Sci.*, 489, Gao, J.; Wang, Y.; Norder, B.; Garcia, S. J.; Picken, S. J.; Madsen, L. A.; Dingemans, T. J., Water and sodium transport and liquid crystalline alignment in a sulfonated aramid membrane, 194-203, Copyright 2015, with permission from Elsevier.[65]

While analysis of the solution structure had been undertaken by prior authors, the exact structure of PBDT supramolecular assemblies was still uncertain. Wang et al. reported a combination of X-ray scattering, NMR, and molecular dynamics (MD) simulation results that support a double helical model for the self-assembly of PBDT in aqueous solution.[67] **Figure 1.12a** shows experimental X-ray scattering results of a magnetically aligned monodomain of PBDT at 20 wt.% in water. A simulated X-ray scattering pattern of a double helical structure is

shown in **Figure 1.12b**, which in turn allowed assignment of the scattering features to their structural origin. The PBDT chains (**Figure 1.12c)** interact through non-covalent physical interactions (**Figure 1.12d**) to result in charged, helical rodlike assemblies in aqueous solution (**Figure 1.12e,f**). By comparison of the experimental and simulated X-ray data, this structural model for the self-assembly and linear aggregation of these helical PBDT dimers provides an explanation of the high intrinsic rigidity of the rodlike assemblies in aqueous solution. Throughout this Dissertation, we refer to these rodlike assemblies as simply "rods", or "charged rods" for simplicity. From the X-ray measurements reported by Wang et al., the diameter of the PBDT rods is known to be near 0.8 nm. Thus, the length of the PBDT rods can be estimated by application of the Onsager theory using the known I-N transition concentration. This procedure yields rod contour lengths of several hundred nanometers, which varies depending on the molecular weight of the synthesized PBDT.

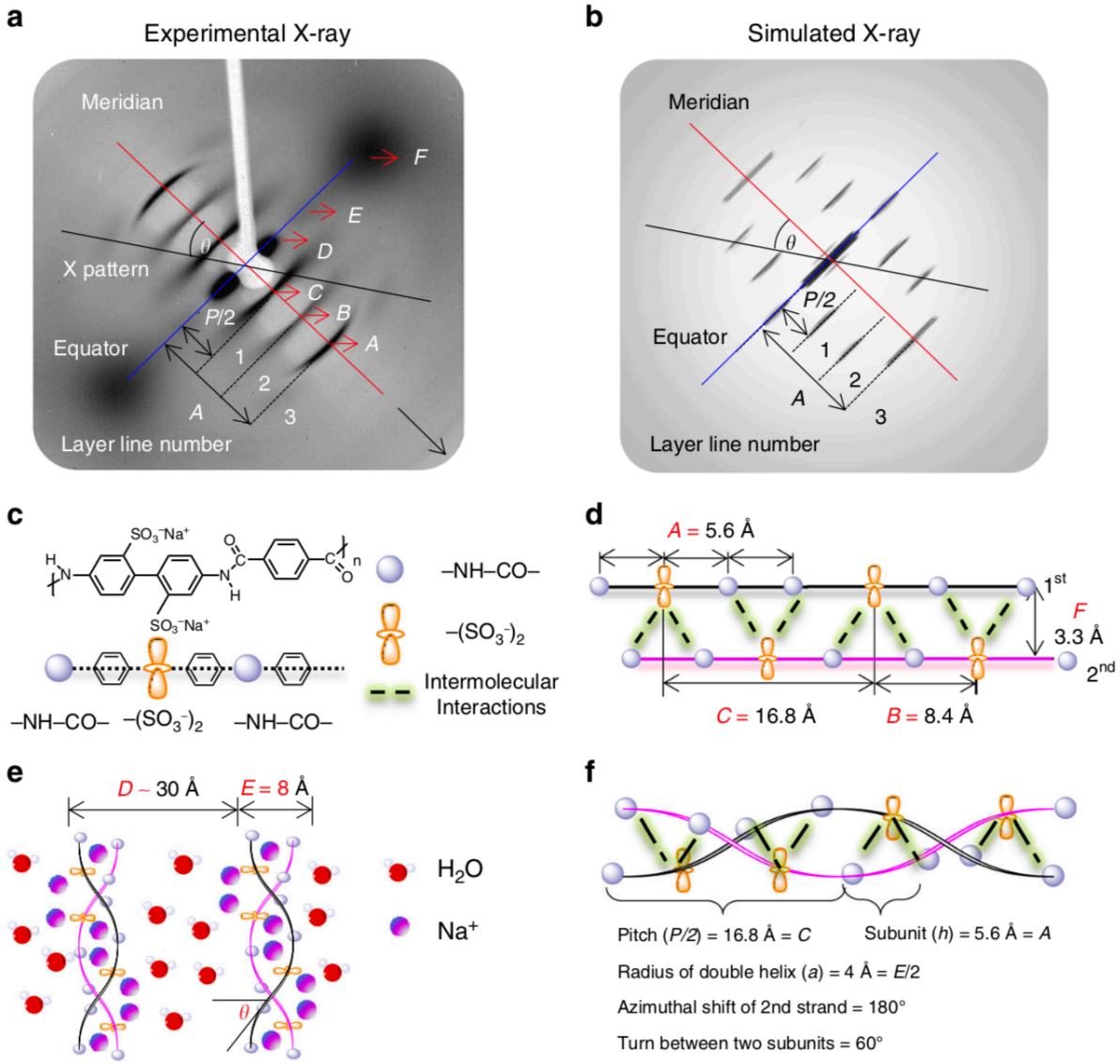

Figure 1.12. X-ray scattering data and analysis leading to the double helical structural model of PBDT self-assembly. (a) Experimental X-ray scattering of a 20 wt.% magnetically aligned PBDT solution in water. (b) Simulated X-ray scattering using the software package HELIX. (c) Chemical structure and schematic representation of PBDT. (d) Constituent structural length scales and physical interactions between PBDT chains. (e) In aqueous solution, the helical dimers are positionally localized at a concentration-dependent correlation length due to the electrostatic repulsion between helical dimers. (f) Assignment of structural length scales and intra-dimer conformation from analysis of the X-ray scattering. Reprinted with permission under Creative Commons CC BY license from Springer, Nature Communications, Double helical conformation and extreme rigidity in a rodlike polyelectrolyte, Wang, Y.; He, Y.; Yu, Z.; Gao, J.; Ten Brinck, S.; Slebodnick, C.; Fahs, G. B.; Zanelotti, C. J.; Hegde, M.; Moore, R. B.; Ensing, B.; Dingemans, T. J.; Qiao, R.; Madsen, L. A., 2019.[67]

1.5. POLYMER ELECTROLYTE MEMBRANES

With the knowledge of the structure and molecular alignment of PBDT rods in solution and the solid-state established from these earlier works, Wang et al. prepared a novel type of ion gel with PBDT and a room-temperature ionic liquid (IL).[68] Ion gels fabricated with ILs are of interest for their use in a variety of transport applications, such as solid-state battery membranes, proton exchange membranes, and gas separation membranes. A combination of high modulus, derived from the polymer, and high ionic conductivity, derived from the IL, is considered to be a key factor in designing next-generation devices for energy storage and generation. In this work, an IL was poured on top of a magnetically aligned nematic PBDT in water within a 5 mm glass tube and a viscoelastic interface forms between the two solutions, preventing convective mixing. Instead, due to the concentration gradients set up by this process, the IL and Na^+ ions undergo an ion exchange process, shown in **Figure 1.13a**. After equilibration, a portion of the native Na^+ ions are replaced within the PBDT nematic monodomain (**Figure 1.13b**) and results in a solid ion gel at very low polymer concentrations (5—20 wt.%).

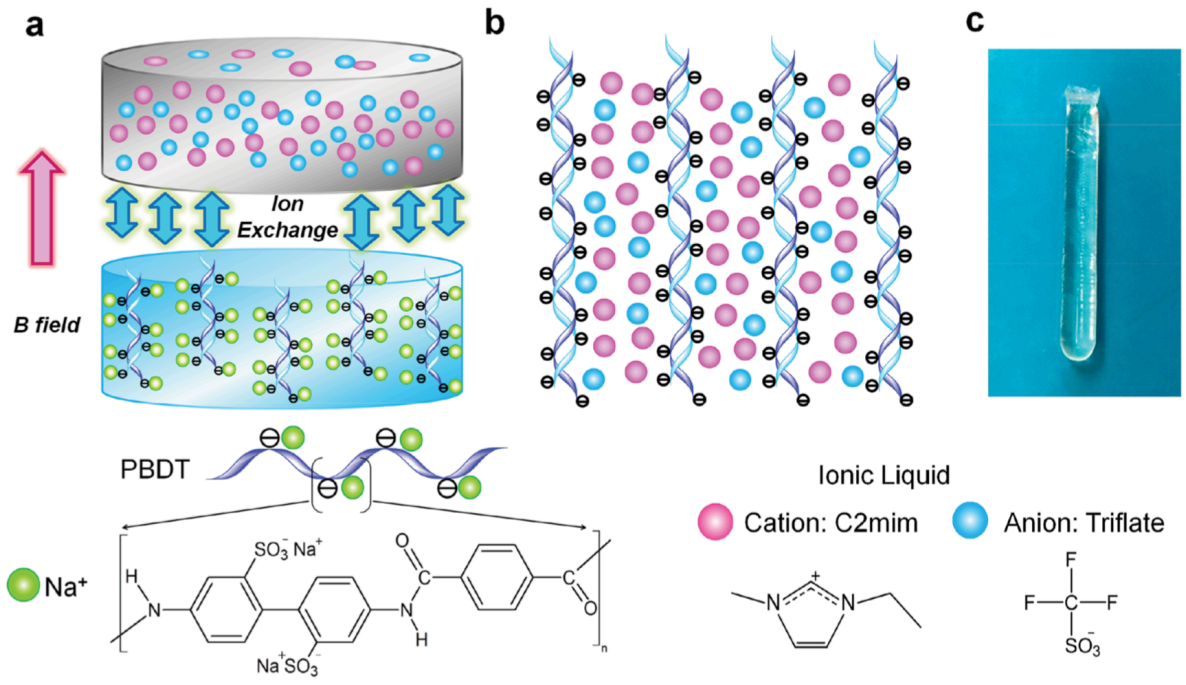

Figure 1.13. Liquid crystalline ion gels formed from PBDT and a room-temperature ionic liquid (IL). (a) Ion exchange between the Na^+ ions within the nematic PBDT monodomain and the IL phase in the presence of a magnetic field. (b) After ion exchange, IL condenses along the backbone of the PBDT helical assemblies. (c) Solid ion gel after ion exchange of the Na^+ counterions with IL. The polymer chains are nematically aligned along the long axis of the cylinder. Reprinted from *Adv. Mater.*, 28, Wang, Y.; Chen, Y.; Gao, J.; Yoon, H. G.; Jin, L.; Forsyth, M.; Dingemans, T. J.; Madsen, L. A., Highly Conductive and Thermally Stable Ion Gels with Tunable Anisotropy and Modulus, 2571-2578, Copyright 2016, with permission from John Wiley & Sons, Inc.[68]

The ionic conductivity of the IL within the polymer matrix and electrochemical stability of these materials was investigated with PFG NMR. At polymer concentrations of 5 wt.%, the ionic conductivity was ~8 mS cm^{-1} and was isotropic with respect to the initial alignment direction. At a higher concentration of 21 wt.%, the ionic conductivity was reduced to 4 mS cm^{-1} along the alignment direction with an anisotropy ratio of ~3.5. Note that the pure IL possesses an ionic conductivity of 11 mS cm^{-1}, meaning that the ion transport within the PBDT-IL materials is only minimally restricted in the presence of the PBDT network. Remarkably, the elastic modulus of these PBDT-IL gels was reported at room temperature to range from 20 MPa at 5 wt.% PBDT to

up to 2 GPa at room temperature. This extreme combination of both high ionic conductivity and high elastic modulus suggests a promising route towards high-performance membrane materials utilizing PBDT and ionic liquids.

The role of hydrogen bonding on the physical properties of these PBDT-IL gels was investigated by attempting to fabricate the gels using D_2O instead of H_2O. As is well-known, the shorter O-D bond length in comparison to O-H results in D_2O solutions exhibiting stronger hydrogen bonding interactions than H_2O. Interestingly, the authors report that they were not able to prepare well-formed gels while using D_2O instead of H_2O. Thus, they proposed that a balance of hydrogen bonding and electrostatic interactions plays a critical role in the development of the PBDT-IL gels.

In light of this experimental data on high ionic conductivity and high modulus PBDT-IL materials, molecular dynamics (MD) simulations were carried out by Yu et al. to investigate the new PBDT-IL composites.[69, 70] The authors sought to understand the structure and dynamics of the IL cations and anions in the vicinity of the rodlike polymer and what the influence of the residual Na^+ cations is on these properties. The observation window of the MD simulation is shown in **Figure 1.14a**, where the cations (blue), anions (red), and rodlike PBDT assemblies (grey) decorated with regularly spaced, charged sodium sulfonate groups (orange/green) are shown.

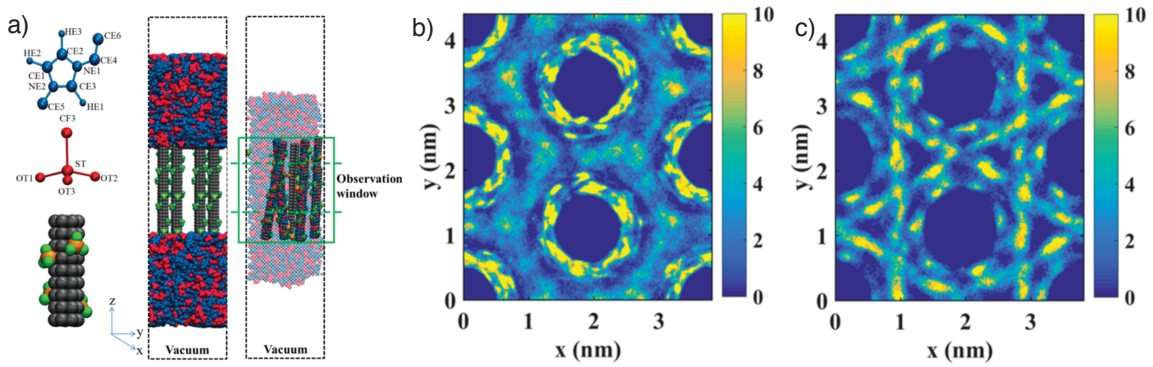

Figure 1.14. Molecular dynamics (MD) simulations of PBDT-IL composite materials. (a) Observation window of rodlike PBDT in the presence of a sea of ionic liquid. (b) Ion density map of cations and (c) anions within the interstitial volume between the PBDT rods. The units of the color scale is nm^{-3}. Adapted with permission from Yu, Z.; He, Y.; Wang, Y.; Madsen, L. A.; Qiao, R., Molecular Structure and Dynamics of Ionic Liquids in a Rigid-Rod Polyanion-Based Ion Gel. *Langmuir* **2017,** *33* (1), 322-331. Copyright 2017 American Chemical Society.

By mapping out the spatial distribution of both cations and anions, shown in **Figure 1.14b** and **Figure 1.14c**, respectively, MD simulations showed the formation of ordered layers around the PBDT rods. Along the main polymer chain, cations strongly localized near the negatively charged sulfonates and anions occupied locations near the uncharged residues, forming a mixed nearest neighbor coordination shell. Past the nearest neighbor correlations, a distinct organization of cations and anions is observed, leading the authors to conclude that the formation of a long-range electrostatic network is, in part, responsible for the high mechanical properties of the PBDT-IL composite materials. However, in these simulations it was assumed that the rods are mobile, not in physical contact with one another, regularly spaced, and spatially homogeneous in these simulations. The extent to which these are valid requires more detailed analysis of the structure and properties of PBDT-IL composites.

1.6. GRAPHENE OXIDE NANOCOMPOSITES

A major research thrust in the materials science community is the design of polymer nanocomposite with enhanced mechanical and thermal properties over the native polymer. Graphene, single sheets of sp^2 carbon, is an attractive nanomaterial for use in reinforcing polymers due to its high elastic modulus ($E \sim 1$ TPa), ultimate strength ($\sigma \sim 130$ GPa), thermal and barrier properties.[71] However, its' tendency to aggregate into 3D stacks, i.e., graphite, at high concentrations reduces the specific surface area and allows inter-sheet sliding via weak van der Waals interactions to dominate as a failure mechanism, rather than bond scission.[72] Both of these effects cause a reduction in reinforcement efficiency, and typically an optimal concentration is found for mechanical properties. As a result, graphene oxide (GO), obtained by chemical oxidation of graphene, has been explored as a nanofiller instead of graphene. This achieves two goals simultaneously, (i) allowing facile dispersion of single layer sheets in polar solvents, including water,[73] and (ii) improved polymer-nanofiller interfacial adhesion due to physical interactions between GO functional groups and polymer.[74] However, GO has a lower modulus ($E \sim 200—250$ GPa) than graphene as a result of partial sp^3 hybridized and lattice defects arising from the oxidation process,[75,76] reducing the maximum theoretical reinforcement in comparison to graphene. In 2011, several reports of liquid crystalline graphene oxide (LCGO) emerged, composed of aqueous dispersions of oxidize graphene sheets.[77-82] The single sheets of GO have high aspect ratio, with lateral dimensions on the 1—10 μm scale, and thickness of 0.8 nm, resulting in an aspect ratio of ca. 10^3. The large aspect ratio enables the formation of a nematic phase at relatively low concentrations, near 0.1 wt.%

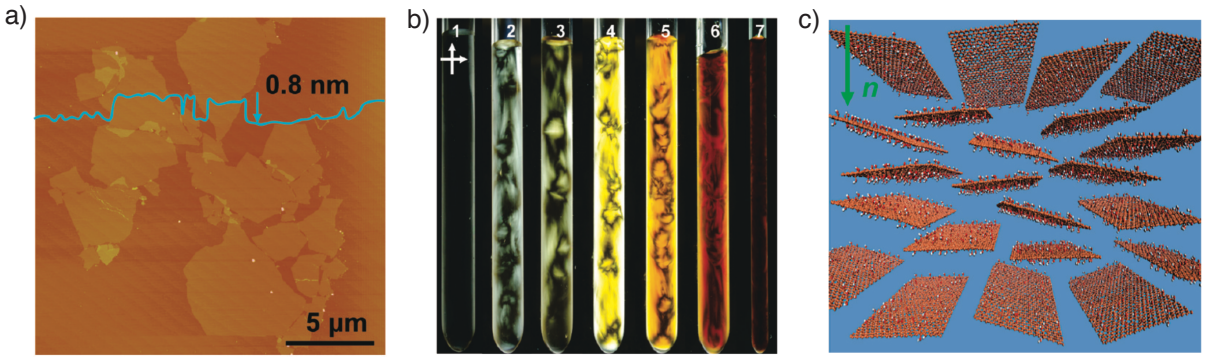

Figure 1.15. Characteristics of single layer graphene oxide (GO) sheets that form a phase of liquid crystalline graphene oxide (LCGO) in water. (a) Atomic force microscopy of single layer graphene oxide sheets deposited on mica. (b) Birefringent dispersions of liquid crystal graphene oxide dispersions in water viewed through crossed polarizers with increasing concentration. (c) Schematic of the orientational order of LCGO sheets within the nematic phase. Reprinted with permission from Xu, Z.; Gao, C., Aqueous Liquid Crystals of Graphene Oxide. *ACS Nano* **2011,** *4*, 2908-2915. Copyright 2011 American Chemical Society.

All reported investigations to date utilizing lyotropic LCGO have combined this material with polymers that are isotropic, i.e., non-liquid crystalline. In one of the first reports of LCGO in 2011, poly(acrylic acid) (PAA) was mixed with LCGO in aqueous solution and hand drawing was used to obtain a nanocomposite fiber.[79] This fiber was birefringent under crossed polars, attributed to the nematic-like orientation of LCGO along the fiber axis. This result inspired a number of reports attempting to produce improved nacre-mimetic fibers consisting of polymer-LCGO, with a "brick-and-mortar" internal structure.[83-86] Hyperbranched polyglycerol-LCGO (HPG-LCGO) wet-spun nanocomposite fibers were prepared by Hu et al. and achieved a Young's modulus of 8 GPa and tensile strength of 125 MPa.[83] Ionic crosslinking with a divalent cation, Mg^{2+}, slightly increased the modulus and tensile strength of the nanocomposite fiber to 10 GPa and 145 MPa, respectively. Later work by the same group demonstrated that using ultra-large LCGO could produce HPG-LCGO nanocomposite fibers with tensile strengths as high as

555 MPa.[84] Chemical crosslinking with glutaraldehyde (GA) provided a further increase in tensile strength to 652 MPa.[84]

Liquid crystal phases of poly(acrylonitrile) (PAN) functionalized LCGO in polar organic solvents were obtained for the first time by Liu et al., and fibers spun from this nanocomposite LC dope achieved a tensile strength as high as 542 MPa and a Young's modulus of 8 GPa.[86] Stiffer PAN-LCGO fibers (80 wt% LCGO, 20 wt% PAN) were obtained by Kim et al. with a Young's modulus as high as 19 GPa, but the tensile strength was only 220 MPa.[87] Using elastomers, Seyedin et al. utilized LCGO-driven alignment for the mechanical reinforcement of polyurethane (PU) nanocomposite fibers.[88] The authors investigated the role of flake size on mechanical reinforcement efficiency and found that the best results were obtained for the largest flake sizes. Another contribution by the same group demonstrated that thermal reduction of PU-LCGO fibers enables electrically conductive elastomer with linear strain sensing abilities up to 70% strain.[89]

LCGO's self-alignment capabilities provides a facile route for large-scale production of aligned nanocomposite films. Towards this end, Yousefi et al. fabricated polyurethane nanocomposites incorporating large-flake LCGO.[90] These nanocomposite films exhibited enhanced in-plane flake alignment at high LCGO concentration, which was confirmed by polarized Raman spectroscopy and in-plane electrical conductivity measurements. Later work by these authors explored epoxy nanocomposites produced by the same method and indicated that this strategy is generalizable to other polymer systems, and useful for applications such as electromagnetic interference shielding.[91, 92] In fact, the self-alignment property of LCGO may actually frustrate electrical percolation and cause an increase in the percolation threshold, providing a new route towards high dielectric constant (high-*k*) materials.[93] In a related report,

Lee et al. fabricated elastomeric poly(dimethylsiloxane) (PDMS) nanocomposites by freeze-drying LCGO films to obtain aligned, porous films and backfilled the material with PDMS precursor.[94] These studies have demonstrated that LCGO can be incorporated into polymer matrixes which promote in-plane alignment during film formation.

Recently, Hegde et al. reported that mixtures of the nematic phase of PBDT and LCGO results in a stable, hybrid liquid crystalline phase that exhibits biaxiality ($^{h}N_b$) above a critical concentration, see **Figure 1.16**.[66] A biaxial phase of rodlike and disklike mesogens, where the directors of the rods and disks are orthogonal, is theoretically predicted to occur over a specific concentration regime.[95, 96] When the concentration of PBDT was too low to form a nematic phase, the polymer simply caused flocculation of GO, suggesting that the nematic phase of PBDT is necessary for stabilization of the hybrid nematic phase. Film casting of the $^{h}N_b$ phase resulted in solid-state nanocomposites that exhibited significant enhancement of the mechanical properties over the neat polymer. In contrast, when the hybrid nematic dispersions were not in the $^{h}N_b$ phase, no mechanical reinforcement was observed.

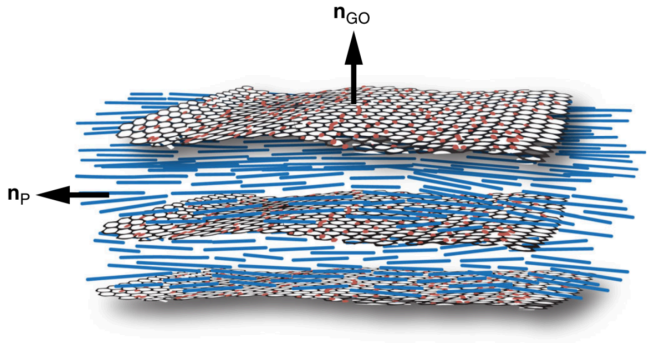

Figure 1.16. Schematic of the perpendicular orientation of the polymer director ($\boldsymbol{n_p}$) and GO director ($\boldsymbol{n_{GO}}$) in the hybrid liquid crystalline phase. Reprinted with permission under Creative Commons CC BY license from Springer, Nature Communications, Strong Graphene Oxide Nanocomposites from Aqueous Hybrid Liquid Crystals, Hegde, M.; Yang, L.; Vita, F.; Fox, R. J.; Watering, R. v. d.; Norder, B.; Lafont, U.; Francescangeli, O.; Madsen, L. A.; Picken, S. J.; Samulski, E. T.; Dingemans, T. J., 2020.

In summary, we have reviewed the preceding literature that reported on the solution structure and applications of the sulfo-aramid, PBDT. However, several open questions remain with respect to the structure, self-assembly and rheological behavior of PBDT solutions that have yet to be elucidated. These questions have significant implication for the processing, solid-state structure, and mechanical properties of PBDT materials that will impact their performance in applications.

1.7. DISSERTATION OUTLINE

While the effect of concentration and ionic strength on the viscosity of PBDT solutions has been reported using capillary viscometry, a thorough understanding of the rheological behavior of PBDT is lacking. In **Chapter 2**, we present the first rheological measurements of fully nematic PBDT solutions in water. Under steady shear, we observe anomalous shear thickening behavior, followed by a hesitation in the viscosity accompanied by an extremely narrow range of negative first normal stress difference. The Peclet number (Pe, shear rate normalized by rod rotational diffusivity) for the onset of shear thickening is in agreement with predictions from previous, high-resolution numerical simulations of the Doi-Edwards-Hess kinetic theory. We interrogate these dynamic responses through shear step-down experiments, revealing a complex evolution of transient responses. Detailed analysis of the stress transients provides compelling evidence that the nematic director undergoes a cascade of transitions and coexistence of periodic states known as kayaking, tumbling, and wagging, before transitioning to steady flow alignment above a critical shear rate. Our results on nematic PBDT solutions reveal the nature of periodic director states and introduce a new model system to study the complex rheology of LCPs.

In **Chapter 3**, we extend our rheological characterization of PBDT to both the isotropic and nematic phases and employ small-angle neutron scattering to quantify the orientational order

under shear. The concentration dependence of the zero-shear viscosity, longest relaxation time, and terminal modulus of quiescently isotropic solutions are compared to the Doi-Edwards theory for hard rods. Within the concentrated isotropic regime, we find a non-monotonic shear rate dependence of the first normal stress difference, reminiscent of a sheared nematic phase. In the fully nematic phase, we investigate the steady-state and transient nonlinear rheological measurements to characterize the flow behavior. The steady-state viscosity as a function of shear rate is characterized by anomalous shear thickening behavior, which we assign as originating from the kayaking response of the nematic director. Utilizing transient shear step-down experiments, we characterize the response of the nematic director by constructing dynamic stress paths, where the shear stress is plotted as a function of the first normal stress difference. The rotation direction of the stress path indicates the relative importance of the viscous and elastic contributions to the stress tensor, which we find undergoes a transition from elastic to viscous at the onset of shear thickening. We conclude that the observed shear thickening behavior of nematic PBDT solutions arises from viscous stress contributions due to director kayaking, rather than an elastic stress contribution due to broadening of the molecular ODF under shear.

In **Chapter 4**, we report on the structure and rheology of nematic PBDT solutions at high concentrations, far above the concentration for fully nematic phase behavior. At rest, the liquid crystalline solutions are kinetically stable against gelation and exhibit low viscosity and shear-thinning behavior. Under steady shear at, or above, a critical shear rate, a physically crosslinked, nematic gel network progressively forms due to linear growth and branching of the rods. The time scale of gelation can be tuned from hours to nearly instantaneously by varying the shear rate above a critical shear rate and solution concentration. The shear-activated gels are distinct in their structure and rheological properties from thermoreversible gels, maintaining their local

positional correlations and nematic orientational ordering. At a fixed concentration, the induction time prior to gelation decreases exponentially with the shear rate, reminiscent of a thermally activated Arrhenius process. This result indicates that shear-activated thermalization of the electrostatically stabilized rods overcomes the energy barrier for rod-rod contact, enabling rod fusion and subsequent irreversible network formation. To our knowledge, this is the first example of irreversible shear-activated gelation in a liquid crystalline polymer, possibly providing a novel route towards a unique microstructure of physically crosslinked rodlike polymer.

In **Chapter 5**, we investigate the structure and mechanical reinforcement of solid-state PBDT nanocomposites reinforced with LCGO. Solution mixing of the nematic phase of PBDT with LCGO results in a homogeneous hybrid liquid crystalline phase. We fabricated nanocomposite films by shear-casting and subsequent in-situ thermal reduction of LCGO to reduced GO (rGO). Wide-angle X-ray scattering of nanocomposite films reveals an increase in PBDT polymer alignment both in-plane and along the casting direction. Scanning electron microscopy and modulus mapping using atomic force microscopy of nanocomposite cross-sections reveals a stratified morphology and enhanced local stiffness of polymer in the vicinity of LCGO sheets. We observed a comprehensive improvement in tensile properties, with an increase in Young's modulus from 16 to 37 GPa, and tensile strength from 210 to 678 MPa at 1.8 vol.% rGO. Dynamic mechanical thermal analysis and time-temperature superposition measurements revealed an increased activation energy of a local polymer relaxation due to the presence of LCGO. Our high-performance nanocomposites exhibit a 26 GPa storage modulus with 1.8 vol.% rGO at 400 °C. These findings demonstrate that extreme mechanical reinforcement of liquid crystalline polymers is achieved by utilizing LCGO through hybrid liquid crystalline dispersions.

In **Chapter 6**, we present a structure-property relationship study of conductive PBDT-IL composites. In the presence of IL, PBDT forms glassy and high aspect ratio hierarchical nanofibrils, which enables fabrication of polymer electrolyte membranes (PEMs) with both high volume fractions of IL and high elastic modulus. We report direct evidence for nanofibrillar networks of PBDT that serves as a matrix for dispersed IL using atomic force microscopy and small- and wide-angle X-ray scattering. These supramolecular nanofibrils form through myriad non-covalent interactions to produce a physically crosslinked glassy network, which boasts the best combination of room temperature modulus (0.1–2 GPa) and ion conductivity (4–8 mS cm^{-1}) of any polymer-IL electrolyte reported to date. The high thermo-mechanical properties of our PBDT-IL composites, i.e., $E \approx 1$ GPa, at temperatures up to 200 °C, enable a wide device operation window with stable mechanical properties. Together, the high-performance nature of sulfo-aramids in concert with the inherent properties of ILs impart PBDT-IL composites with thermal stability up to 350 °C. Thus, nanofibrillar ionic networks based on sulfo-aramids and ILs represent a new design paradigm enabling PEMs with exceptionally high moduli at exceedingly low polymer concentrations.

CHAPTER 2: OBSERVATION OF TRANSITION CASCADES IN A SHEARED LIQUID CRYSTALLINE POLYELECTROLYTE[1]

2.1. INTRODUCTION

Under steady shear, rodlike liquid crystalline polymers (LCPs) in the nematic phase notoriously exhibit either sustained oscillatory motion or steady alignment, both within and outside the shear plane (containing the flow (x) and flow-gradient (y) directions, orthogonal to the vorticity (z) axis).[32,33] These shear responses give rise to remarkable rheological properties. In contrast, when an isotropic phase of LCPs is sheared, stationary alignment in the shear plane always occurs.[97] In the nematic phase under shear, the temporal evolution of the principal axis of the rod orientational distribution function (ODF), termed the nematic director, either traces out closed orbits or sits at a stationary point on the 3D unit sphere.[97,98] The periodic orbits of the director induce oscillations in the shear stress σ_{xy} of a sheared nematic monodomain (a domain free of topological defects in the rod orientation field). Under transient flow of LCPs, such as flow reversal or start-up, the dynamic behavior of the rod ensemble can result in stress overshoots or undershoots, with significant implications for shear-dominated flow processing of these materials.[26,99-107]

Qualitatively, the trajectories of the nematic director are used to classify the shear response of the entire ODF, described as residing within, oblique to, or perpendicular to the shear plane.

[1]This chapter previously appeared as an article in *Soft Matter*. The original citation is as follows: Fox, R. J.; Forest, M. G.; Picken, S. J.; Dingemans, T. J., Observation of Transition Cascades in Sheared Liquid Crystalline Polymers. *Soft Matter*, **2020,** *16, 3891-3901*.

When the director trajectory remains within the shear plane, the following states arise: tumbling (persistent rotation), wagging (finite oscillations about a mean angle α with respect to the flow direction), or flow-aligning (stationary at angle α with respect to the flow direction).[25-27, 29, 97, 98, 108] Simulations by Marrucci and Maffettone restricted to nematic orientation within the shear plane detailed each of these in-plane director states, where the wagging regime is the transition state between director tumbling and flow alignment.[25, 26, 29] Later, unconstrained orientational simulations by Larson revealed new states where the director escapes the shear plane: kayaking (continuous rotation around the vorticity axis akin to the paddle of a kayaker) and logrolling (stationary alignment with the vorticity axis).[109] Subsequent numerical simulations revealed yet new shear-induced states: tilted kayaking (rotation of the peak of the ODF about an axis between the vorticity axis and shear plane), out-of-plane steady (stationary alignment oblique to the shear plane), and chaotic states.[97, 98, 110-115] Moreover, phase diagrams of all stable attractors[3,4] reveal domains of coexistence of multiple stable states for a given strength $\varphi L/D$ of the nematic potential (φ is the rod volume fraction, L/D is the rod aspect ratio) and imposed Peclet number $Pe = \dot{\gamma}/D_r$, where $\dot{\gamma}$ is the shear rate and D_r is the rod rotational diffusion coefficient. We note that, in general, the Doi-Hess-Edwards model simulations do not incorporate the effect of finite rod stiffness, which is known to enhance the tendency for the rods to adopt non-stationary director orbits.[35, 36, 116] This effect from rod flexibility broadens the Pe range of unsteady, periodic director responses.

Historically, experimental results have been almost exclusively interpreted in the context of purely in-plane director states, i.e., tumbling, wagging, and flow alignment. However, it is now known that kayaking, rather than in-plane tumbling, is always selected as the preferred stable director state at low shear rates.[97, 98] For example, Mewis et al. found an anomalous oscillatory

regime in liquid crystalline solutions of poly-γ-(benzyl glutamate) (PBG) in *m*-cresol between the low-shear viscosity plateau and high-shear shear thinning.[117] These authors concluded this was due to the transition from director tumbling at low shear rates, wagging at moderate shear rates, and finally in-plane flow-alignment at high shear rates. On a different model system, work by Lettinga et al. on nematic suspensions of the rodlike *fd* virus invoked the tumbling-to-wagging transition to explain unusual shear thickening behavior.[118, 119] The results on nematic *fd* virus suspensions are notable, in that they exhibit rheological behavior that indicates the elasticity associated with director heterogeneity, i.e., polydomain defect texture, is weak. As such, the imposed shear field strongly couples with the molecular ODF, similar to the situation in numerical simulations, and a broadening of the ODF due to director wagging was suggested to cause the observed shear thickening behavior.

In addition, transient rheological experiments on liquid crystalline solutions of PBG in *m*-cresol by Grosso et al. found a narrow shear rate regime with sustained stress oscillations following step-down from high shear rates.[112] Fourier transformation of the oscillating stress, in comparison to numerical simulations, led the authors to conclude that a combination of director wagging and logrolling must coexist over a certain shear rate regime, consistent with the most current numerical simulation results.[97, 98, 110-115] However, the assignment of director wagging is uncertain because the associated strain period of stress oscillations from the kayaking and wagging states were shown to be identical by Tao et al.[120-122]

Director coexistence, suggested by Grosso et al., is only possible experimentally when sheared nematics exhibit a polydomain texture with orientational defects between monodomains. Furthermore, the initial-boundary conditions of nematic liquids influence the observed dynamic or stationary states at steady-state conditions.[109] Moreover, specific surface anchoring conditions

of the nematic director may lead to spatial heterogeneities in the director dynamics and local orientational order under shear.[123, 124] We note that, even though logrolling is a stationary state with no director oscillations, when the shear rate $\dot{\gamma}$ of an initially flow-aligned sample is suddenly decreased into a lower $\dot{\gamma}$ regime, as in these authors' experiments, transient and long-lived oscillations manifest as a signature of the transition from flow-alignment to logrolling behavior.[112] These results suggest that further experimental investigations must be informed by nematic director phase diagrams developed through high-resolution numerical simulations of the full ODF.[97, 98]

Herein, we report steady-state and transient rheological experiments on a nematic LCP that provide unprecedented signatures of transitions between, and coexistence of, dynamic director states. Moreover, these sheared nematic solutions exhibit an anomalous shear-thickening response that, in conjunction with previously reported numerical phase diagrams, are associated with dynamic transitions between attracting states of the ODF. The discovery of this shear-thickening response in a polymeric nematic is notable, because shear thickening of a liquid crystalline phase has only been previously observed in nematic suspensions of rodlike *fd* virus particles.[118, 119] Importantly, our results lead us to conclude a different origin for the shear thickening regime, namely the kayaking state, rather than director wagging as suggested for nematic *fd* virus. The results presented herein reveal that shear thickening due to director dynamics, as predicted by numerical simulations of nematic monodomains, is experimentally observed if textural elasticity from the polydomain texture is weak.

2.2. EXPERIMENTAL

Synthesis and Sample Preparation. The polymer was synthesized using a modified literature procedure previously reported.[56, 65, 125] The reaction time of the interfacial polymerization was

extended to 16 h, and PEG300 and Na_2CO_3 were eliminated from the reaction mixture. After washing by four reprecipitations into acetone from water, the polymer was dried under vacuum. The intrinsic viscosity of the synthesized PBDT was measured in 96% sulfuric acid using a suspended level Ubbelhode viscometer (CANNON Instrument Company, model E316). The Huggin's equation was fit to the specific viscosity divided by the mass concentration from a dilution series. The intrinsic viscosity was 2.58±0.02 dL g–1 and the Huggins coefficient was 0.52±0.02. Polymer solutions were prepared by mixing PBDT and water and heating at 60 °C for 1 week. The samples were allowed equilibrate for over 1 month before measurements, and no aging effects were noted for the samples over the course of several weeks. Fully nematic phase behavior was observed at solution concentrations at 1.9 wt.% and above by polarized optical microscopy.

Rheology. For all rheological measurements presented, we employed a stress-controlled Anton Paar MCR-302 rheometer operating in strain-controlled mode with a 50 mm $\beta = 0.982°$ cone and plate geometry. Preliminary experiments were conducted with a strain-controlled ARES-G2 rheometer with a dual-head design that decouples the strain application and torque measurements. The presence of steady-state shear thickening was confirmed using both rheometers. Moreover, the qualitative behavior of the stress transients in flow reversals and shear step-downs (i.e., non-strain scaling stress transients and large stress overshoots) were observed with both rheometers. We were only able to accurately measure the small normal forces under shear using the MCR-302, thus we only show the data collected with this rheometer. The temperature was controlled at 25 ± 0.01 °C by a circulating water bath under the bottom stationary plate. A low viscosity oil bath around the sample edges prevented evaporation that enabled sample stability over long time periods. Prior to any rheological measurements, the

samples were pre-sheared for several thousand strain units at the highest shear rate investigated here (1000 s^{-1}) until equilibration of the viscosity. This procedure ensured elimination of the sample's shear history due to sample loading. The calculated N_1 values were corrected for inertia by using $N_1 = [2F_z/(\pi R^2)] + [(3\pi\rho\omega^2 R^4)/40]$, where $\omega = \beta\dot{\gamma}$ is the angular rotation rate.[126] The baseline in N_1 was determined by taking the average of the instrumental background for 100 s before and after measurement at each shear rate. During steady shear, N_1 was averaged over at least 500 strain units at steady state, after decay of the initial stress transient.

Small-angle X-Ray Scattering. SAXS measurements were taken of a 2.8 wt.% PBDT solution in a thin-walled boron-rich 1.5 mm diameter capillary (Charles Supper) with a SAXSLab Ganesha equipped with a Cu 50 kV Xenocs Genix ULD SL X-ray source producing an incident X-ray beam of λ = 1.54 Å and a 2D detector. The detector chamber is evacuated to 10^{-2} mbar to reduce scattering from air. A sample-to-detector distance of 431 mm was used, and the 2D scattered intensity was azimuthally averaged over the scattering vector range of q = 0.05–0.13 $Å^{-1}$ using the Nika package for Igor Pro 8.[127]

2.3. RESULTS AND DISCUSSION

2.3.1. Nonlinear Transient and Steady-State Rheology

The LCP we investigate is a sulfonated all-aromatic polyamide (sulfo-aramid), poly(2,2'-benzidine-4,4'-disulfonyl terephthalamide) (PBDT), which self-assembles into helical rodlike assemblies (rods) with a diameter D = 0.8 nm when dissolved in water.[56, 58, 62, 65-68, 125] We show the molecular structure and a schematic of the PBDT rods in **Figure 2.1a**. Fitting the 1D SAXS intensity as a function of q in the high-q regime with the form factor of a rigid rod with a Gaussian monomer radial distribution function, where the intermolecular scattering contribution is negligible, reveals the slender cross-sectional dimension of the PBDT rods

(**Figure A.1**). The high-aspect-ratio of PBDT rods is exemplified by the low isotropic-nematic (I-N) transition concentration, $c^* = 1.2$ wt.%, and threshold for a fully nematic phase at $c^{**} = 1.9$ wt.%, confirming the large length of the rodlike assemblies.

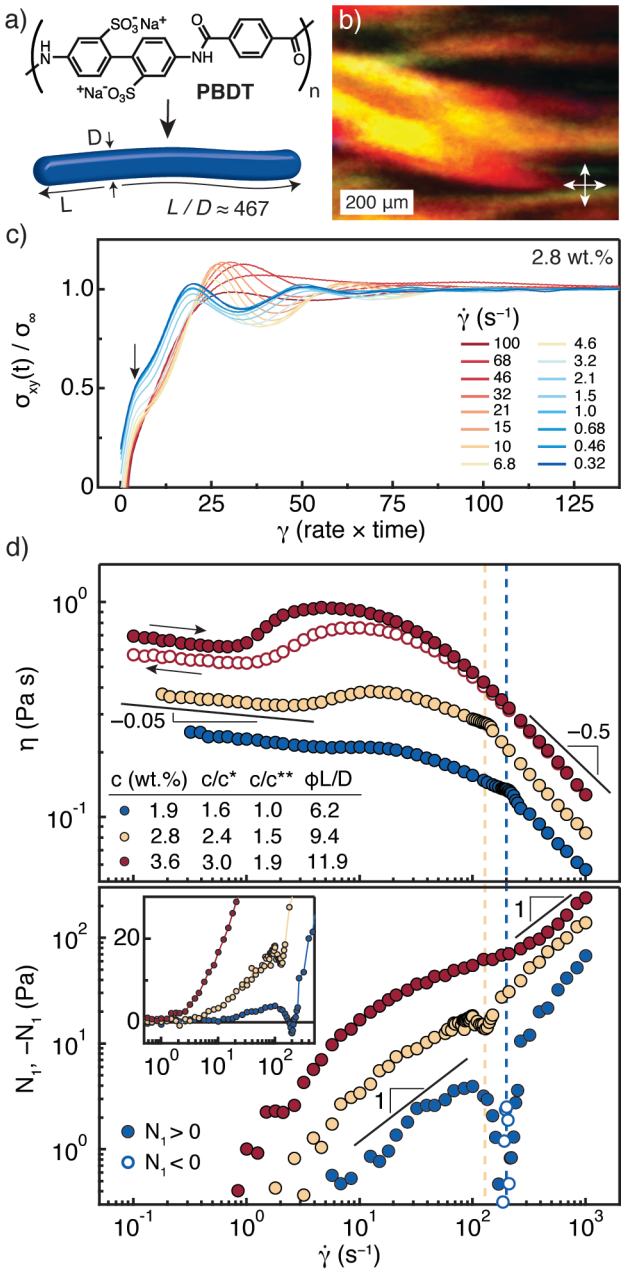

Figure 2.1. Characterization of the transient and steady-state nonlinear rheology of nematic PBDT rodlike assemblies in water. (a) Molecular structure and self-assembly of PBDT into rodlike assemblies.

(b) Polarized optical micrograph of the polydomain texture of a 2.8 wt.% PBDT nematic solution in water. (c) Normalized shear stress $\sigma_{xy}(t)/\sigma_{\infty}$ following flow reversal of a 2.8 wt.% solution at shear rates $\dot{\gamma}$ indicated in the figure legend. (d) Steady-state shear viscosity η (*top*) and first normal stress difference N_1 (*bottom*) versus $\dot{\gamma}$ for nematic PBDT solutions. Open circles indicate decreasing $\dot{\gamma}$ (*top*) and negative N_1 values (*bottom*).

To estimate the PBDT rod dimensions, we employ the Onsager relation to the I-N concentration, given as $\varphi^* = 4/p$, where φ^* is the critical volume fraction, and $p = L/D$ is the aspect ratio of the rigid rod.[16, 21] This relationship provides an estimate of the aspect ratio of the constituent anisotropic rods that induce the formation of the nematic phase. Similarly, Picken and coworkers employed the Onsager relation to estimate of the dimensions of similar rodlike supramolecular assemblies of sulfonated derivatives of the well-known aramid, poly(*para*-phenylene terephthalamide) (PPTA).[51, 53] Assuming a density of PBDT of 1.4 g mL^{-1}, then $\varphi^* = 0.0085$ and $p = 467$. The diameter of PBDT rods is ~0.8 nm; thus, the estimated L is 373 nm. This value for L should be taken as an estimate of the contour length (l_c) of the PBDT rods studied here, as higher molecular weight PBDT has been shown to result in a lower I-N transition concentration.[128] Thus, the nematic PBDT rods studied here likely have l_c smaller than their persistence length (l_p), although exact values for l_p of PBDT rods in aqueous solution have not yet been reported.

In **Figure 2.1b**, we show a polarized optical micrograph of a 2.8 wt.% PBDT solution viewed within a 200 μm pathlength rectangular glass capillary. The Schlieren texture confirms liquid crystallinity, and the unusually large domains on the order of 100 μm suggests that the stresses arising from distortions of domain boundaries (i.e., Frank elasticity) are small in the quiescent state.[30] Frank elastic stresses, which contribute to the total stress of the flowing nematic, arise from gradients in the nematic director (i.e., the polydomain texture with disclinations/defects

between monodomains).[30, 129] Stresses due to distortion of these disclinations under shear also contribute to the total stress measured.[30, 130] Observations of sheared thermotropic nematics where a sudden proliferation of disclinations at a critical shear rate have been made,[131] but shear thickening behavior directly associated with these defects has not been found.[130] The length scales involved in these two contributions are mesoscopic in nature, on the order of 1—10 μm.[132] Here, we observe that the domain features arising from disclinations are at least an order of magnitude greater in size than typically observed, similar to the observations of Lettinga et al. made on nematic *fd* virus suspensions,[118] and expect their contribution to the total stress will be correspondingly lower.

While we have not investigated the defect texture under shear of nematic PBDT solutions, our rheological measurements suggest that the stress contribution from director gradients are not dominant over experimentally accessible shear rates. First, we do not observe any evidence of so-called "Region I" shear thinning,[133] which is characterized by a shear thinning exponent of the steady-state viscosity near –0.5 at low shear rates.[134] In model LCPs, such as PBG, the nematic polydomain defect texture contributes significantly to the rheological response, even when Region I shear thinning is not observed.[135-138] The stress contribution from the defect texture manifests itself by exhibiting strain-scaling behavior (i.e., collapse of the data when the transient normalized shear stress $\sigma_{xy}(t)/\sigma_{\infty}$ is plotted as a function of applied strain $\gamma = \dot{\gamma}t$ following flow reversal) under transient flow reversal experiments in the Newtonian regime of the flow curve.[138] This strain scaling, generally expected for a solid-like response, is attributed to the viscoelastic response being dominated by the non-Brownian length scale associated with the nematic domain size.[134, 139-141]

In **Figure 2.1c,** we show transient flow reversal measurements where the flow direction is suddenly reversed without changing the shear rate $\dot{\gamma}$ for $c = 2.8$ wt.%. The transient $\sigma_{xy}(t)/\sigma_{\infty}$ versus γ following flow reversal do not exhibit strain scaling behavior over any $\dot{\gamma}$ investigated. It is possible that strain scaling behavior may be recovered at lower shear rates, however the long times required for stress equilibrium and instrumental torque resolution precluded us from further investigation. Thus, the response of PBDT solutions under shear is dominated by coupling of the molecular orientational distribution function (ODF) to the imposed shear field, similar to the behavior observed in nematic *fd* virus suspensions under shear.[118, 119]

Further, we observe a shoulder in $\sigma_{xy}(t)/\sigma_{\infty}$ at small γ, labeled by the vertical arrow, that has been suggested to arise purely from the nematic fluid and distinct from the response of the nematic texture.[137] It is interesting to observe that the shoulder in $\sigma_{xy}(t)/\sigma_{\infty}$ after reversal is strongly modulated as a function of $\dot{\gamma}$, even in the pseudo-Newtonian regime (for $c = 2.8$ wt.%, the pseudo-Newtonian regime spans the $\dot{\gamma}$ range of $0.32—3.2$ s^{-1}). In contrast, this shoulder remains constant within the strain scaling regime of highly textured nematics, which indicates that the molecular ODF is unperturbed by the shear flow.[134, 139-141] The strong dependence of this shoulder in flow reversals further supports our conclusion that the molecular ODF of the nematic PBDT rod ensemble couples to the shear field over the entire $\dot{\gamma}$ regime investigated here.

Through brief analysis of flow reversal experiments, we have established that the viscoelastic response of PBDT solutions is distinct from other polymeric LCPs in that the contribution of the polydomain nematic texture is low. Further differences arise when analyzing the steady-state flow curves of PBDT solutions under nonlinear, steady shear. We plot the steady-state viscosity η (*top*) and first normal stress difference N_1 (*bottom*) of nematic PBDT solutions at $c = 1.9$, 2.8, and 3.6 wt.% in **Figure 2.1d**. The reduced concentrations c/c^* and c/c^{**} and strength of the

nematic potential $\varphi L/D$ are given in the figure legend. Note that all flow curves were constructed after a pre-shear (see Experimental section), and no significant hysteresis was observed upon increasing or decreasing $\dot{\gamma}$ for the two lower concentrations. However, for the 3.6 wt.% solution, we plot flow curves with both increasing (*filled circles*) and decreasing (*open circles*) $\dot{\gamma}$, indicating a slight reduction in the magnitude of shear thickening response and low-shear rate viscosity after exposure of this sample to prolonged shearing at high shear rates.

Each sample exhibits three distinct regimes of η versus $\dot{\gamma}$ behavior: a weak shear thinning regime at the lowest $\dot{\gamma}$ (power law slope ≈ –0.05), followed by a continuous and reversible shear thickening, and finally shear-thinning at the highest $\dot{\gamma}$ used in the experiment (power law slope ≈ –0.5). A hesitation in the flow curve precedes high-$\dot{\gamma}$ shear thinning for the two lower concentrations, indicated by the vertical dashed lines, while the transition is smooth at $c = 3.6$ wt.%. This hesitation is a classic signature of the anomalous flow behavior of LCPs, and signifies the onset of flow-alignment, or "arrested tumbling" as termed by Larson,[142] as observed in nematic PBG[143, 144] and HPC[105] solutions under shear.

The unusual feature in the flow curves of nematic PBDT solutions is the existence of a pronounced shear thickening response in the moderate $\dot{\gamma}$ regime. The shear thickening response is qualitatively different than the behavior expected from the formation of a shear-induced network, as in dilute wormlike micelle solutions. In shear-thickening micellar solutions, the viscosity generally exhibits an induction period (prior to an increase in viscosity)[145], accompanied by sustained temporal stress fluctuations under steady shear.[145, 146] Moreover, shear-induced network formation is expected to result in a strong hysteresis effect, with increased viscosity and strong power law behavior as $\dot{\gamma}$ decreases towards zero.[147, 148] In contrast, the lack of hysteresis in the $c = 2.8$ wt.% solution, which exhibits pronounced shear thickening, is not

consistent with network formation. In addition, if network formation would occur at high $\dot{\gamma}$, we would expect that the final viscosity of the $c = 3.6$ wt.% sample would be higher than the initial viscosity, not lower (as we observe), when the shear rate is reduced from high to low rates during the hysteresis loop shown in **Figure 2.1d** (*top*).

We considered the influence of secondary flow instabilities or instrumental artifacts as a source of the observed shear thickening. First, we note that we observed shear thickening in the steady-state flow curves using two different rheometers (TA Instruments ARES-G2 and Anton Paar MCR-302). The geometries utilized for the two instruments have different surface treatments and configuration of the geometry sample edges. In the case of the ARES-G2, the lower plate (60 mm diameter, hardened chromium surface) extends beyond the diameter of the 50 mm cone (stainless steel surface), while in the case of the MCR-302 the lower fixture and upper geometry (both stainless steel surfaces) were exactly matched in terms of their diameter. It is unlikely that the exact same sample edge conditions between the two rheometers was realized; thus, edge effects were eliminated as an origin. Second, secondary flows from elastic instabilities are known to develop[149] that can result in apparent shear thickening. However, the shear rates for which we observed shear thickening do not exhibit characteristics of this well-known flow instability, such as appearing after prolonged shearing.[150] Finally, while we have not measured the velocity profile directly for the solutions reported herein, radial pressure measurements of sheared nematic PBG solutions are consistent with a viscometric flow profile,[151, 152] and we did not observe any signatures of edge fracture.[153] Thus, we turn to explain the observed shear thickening in terms of the dynamics of the nematic orientation distribution under shear.

If the observed shear thickening originates from a transition in the dynamics of the nematic director, we expect the onset to occur at similar Pe for all solutions, with variations that are

predicted by numerical simulations of the rheological properties of these states.[97, 98] We calculated the Pe for the onset of shear thickening by scaling the onset $\dot{\gamma}$ to the rotational diffusion coefficient for a rod in a nematic, semidilute solution, given as $\overline{D}_r \cong 10^3 D_{r,0}(\bar{c}L^3)^{-2}\left(1 - S_{eq}^2\right)^{-2}$, where $D_{r,0} = 3k_BT\ln(L/D)/(\pi\eta_s L^3)$ is the diffusion coefficient for a rod in dilute solution, k_BT is the thermal energy, η_s is the solvent viscosity, $\bar{c}$ is the rod number density, and S_{eq} is the equilibrium scalar order parameter.[6] While rigorous calculation of $\overline{D}_r$ requires explicit consideration of the orientational dependence, assuming it is constant does not qualitatively change the flow-phase diagram in numerical simulations.[98, 109] For PBDT solutions deep into the nematic phase, as is the case here, S_{eq} is high and does not vary with c significantly;[62] we use a value of S_{eq} = 0.886 we measured by small-angle X-ray scattering (see **Figure A.2**). This value of S_{eq} is close to the saturation value observed in nematic *fd* virus suspensions.[48] The calculated $\overline{D}_r$ values are 1.95, 0.84, and 0.53 s^{-1} for $c = 1.9$, 2.8, and 3.6 wt.%, respectively. In our measurements, the $\dot{\gamma}$ for the onset of shear thickening decreased by approximately one decade by increasing c by a factor of ~2. However, we find that the onset of shear thickening occurs at an approximately constant Pe near 3 for each of the three solutions studied. This range of Pe has been correlated with bifurcations among stable director states by numerous numerical simulations.[27, 97, 98, 109, 110, 113-115, 154] Despite the fact that there are a number of approximations in this calculation (i.e., the L/D value is deduced from Onsager theory for rigid rods, neglect of electrostatic contributions on $\overline{D}_r$, use of S_{eq} instead of experimentally measured order parameter under shear from the 1—3 and 1—2 shear planes, as done recently for *fd* virus[14]), we conclude that the origin of shear thickening lies with dynamical director state transitions that depend on a critical Pe.

We gain further insight into the steady-state flow curve by the N_1 dependence on $\dot{\gamma}$ and how N_1 correlates with changes in η, plotted in **Figure 2.1d** (*bottom*). We took extreme care to control for the instrumental drift in the N_1 baseline during the steady-state measurements and ensured correct determination of the true zero level of N_1.[155] Given that the absolute values of the normal force F_z were small, we averaged over at least 500 strain units, and up to 2500 strain units for small values of F_z, after complete decay of the initial stress transient to improve resolution in N_1. Moreover, we applied standard corrections to the N_1 data to account for sample inertia, which are known to cause spurious negative N_1 regions.[126, 144] For all three solutions, N_1 scales linearly at low and high $\dot{\gamma}$, in accordance with prior experiments on other LCPs.[143, 156] The lowest concentration, $c = 1.9$ wt.%, shows the most salient features between the three solutions studied here. After reaching a local maximum near $\dot{\gamma} = 100$, N_1 then sharply decreases and becomes negative over a narrow range of $\dot{\gamma}$ and reaches its minimum value at 200 s^{-1}, before sharply transitioning back to positive values. The inset of **Figure 2.1d** (*bottom*) shows a semi-log representation evidencing the positive-negative-positive transition in N_1 for $c = 1.9$ wt.%.

The regime of negative N_1 is a hallmark feature in the shear rheology of LCPs, and arises from, in general, a broadening of the molecular ODF.[27, 29] Tao et al. have shown through event-driven Brownian dynamics simulations that broadening of the ODF due to director wagging originates from the loss of synchrony between the constituent rod motion and the director, thus decoupling the mesogens and director motion.[120] This loss of synchrony causes a broadening of the molecular ODF, and results in a normal force that pulls the rheometer plates together.[29] Note that, as we have discussed earlier, multiple director states may coexist over certain shear rate regimes, and this fact must be kept in mind in the following discussion. Given this fact, we conclude that the signatures of director wagging behavior are evident in nematic PBDT solutions

at $\dot{\gamma}$ for which we observe negative N_1. Interestingly, we note that this regime is highly localized in $\dot{\gamma}$, in contrast to other LCPs that exhibit nearly one decade of $\dot{\gamma}$ with a negative N_1, depending on the solution concentration.[105, 143, 144, 157]

With increasing concentration, the regime of negative N_1 is eliminated, but the $c = 2.8$ wt.% retains a pronounced dip in N_1 at a slightly lower $\dot{\gamma}$ than the most negative value of N_1 at $c = 1.9$ wt.%. To the best of our knowledge, the observation of a dip in N_1, while remaining positive, has only been previously observed in highly concentrated solutions of HPC in m-cresol.[153] Baek et al. suggested that either a change in director dynamics or an increase in the viscous stress contribution, in contrast to the elastic stress, would explain the elimination of a negative N_1 regime, while still exhibiting a dip in N_1. However, the enhanced contribution of the viscous stress under flow could not explain the complete elimination of a local minimum in N_1, as observed in the melt phase of HPC[153] and the PBDT solution at $c = 3.6$ wt.% studied herein, and possibly reflects a change in the nature of the director dynamics. Here, we argue that director wagging with a negative contribution to the N_1 signal is likely present at $c = 2.8$ wt.%, but in coexistence with a director state that contributes strongly to a positive N_1. At the higher solution concentration, we suggest that director wagging is completely suppressed, similar to the behavior of thermotropics that do not exhibit a regime of negative N_1.[153, 158, 159] It is remarkable to observe that a relatively low concentration PBDT solution, around 3 wt.%, eliminates the director wagging behavior in a potentially similar manner to thermotropic LCPs.

Nematic *fd* virus suspensions, a type of rodlike particle, also exhibit steady-state shear thickening, which Lettinga et al. attributed to the director wagging state.[118, 119] Moreover, they found strong stress oscillations in flow reversals with a minimum in strain period at the peak in the steady-state η. These authors suggested that the broadening of the molecular ODF from

director wagging caused the increase in steady-state η. Unfortunately, the viscosity of *fd* virus suspensions was too low to measure N_1, which would provide evidence for the transition from director tumbling to wagging in case of the presence of a negative N_1 regime. It is important to note that the shear thickening observed by these authors exhibited both qualitative and quantitative differences to the shear thickening shown here by PBDT solutions. First, the relative magnitude of η change from shear thickening in *fd* virus suspensions was smaller, around 10—15%, compared to ~50% observed for PBDT at $c = 3.6$ wt.%. Second, the shear thickening observed in *fd* virus occurred over a very narrow range of $\dot{\gamma}$, and immediately preceded high-$\dot{\gamma}$ shear thinning, whereas we observe a broad $\dot{\gamma}$ regime for shear thickening prior to the hesitation in η, when present. Third, the onset $\dot{\gamma}$ for shear thickening in nematic *fd* virus suspensions increased with increasing c, in contrast to decreasing $\dot{\gamma}$ with c in PBDT solutions. These qualitative differences suggest that a different director state is responsible for the shear thickening observed in *fd* virus suspensions in comparison to the shear thickening of PBDT solutions.

2.3.2. Assignment of Director State Transition Cascade

For nematic PBDT solutions, the signatures associated with the transition from coexistence of kayaking and tumbling to kayaking and wagging, i.e., the tumbling-to-wagging transition referred to by several authors,[117,118] are observed here between $\dot{\gamma} \approx 100—200$ for $c = 1.9$ wt.% and are well resolved from the shear thickening regime that occurs at lower $\dot{\gamma}$. Exhaustive numerical simulations by Forest et al. provide a guide for interpretation of the rheological behavior of nematic rodlike particles under shear, and we utilize their chosen terminology for the director states.[97,98] Using these results in conjunction with our rheological measurements, we divide the steady-state flow curve for the $c = 1.9$ wt.% solution and assign the cascade of

transitions in the nematic director response in **Figure 2.2**. We caution that these assignments remain tentative, since small changes in concentration can dramatically change the series of stable directors possible for the nematic fluid under shear.

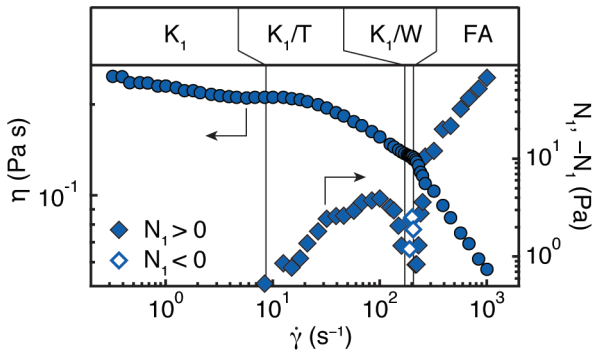

Figure 2.2. Steady-state flow curve of nematic PBDT in H_2O at $c = 1.9$ wt.%, with the assignment of director state transitions as guided by the simulations of Forest et al.[97,98] The following director responses are suggested to occur as $\dot{\gamma}$ is increased: kayaking (K_1), kayaking and tumbling (K_1/T), kayaking and wagging (K_1/W), and steady flow alignment (FA).

At low $\dot{\gamma}$, kayaking is the unique stable state and exhibits an onset of shear thickening near $Pe = 3$, with increasing N_1 values, at a solution concentration slightly above the fully nematic concentration. The transition between bi-stable kayaking/tumbling, where kayaking and in-plane tumbling coexist, is predicted to occur at the transition between shear thickening and shear thinning in the steady-state viscosity. The transition from bi-stable kayaking and tumbling to kayaking and wagging occurs at the crossover from positive to negative N_1, occurring between $\dot{\gamma} = 160$ and 180 s^{-1}. At the maximum negative value of N_1, kayaking and wagging states yield to flow alignment. At $\dot{\gamma}$ above the onset of flow alignment, the viscosity monotonically decreases in a power law manner as the larger shear rate induces a narrower molecular ODF. We note that tilted kayaking and an out-of-plane steady state are predicted to be observed prior to flow

alignment, but we cannot resolve rheological signatures that would provide evidence for them in these data.

Another director state that has been shown to be shear thickening is the logrolling state, where the average rod orientation is fixed along the vorticity axis. The logrolling attractor exhibits weak shear thickening and positive N_1 behavior, similar to kayaking which rotates about the vorticity axis. This director state is predicted for high enough concentrations and low $\dot{\gamma}$. Indeed, logrolling has been observed in a thermotropic polyester under shear; however, shear thickening was not observed.[158, 160] Here, the magnitude of the viscosity increase we observe in nematic PBDT solutions at high concentrations with increasing $\dot{\gamma}$ is more consistent with the predictions for kayaking, rather than logrolling.

2.3.3. Transient Shear Step-Downs

To gain further insight into the unique rheological behavior of nematic PBDT solutions, we performed shear step-down transient experiments. First, we subject the sample to a high $\dot{\gamma}$ in order to prepare a steady flow-aligned ODF and then introduce a step change in $\dot{\gamma}$ without changing direction. This type of experimental protocol previously revealed an anomalous oscillatory regime associated with the wagging state in nematic PBG solutions in *m*-cresol.[112, 117] We used an initial shear rate $\dot{\gamma}_i$ that was well within the flow-alignment regime, as determined by the local minimum in N_1 from the steady-state flow curves, to ensure a homogeneous and stationary director field. For $c = 1.9$ and 3.6 wt.%, we utilized $\dot{\gamma}_i = 370$ and 100 s^{-1}, respectively, as shown by the arrows in **Figure 2.3a** and **Figure 2.3b** (*top*). Exact calculation of the Pe that these $\dot{\gamma}_i$ correspond to is unreliable, as we have already shown that the molecular ODF is coupled to the shear field, thus $\overline{D}_r$ is a function of $\dot{\gamma}$ through its' dependence on S. After a steady state is reached at $\dot{\gamma} = \dot{\gamma}_i$, $\dot{\gamma}$ is reduced to a lower $\dot{\gamma} = \dot{\gamma}_f$ without changing the flow

direction, and the transient stress is monitored as a function of total strain applied $\gamma = \dot{\gamma}_f t$. We have divided the flow curves into zones labeled **I**, **II**, **III**, and **IV** that correspond to the plots of the $\sigma_{xy}(t)/\sigma_\infty$ after step-down, in **Figure 2.3a** and **Figure 2.3b** (*bottom*). Note that these zones simply delineate the regions of $\dot{\gamma}_f$ used in the step-down experiments, and the color gradients correspond to the stress transient curve colors in the figures.

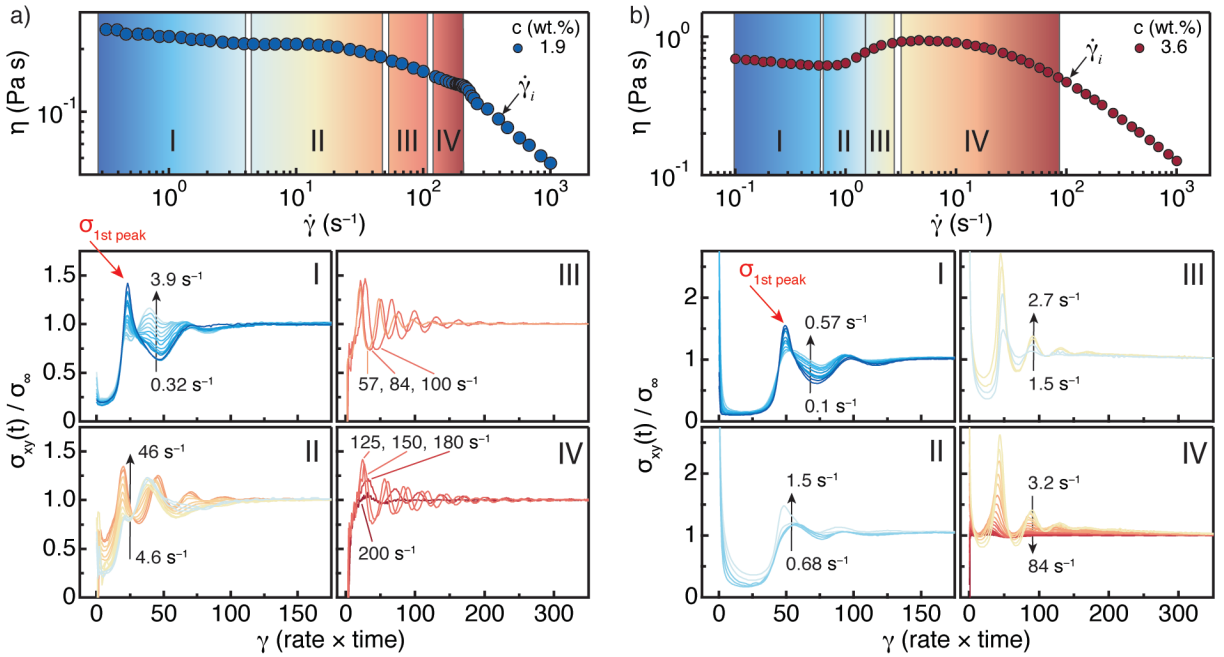

Figure 2.3. Steady-state flow curve (*top*) and normalized transient shear stress $\sigma_{xy}(t)/\sigma_\infty$ as a function of strain γ following shear step-down (*bottom*) at (a) c = 1.9 wt.% and (b) 3.6 wt.%. The initial shear rate $\dot{\gamma}_i$ is indicated by the arrows on the flow curve. The final shear rates $\dot{\gamma}_f$ fall into zones labeled I, II, III, and IV. The zone color gradients labeled on the flow curve and colors of transient stress curves are correlated. Arrows in the plots of the transient stress indicate the direction of increasing $\dot{\gamma}_f$. The stress overshoot of the first peak is labeled by the red arrows (plotted as a function of the final shear rate in **Figure 2.4b**).

Through semi-quantitative analysis of the changes in the stress transient, we identify signatures of transitions in the director response from its' initial flow-aligned state. First, we discuss the transient behavior observed in **Figure 2.3a** (*bottom*) for c = 1.9 wt.%. At low $\dot{\gamma}_f$, corresponding

to the beginning of Zone I, the transient stress is characterized by an initial undershoot near $\sigma_{xy}(t)/\sigma_{\infty} \approx 0.2$, followed by a sharp overshoot that approaches 1.5, then second local minima and maxima, before the oscillations are suppressed at higher γ. As $\dot{\gamma}_f$ is increased through Zone I, the qualitative behavior of the transient stress gradually evolves into a new form. The magnitude of the initial maximum decreases with $\dot{\gamma}_f$ while the peak γ position remains constant. This reduction in the initial peak is concomitant with the emergence of a new, broader peak, with maxima near $\gamma = 40$, that grows in intensity with increasing $\dot{\gamma}_f$ up to 3.9 s^{-1}. This broader peak, which does not show any oscillatory behavior at larger γ, dominates the transient stress at the end of Zone I and beginning of Zone II. With increasing $\dot{\gamma}_f$ in Zone II, the opposite trend occurs as observed in Zone I. The broad peak (near γ of 40) decreases in intensity and the sharp peak (near γ of 20) increases, both maintaining constant γ position. At a $\dot{\gamma}_f$ of 18 s^{-1}, the broad peak (near γ of 40) stops decreasing in intensity and begins to shift to higher γ. This apparent shift in peak position arises from the elimination of the prior broad peak and the emergence of a damped oscillatory signal that dominates towards the end of Zone II. This signal is distinct from the oscillatory behavior observed at the beginning of Zone I, where four peaks are now observed extending out to γ of 70 and 95 at a shear rate of 46 s^{-1}.

Increasing the shear rate into Zone III, the oscillatory behavior becomes more pronounced and the damping is further inhibited. At a shear rate of 57 and 84 s^{-1}, we observe up to 6 oscillations extending out to a strain of ~140. The peak positions and oscillation strain periods between these two $\dot{\gamma}$ are nearly identical. However, with a small increase in shear rate to 100 s^{-1}, we observed a sudden shift of the first peak to higher strain and an increase in oscillation strain period, in addition to a further reduction in oscillation damping. The trend of increasing oscillation strain period and reduction in damping is continued into Zone IV, until at a shear rate of 200 s^{-1} the

oscillatory stress transient is completely suppressed. We note that the suppression of oscillatory behavior at 200 s^{-1} exactly corresponds to the minimum value of N_1 in the steady-state flow curve.

The primary differences between the steady-state flow curve of the $c = 3.6$ wt.% solution in comparison to 1.9 wt.% is the increased magnitude of shear thickening and elimination of the negative N_1 regime prior to flow alignment at high $\dot{\gamma}$. As a result, the zones labeled at 3.6 wt.% are over different $\dot{\gamma}$ regimes than at 1.9 wt.%. However, the qualitative change in the stress transients at 3.6 wt.% with $\dot{\gamma}$ are similar to 1.9 wt.%, but the oscillatory behavior is broader and more damped. The stress undershoots in Zone I and II reach lower values and remain in a low-stress state for larger strain values than at 1.9 wt.%. That is, higher c enables the flow-aligned state to be maintained for larger strain values at low $\dot{\gamma}$ following step-down.

As we have previously discussed, director wagging is associated with the hesitation in the flow curve and negative N_1, observed at $c = 1.9$ wt.%. At 3.6 wt.%, this negative N_1 regime, and the corresponding strongly oscillating stress transients (see Zone IV for $c = 1.9$ wt.%), are eliminated. Moreover, the transition from shear thickening to shear thinning at high $\dot{\gamma}$ for $c = 3.6$ wt.% in the steady-state measurement is reflected in a more gradual elimination of oscillatory behavior in Zone IV with increasing $\dot{\gamma}$. Thus, we conclude the stress transient signature associated with director wagging is present at $c = 1.9$ wt.% but is suppressed at 2.8 and entirely eliminated at 3.6 wt.%.

We further analyze the shear step-down experiments by plotting η normalized to its value at 0.5 s^{-1}, and the normalized stress overshoot value of the first peak, $\sigma_{1st\ peak}/\sigma_\infty$, following step-down as a function of $\dot{\gamma}$ in **Figure 2.4a—b**, respectively. The shear rate dependence of $\sigma_{1st\ peak}/\sigma_\infty$ reports on the nature of the transient behavior of the nematic director as it evolves

from the initial, stationary, flow-aligned state (at high shear rates) to the final, periodic, state at lower shear rates (i.e., kayaking, tumbling, wagging, or coexistence of states). The strong first peak following step-down, labeled with red arrows in **Figure 2.3**, observed at the beginning of Zone I, systematically decreases in its' normalized stress value as the shear rate increases into the beginning of Zone II (i.e., onset of shear thickening). At the onset of steady-state shear thickening, we find that $\sigma_{1st\ peak}/\sigma_\infty$ then rapidly increases in value with increasing shear rate, concomitant with the emergence of long-lived stress oscillations. Thus, we conclude that the shear rate dependence of $\sigma_{1st\ peak}/\sigma_\infty$ and steady-state viscosity are essentially signatures of the same underlying director response.

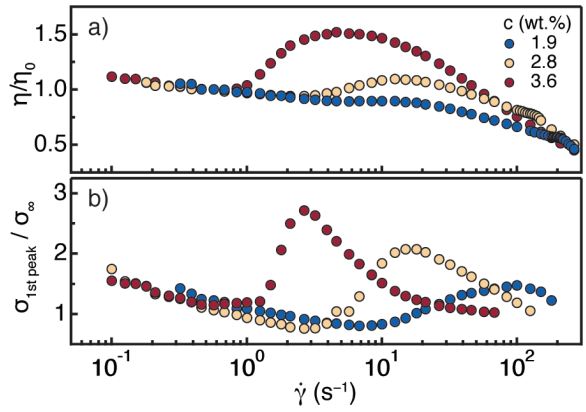

Figure 2.4. Correlation of the steady-state rheological properties with the stress transients following shear step-down. (a) Normalized steady-state flow curve and (b) normalized stress overshoot value of the first peak following shear step-down as a function of shear rate (see red arrows in **Figure 2.3**). The initial shear rates in (b) are 370, 230, and 100 for c = 1.9, 2.8, and 3.6 wt.%, respectively.

At low $\dot{\gamma}$, the normalized η collapse onto each other and follow similarly weak shear thinning behavior with increasing $\dot{\gamma}$ up to ~1 s^{-1}, consistent with similar director dynamics between the three solutions at low $\dot{\gamma}$. As shown previously, the onset of shear thickening occurs at different $\dot{\gamma}$, but similar Pe. The dependence of the stress overshoot on $\dot{\gamma}$ shows that the overshoot values also

collapse at low $\dot{\gamma}$ and decrease with increasing $\dot{\gamma}$ up until the onset of shear thickening. For c = 1.9 and 2.8 wt.%, the stress overshoot dips below unity prior to increasing, while at 3.6 wt.% the stress overshoot is always greater than unity. The shear thickening observed in the flow curve correlates with an increase in the stress overshoot of the first peak. The sharpness of the transition from decreasing to increasing stress overshoot value apparently correlates with the relative magnitude of the steady-state shear thickening response.

To understand this unusual behavior in the stress overshoot, we compare to the results of Mewis et al. on nematic PBG solutions.[117] These authors reported an anomalous oscillatory regime following shear step-down that they attributed to director wagging, in contrast to director tumbling behavior they suggested within the strain-scaling region of the flow curve. The transient stress data following step-downs within a narrow range of $\dot{\gamma}$ exhibited strong oscillations that were damped after γ values greater than 100. Normalization of the transient stresses show the stress overshoot values of the first peaks were very close to unity. Similarly, the flow reversal results of Lettinga et al. on nematic *fd* virus suspensions in the shear rate regime they assign to director wagging show stress overshoot values that reach, at most, normalized stress values of near 1.1.[118] That is, the stress overshoots observed in PBDT solutions that approach normalized stress values in excess of 2.5 (at 3.6 wt.%) following step-downs is inconsistent with the behavior generally associated with the director wagging regime in the literature. As such, we suggest that the large stress overshoots are signatures for the occurrence of the kayaking director state as it evolves from a flow-aligned condition to its' out-of-plane periodic orbit, centered along the vorticity axis. Presumably, the change in director orientation from an in-plane stationary state (flow alignment) to the out-of-plane orbit in kayaking results in

a strong elastic response that manifests as significant stress overshoots in the transient rheological experiments.

Extracting the strain period of the oscillations, which is directly related to the rotational period of the director, is not straightforward as our step-down measurements exhibit complex behavior and evolution with $\dot{\gamma}$. Moreover, manual measurement of the stress oscillations (i.e., strain period between stress peaks) will yield a single oscillation period, when there may be two or more frequency components present.[112] Thus, we decomposed the transient stress into its component frequencies by utilizing a fast Fourier transform (FFT) of the transient oscillatory stress. We show the FFT spectra for $c = 1.9$ wt.% in **Figure 2.5** over a wide range of $\dot{\gamma}_f$. As we integrate over γ in the FFT, the ordinate of the power spectra is the inverse strain period, $P = 1/\gamma = T\dot{\gamma}$, where T is the oscillation time. In addition, we plot the predictions of the strain period for the kayaking/wagging states of Tao et al. found by Brownian dynamics simulations,[120-122] which gives the oscillation period as $P = 4.2\varphi L/D$. Note that they found P to be nearly constant in both the kayaking and wagging states. This prediction systematically overpredicts P for nematic *fd* virus suspensions,[118] but this discrepancy was attributed to rod flexibility.[36]

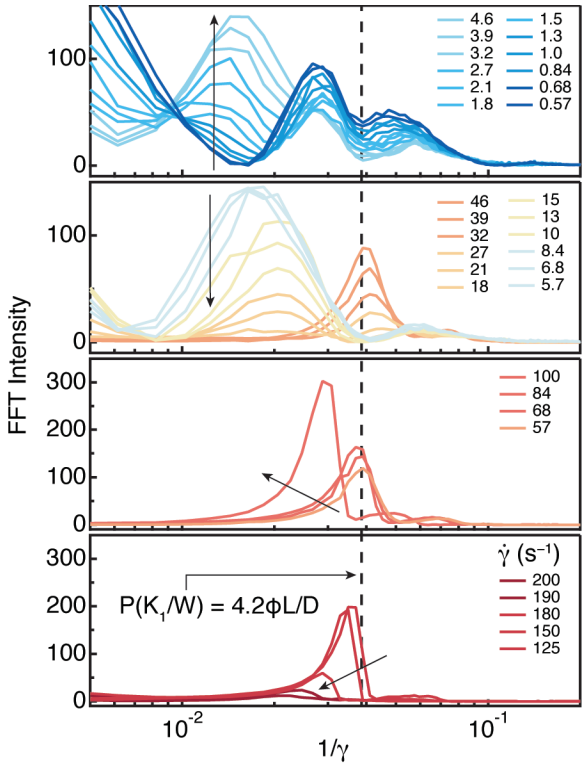

Figure 2.5. Fourier transform power spectra of transient stress following shear step-downs at $c = 1.9$ wt.% and comparison with the oscillation periods found in prior simulations. The initial shear rate was 370 s^{-1} and the final shear rates are given in the figure legends. Solid arrows indicate increasing $\dot{\gamma}_f$, and the vertical dashed line is the tumbling period prediction by Tao et al. for both the kayaking and wagging director states.[120-122]

The peaks observed in the power spectra relate to the constituent frequency components of the transient oscillatory stress following step-down. Close to the origin, more strongly observed at low $\dot{\gamma}$, we observe a signal that matches the strain period of a full rotation of the motor corresponding to $\gamma \cong \phi/\beta = 2\pi/0.017139 = 366.6$, $1/\gamma = 1/366.6 = 0.0027$, where ϕ is the motor angular deflection, and hence ignored. The FFT spectra peaks are broad, due to the damped nature of the oscillating transient stresses.[161] In the power spectra at low $\dot{\gamma}$, we clearly observe the presence of multiple frequency components within the transient stress, as previously suggested by visual inspection of **Figure 2.3a** (*bottom*). At low $\dot{\gamma}$, a double topped feature exists,

which gives way to a single strong band near $1/\gamma = 0.018$. Further increases in the $\dot{\gamma}$ into the negative N_1 regime cause this band to be suppressed and a narrower band near $1/\gamma = 0.038$ to grow in. This band, which dominates the FFT spectra over the $\dot{\gamma}$ regime that we observe a negative N_1 for this c, is in quantitative agreement with the predictions for the oscillation period found by Tao et al. for kayaking/wagging in their simulations, shown as the dashed vertical line.[120-122]

With further increases in $\dot{\gamma}$ up to 200 s^{-1}, as the transition to flow alignment occurs, the FFT peak shifts to lower $1/\gamma$ (higher γ period) and reduces in intensity. This signifies the suppression of the oscillatory behavior of the nematic director by increasing its strain period and decreasing its intensity as it progresses to stationary flow aligning behavior following step-down. Our data suggests that a constant P exists only over a limited $\dot{\gamma}$ regime, and more complex behavior of the nematic director that encompasses director state coexistence must be considered to fully explain the flow behavior that we observe in liquid crystalline solutions of PBDT rods. Direct measurement of the director orientation under shear using time-resolved X-ray scattering under the transient flow conditions utilized in this work would provide more conclusive understanding of the rheological behavior we observe in nematic PBDT solutions.[162, 163]

2.4. CONCLUSIONS

In conclusion, we have reported on the steady-state and transient rheology of nematic solutions of charged, rodlike polymer aggregates that exhibit anomalous shear thickening and negative N_1 behavior. We identify the origin of shear thickening to "director kayaking", as predicted by prior numerical simulations of the coupled kinetic-hydrodynamic theory for nematic rodlike

polymers.[3,4] Our results, in conjunction with the results of Lettinga et al. on nematic *fd* virus suspensions,[118, 119] provide experimental evidence that shear thickening in nematic solutions may originate from at least two distinct responses, described in terms of the principal axis, or nematic director, of the orientational distribution of the rod ensemble. We revealed the coexistence of unsteady, periodic director states by Fourier analysis of the transient stress following shear step-down, as found over a narrow range of shear rates for PBG solutions.[112] Over a limited $\dot{\gamma}$ regime, we found agreement of the experimental oscillation periods we assigned as kayaking/tumbling and kayaking/wagging with the predictions derived from the simulations of Tao et al.[120-122] However, our experimental data of the oscillation periods at low shear rates significantly deviates from these prior simulations at lower shear rates, indicating some discrepancy between experiments and simulations of sheared nematic polymers. In summary, our results provide insight into the behavior of unique and coexisting sheared nematic director states, and how these states influence bulk rheological properties.

CHAPTER 3: FINGERPRINTING THE NONLINEAR RHEOLOGY OF A LIQUID CRYSTALLINE POLYELECTROLYTE

3.1. INTRODUCTION

All-aromatic polyamides (aramids) are a class of rigid, thermally stable polymers, most notably poly(*p*-phenylene terephthalamide) (PPTA), used commercially in the production of high-strength fibers.[11] When dissolved in 100% H_2SO_4 above a critical concentration, PPTA rodlike polymers spontaneously align into a liquid crystalline (nematic) phase due to an anisotropic intermolecular potential.[164] Within a single nematic domain, the average polymer orientation points along a common direction, termed the director.[6] On mesoscopic length scales in the quiescent state, the average orientation of individual nematic domains are isotropic and are separated by disclination lines giving rise to the characteristic Schlieren texture (i.e., polydomain defect texture).[5] The flow behavior of nematic liquid crystalline polymers (LCPs) in general is complex and only partially understood.[9, 165, 166] These complexities arise, in part, from the transient behavior of individual nematic directors and the collective domain structure that manifests under shear flow.[30-32] Thus, from both a technological and scientific perspective, it is important to further investigate the rheological behavior of LCPs and connect their bulk rheology to the behavior of the nematic director.

Unlike PPTA, where dissolution requires strong mineral acids, sulfonated derivatives of aramids (sulfo-aramids) can be dissolved into water.[53, 54, 56, 57, 65, 167] A variety of sulfo-aramids are known to form high-aspect-ratio supramolecular assemblies in aqueous solution, resulting in the formation of liquid crystalline phases at relatively low concentrations (~1—2 wt.%). The liquid

crystallinity and water solubility of sulfo-aramids enable fabrication of solid-state membranes with anisotropic morphologies and structures via environmentally-benign processing conditions. As a result, sulfo-aramids have been investigated for use in proton exchange membranes for fuel cells,[55, 168] matrices for solid-state battery electrolytes incorporating ionic liquids,[68, 69, 125, 128] water transport membranes,[65] dual-network hydrogels,[169] and hybrid biaxial liquid crystalline nanocomposites.[66]

While it can be expected that the rheological behavior of these liquid crystalline sulfo-aramid solutions is similar to other lyotropic LCPs, this has not been extensively investigated. Viale et al. reported small-angle neutron scattering spectra under shear (rheo-SANS) on a 1 wt.% solution of sulfo-PPTA in water with Li^+ counterions.[52] Strongly anisotropic scattering patterns were observed under shear, indicating a high degree of molecular alignment. The 1—3 plane (flow-vorticity plane) apparent order parameter, which is unity for perfect orientation and zero in the isotropic case,[170] increased from 0.3 at a shear rate of 25 s^{-1} to 0.55 at 2500 s^{-1}. Upon flow cessation, the relaxation of shear-induced orientation was extraordinarily slow and attributed to the presence of high-aspect-ratio needlelike aggregates. However, measurements of basic rheological properties, such as the viscosity and first normal stress difference in steady and transient flows, and their correlation to observed scattering anisotropy, has not been reported for lyotropic sulfo-aramids.

Herein, the sulfo-aramid that we investigate is poly(2,2'-disulfonyl-4,4'-benzidine terephthalamide) (PBDT) with Na^+ counterions. Fully nematic solutions of PBDT can be obtained at solution concentrations of ~2 wt.% in water.[62, 65, 68] In **Chapter 2**, we reported on the steady-state and transient nonlinear rheology of PBDT solutions in water.[171] We found that PBDT exhibits rheological behaviors that are prototypical for LCPs in the nematic phase, such as

a negative first normal stress difference N_1 regime, and hesitation of the viscosity prior to shear thinning at high shear rate.[29, 143, 144] Notably, the negative N_1 regime occurred over an extremely narrow shear rate range, unlike the widely studied model LCPs, poly(benzyl glutamate) (PBG)[117, 143, 144, 172, 173] in *m*-cresol and hydroxypropyl cellulose (HPC) in water[101, 105] or *m*-cresol.[153, 157] In addition, we also observed anomalous shear thickening in the steady-state flow curves and regimes of strongly oscillating stress transients following shear step-downs from the flow-aligned state. We suggested that the behavior of nematic PBDT solutions under shear were distinct from the oscillating stresses previously reported by Mewis et al.[117] on PBG in *m*-cresol and found by Lettinga et al.[118, 119] on *fd* virus suspensions, attributed by both of these authors to wagging of the nematic director. This wagging state was originally believed to separate low-shear rate director tumbling and high-shear rate director flow alignment. Using the high-resolution numerical simulations by Forest et al.,[97, 98] we instead assigned the origin of the anomalous shear thickening of nematic PBDT as arising from director kayaking – marked by periodic rotation of the director around the vorticity axis, akin to the oars of a kayaker.

In this Chapter, we report measurements of the nonlinear rheological properties of PBDT in D_2O, spanning the isotropic and fully nematic concentration regimes. The zero-shear viscosity, relaxation time, and terminal modulus are determined as a function of concentration and compared to the Doi-Edwards predictions for rigid rods.[6, 32, 174, 175] Quiescently isotropic solutions in the concentrated isotropic solution regime exhibit anomalous, non-monotonic behavior in the first normal stress difference N_1. In the quiescent, fully nematic phase, the steady-state flow curves exhibit an unusual shape that features two distinct regimes of shear thickening. We investigate these flow regimes using transient rheological measurements (flow reversals and shear step-downs) and steady-state rheo-small-angle neutron scattering (rheo-SANS)

measurements. A hesitation in the flow curve is concomitant with the onset of negative N_1 and strongly oscillating stress transients, as observed in other lyotropic systems.[112, 117-119] We find a narrow shear rate regime of weak shear thickening immediately prior to flow alignment, which does not exhibit oscillating stress transients, providing potential evidence for the out-of-plane steady director state as found in numerical simulations.[98] Finally, using transient shear step-down experiments, we construct so-called "dynamic stress paths" (i.e., the first normal stress difference versus the shear stress) whose rotational chirality indicates the relative importance of elastic and viscous stresses.[101, 173] We find that the shear thickening behavior is associated with a dominance of the viscous stress contribution, supporting assignment of kayaking as the responsible director state. Our results provide new insights into the flow behavior of nematic LCPs that are not dominated by the elasticity of the polydomain defect texture.

3.2. EXPERIMENTAL

Materials. The polymer sample used here is the same as that in used in **Chapter 2**.[171] The polymer samples were prepared by mixing PBDT and deuterium oxide (D_2O) and heating at 60 °C for at least 1 week with magnetic stirring. Polymer solutions exhibited the onset of nematic phase behavior above 10 g L^{-1}, and fully nematic phase behavior at concentrations at 19 g L^{-1} and above in D_2O, consistent with our previous investigation in water.

Rheology. For all rheological measurements presented, we employed a stress-controlled Anton Paar MCR 302 rheometer operating in strain-controlled mode with a 50 mm $\beta = 0.982°$ cone and plate geometry. The temperature was controlled at 25 ± 0.01 °C by a circulating water bath under the bottom stationary plate. A low viscosity oil bath around the sample edges prevented evaporation that enabled sample stability over long time periods. All samples were pre-sheared for several thousand strain units at the highest shear rate investigated for each individual

flow curve. This procedure erased of the sample's shear history and provided a consistent starting point for each concentration from which to construct the steady-state flow curves and measure stress transients. The calculated N_1 values were corrected for inertia by using $N_1 = [2F_z/(\pi R^2)] + [(3\pi\rho\omega^2 \mathrm{R}^4)/40]$, where $\omega = \beta\dot{\gamma}$ is the angular rotation rate.[126] The baseline in N_1 was determined by taking the average of the instrumental background for 100 s before and after measurement at each discrete shear rate. During steady shear, N_1 was averaged over at least 500 strain units at steady state, and up to 2500 strain units for small values of N_1, after decay of the initial stress transient.

Rheo-SANS. Rheo-SANS measurements were performed at the Extended Q-Range Small-Angle Neutron Scattering Diffractometer (EQ-SANS) at the Spallation Neutron Source (SNS) at Oak Ridge National Laboratory (ORNL). One configuration was used, with a sample-to-detector distance of 1.3 m with an incident neutron wavelength of 8 Å, which provided data over a q-range of 0.05 to 0.3 Å^{-1}. An Anton Paar MCR 502 was utilized with a 49 mm concentric cylinder geometry. The liquid crystalline solutions were poured into the outer quartz cell, and the Ti inner cylinder was lowered into position. Solvent evaporation was prevented by an oil-sealed solvent trap, which saturated the sample headspace with solvent vapor. The shear gap was 1 mm, thus the total sample pathlength was 2 mm. All scattering measurements were corrected for detector background, sensitivity, and empty cell scattering, and sample transmission using standard methods at the EQSANS beamline in MantidPlot. Scattering data was converted to absolute units using a calibrated standard. The 2D scattered intensity was azimuthally integrated using the Nika package for Igor Pro 8,[127] and fit with the Maier-Saupe orientational distribution function to calculate the 1—3 plane apparent order parameter.[170]

3.3. RESULTS AND DISCUSSION

3.3.1. Nonlinear Rheology in the Isotropic Phase

We plot the steady-state viscosity as a function of shear rate for quiescently isotropic PBDT solutions in **Figure 3.1**. The qualitative shape of the flow curves is typical of isotropic polymeric solutions, exhibiting a zero-shear viscosity plateau and shear thinning at shear rates greater than a critical shear rate. In the isotropic state, the critical shear rate for the onset of shear thinning corresponds to the inverse of the longest relaxation time of the constituent particles. For dilute rodlike particles in the isotropic phase, the longest relaxation time is the rotational diffusivity, given by $D_r^0 = k_B T/\zeta_{str} = 3k_B T[\ln(L/D) - 0.8]/(\pi\eta_s L^3)$ where $k_B T$ is the thermal energy, ζ_{str} is the rod-solvent friction coefficient, L and D are the length and diameter of the rod, and η_s is the solvent viscosity.[6] Taking $L = 373$ nm, $D = 0.8$ nm, and $\eta_s = 0.89 \times 10^{-3}$ Pa s, we calculate $D_r^0 = 455$ s^{-1}, yielding a relaxation time of $\tau = 1/(2D_r^0) = 1.1 \times 10^{-3}$ s, and an approximate critical shear rate $\dot{\gamma}_c \approx 1/\tau \approx 910$ s^{-1}. The calculated critical shear rate is in good agreement with the onset of shear thinning at the lowest concentrations studied here.

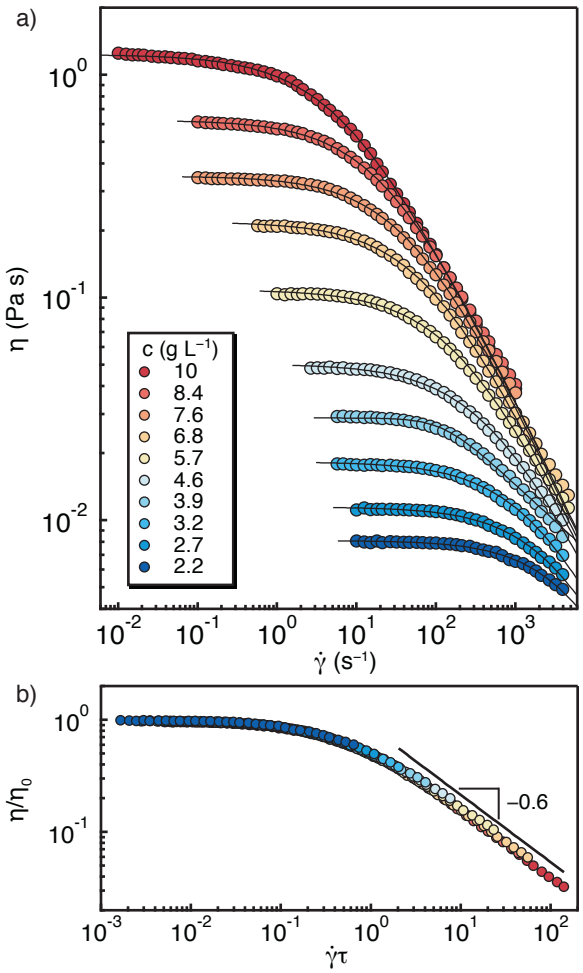

Figure 3.1. Nonlinear rheology of quiescently isotropic PBDT solutions in D_2O. (a) Steady-state viscosity as a function of shear rate with increasing concentration (blue to red). Solid lines are fits to the Cross model. (b) Normalized viscosity versus rescaled shear rate obtained from fitting the flow curves.

As the solution concentration is increased, the onset of shear thinning shifts to lower shear rates and the relative magnitude of viscosity shear thinning increases. For polymer solutions in general, shear thinning originates from shear-induced alignment along the elongational component of the shear field. Compared to flexible polyelectrolytes, such as poly(2-vinylpyridine) (PVP) at similar solution viscosities,[46] the observed shear thinning is more dramatic for isotropic PBDT solutions. For example, PVP in NMF with a zero-shear viscosity of ~1 Pa s decreases by a factor of two as the shear rate is increased by a factor of 400, whereas the

viscosity of a 10 g L^{-1} PBDT solution decreases by a factor of 50 over the same shear rate range. This is likely due to the large aspect ratio of the PBDT rodlike particles and strong orientational effect of the shear flow. To extract the zero-shear viscosity and longest relaxation time for the isotropic PBDT solutions, we fit the data with the empirical Cross model

$$\eta = \eta_\infty + \frac{\eta_0 - \eta_\infty}{1 + (\tau\dot{\gamma})^m} \quad \textbf{(Eqn. 3.1)}$$

where η_∞ and η_0 are the infinite- and zero-shear viscosity, respectively, τ is the longest relaxation time, and m is the shear thinning exponent. We set η_∞ to zero while fitting the flow curves, as we did not observe an onset of an infinite-rate plateau viscosity. The Cross-model fits to the steady-state flow curves are shown as the solid lines in **Figure 3.1a**. We also attempted to fit the steady-state flow curve with the Carreau model; however, the model could not capture the qualitative shape of the flow curve satisfactorily. While both models fit the data well at low shear rates and deviate at high shear rates, shown in **Figure B.1**, the Carreau model exhibits a much sharper transition at the critical shear rate when compared to the Cross model. This is in contrast to the data of Lang et al. on isotropic suspensions of rodlike *fd* virus, who found good agreement with the Carreau model.[14] The differences between PBDT and fd virus suspensions, and discrepancy between the two model fits, may originate from the polydispersity of PBDT rods that results in a distribution of relaxation times. In contrast, *fd* virus suspensions are monodisperse and the longest relaxation time is well-defined.[119] However, the strong shear thinning that both systems exhibit originate from the development of a highly aligned shear-induced paranematic state.[14, 119]

Through fitting the flow curves with the Cross model, we normalize the viscosity to the zero-shear viscosity and rescale the shear rate by the longest relaxation time and were able to collapse the data into a single mastercurve, plotted in **Figure 3.1b**. The collapse of the data shows that the

flow behavior of isotropic PBDT solutions are well-described by these two parameters. We observe a common shear thinning exponent for all concentrations at high shear rates, shown by the power law with slope –0.6 in the figure. This value is similar to the shear thinning power laws found for fully nematic PBDT solutions under shear (see below), consistent with enhanced orientation of the rods under shear.

The zero-shear viscosity obtained from the flow curve fitting is plotted in **Figure 3.a** as a function of concentration. The maximum in the zero-shear viscosity approximates the I-N transition concentration above which the isotropic phase is unstable to incipient nematic ordering.[6] Below this concentration, we find three distinct regimes of power law scaling of the zero-shear viscosity that correspond to the dilute, semidilute, and concentrated isotropic regimes, respectively, indicated by breaks in the power law fits to the data.

For rigid rods in a dilute, isotropic solution, η_0 is predicted to increase linearly with concentration, found here below ~2.7 g L^{-1}. In the semidilute concentration regime, the predicted and experimentally found scaling relationship for η_0 versus concentration and molecular weight (i.e., length) in the semidilute isotropic regime is 3 and 6, exhibiting a strong entanglement effect.[32, 176] Here, we find that the scaling relationship $\eta_0 \sim c^3$ is consistent with these predictions in the semidilute isotropic regime. At higher concentrations, the viscosity scaling increases to $\eta_0 \sim c^5$, which is not predicted by the Doi-Edwards theory, but has been suggested to arise from rod-jamming effects.[177]

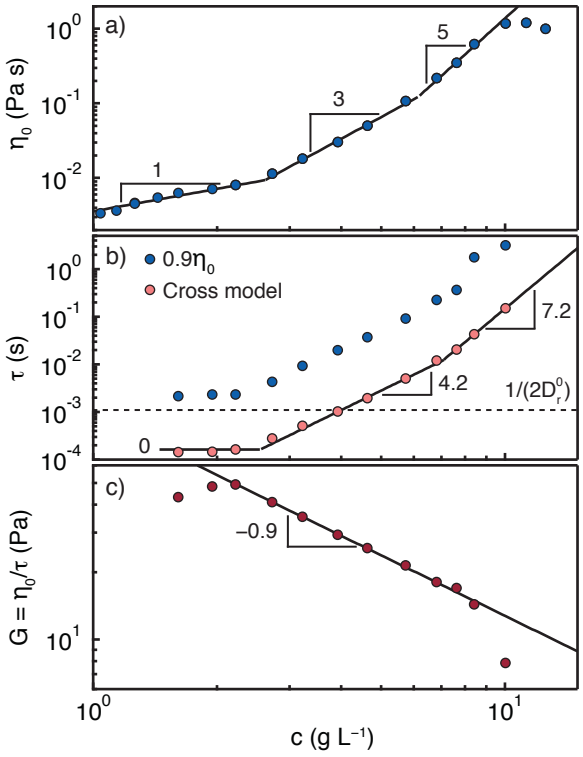

Figure 3.2. Concentration scaling of Cross model results from fitting the flow curves of quiescently isotropic PBDT solutions: (a) zero-shear viscosity, (b) terminal relaxation time, and (c) terminal modulus.

The τ obtained by fitting the flow curve with the Cross model is plotted in **Figure 3.b** as a function of concentration. In addition, we estimated τ in a model-independent fashion by taking the inverse of the shear rate when the steady-state viscosity reaches 90% of the zero-shear viscosity,[178] see **Figure B.1**. Fitting the Cross model to the data gave relaxation times smaller than the model-free procedure by about a factor of 20, but both methods gave the same concentration scaling laws, giving confidence to the reported power law exponents and trends of the data.

Below ~2 g L^{-1}, the experimentally determined τ remains constant, consistent with dilute solution conditions. We calculated τ for rods in dilute solution, given as $\tau \approx 1/(2D_r)$, using the known diameter[62, 67] and estimated length of PBDT rods of 373 nm (based on the application of

the Onsager theory for hard rods to the isotropic-nematic (I-N) transition concentration we find here[21]), shown as the horizontal dashed line in **Figure 3.b**. The calculated relaxation time is in approximate agreement with the relaxation time found from the model-free fitting procedure.

In the semidilute regime, we find $\tau \sim c^{4.2}$, whereas the Doi-Edwards model predicts a quadratic dependence, showing a much stronger entanglement effect on the rotational dynamics. The effect of finite stiffness in the experimental system, possibly leading to the presence of hairpin defects,[39] may contribute to the stronger concentration dependence of the relaxation time. At the crossover from semidilute to the concentrated isotropic solution regime at 6.8 g L^{-1}, we find a strong power law scaling $\tau \sim c^{7.2}$ until the I-N transition concentration at ~11 g L^{-1}. As the concentration approaches the I-N transition, the relaxation time is expected to diverge, although this is never experimentally observed due to phase separation into an anisotropic phase.[6] Overall, these data evidence a significant slowing down of the rod dynamics under shear as the solution concentration is increased throughout the isotropic regime.

We estimated the solution terminal modulus $G = \eta_0/\tau$, using τ obtained from the Cross model fitting, and plot G as a function of concentration in **Figure 3.c**. This method is known to accurately estimate G that would be found from linear viscoelastic measurements for salt-free polyelectrolyte solutions.[179] For semidilute, unentangled polyelectrolyte solutions, G is predicted to scale linearly with concentration with a contribution of k_BT per chain.[43] Here, below a concentration of ~2.2 g L^{-1}, G appears to be increasing before reaching a maximum, then decreases with concentration following a power law of –0.9. At 10 g L^{-1}, G suddenly decreases and appears to diverge towards zero. The decreasing trend of G indicates that the solution rheology of PBDT over the semidilute and concentrated isotropic concentration regimes are strongly affected by the presence of local orientational fluctuations.[6]

To compare the terminal modulus obtained from the nonlinear rheology measurements to the moduli obtained from linear oscillatory measurements, we measured the frequency dependence of G' and G'' in the linear viscoelastic regime for solutions between 4.6 and 10 g L^{-1}, given in **Figure B.2**, and find a liquid-like response ($G'' > G'$). The limiting slopes at low frequencies are $G'' \sim \omega^1$ and $G' \sim \omega^{1.5}$, in contrast to the predicted scaling of terminal flow of $G'' \sim \omega^1$ and $G' \sim \omega^2$. Deviations from terminal flow frequency scaling of G' and G'' are well-known to occur in concentrated solutions of isotropic rodlike polymers.[144] We plot G' evaluated at 10 rad s^{-1} in **Figure B.3**, and find a strong concentration dependence scaling as $G' \sim c^{5.8}$. The differences observed between the linear oscillatory measurements and nonlinear rheology are consistent with strong orientational effects under nonlinear shear.

Pretransitional effects, such as local orientation fluctuations in quiescently isotropic solutions, is further supported by the steady-state behavior of the first normal stress difference N_1, shown in **Figure 3.3**. For Gaussian coils or isotropic rod dispersions that are aligned by a shear flow, with increasing alignment at progressively higher shear rates, N_1 is a monotonically increasing function of shear rate.[180] At concentrations within the semidilute regime, 4.6 and 6.8 g L^{-1}, we observe a monotonic increase in N_1 with shear rate consistent with the development of progressively increasing orientational order, consistent with expectations.

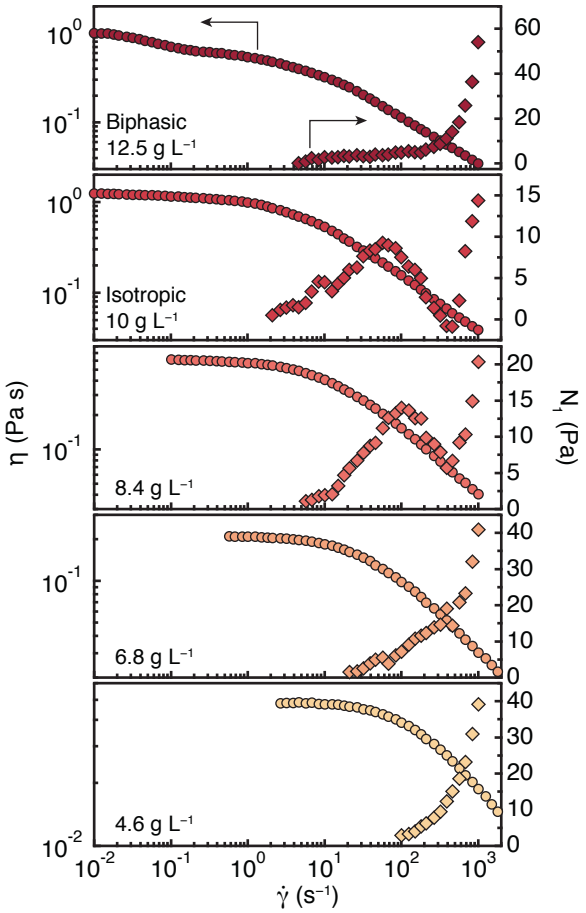

Figure 3.3. Steady-state viscosity η (circles, left axis) and first normal stress difference N_1 (diamonds, right axis) as a function of shear rate of quiescently isotropic (c = 4.6, 6.8, 8.4, and 10 g L^{-1}) and biphasic (c = 12.5 g L^{-1}) PBDT solutions under shear.

However, as the solution concentration is increased into the concentrated isotropic regime, at 8.4 and 10 g L^{-1}, we observe a non-monotonic dependence of N_1 with a local minimum near 400 s^{-1}. At 10 g L^{-1}, the local maximum prior to this local minimum at high shear rates likely corresponds to the point at which the stationary shear-induced nematic director becomes unstable to periodic responses, causing a negative deviation in N_1 due to the broadening of the local orientational distribution function.[27, 29] At higher shear rates, the director yields to stationary flow-aligning behavior with a monotonically increasing N_1. This non-monotonic behavior of N_1 is generally observed in fully liquid crystalline solutions of rigid polymers, such as PBG,[143, 144, 181]

Moreover, quiescently isotropic solutions of rodlike polymers are expected to exhibit a monotonically increasing N_1 below the I-N transition concentration.[143, 144] Due to the effect of finite stiffness for PBDT rods, the effect of rod flexibility may in fact induce a shear rate regime of quiescently isotropic solutions with periodic responses of the rod ODF, delaying steady flow-alignment until higher shear rates.[36, 116]

Within the biphasic region at 12.5 g L^{-1}, the viscosity flow curve exhibits two inflections with increasing shear rate, consistent with two phases with distinct relaxation times. Moreover, the observed local minimum in N_1 at 8.4 and 10 g L^{-1} is eliminated above the I-N transition concentration, within the biphasic concentration regime. It appears that phase separation into isotropic and nematic stabilizes rod flow alignment under shear in comparison to concentrations just below the I-N transition. Further measurements to explore these pretransitional effects are needed to clarify the experimental picture before definitive conclusions can be drawn.

3.3.2. Nonlinear Rheology in the Nematic Phase

At solution concentrations of 19 g L^{-1} and above, we observe fully liquid crystalline phase behavior as observed via polarized optical microscopy. We investigated the non-linear rheology of the nematic solutions slightly above the fully nematic concentration to reduce the elastic contribution to the shear stress arising from domain distortion. In **Figure 3.4**, we plot the steady-state η (*top*) and N_1 (*bottom*) as a function of shear rate for solution concentrations of 21, 23 and 30 g L^{-1}.

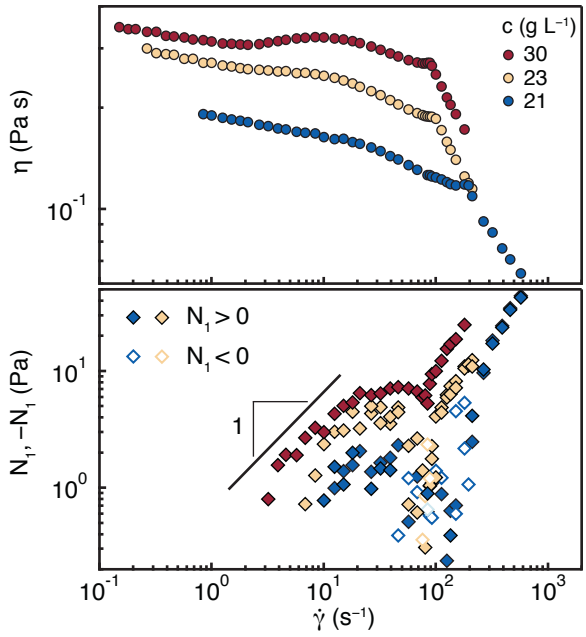

Figure 3.4. Steady-state η (top) and N_1 (bottom) of fully nematic PBDT solutions in D_2O at solution concentrations of 21, 23 and 30 g L^{-1}. The data have been measured by starting from the highest shear rate shown and decreasing in a stepwise fashion. Two curves are shown for the N_1 data for 21 and 23 g L^{-1}, measured on the same solution in a stepwise decreasing manner, to check for sample hysteresis and measurement uncertainty. Open diamond symbols (bottom) indicate negative N_1 values.

The flow curves of the nematic solutions are qualitatively different than the quiescently isotropic PBDT solutions, shown previously in **Figure 3.1**. A zero-shear viscosity plateau is not clearly present, as is the case in the isotropic phase of PBDT. Although the observed shear thinning at low shear rates is quite weak, it is clearly present when a direct comparison is made to isotropic solutions of similar viscosity. Due to the low torque signal at low shear rates and large strains required to reach steady state, we did not investigate lower shear rates to determine if a Newtonian plateau region was present.

In general, the flow curves of LCPs are described by a three flow curve model given by Onogi and Asada,[133] with shear thinning at low and high shear rates (Regions I and III) separated by a pseudo-Newtonian plateau at moderate shear rates (Region II). For PBG, the Region II plateau and Region III shear-thinning regimes are generally observed over the experimentally accessible

shear rate regime, but Region I shear thinning is not observed.[143, 144, 172] Region I shear thinning is generally characterized by a low degree of shear-induced alignment and a shear thinning power law of –0.5 at low shear rates.[135, 136, 138, 182] Based on the lack of a plateau viscosity at the lowest shear rates studied here, and absence of strong shear thinning behavior, we suggest that the entire flow curve for the liquid-crystalline PBDT solutions studied here is likely within Region III. This is likely due to the high aspect ratio of PBDT rods (>400), in comparison to molecular liquid crystalline polymer solutions with lower aspect ratios.

If we take the limiting value of the viscosity at low shear rates as an indication of the zero-shear viscosities, i.e., a Region II plateau, solution concentrations for which fully nematic phase behavior is observed show a monotonic increase in viscosity with concentration. The Doi-Edwards theory predicts an increase in the local orientational order from the increasing strength of the nematic potential, thus reducing the viscosity of the nematic.[6] The increasing viscosity with concentration suggests that the local orientational order does not increase significantly over this concentration regime. The increasing viscosity with concentration could arise from two effects, textural or viscous stresses, which are both monotonically increasing functions with concentration.[129] However, we will show later that the effect of textural elasticity in the shear rate regime we investigate here is not dominant, due to the lack of strain scaling of flow reversal experiments that we observe in the low shear rate regime. As such, we suggest that the increasing viscosity with concentration in this regime relates to the increasing contribution of viscous stresses to the total shear stress.

Instead of a monotonic and smoothly decreasing viscosity with shear rate, as observed for quiescently isotropic solutions, the viscosity of the 21 g L^{-1} solution develops a slight plateau at moderate shear rates of 3—30 s^{-1}, before shear thinning more rapidly up to another region that

shows a hesitation in the viscosity. At 30 g L^{-1}, the viscosity even exhibits an increase over this shear rate regime, i.e., shear thickening behavior. In this regime, N_1 increases linearly with shear rate and reaches a local maximum that increases in magnitude with concentration, consistent with prior observations.[143, 156]

At shear rates in the 80—200 s^{-1} range, we observe a pronounced kink, or hesitation, in the viscosity and the emergence of a negative N_1 regime for the 21 and 23 g L^{-1} solutions, or positive dip at 30 g L^{-1}. To better visualize this range, we replot the steady-state viscosity flow curve data from **Figure 3.4** in **Figure 3.5** in a semi-log representation. For liquid crystalline PBDT solutions in D_2O, this hesitation regime is quite well-defined and pronounced, as compared to the broad hesitation in the flow curve observed in liquid crystalline PBG.[143, 144, 173] The arrows in **Figure 3.5** indicate, for each concentration, the shear rate at the minimum N_1 value.

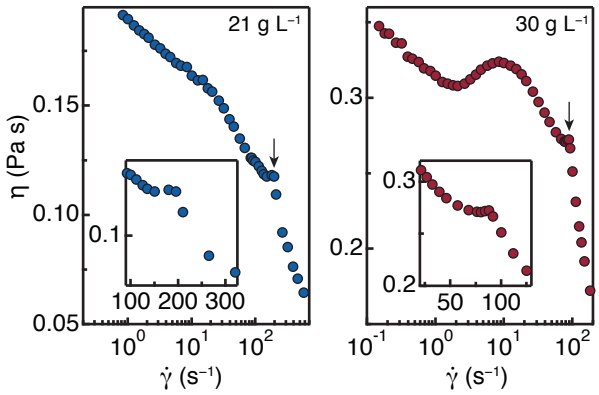

Figure 3.5 Semi-log representation of the steady-state η as a function of shear rate for nematic PBDT solutions in D_2O. The insets show the same data on linear axes in the vicinity of the transition to flow alignment, more clearly showing the slight shear thickening behavior.

This hesitation in the viscosity is a classic signature of the flow behavior of nematic LCPs under shear that originates from a broadening of the molecular orientational distribution function (ODF).[27, 29] At shear rates higher than the minimum N_1 value, the director is supposed to adopt a

stationary angle with respect to the flow direction, rather than undergo periodic oscillations. It is noticeable here that we not only observe a pronounced hesitation, but a very narrow regime where the viscosity undergoes slight shear thickening, observed at 21 and 30 g L^{-1}, immediately prior to high-shear rate shear thinning (flow alignment). This very narrow regime of shear thickening was confirmed by measuring a 2nd flow curve on the same solutions, and with separately loaded, independent solutions. Numerical simulations by Forest et al.[29,30] have predicted a very narrow regime of shear rates that correspond to a director state, called the out-of-plane steady (OS) regime, where the director adopts a stationary angle out of the shear plane and at a slightly negative angle with respect to the flow direction. This OS state is predicted to exhibit slight shear thickening immediately prior to shear thinning associated with flow alignment. Later, we will show that the shear rates that exhibit this shear thickening do not exhibit oscillating stress transients following step-down, consistent with a stationary director state. To the best of our knowledge, this result provides the first experimental evidence for the existence of the OS director state, although this assignment remains tentative.

We previously reported nonlinear flow curves of the same PBDT solutions in water, and also found steady-state shear thickening at moderate shear rates, similarly observed here. The magnitude of the shear thickening response is significantly smaller in D_2O than in water. The suppression of shear thickening in D_2O, compared to water, was confirmed by repeated measurements on solutions with nearly identical concentrations from the same polymer batch. Moreover, the sudden increase in viscosity, which we tentatively assigned as an OS director, did not appear in the rheological measurements in water. However, we cannot exclude the existence of the slight shear thickening in water because the regime appears to occur over an extremely narrow shear rate regime, consistent with simulations.

To the best of our knowledge, this isotope effect on the rheology of a LCP has not been previously reported, although it may arise from several factors that are known to be different in D_2O as compared to water. The enhanced local structure of D_2O stiffens the solvation shell and may lead to an enhancement of the persistence length.[183] Alternatively, the differences between water and D_2O in solvent viscosity may cause a subtle change in the polymer-solvent friction coefficient.[184] We also observed that degradation of the viscosity for PBDT solutions in D2O if the sample experienced shear rates far above the onset of flow alignment. As such, we have limited the shear rates investigated to ranges over which the viscosity did not exhibit measurable hysteresis over the course of the rheological experiments. We speculate that rod breakage, resulting in a reduction in the average length of PBDT rods, occurs at high shear rates in D2O leading to this viscosity reduction.

We note that the shear rate for the hesitation in the viscosity and subsequent onset of flow alignment in PBDT solutions exhibits an anomalous trend with concentration than predicted by theory. For PBG in *m*-cresol, increasing the solution concentration results in a monotonic shift of the N_1 regime to higher shear rates.[143, 144] The increase in concentration results in an increase in the strength of the nematic potential acting upon individual rodlike polymers, and enhances the local molecular orientation. This reduction in misalignment of the rods due to an increase in nematic potential requires a larger shear flow to induce a reduction in the molecular ODF, thus increasing the shear rate for the onset of negative N_1 and the viscosity hesitation.

For HPC in *m*-cresol at solution concentrations up to 35 wt.%, the shear rate for the minimum in N_1 increases with concentration,[98] similar to PBG.[143, 144] At solution concentrations between 35—50 wt.%, the shear rate for the minimum in N_1 reverses trend, and decreases with increasing concentration. At 55 wt.%, the negative N_1 regime is eliminated, but a positive local minimum

remained, creating a dip in the shear rate dependence of N_1. Baek et al.[64,69] proposed that the increasing influence of the viscous contribution to the stress tensor explains the elimination of the negative N_1 regime, while maintaining a positive dip in N_1. At a given dimensionless shear rate $\dot{\gamma}/D_r$, the ratio of the viscous to elastic stress contributions is controlled by the parameter $\beta_V = \zeta_{str} D_r / k_B T$. Initial considerations of the concentration dependence of β_V would indicate that it should be constant, as $D_r \sim \zeta_{str}^{-1}$.[6] However, at high enough solution concentrations the increasing importance of polymer-polymer friction may lead to an increasing ζ_{str} without a corresponding decrease in D_r, causing β_V to increase with concentration. The calculations of these authors showed that an increasing β_V resulted in the elimination of a negative N_1 regime, while a positive dip in N_1 remains, as observed experimentally.[153] However, this rationale does not explain the complete elimination of a local minimum in N_1, since the viscous stress contribution itself exhibits a local minimum in N_1. Thus, the effect of increasing polymer concentration may not only change β_V, which modulates the reduction in N_1 at shear rates that broaden the molecular ODF, but also the director state may in fact change. Indeed, numerical simulations of the director phase space shows that, near the fully nematic phase boundary, slight changes in concentration dramatically influence the selected director state.[97,98]

We plot the steady-state viscosity and N_1 for 38 and 45 g L^{-1} solutions in **Figure 3.6**. Power law fits to the low shear rate data in comparison to the prediction for Region I shear thinning (–0.5) suggest that the observed behavior does not originate from elasticity associated with the polydomain defect texture. The most noticeable feature is the presence of the clearly observable shear thickening regime at moderate shear rates, further confirming our observations at lower concentrations. Moreover, we find that the hesitation in the viscosity that we observed at lower concentrations prior to shear thinning at high shear rates is absent. Rather than a regime of

negative N_1, we observe a positive dip in N_1 at 38 g L^{-1} over the shear rate range of 50—100 s^{-1}, before increasing again at higher shear rates. At 45 g L^{-1}, this dip in N_1 is eliminated and we observe a monotonically increasing N_1, which scales nearly linearly over two decades in shear rate. That is, the rheological signatures associated with director wagging, which manifests as a negative N_1 signal, becomes suppressed and subsequently eliminated as the solution concentration is increased to 38 and 45 g L^{-1}, respectively.

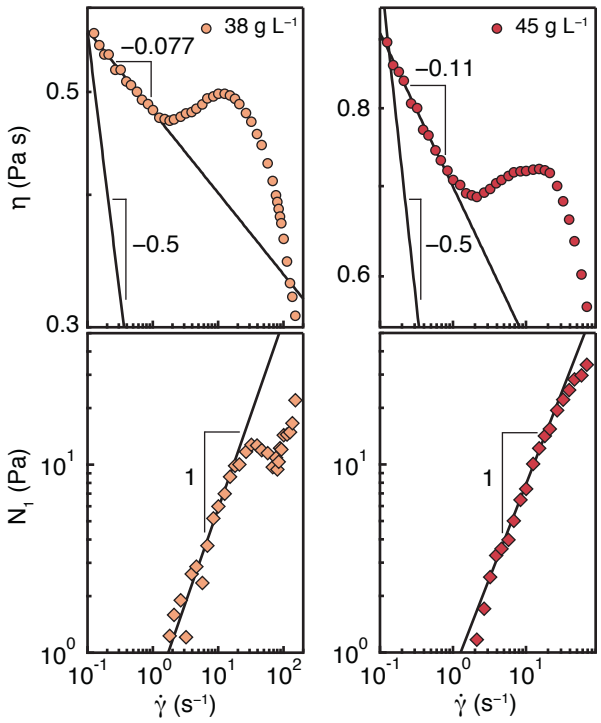

Figure 3.6. Steady-state η and N_1 of liquid crystalline PBDT in D_2O as a function of shear rate for 38 and 45 g L^{-1}. All axes are on a logarithmic scale. Power law fits to the viscosity at low shear rate show weak shear thinning exponents (approximately –0.1) and are compared to the prediction for Region I shear thinning of –0.5. Linear fits to the N_1 data are shown, evidencing the positive dip in N_1 for the 38 g L^{-1} solution, and a monotonically increasing N_1 for the 45 g L^{-1} solution.

3.3.3. Alignment under Nonlinear Shear from Rheo-SANS

We investigated the shear-induced alignment of PBDT in D_2O using rheology and in-situ small-angle neutron scattering (rheo-SANS) at the Extended Q-Range SANS (EQSANS) instrument at Oak Ridge National Laboratory. Liquid crystalline solutions were sheared using a Couette geometry, where the incident neutron beam was parallel to the velocity gradient direction, yielding the scattering patterns to be a projection in the 1—3 plane (flow—vorticity plane). The 2D scattering patterns of a representative 30 g L^{-1} solution are given in **Figure 3.7a** at shear rates of 1, 10, and 100 s^{-1}, and each 2D scattering pattern has identical intensity scaling. Consistent with previous scattering data on PBDT solutions, we observe a scattering peak from the structure factor that corresponds to the intermolecular rod-rod distance.[62, 67] Under low shear rates, we observe substantial scattering anisotropy that is localized along the vorticity axis, indicating that the time-averaged director orientation is aligned along the flow direction. Increasing the shear rate causes the scattering anisotropy to increase in sharpness along the vorticity axis, indicating an increase in the time-averaged degree of orientation along the flow direction.

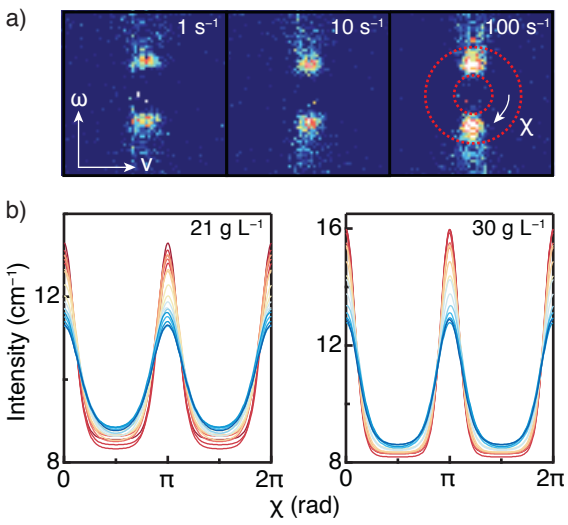

Figure 3.7. Measurement of shear-induced alignment of nematic PBDT in D_2O using rheo-SANS. (a) 2D rheo-SANS patterns of PBDT in D_2O at 30 g L^{-1} under shear rates of 1, 10, and 100 s^{-1} projected in the 1—3 shear plane. The flow (v) and vorticity (ω) directions are shown by the arrows. (b) Maier-Saupe fits to the azimuthal intensity dependence over the q-range corresponding to the intermolecular structure factor peak at 21 and 30 g L^{-1}. Blue to red colors indicate increasing shear rates from 1—460 s^{-1} and 0.21—210 s^{-1} for 21 and 30 g L^{-1}, respectively.

We quantified the orientational order by performing azimuthal intensity integrations within a narrow q-range that contained the structure factor peak, corresponding to the lateral rod-rod correlation length, shown by the dashed red lines in **Figure 3.7b**. We fit the azimuthal intensity dependence with a Maier-Saupe type distribution function to calculate apparent order parameter in the 1—3 plane, S_{13}. We stress that this procedure does not provide a rigorous description of the 3D ODF, which can be obtained through model-independent methods.[185] Here, we simply utilize this method to obtain a qualitative description of the time- and spatially-averaged rod orientation in the 1—3 projection under shear. Note that S is proportional to the product of the molecular order parameter, S_m, and the order parameter of the mesoscopic nematic domains, $\bar{S}$.[170] In **Figure 3.7b**, we show the resulting Maier-Saupe fits for 21 and 30 g L^{-1}, where the shear rate increases from blue to red. The underlying data and fits are shown for each shear rate in

Figure B.4 and **Figure B.5**. As can be observed, the degree of anisotropy increases with the applied shear rate, corresponding to increased orientation.

The shear rate dependence of S_{13} obtained from the Maier-Saupe fits to the azimuthal scattering anisotropy is plotted along with the steady-state viscosity in **Figure 3.8** for solution concentrations of 21, 30, and 45 g L^{-1}. The absolute values of S_{13} are remarkably high compared to rheo-SANS data obtained on molecular liquid crystalline solutions of PBG[186] or HPC.[187] Interestingly, S_{13} is significantly higher than nematic solutions of sulfo-PPTA under shear, which plateaus near 0.55 at shear rates in excess of 1000 s^{-1}.[52]

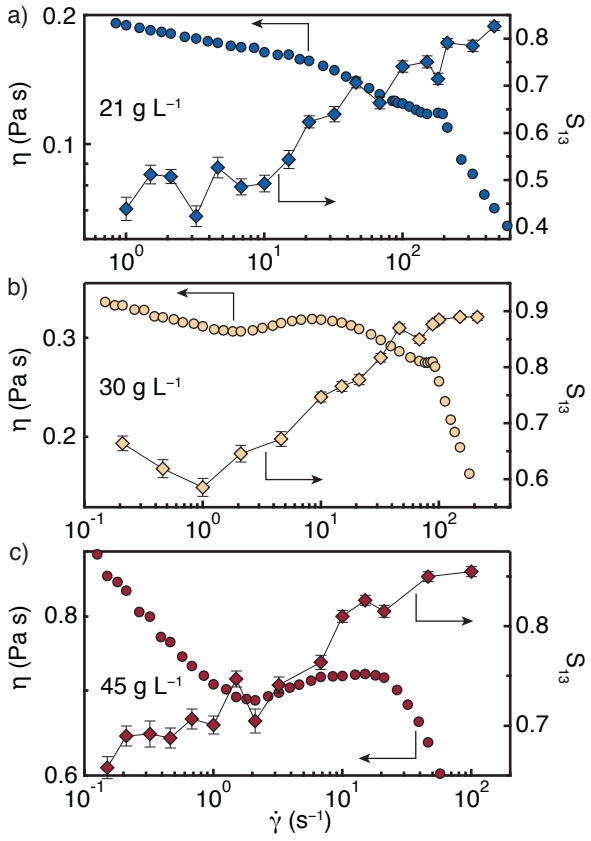

Figure 3.8. Steady-state η (left axis, circles) and 1—3 plane apparent order parameter S_{13} (right axis, diamonds) as a function of shear rate for (a) 21, (b) 30, and (c) 45 g L^{-1}. Note that the viscosity axis is on a logarithmic scale.

At 21 g L^{-1}, S_{13} appears to approach a plateau value at low shear rates, although the scatter in the data makes this conclusion tentative, while the viscosity exhibits weak shear thinning. At a shear rate of 10 s^{-1}, S_{13} begins to steadily rise from ~0.45 to ~0.65 as the viscosity exhibits a break and shear thins more strongly with increasing shear rate. The slight increase in viscosity at a shear rate of 195 s^{-1} appears to correlate with a local reduction in S_{13}, before again increasing up to greater than 0.8 at the highest shear rates investigated. Presumably, higher shear rates would result in a plateau in the measured S_{13}, but we limited our shear rates investigated in rheo-SANS due to the viscous heating at high shear rates that can only be controlled by air cooling.

At 30 g L^{-1}, S_{13} appears to decrease at low shear rates, but we caution against deeper interpretation of the trends observed at low shear rates because of the noise in the data Above a shear rate of 1 s^{-1}, S_{13} exhibits a steady increase from ~0.6 to ~0.85 at 46 s^{-1}, while the viscosity exhibits moderate shear thickening, followed by shear thinning behavior. At slightly higher shear rates where we observe the slight and sudden increase in viscosity just prior to shear thinning, S_{13} undergoes a similarly sudden reduction, before increasing to reach a saturation value of ~0.9 at higher shear rates.

At 45 g L^{-1}, S_{13} exhibits a near monotonic increase from shear rates of 0.1 up to 100 s^{-1}. Two local minima in S_{13} correspond to the beginning and peak of shear thickening behavior in the steady-state viscosity, although the data point density from this data prohibits us from certainty in these features. From this data, however, we do conclude that the shear thickening in the steady-state flow curves is correlated with an increase in S_{13}. In addition, we do not observe any signature of director logrolling (a director state that also causes shear thickening), which would manifest as a rotation of the scattering anisotropy from along the vorticity (vertical in **Figure 3.7a**) to along the flow direction (horizontal in **Figure 3.7a**), i.e., a change in average rod

orientation from along the flow direction to along the vorticity axis. The hesitation in the viscosity, and sudden increase immediately prior to flow alignment, appears well correlated with a local reduction in S_{13}.

The fact that the shear thickening regime occurs along with an increase in S_{13} is counter-intuitive, as one expects increasing orientational order to correlate with decreasing viscosity. However, in LCPs, both the microscopic and mesoscopic orientational distribution functions must be taken into consideration.[9] For example, a decrease in the local order parameter occurs at the tumbling-to-wagging transition, but can simultaneously occur with an increase in the mesoscopic domain order parameter. If the mesoscopic domain order parameter increase is greater than the decrease in the local order parameter, this cumulative effect would then act to increase S_{13}.

Here, we suggest the following picture to explain the observed S_{13} trend and connect it to the steady-state viscosity flow curve. We have proposed that the origin of shear thickening occurs due to director kayaking, as predicted by prior numerical simulations.[97,98] The scattering spectra of director kayaking in the $1-3$ plane would appear as if the director is, on average, aligned along the flow direction with some angular distribution, as observed here. Increasing the shear rate may couple to the rotational frequency of the kayaking orbit, such that the rods spend more time with their axis pointed close to the flow direction. This longer time for rotation of the kayaking orbit would increase S_{13} as measured by rheo-SANS. At high shear rates prior to flow alignment, in the hesitation regime of the flow curve and at the point where the viscosity undergoes a slight, second shear thickening, we consistently observe that S_{13} undergoes a local minimum. In the next section, we show that this shear rate corresponds to a non-oscillatory response of the stress upon flow reversal. As such, we suggest that this measured reduction in

S_{13} is correlated with a stationary out-of-plane director state, also predicted by the numerical simulations of Forest et al. to exist just below the shear rate for the onset of flow alignment.[98]

3.3.4. Transient Rheology of the Nematic Phase

Transient rheological experiments are useful in interpreting the behavior of the nematic director that invariably dictate the steady-state rheological response. Thus, we investigated the 21 g L^{-1} solution using flow reversals, where the direction of the shear is suddenly reversed at constant shear rate. In this transient experiment, it is thought that the sudden change in flow direction causes a 180° flip of the director, inducing coherence of the oscillating nematic directors that then gradually dephase due to interdomain interactions.[141] In **Figure 3.9a**, we plot the transient shear stress, normalized to the steady-state value, as a function of applied strain following flow reversal. To aid visualization, we have separated the data into separate subplots and indicate the shear rate used (and corresponding color of stress transient) in the figure.

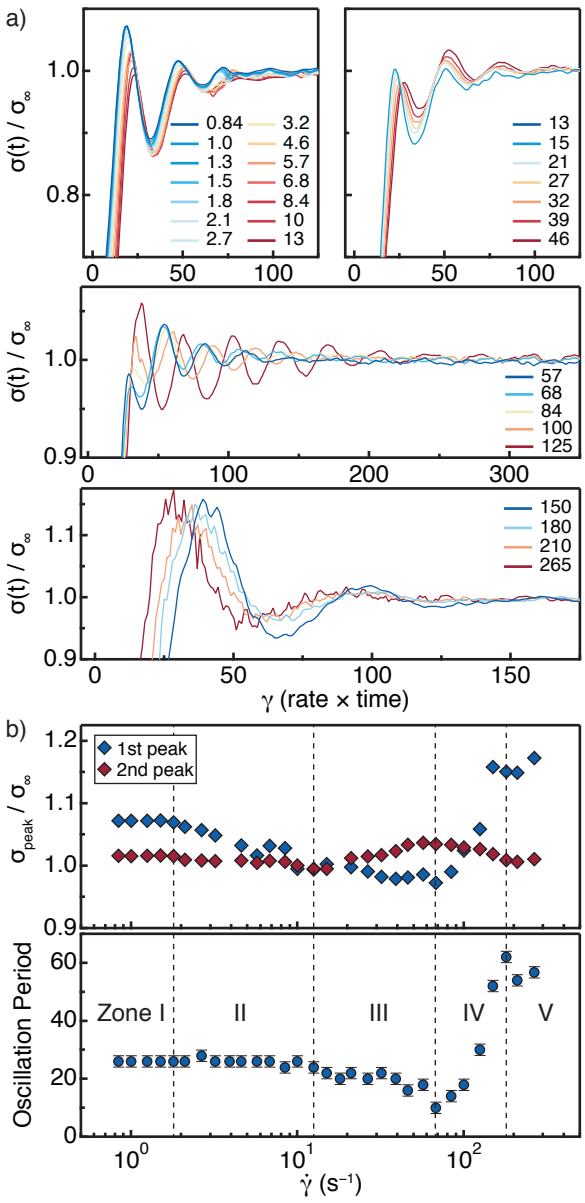

Figure 3.9. Analysis of shear flow reversal experiments for $c = 21$ g L^{-1}. (a) Transient shear stress following flow-reversal as a function of strain. The shear rates are given in the figure suplot legends and the units of all abscissae are identical. (b) Normalized stress value of first and second peak (*top*) and oscillation period in strain units (*bottom*) as measured by twice the distance between the first peak and first valley. Error bars for the oscillation periods are estimated as ±1 strain unit.

We do not observe strain-scaling behavior in the flow reversal experiments over any shear rate range, further suggesting that these solutions are not strongly affected by the nematic texture. At low shear rates (0.84—13 s^{-1}), the data can be described as a damped oscillatory pattern,

exhibiting two to three peaks before reaching the equilibrium stress value at strains greater than approximately 100. This qualitative description of the transient stress following flow reversal is the same as that observed for liquid crystalline solutions of PBG[181] in the linear regime of the flow curve. However, as the shear rate is increased through this regime, the normalized stress values of the first two peaks decreases and shifts to larger strain values, resulting in non-strain scaling behavior.

In the moderate shear rate regime (13—46 s^{-1}), the normalized stress of the first peak continues to decrease, but eventually reaches a plateau values, while the second peak increases throughout this shear rate regime. As the shear rate is increased past 57 s^{-1}, the normalized stress value of the first peak, which reached a plateau value in the prior range, begins to increase while the second peak decreases in value. Both peaks begin to shift to larger strain values and a rapid increase in the oscillation period occurs over this range. At a shear rate of 125 s^{-1}, we observe the emergence of strongly oscillating stress transient that is suppressed when the shear rate is slightly increased to 150 s^{-1}. That is, strong oscillatory stress transients are only observed over a very narrow range of shear rates, close to, but below, the minimum in the steady-state N_1 and the sudden increase in viscosity for this concentration (see **Figure 3.4** and **Figure 3.5**).

To provide some quantitative description of the evolution of the stress transients observed in the flow reversal experiments, we plot the normalized stress value of the first and second stress peak in **Figure 3.9b** (*top*). In addition, the oscillation period of the stress transients, as measured by twice the strain period between the first peak and first valley, we similarly plot in **Figure 3.9b** (*bottom*). Comparison of these two data sets with the qualitative evolution of the stress transients leads us to divide the data into five distinct zones, labeled and delineated by the dashed vertical lines.

As the shear rate is reduced towards Zone I and lower, the normalized stress peaks and oscillation periods approach plateau values. However, as observed in the transient data, they are not strain-scaling because the entire transient curve shifts to larger strains with increasing shear rate. As such, it is unclear if strain-scaling behavior will be recovered at lower shear rates, but the low torque values and large strains required for reaching a steady state limit our experimental investigation.

In Zones II and III, the oscillation period decreases, first slowly, then more rapidly, and reaches a minimum at 68 s^{-1}. Moreover, the changes in the relative magnitude of the first and second stress peaks upon flow reversal between Zone II and III suggest that a qualitative change in the nature of the tumbling dynamics occurs over this shear rate regime.

The strongly oscillating stress transient behavior of Zone IV appears to be similar to results attributed to the so-called wagging regime, identified previously in PBG[112, 117] and *fd* virus suspensions.[118, 119] In this zone, both the normalized stress overshoot and the oscillation period, i.e., strain period of the director oscillations, both increase dramatically over a narrow shear rate regime. As the shear rate is increased past the wagging regime into Zone V, we conclude the director achieves stationary flow alignment as evidenced by the non-oscillating stress transients and transition from decreasing to increasing steady state N_1 values.

To further probe the evolution of the nematic director of nematic PBDT under flow across the flow curve, we utilized transient step-down experiments. In a step-down experiment, the solution is sheared until a steady-state is reached in the flow-alignment regime, where the director adopts a stationary angle. After a steady-state stress is attained, the shear rate is suddenly reduced without changing direction. By monitoring the transient stress as a function of applied strain following the step-down, the data reports on the temporal evolution of the nematic director.[117]

The transient behavior of LCPs in flow reversal and step-down experiments are intimately related. However, the effects are magnified in a step-down experiment as the difference in the dynamical behavior of the director of the initial and final states can be dramatically different, while in flow reversals they are identical.[117] We plot the results of this experiment for 21 g L^{-1} in **Figure 3.10a—d**, separating the stress transients into different plots for visual clarity.

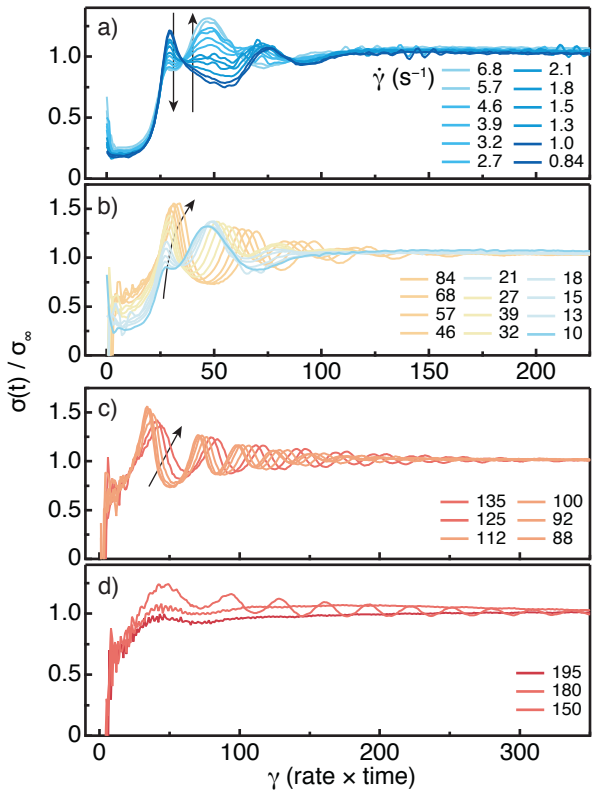

Figure 3.10. Normalized stress transient following shear step-down from 570 s^{-1} to the shear rate indicated in the figure for 21 g L^{-1}. The arrows indicate increasing the value of the final shear rate following the step-down.

The qualitative behavior of the transient stress following step-downs is similar to that observed in flow reversal experiments, but the effect of varying the final shear rate is more dramatic. It becomes clear from the evolution of the transient stress in **Figure 3.10a**, where the final shear

rate is varied through Zones I and II as identified in the flow reversal experiments (see **Figure 3.9b**), that a particular dynamical response is increasing in magnitude while another is being suppressed as the shear rate is increased, shown by the two vertical arrows showing the direction of increasing shear rate. As the shear rate is varied, a point along the strain axis maintains its normalized stress value, creating an effect similar to an isosbestic point, indicating that the system is changing linearly from one state to another.[188] That is, the emergence of one director response upon shear step-down likely occurs at the expense of the prior state with a linear relationship in terms of their contribution to the shear stress. To the best of our knowledge, no experimental data of this nature on nematic LCPs other than PBDT has been reported in the literature.[171]

As the shear rate increases in **Figure 3.10b**, the stress overshoot of the first peak increases and the oscillations become less damped. This trend continues into **Figure 3.10c**, producing strong and persistent oscillating stress transients, most pronounced at a final shear rate of 135 s^{-1}. **Figure 3.10d** shows that the oscillations become increasingly suppressed as the final shear rate is increased above 150 s^{-1}. Note that the local maximum in the steady-state viscosity for 21 g L^{-1}, and minimum in N_1, occurs at a shear rate of 195 s^{-1} (see **Figure 3.4**). At this final shear rate, we do not observe any oscillatory stress response following shear step-down. This is consistent with the results of Mewis et al., who found that the anomalous stress oscillations observed after shear step-downs were eliminated at the shear rate corresponding to the minimum in the steady-state N_1.[117] Here, we suggest that the observed local maximum in the viscosity and minimum in N_1, as well as the elimination of oscillating stress transients, are due to the presence of an out-of-plane steady director state, as previously predicted in numerical simulations.[97,98]

Increasing the solution concentration of PBDT causes the emergence of a broad shear thickening regime at moderate shear rates in the steady-state flow curve (see **Figure 3.4** and **Figure 3.5**). To understand this behavior, we investigated the 30 g L^{-1} solution using the same shear step-down experimental protocol as performed for 21 g L^{-1}. We plot the transient stresses following step-downs for 30 g L^{-1} in **Figure 3.11**, and separate the data into subplots for visual clarity. At 30 g L^{-1}, we observe shear thickening behavior in the steady-state viscosity over the shear rate regime of 2.1—21 s^{-1}, while N_1 is still an increasing function of shear rate, with the first local maximum of N_1 occurring at a shear rate of 46 s^{-1} (see **Figure 3.4**). Comparison of the transient data from the two concentrations indicate that the evolution in the stress transients at low shear rates are qualitatively similar. The initial transient consists of a peak, valley, and second peak before being damped to its equilibrium stress value. As the shear rate increases, the behavior transitions smoothly into a transient that exhibits an initial shoulder followed by a broad maximum and minimum, before reaching the equilibrium stress value. The point of constant normalized stress upon increasing shear rates from 0.84 to 3.2 s^{-1} is also observed at 30 g L^{-1}, as seen in the lower concentration.

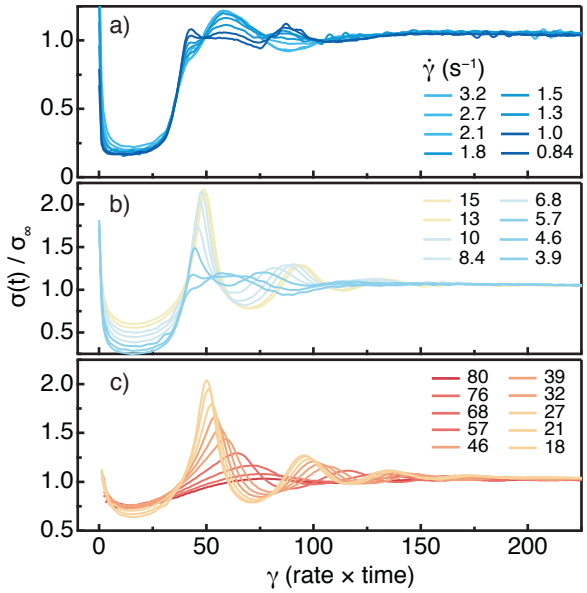

Figure 3.11. Normalized stress transients following step-down from an initial shear rate of 180 s^{-1} for 30 g L^{-1}. The peak in the steady-state viscosity occurs at ~15 s^{-1}, and the dip in the steady-state N_1 occurs over the shear rate range of 46—88 s^{-1}.

The most striking difference between the two concentrations is that the magnitude of the stress overshoot of the first peak for 30 g L^{-1}, which are significantly higher than observed at 21 g L^{-1}, reaching over two times the equilibrium stress value. The maximum value of the stress overshoot occurs at a shear rate that is close to the peak in the shear thickening of the steady-state viscosity. The qualitative behavior of the transient stress following step-down, with extremely large stress overshoots, *are not consistent with the observed behavior that has been assigned as director wagging in other systems*.[112, 117, 118] Moreover, note that the positive dip in N_1 for 30 g L^{-1}, which has been correlated with the existence of director wagging,[153] spans the shear rate regime of 46—88 s^{-1}, clearly occurring at higher shear rates than the large stress overshoots.

We extract further information about the nature of the director responses by investigating how the transient N_1 signal evolves after the shear step-down, and its relation to the shear stress. We plot the transient shear stress for the 21 g L^{-1} solution (as in **Figure 3.10**) and N_1, after

subtraction of the steady-state N_1 value, for a select group of shear rates in **Figure 3.12**. For completeness, we give the transient shear stress and N_1 data for every shear rate investigated for 21 g L^{-1} in **Figure B.6** and **Figure B.7**, and for 30 g L^{-1} in **Figure B.8** in **Appendix B**.

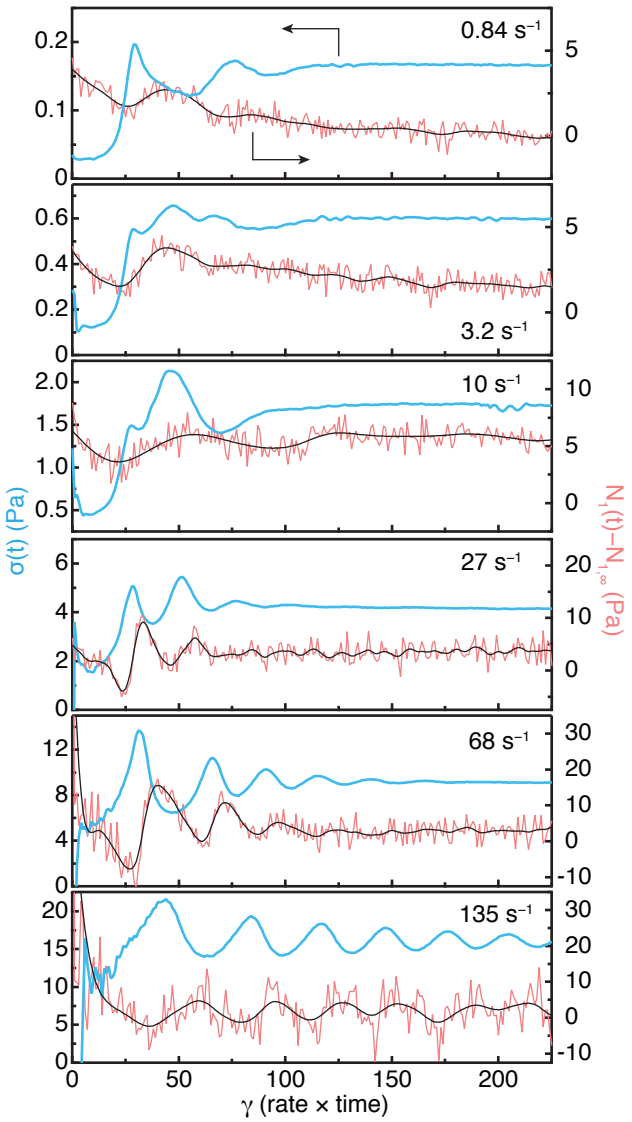

Figure 3.12. Comparison of the shear stress $\sigma(t)$ and first normal stress $N_1(t)$ transients following shear step-down for $c = 21$ g L^{-1}. Shear stress (blue, left) and N_1 after subtraction of the steady-state N_1 value (red, right) transients following shear step-down from 570 s^{-1} to the final shear rate indicated in the figure legend. The black lines are smoothed fits to the raw N_1 for visual clarity.

At final shear rates of 27 and 68 s^{-1}, we observe the onset of strong negative deviations in the transient N_1 signal following step-down and the emergence of a damped oscillatory pattern similar to the behavior in the shear stress. In general, the peaks in the shear stress follow the minimum in N_1, in terms of their strain position, following shear step-down. Moreover, the strain period of oscillations of the shear stress and N_1, as measured by the peak-to-peak distance, are identical within experimental uncertainty. However, as the final shear rate is increased to 135 s^{-1}, the oscillations in the transient shear stress and N_1 data broaden and become more sustained, extending out to over 300 strain units before damping down to the final steady state.

3.3.5. Construction of Dynamic Stress Paths

The microscopic origin of the viscoelastic behavior of LCPs can arise from either elastic or viscous contributions to the stress tensor. Elastic stresses arise from distortions of the molecular ODF, while viscous stresses originate from polymer-solvent frictional forces, as discussed previously. To understand the relative magnitudes of these two stress contributions, Maffettone et al. performed numerical simulations in the high-shear rate regime in transient flow reversal, step up, and step-down experiments.[173] Their simulations showed that construction of so-called dynamic stress paths, i.e., transient N_1 versus shear stress, indicate the relative importance of the elastic and viscous stresses by the "chirality" of the stress path. In this representation, the chirality refers to the direction of the stress path rotation, either clockwise or counterclockwise. In the case of purely elastic stresses, the stress paths exhibited clockwise rotations, while conversely for purely viscous stresses. If a combination of elastic and viscous stress contributions is present, the direction of rotation of the stress path may undergo an inversion during the transient experiment. The authors compared their numerical simulations to experiments on liquid crystalline PBG in m-cresol. In all transient flow experimental protocols,

including flow reversals and shear step-downs, the stress paths exhibited a counterclockwise rotation. This led to the conclusion that the viscous stress contribution is dominant at high shear rates. Moreover, the parameter β_V, which is a measure of the relative importance of the viscous to elastic stresses, was thus estimated to be near the dilute limit, i.e., $\beta_V = 0.15$ for PBG in *m*-cresol. Later work by Larson reassessed the relative magnitudes of the viscous and elastic stresses by analyzing the concentration dependence of the viscosity over the I-N transition and in the fully nematic phase and estimated $\beta_V = 0.03$, which is about five times smaller than the dilute limit.[129] This result suggested that the elastic stresses remain significant in the case of lyotropic PBG solutions at low shear rates, but at higher shear rates the viscous stresses become increasingly important.

To probe the relative importance of viscous and elastic stresses of nematic PBDT under shear, we constructed dynamics stress paths from the shear step-down experiments for $c = 21$ and 30 g L^{-1} in **Figure 3.13** and **Figure 3.14**, respectively. The arrow heads along the stress paths indicate the direction of increasing strain following the step-down. For all stress paths, we plot the first 200 strain units to capture the initial transient stress information, which is sensitive to the nematic director's response as it evolves from a flow aligned state to a stable director state at lower shear rates.

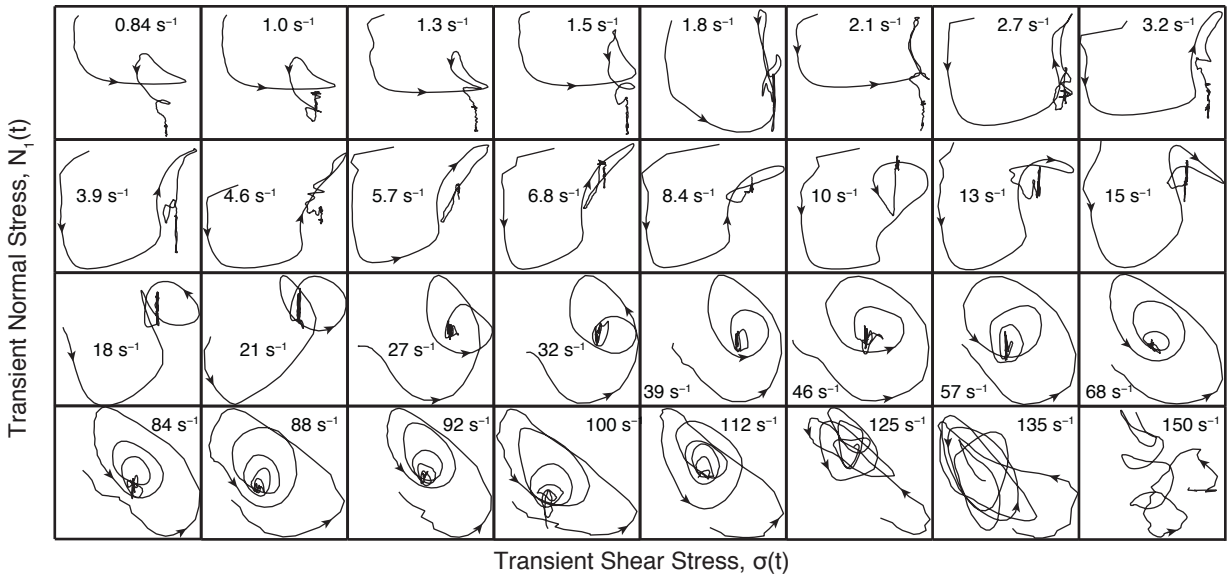

Figure 3.13. Transient stress paths following shear step-down for 21 g L^{-1} from an initial shear rate of 570 s^{-1}. The first 200 strain units are plotted, and the direction of increasing strain is indicated by the arrow heads. The final shear rates are indicated in the figures.

The stress paths following step-down undergo a dramatic evolution as the final shear rate is increased from the low-shear rate shear thinning regime, up to the hesitation in the flow curve near 150 s^{-1}. At the lowest shear rates, the stress paths form a counterclockwise, irregularly shaped looping pattern, that is eliminated as the shear rate is increased up to 2.1 s^{-1}. From 2.1 to 4.6 s^{-1}, the stress paths proceed initially counterclockwise but then nearly trace over themselves as the transient progresses. Over a narrow shear rate range, from 5.7 to 8.4 s^{-1}, we observe the onset of clockwise loop formation following the initial counterclockwise procession, before eventually giving way to a counterclockwise spiral towards the end of the path. As the shear rate is increased into the range of 21—100 s^{-1}, the initial clockwise loop is eliminated, and well-defined counterclockwise spirals develop. This shear rate regime corresponds to the onset of stronger shear thinning in the steady-state flow curve, and decreasing N_1, for this concentration. Near the minimum N_1 value, at final shear rates of 125—150 s^{-1}, the stress paths become

increasingly chaotic. However, the stress paths remain qualitatively similar in that they exhibit counterclockwise looping patterns, suggesting the dominance of viscous stresses.[173]

The stress paths following step-down for 30 g L^{-1} exhibit qualitative differences at low shear rates compared to the 21 g L^{-1} sample. The magnitude of N_1 for the higher concentration is larger by a factor of five, lending confidence to the observed features. Instead of a counterclockwise looping pattern, suggestive of a dominance of viscous stresses at most shear rates, at shear rates between 0.84—2.1 s^{-1} the stress paths trace out what can be described as three sides of a rectangle that progresses in a clockwise fashion, before looping upwards towards its final behavior with small counterclockwise loops. This behavior suggests the importance of the elastic contribution here due to coupling of the molecular ODF and the shear field, consistent with predictions from theory.[27, 29, 173]

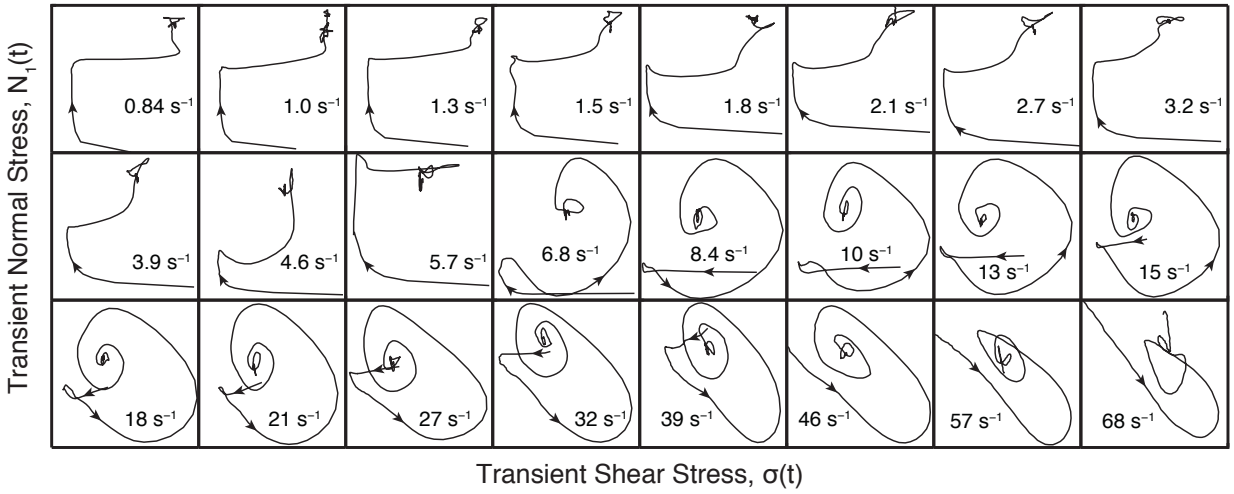

Figure 3.14. Transient stress paths following shear step-down for 30 g L^{-1} from an initial shear rate of 180 s^{-1} for the first 200 strain units. The final shear rate is indicated in the figures, and the arrow heads along the stress path indicate the direction of increasing strain following step-down.

Beginning at a shear rate of 6.8, corresponding to a slightly lower shear rate than the maximum in the steady-state viscosity, and continuing to 21 s^{-1}, the stress path behavior suddenly changes

from its qualitative shape at low shear rates. A well-defined clockwise loop is completed over the initial stress path before completing several circular counterclockwise loops. As suggested by Maffettone et al., this behavior signifies that an elastic contribution dominates the stress path initially, then followed dominance from viscous stresses.[173] We suggest that this elastic, clockwise loop corresponds to the relaxation of the molecular ODF as the director transitions from the initial flow-aligned state at high shear rates. The final state, assigned to be kayaking, results in the shear thickening behavior seen in the steady-state viscosity.

Increasing the final shear rate above 21 s^{-1} results in the elimination of the initial clockwise loop pattern, where shear thinning is recovered in the steady-state flow curve. Furthermore, the counterclockwise loops of the stress paths gradually become more elongated and progressively tilt towards an angle along an axis at –45° as the shear rate is increased into the regime of the local minimum in N_1 for $c = 30$ g L^{-1}. This tilting of the stress path indicates that the shear stress and N_1 become increasingly out of phase as the shear rate is increased near the regime of the dip in N_1.

In summary, construction of these dynamic stress paths has enabled us to further characterize the director dynamics that lie as the origin of the steady-state rheological response. We have made conclusions regarding shear rate regimes that correspond to primarily elastic (with clockwise stress path rotation) and viscous (with counterclockwise stress path rotation), or a combination that vary over the course of the stress transient. Using the framework set forth by Maffettone et al. to interpret these data, we conclude that the origin of the steady-state shear thickening lies with the viscous stress contribution.[173] This dominance of viscous stresses is consistent with the shear thickening arising from motions of the rods in the kayaking state, supporting our prior conclusion.[171] In contrast, this behavior is inconsistent with shear thickening

arising from a broadening of the molecular ODF due to the wagging state, suggested to be the origin of shear thickening observed in nematic *fd* suspensions.[118, 119] While the results we have presented have been mainly observational, we think that this data will provide guidance for future numerical simulations that aim to capture the behavior of experimental nematic polymers under shear.

3.4. CONCLUSIONS

In conclusion, we have presented transient and steady-state rheological data of charged, rodlike sulfo-aramid assemblies in the isotropic and liquid crystalline phases. The flow behavior of the isotropic solutions suggests a shear-induced I-N transition that exhibits the anomalous features typically associated with nematic LCPs, namely a non-monotonic shear rate dependence of N_1. The flow curves of nematic PBDT solutions exhibit an unusual shape, with two regimes of shear thickening. Using rheo-SANS and transient rheological measurements, we suggested the origins of these shear thickening regimes as director kayaking and out-of-plane steady states, respectively. We analyzed the transient rheological shear step-downs by constructing stress paths, which indicated a transition from primarily elastic to the viscous stress contribution at the onset of steady-state shear thickening. These stress paths provide a fingerprint of the nonlinear rheological behavior of nematic liquid crystalline polymers under shear and provide new experimental information to compare with simulations.

CHAPTER 4: IRREVERSIBLE SHEAR-ACTIVATED GELATION OF A LIQUID CRYSTALLINE POLYELECTROLYTE[2]

4.1. INTRODUCTION

Associating polymers (APs) form transient networks through intermolecular physical crosslinks to yield 'elastically active chains' that dictate the solution viscoelastic properties.[189-191] Semirigid APs, such as polypeptides,[192-194] biopolymers,[195-198] or polymer-grafted virus particles,[199, 200] can form physical gels when the solution colligative properties, such as solvent quality, temperature, or ionic strength, are varied and, in turn, change the network topology. In a similar manner, external fields such as shear flow, can also induce the formation of a physical network structure, known to occur, for example, within spider silk spinning dope,[201, 202] and within the synovial joint fluids of mammals.[203]

In the case of shear thickening wormlike micelles (WLMs), shear-induced structures (SIS) are formed that can be reversible[146, 204-211] or irreversible.[145, 212] The formation of SIS in WLMs is thought to arise, in part, from the shear-induced growth of micelle length via the Turner-Cates fusion mechanism.[213, 214] In general, this phenomenon is observed in dilute solution conditions, when the mean separation distance between WLMs exceeds their length; an aligned phase is formed with increased birefringence, viscosity, modulus, and first normal stress difference. A variety of hydrodynamic and elastic instabilities, or shear-induced local concentration

[2]This chapter has been accepted for publication as a letter in *ACS Macro Letters*. The original citation is as follows: Fox, R. J.; Hegde, M.; Zanelotti, C. J.; Kumbhar, A. S.; Samulski, E. T.; Madsen, L. A.; Picken, S. J.; Dingemans, T. J., Irreversible Shear-Activated Gelation of a Liquid Crystalline Polyelectrolyte. *ACS Macro Lett.*, *In Press*.

fluctuations may result under shear in WLMs.[215-223] Here, we explore the role of structural changes on the rheological behavior of PBDT solutions at high concentrations, far above the onset and fully nematic critical concentrations. Surprisingly, we find that PBDT undergoes irreversible gelation when sheared above a critical shear rate at sufficiently high concentrations, and we elucidate some aspects of the mechanisms of this unusual behavior.

4.2. EXPERIMENTAL

The polymer sample used in this study was synthesized following published procedures,[56, 65] and was previously characterized with a viscosity average molecular weight of 14.7 kDa as measured in 96% sulfuric acid by capillary viscometry.[125] Aqueous solutions were prepared by mixing dry polymer and deionized water in tightly sealed vials. The vials were heated upon a hot plate set to 80 °C for over 1 week with frequent mixing to ensure complete dissolution. Polarized optical micrographs were taken with a Nikon Microphot-FX microscope using an OMAX 18 MP digital microscope camera. Rheological testing was carried out with a TA Instruments ARES G2 rheometer with a Peltier temperature control system. A Taylor-Couette geometry having a rotating outer and fixed inner cylinder with a recessed end (height H = 41.518 mm, inner radius R_i = 13.829 mm, gap e = 1.171 mm) was used for experiments shown in **Figure 4.2** and **Figure 4.3**. A 50 mm 1° cone and plate geometry was used for the experiments shown in **Figure 4.4**. Solvent traps for all geometries was used to prevent the evaporation of water during measurement and the temperature was controlled with a Peltier system. For TTS, a 25 mm parallel plate geometry was used for the data presented in **Figure 4.3**. In the case of cone and plate and parallel plate measurements, a thin oil layer was coated along the sample edges to suppress evaporation. SAXS measurements were taken with a SAXSLab Ganesha equipped with a Cu 50 kV Xenocs Genix ULD SL X-ray source producing an incident X-ray beam of λ = 1.54

Å and a 2D detector. The data was azimuthally averaged, reduced into 1D using SAXSLab software. Solutions or gels were loaded into 1.5 mm a thin-walled boron-rich 1.5 mm diameter capillary (Charles Supper) for SAXS measurements. SEM images were taken using a Hitachi S-4700 cold cathode field emission scanning electron microscope operating at 20 kV and 11.4 mm working distance. Samples were sputtered with 3 nm Au prior to imaging. For NMR measurements, PBDT samples with concentrations of 0.5 – 10 wt% were made in ^2H_2O in standard NMR tubes. Quantitative ^2H spectra were measured using a 400 MHz Bruker Avance III WB NMR spectrometer equipped with a mic probe coupled with a 5 mm ^2H rf coil, and using $\pi/2$ pulse length of 10.6 μs, acquisition time of 1.8 s, and relaxation delay of 12 s. Nematic, isotropic, and coexistence regions were quantified by ^2H NMR signal integrations as previously described for PBDT solutions.[62]

4.3. RESULTS AND DISCUSSION

4.3.1. Rodlike Assemblies and Nematic Phase Diagram

In this Chapter, we report the first example of irreversible shear-activated gelation in liquid crystalline solutions of a rigid polyelectrolyte, a sulfonated all-aromatic polyamide, 2,2'-disulfonyl-4,4'-benzidine terephthalamide (PBDT), shown in **Figure 4.1a**.[56, 58, 62, 65-68, 125]

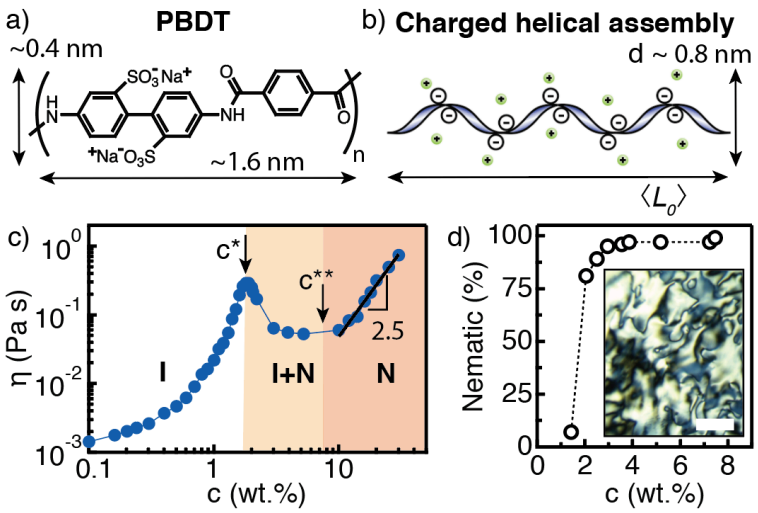

Figure 4.1. Structure and nematic phase behavior of PBDT in salt-free water. (a) Molecular structure of the sulfonated, all-aromatic polyamide (PBDT) with the monomer dimensions shown. (b) Cartoon of the charged, double helical assemblies of PBDT in aqueous solution as reported by Wang et al.[67] (c) Steady-state viscosity of PBDT solutions in water in the isotropic (I), biphasic (I+N), and fully nematic phase (N). The I-N transition concentration c^* and the fully nematic transition concentration c^{**} are shown by the arrows. (d) Phase diagram measured by ^{2}H NMR spectroscopy and (*inset*) polarized optical micrograph of a 12 wt.% PBDT solution in water under a cover slip (×10 magnification), exhibiting a fully nematic Schlieren texture. Scale bar is 200 μm.

PBDT is a water-soluble polyanion with a molecular diameter of ~0.4 nm that self-assembles into helical dimers (hard core diameter ≈ 0.8 nm), **Figure 4.1b**.[67] These dimers, in turn, undergo linear aggregation into rodlike assemblies, we refer to here as PBDT rods, with a quiescent mean length $\langle L_0 \rangle$ that is determined by a balance of thermal energy and repulsive electrostatics with attractive intermolecular interactions (e.g., hydrogen bonding and hydrophobic association). Positional localization of counterions into 1D charge density waves along the rods may also induce an effective attractive force that promotes association.[224, 225] Other sulfonated, all-aromatic macromolecules are known to form similar rodlike, high-aspect-ratio assemblies that are soluble in water and can form anisotropic phases,[50-54, 56, 226-231] suggesting that the gelation behavior reported herein may be a general phenomenon.

PBDT rods exhibit a low isotropic-nematic (I-N) transition concentration of ~1 wt.%, consistent with an extremely high aspect ratio. Note that PBDT rods should be considered a type of equilibrium assembly, analogous to WLMs, since the aggregation number N_p and $\langle L_0 \rangle$ are thermodynamic quantities.[232] $\langle L_0 \rangle$ can be estimated by application of the Onsager theory to the I-N transition concentration.[15, 16, 21] The local maximum in the viscosity versus concentration, shown in **Figure 4.1c**, provides an estimate the I-N transition concentration, $c^* = 1.9$ wt.%.[6] Taking $\phi^* \approx 0.015$, we estimate $\langle L_0 \rangle \approx 210$ nm at the I-N transition in the quiescent state; this is an upper bound, as we expect a distribution of rod lengths, and longer rods will preferentially partition into the N phase.[233] The nematic phase diagram measured by ^{2}H NMR is shown in **Figure 4.1d**, and above $c^{**} = 7.5$ wt.%, the entire solution exhibits a homogeneous, characteristic Schlieren texture under polarized optical microscopy (see inset for a 12 wt.% solution). The viscosity increases above c^{**} as $\eta \sim c^{2.5}$, indicating that the stresses arising from rod-solvent and/or rod-rod interactions may increase with concentration.[129]

4.3.2. Nonlinear Rheology and Irreversible Gelation

We investigated the rheological properties of salt-free PBDT solutions at concentrations in the fully nematic phase. The samples range in concentration from 10–30 wt.% at pH = 9, and the viscosity as a function of shear rate is shown in **Figure 4.2a**. Up to 14 wt.%, the flow curves are nearly Newtonian and/or exhibit very weak shear thinning. We begin to observe slight shear thickening at 16 wt.%, but the flow curve remains continuous. For this concentration, a noticeable change in color was observed, from yellow to off-white, suggesting a change in network topology, despite the fact that the solution did not form a solid gel.

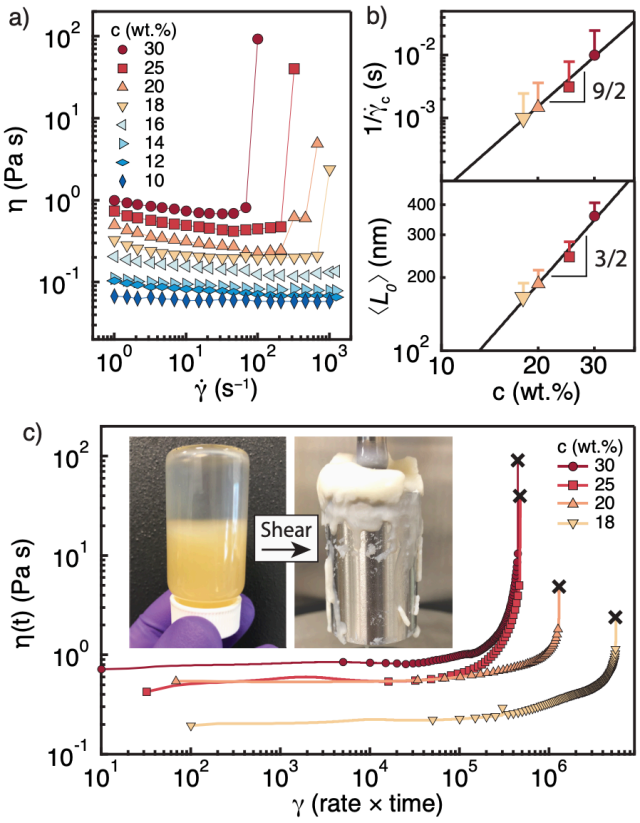

Figure 4.2. Nonlinear rheology of nematic PBDT solutions. (a) Steady-state flow curves for fully nematic PBDT solutions at 10–30 wt.%. The last data point for samples that undergo irreversible gelation is taken as the maximum recorded viscosity before gel fracture/sample expulsion. (b) The inverse critical shear rate (*top*) corresponding to the onset of irreversible, discontinuous shear thickening and average length (*bottom*) of the PBDT rods, calculated by **Eqn. 4.1**, as a function of concentration. (c) Transient viscosity at the critical shear rate as a function of dimensionless strain (shear rate × time). The black crosses mark the termination of the experiment due to sample expulsion from the shearing gap. The inset shows digital photographs that demonstrate the transition of a 25 wt.% PBDT sample from a low viscosity nematic solution prior to shear (*left*) to a physical gel (*right*) after shear-activated gelation.

The order of magnitude discontinuity in the flow curve at 18 wt.% at $\dot{\gamma}$ = 1000 s^{-1} represents a stark departure from the behavior observed at lower concentrations. Higher concentrations (20–30 wt.%) produce larger discontinuities in the viscosity that occur at lower shear rates. In fact, the final viscosity values shown are underestimates, as sample expulsion from the shearing gap terminates the experiment.

We rationalize the reduction in the critical shear rate by noting that the onset of rod growth in the Turner-Cates fusion mechanism under shear flow occurs when the Peclet number $Pe = \dot{\gamma}/D_r$ where D_r, the rotational diffusion coefficient, is of order unity.[213, 214] From this definition, $\dot{\gamma}_c$ for the growth of rods of mean length $\langle L_0 \rangle$ is

$$\dot{\gamma}_c = \frac{k_B T}{\eta_s \langle L_0 \rangle^3} \qquad \textbf{(Eqn. 4.1)}$$

where $k_B T$ is the thermal energy, and η_s is the solvent viscosity. Note that this expression is derived by assuming the rotational diffusivity of the rod in dilute solution. However, it has been shown that the diffusivity of rods in the liquid crystalline state at high shear rates is much lower than at the same concentration in the isotropic state.[129, 173] Thus, we propose that **Eqn. 4.1** is an appropriate means to determine the concentration scaling of the rod length from the critical shear rate.

The inverse critical shear rate $1/\dot{\gamma}_c$ for the onset of this irreversible gelation as a function of concentration is given in **Figure 4.2b** (*top*). The onset shifts systematically to lower $\dot{\gamma}$ with increasing concentration and scales as $1/\dot{\gamma}_c \sim c^{9/2}$. Using **Eqn. 4.1** and the measured values of $\dot{\gamma}_c$, we plot $\langle L_0 \rangle$ as a function of concentration in **Figure 4.2b** (*bottom*). The $\langle L_0 \rangle$ values are in approximate agreement with $\langle L_0 \rangle$ as calculated from the I-N transition concentration, and scales with concentration as $\langle L_0 \rangle \sim c^{3/2}$. This scaling exponent is three times the classic result for WLMs in salt-free solution, $\langle L_0 \rangle \sim c^{1/2}$.[234] The stronger concentration dependence of $\langle L_0 \rangle$ likely originates from the unscreened Coulombic interactions in salt-free PBDT solutions that favor the formation of end-caps, and thus shorter rods.[235] At low ionic strength, Safran et al predicts a growth law to take the form of an apparent power law $\langle L_0 \rangle \sim c^{1/2\,(1+\Lambda)}$ with $\Lambda > 0$, consistent with our data.[235]

The transient viscosities $\eta(t)$ at $\dot{\gamma} = \dot{\gamma}_c$ between 18–30 wt.% are shown as a function of dimensionless strain (γ = shear rate × time) in **Figure 4.2c**. We observe strong rheopectic behavior, where $\eta(t)$ increases with time at constant $\dot{\gamma}$, first gradually through an induction period and followed by rapid acceleration and gel formation at the highest strains. The transition from a low viscosity fluid to a physical gel is demonstrated by the digital photographs in the inset of **Figure 4.2c** before loading (*left*) and after experiment termination (*right*). Note that the image shows the gel after expulsion from the shearing gap of the Couette cell, and no foaming was observed. The structure developed under steady shear does not relax when the flow is stopped, or indeed after removal from the rheometer, demonstrated in **Figure D.1**, and is composed of solid-like birefringent fibrillar structures. This morphology is consistent with rod growth and irreversible network formation at the critical shear rate.

4.3.3. Linear Rheology and Structural Characterization

We investigated the viscoelastic behavior of the PBDT gels resulting from the experiments shown in **Figure 4.2** with linear rheology. We performed isothermal frequency sweeps from 100 to 0.1 rad s^{-1} between 25 and 75 °C and applied time-temperature superposition (TTS) to horizontally shift each isotherm along the frequency axis to construct master curves at T_{ref} = 25 °C spanning nearly 10 decades in frequency for each concentration (see **Figure D.2a**). Furthermore, we collapsed the concentration series using time-concentration superposition (TCS) to generate a single master curve spanning over 20 decades in frequency and over 5 decades in dynamic moduli, shown in **Figure 4.3a**.

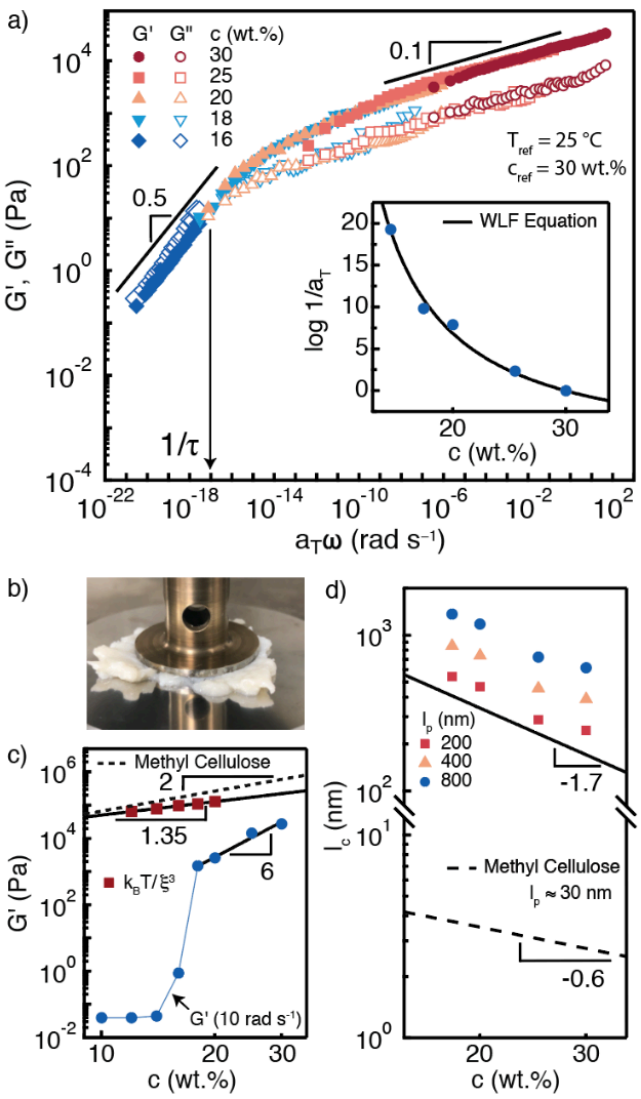

Figure 4.3. Linear rheology of PBDT gels. (a) Storage (G', filled symbols) and loss (G'', open symbols) moduli master curve as a function of shifted frequency from TTS at T_{ref} = 25 °C and TCS at c_{ref} = 30 wt.%. The network lifetime ($1/\tau$) is found at the crossover of G' and G''. The inset shows the shift factors derived from TCS as function of concentration and fit using the William-Landel-Ferry (WLF) equation given by **Eqn. 4.2**. (b) Digital photograph of a 25 wt.% shear-activated gel after loading into the rheometer, evidencing solid-like behavior. (c) G' at 10 rad s^{-1} and 25 °C (filled circles) for the gels as a function of concentration. The calculated G' based on polyelectrolyte scaling theory ($G' \approx k_BT/\xi^3$) is shown (filled squares). The extrapolated G' for an isotropic methyl cellulose (MC) gel is given for comparison (dashed line) from ref[236]. (d) Distance between physical crosslinks (l_c) calculated from **Eqn. 4.3** as a function of concentration. The extrapolated l_c for MC gels is given for comparison.

The collapse of the data using TTS and TCS indicates that the nature of the gel structure is concentration independent. The TCS shift factors a_T are plotted in the inset of **Figure 4.3a** and are well-described by a modified William-Landel-Ferry (WLF) equation

$$\log 1/a_T = \frac{A(c - c_{ref})}{B+(c - c_{ref})} \quad \textbf{(Eqn. 4.2)}$$

where A and B are fitting constants and $c_{ref} = 30$ wt.%. The gels, shown in **Figure 4.3a**, exhibit a solid-like viscoelastic response ($G' > G"$) with a nearly frequency independent modulus ($G' \sim \omega^{0.1}$) over a wide range of frequencies down to the inverse network lifetime $1/\tau \approx 10^{-17}$ rad s^{-1}. At frequencies below $1/\tau$, G' and $G"$ are parallel and scale as $\sim \omega^{1/2}$ over the 5 lowest decades in frequency – no terminal flow behavior is observed ($G' \sim \omega^2$, $G" \sim \omega^1$). A Cole-Cole plot lacks the signature semi-circle shape of an ideal Maxwell fluid, as is found for WLMs,[234] confirming that the gels have a broad spectrum of relaxation times (see **Figure D.2b**).[232] This behavior is similar to that observed in stiff biopolymer networks whose dynamics are governed by transient physical crosslinks.[237]

The low values of G', given in **Figure 4.3c**, highlights the unusual structure of the gels. For comparison, we calculate G' using polyelectrolyte scaling theory[43, 191] $G' \approx k_B T/\xi^3$, where ξ is the lateral correlation length determined from small-angle X-ray scattering (SAXS, see **Figure D.3** and **Figure D.4**), and extrapolate the trend in G' for an isotropic, fibrillar methyl cellulose (MC) gel to equivalent concentrations.[236] The PBDT gels exhibit a remarkably low G' (1–30 kPa) when compared to the scaling calculation and extrapolated modulus of the MC gel. We postulate that the lower G' arises from the local nematic alignment that reduces the number density of physical crosslinks. Above 18 wt.%, the concentration scaling of G' is stronger ($G' \sim c^6$) than both the scaling calculations ($G' \sim c^{1.35}$) and typical fibrillar gels ($G' \sim c^{2-2.5}$),[236, 238-240] likely from the strong dependence of the rod connectivity on the applied shear rate during gelation.

To understand the nature of the gel structure, we calculate the distance between physical crosslinks l_c using a model for the linear elastic modulus G_0 of fibrillar gels[241]

$$G_0 = 6\rho k_B T \frac{l_p^2}{l_c^3} \quad \textbf{(Eqn. 4.3)}$$

where $\rho = \phi/\pi r^2$ is the filament-length density, r is the fibril radius, and l_p is the persistence length. The value of l_p for PBDT rods is at least 200 nm based on the I-N transition concentration reported here, but could be up to 1 μm.[67] **Figure 4.3d** shows the calculated l_c using various values of l_p (200, 400, and 800 nm). The $l_c \approx$ 100–1000 nm values for PBDT shear-activated gels are much higher than the model MC gel, where the extrapolated $l_c \approx$ 1–10 nm,[236, 239] consistent with physical crosslinking occurring at the ends, rather than along the body, of PBDT rods.

Further, we characterized the gel structure pre- and post-shear through SAXS and WAXS, see **Figure D.3**, **Figure D.4**, **Figure D.5**, and related discussion in **Appendix D**. We observe an increase in low-q scattering post-shear, suggesting the onset of network formation on mesoscopic length scales. The position and shape of the structure factor, corresponding to the lateral rod-rod correlation length, does not change after shear, indicating a constant rod diameter. This is in contrast to thermoreversible gels of rodlike polymers and virus, where the suppression of the structure factor is correlated with the onset of gelation.[200, 242] The WAXS spectra, which reports on the local polymer-polymer packing within the rods, is unchanged after gelation, ruling out shear-induced crystallization as a potential gelation mechanism. Observations of a freeze-fractured 16 wt.% post-shear gel via scanning electron microscopy (SEM) were consistent with network formation, see **Figure D.6**. Our SEM observations are similar to what is observed after irreversible gelation of WLMs due to branching and junction formation of micellar bundles.[212]

We investigated the role of electrostatic interactions on gel formation by measuring the SAXS spectra and flow curve of a 3 wt.% PBDT solution with increasing concentration of monovalent salt (NaCl), see **Figure D.7a—c** and related discussion in **Appendix D**. The addition of salt gradually suppresses the structure factor peak, arising from rod-rod electrostatic repulsion, indicating a suppression of positional correlations between rods. Moreover, the nonlinear rheological behavior of the PBDT solution with added salt evidences a weak gel with no measurable hysteresis. Both of these observations are in contrast to the behavior observed when PBDT gels are formed under shear, suggesting a different mechanism for gel formation.

4.3.4. Shear Rate Dependence of the Induction Time

To probe the underlying gelation mechanism of nematic PBDT rods, we quantified the shear rate dependence of the induction time at a fixed concentration. We utilized a cone and plate geometry to shear a 30 wt.% PBDT solution at a fixed shear rate until the initially low viscosity solution underwent gelation, shown in **Figure 4.4a**. The critical shear rate found for this concentration is not directly comparable to the experiments in **Figure 4.2**, as the solution used here was aged for 12 mo following the initial set of experiments. No signs of aggregation by optical microscopy were evident over this time period. However, the critical shear rate increased from 100 s^{-1} to 680 s^{-1} for this concentration, corresponding to a decrease in rod length from 408 to 215 nm via **Eqn. 4.1**. We determine the induction time t_c by extrapolating the initial and final slopes in the viscosity transient to their intersection point, shown by the dashed lines, shown in **Figure 4.4a**.

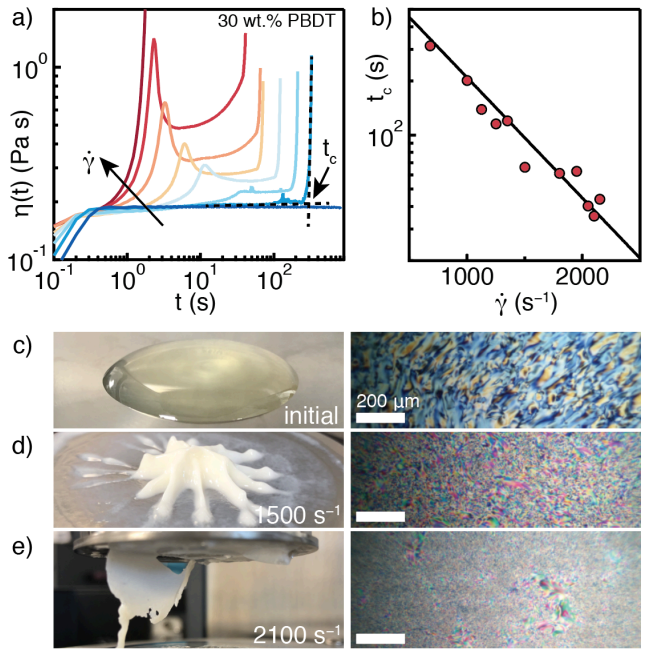

Figure 4.4. Induction time prior to gelation at $c = 30$ wt.%. (a) Transient viscosity as a function of time at a fixed shear rate for a 30 wt.% PBDT solution for shear rates 460, 680, 1000, 1250, 1500, 1800, 2100, and 2300 s^{-1} (blue to red). The induction time (t_c) is found by the intersection of the initial and final slopes. (b) t_c as a function of applied shear rate for $c = 30$ wt.%, fit with a single exponential (solid line). (c) Digital photographs (*left*) and polarized optical micrographs (*right*) of the initial solution, exhibiting a low viscosity, and after shear-activated gelation at (d) 1500 s^{-1}, and (e) 2100 s^{-1}. The stiffness of the final gel increases with increasing shear rate, and solid polymer domains in a background of fluid nematic phase are observed under POM.

We plot t_c as a function of the applied shear rate in **Figure 4.4b**, and fit the data with a single exponential decay function given as $t_c = t_0 \exp(-\dot{\gamma}/\dot{\gamma}_c)$, where $\dot{\gamma}_c$ is the critical shear rate for a given concentration, and t_0 is a prefactor with units of time. We excluded t_c from the experiment conducted at 2300 s^{-1} because the gelation overloaded the rheometer motor within 2 sec of flow inception. Digital photographs in **Figure 4.4c—e** (*left*) evidence the dramatic change in physical properties of the initial low-viscosity nematic fluid to a gel after shear. Polarized optical micrographs of the gels in **Figure 4.4c—e** (*right*) reveal the transition from a fluid nematic to the development of a solid phase. Both the solid and fluid phases of the shear-activated gels are

highly birefringent, inconsistent with shear-induced demixing into a polymer-lean (isotropic) and polymer-rich phase. These observations are consistent with the formation of a physically crosslinked rod network under shear. This dramatic liquid-to-solid transition may result in a breakdown of viscometric flow field during gelation.

4.3.5. Mechanism of Gel Formation

Finally, we propose a mechanism for the gelation of nematic PBDT under shear. Guery et al. first reported an exponential dependence of t_c on the shear rate for a slightly repulsive, non-Brownian water-in-oil-in-water double emulsion that underwent shear-activated gelation.[243] Later, the exponential relationship was found as well in charged colloidal suspensions, and a theoretical expression for t_c on the spherical particle radius, shear rate, and activation energy for pair-wise collision was developed.[244] In the framework of this theory, shear flow reduces the height of the energy barrier for pair-wise collision, similar to the effect of increasing temperature on a thermally activated Arrhenius process. Because the dispersions were kinetically stable at rest, the shear field induces an effective thermalization of the system and causes particle-particle collision at some frequency that increases with the shear rate. However, note that these previous reports are exclusively for spherical colloids with weak attractive interactions, and the current theories have been developed as such.[243-250] For PBDT rods, the energy barrier for rod-rod contact is the strong electrostatic repulsion, preventing rod aggregation at rest. Shear flow increases the attempt frequency for rod-rod contact, and simultaneously lowers the activation energy for successful contact attempts. In the nematic state, these collisions may occur predominantly end-to-end rather than along the body of the rod. Once in close proximity, strong attractive interactions likely arise from hydrogen bonding and hydrophobic interactions. When the activation energy is reduced via shear below a critical value, increasing the shear rate results in

an exponential decrease in the induction time for gel formation. The gels likely form via rod fusion and branching, possibly through the physical interactions of dangling chain ends of the rods, causing subsequent physical crosslinking and irreversible gel formation. Thus, the final rod network is kinetically trapped and cannot undergo disassociation on experimentally accessible time scales.

4.4. CONCLUSIONS

In conclusion, we have reported the first example of a liquid crystalline polyelectrolyte which undergoes irreversible shear-activated gelation in salt-free solution. The structure and rheology of the shear-activated gels are unusual in comparison to gels formed when monovalent salt is added, or other systems that exhibit thermoreversible gelation. We find an exponential dependence of the induction time on the shear rate for gelation, consistent with shear-activated thermalization of rod-rod collisions. This work provides insights into the complex flow behavior of liquid crystalline, charged rods as a new class of shear-thickening fluids ripe for exploration, and must be considered in the fabrication of new materials from these systems.

CHAPTER 5: MECHANICAL REINFORCEMENT OF LIQUID CRYSTALLINE GRAPHENE OXIDE NANOCOMPOSITES

5.1. INTRODUCTION

Polymer nanocomposites (NCs) fabricated with 2D carbon nanomaterials, i.e., graphene and graphene oxide (GO), have been shown to enhance the mechanical properties of the native polymer.[251, 252] However, the maximum attainable property enhancements in polymer NCs are dependent on stress transfer from matrix to nanofiller, which in turn is predicated on several interdependent factors, such as dispersion quality, alignment, and aspect ratio of nanofiller. Toward these ends, the self-organization of the lyotropic liquid crystalline phase of GO (LCGO)[77-79, 81, 82] has been exploited in order to obtain aligned nanostructures within isotropic polymer films[84, 86, 90] or fibers.[87, 253] Layer-by-layer deposition can also produce aligned structures,[254] but this labor-intensive method is limited by the non-ideal matrix-to-nanofiller stress transfer.[255-257]

In addition to the spatial and orientational configuration of the nanofiller, the conformation of the matrix polymer has a dramatic effect on the mechanical properties of the NC. For example, extremely high-strength and high-modulus polymer NCs incorporating thermally reduced GO (rGO) have been reported with hot-drawn polyethylene (PE) films.[258] Without drawing, the dispersion of rGO in PE is poor and mechanical reinforcement is limited. Thus, the combination of a high degree of orientational and spatial order of both nanofiller and polymer is important for

realization of mechanical reinforcement for high-performance NCs. Moreover, it is desirable to avoid complex processing steps, such as drawing, in order to facilitate new applications.

In this Chapter, we expand upon our recent discovery of a hybrid liquid crystalline phase composed of two uniaxial liquid crystals,[66] LCGO suspensions and solutions of the sulfonated, rodlike polyelectrolyte, poly(2,2'-disulfonyl-4,4'-benzidine terephthalamide) (PBDT),[56-59, 62, 65, 67, 68] as shown in **Figure 5.1a**. When dissolved in water, PBDT forms helical rodlike aggregates with diameter of ~1 nm and lengths on the order of several hundred nm, recently described by Wang et al.[67] These liquid crystalline solutions are of interest for fabrication of water transport membranes,[62, 65] and as matrices for ionic liquids for solid-state battery electrolyte materials.[68, 125, 128] When cast into solid-state films, PBDT helices form networks of higher-order rodlike aggregates characterized by a cross-sectional dimension of 50–200 nm, we show by atomic force microscopy (AFM) in **Figure D.1**. At relatively low concentrations, both PBDT and LCGO form uniaxial nematic phases that are birefringent when viewed between crossed polars, shown experimentally in **Figure 5.1b** and schematically in **Figure 5.1c**. We prepared homogeneous, hybrid nematic (^{h}N) dispersions by mixing LCGO and PBDT solutions.[66] Despite not employing sonication to, no visible LCGO aggregation or phase separation is observed in the dispersions, even after standing for time periods over one year. Upon drying the hybrid nematic, the nanocomposite films exhibit a stratified, uniplanar morphology. Unlike traditional methods that require high-shear mixing or sonication that invariably result in flake scission[259] and/or molecular weight degradation,[260] we achieve homogeneous dispersions that are fully liquid crystalline.

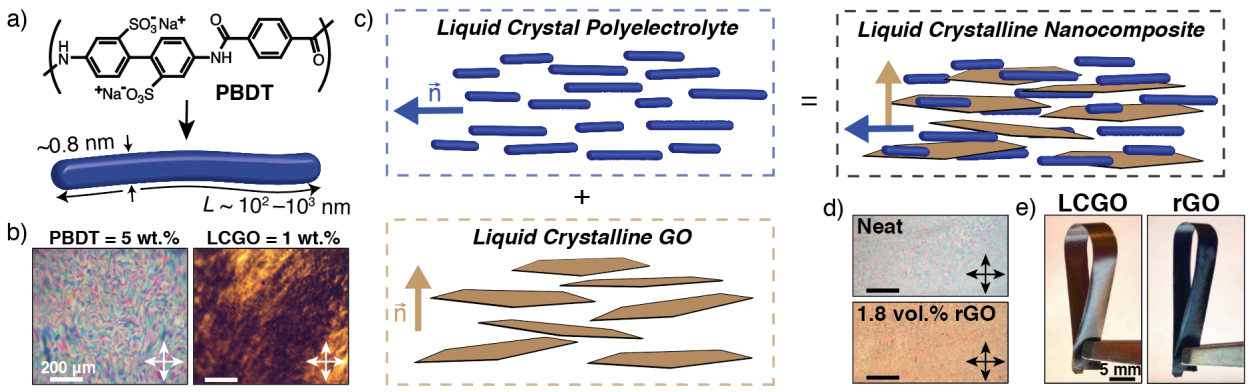

Figure 5.1. (a) Molecular structure and self-assembly of PBDT into helical rodlike aggregates. (b) Polarized optical micrographs of aqueous solutions of neat PBDT (5 wt.%) and LCGO (1 wt.%) demonstrating strong birefringence. (c) Schematic depiction of hybrid liquid crystalline nanocomposites obtained by combining the calamitic (rodlike) PBDT and discotic (platelike) LCGO with two orthogonal local directors. (d) Polarized optical micrograph of a solid-state neat PBDT film and 1.8 vol.% rGO nanocomposite film. No aggregation of LCGO is observed and birefringence of the hybrid nematic phase is observed. (Scale bar = 200 μm) (e) Digital photographs of a 3 wt.% LCGO (1.8 vol.% rGO) film before (*left*) and after (*right*) thermal reduction of LCGO to rGO at 200 °C under N_2.

The liquid crystalline PBDT-LCGO dispersions were deposited onto glass substrates and film casted at a shear rate of 5 s^{-1}; after drying at 60 °C, the nanocomposite films were homogeneously nematic, similar to the neat polymer films (**Figure 5.1d)**. Thermal reduction in-situ of the ~1–2 μm flakes of LCGO to rGO causes a 30% mass reduction **(Figure D.2**, **Figure D.3**, and **Figure D.4**); we corrected the rGO volume fractions for this weight change when reporting concentrations for the PBDT-rGO films. The flexible, mechanically robust, and free-standing films change color from light brown to black after the thermal reduction (**Figure 5.1e**). No change in decomposition temperature was observed for the nanocomposites as compared to the neat polymer (**Figure D.5**).

Herein, we explore the structure and mechanical properties of the hybrid nematic nanocomposite films using a comprehensive set of experimental techniques. Through wide- and small-angle X-ray scattering (WAXS/SAXS), we show that polymer alignment in the

nanocomposite film is easily tuned by simply varying the concentration of LCGO in the hybrid nematic precursor solution. Scanning electron microscopy (SEM) and modulus mapping via atomic force microscopy (AFM) reveal a dramatic enhancement in the stratification and stiffness of polymer fibrils due to confinement between LCGO platelets. Uniaxial tensile measurements reveal superior mechanical reinforcement by using a hybrid liquid crystal dispersion, and modulus reinforcement efficiencies as high as 3.1 TPa are achieved. The benefits of our high-performance liquid crystal polyelectrolyte are exemplified by dynamic mechanical thermal analysis (DMTA) measurements, which show the thermal stability of our NCs up to extreme temperatures of 400 °C. Through time-temperature superposition (TTS) thermo-mechanical measurements, we find that the alignment and confinement of the polymer between LCGO flakes modulates the polymer local relaxation dynamics, and we quantify the activation energy and its change with LCGO concentration. Our data provide compelling new evidence for the potential to exploit hybrid liquid crystalline phases for nanocomposite synthesis.

5.2. EXPERIMENTAL

Materials. Terephthaloyl chloride (TPC) was purchased from Sigma Aldrich and freshly sublimed under vacuum prior to use. 4,4'-diaminobiphenyl-2,2'-disulfonic acid hydrate (BDSA) (95%) was purchased from Alfa Aesar. Purification of BDSA was accomplished by dissolution in NaOH and precipitation into cold EtOH, followed by filtration of the BDSA sodium salt. The salt was dissolved in water and precipitated by the addition of a stoichiometric amount of concentrated HCl (37 wt.%), and the solids were collected by filtration. The process was repeated until the filtrate was clear and white crystals of BDSA were obtained. Polyethylene glycol 300 (PEG300) and sodium carbonate (Na_2CO_3) were purchased from Sigma Aldrich and used as received. Natural flake graphite (Batch #: 13802EH) was purchased from Sigma Aldrich

and used as received. SpectraPor 1 dialysis membranes were purchased from Sigma Aldrich and purified of ethylene glycol with water/EtOH prior to use.

Synthesis and Molecular Weight of PBDT. An interfacial polymerization method was used as previously described by Sarkar et al.[56] A 3L round bottom flask was used as the reaction vessel equipped with an overhead stirrer and placed in an ice bath. In a typical reaction, Na_2CO_3 (9.539 g, 90 mmol) was added with 900 mL deionized water and dissolved with stirring. BDSA (7.748 g, 22.5 mmol) was added to the solution and mixed until dissolved. PEG300 (7.2 g, 24 mmol) was added with 300 mL of $CHCl_3$ and stirred at 2000 rpm until a white emulsion was obtained. Freshly sublimed TPC (4.568 g, 22.5 mmol) was dissolved into 300 mL $CHCl_3$ and added to the reaction mixture while stirring at 2000 rpm. The reaction was allowed to proceed for 1 h with stirring at 2000 RPM, at which point the mixture became a gel. Rotary evaporation was used to distill the $CHCl_3$ from the emulsion to obtain the polymer in aqueous solution. The polymer was washed by repeated precipitations into acetone and dried under vacuum before use. We quantified the molecular weight using intrinsic viscosity measurements in 96% H_2SO_4 (**Figure D.11** and **Table D.1**). Dilute solution viscometry measurements were carried out using a suspended level Cannon® Ubbelohde capillary viscometer (Model 2E-316). Dry PBDT was added to a 25 mL volumetric flask and concentrated (96%) sulfuric acid was used to fill to volume. The solution was shaken overnight until dissolved. 8 mL of the solution was added to the viscometer and equilibrated at 25 °C in a water bath. Measurements were taken by recording the flow time between the viscometer marks, and temperature equilibrium was checked by consecutive measurements being less than 0.5% error. Dilutions were accomplished in-situ by adding pure concentrated sulfuric acid and mixing by bubbling with dry nitrogen. Using Mark-Houwink equation parameters reported for PPTA[261], the viscosity average molecular weight of

PBDT was 19 kg mol^{-1}, consistent with prior results for PBDT.[62, 125] Further details on dilute solution viscosity measurements are provided in **Appendix D**.

Synthesis and Characterization of LCGO. Graphite oxide was prepared from natural flake graphite using the Hummers' method.[262] The obtained graphite oxide slurry was washed 5x with 1 M HCl, dried in air, then dispersed in 500 mL deionized water. Mild bath sonication for 1 h was used to exfoliate the graphite oxide into single layer graphene oxide, at which point the nematic texture of liquid crystal graphene oxide (LCGO) becomes apparent. The exfoliated dispersion was dialyzed against 10 L of deionized water for one week, exchanging daily. After dialysis, the exfoliated dispersion was briefly centrifuged (10^4 RPM, 2 min) to eliminate graphitic sediment, and the supernatant (containing a broad distribution of flake sizes) was decanted. The decanted dispersion was concentrated by centrifugation at 10^4 RPM for 10 h, and the supernatant was decanted. The bottom nematic layer containing a high concentration of large flake GO was collected for use in nanocomposite fabrication. Thermogravimetric analysis (TGA) of LCGO indicated a sharp reduction in weight, centered around 200 °C due to removal of oxygen functionalities from the GO surface (**Figure D.2)**. X-ray photoelectron spectroscopy (XPS) measurements confirmed the carbon-oxygen (C/O) ratio of pristine LCGO as 2.6, in agreement with literature values,[263] and increased to ~6.5 on thermal annealing at 200 °C (for 30 min. in N_2 atmosphere), and have been previously published.[66] We quantified the size distribution of GO flakes using scanning electron microscopy (SEM) after deposition on a O_3-treated Si surface (**Figure D.3a**). The lateral flake size distribution was determined by measurement of their surface area and conversion to an equivalent diameter of a circle (**Figure D.3b**).[253] This equivalent diameter distribution was fit to a Gaussian function, yielding an average diameter of 1.3 ± 0.3 μm.

Preparation of Hybrid Nematic PBDT-LCGO Dispersions and Films. Homogeneous dispersions of LCGO and liquid crystal PBDT solutions were obtained by facile aqueous solution mixing. In all nanocomposite precursor dispersions, the total polymer concentration was set at 5 wt.% and the concentration of LCGO was independently varied. A representative procedure for obtaining a 1.8 vol.% rGO nanocomposite film is given as follows: 1.856 g of a 1 wt.% LCGO dispersion was added to a 20 mL glass vial, followed by dilution with 1.573 g of water. A small stirbar, stirring at 1400 RPM, was used to homogenize the diluted LCGO dispersion (0.541 wt.% GO). Dropwise, 8.571 g of a 7.0 wt.% PBDT solution was added to the LCGO dispersion while mixing and a dark, homogeneous dispersion was obtained. The resulting PBDT-LCGO dispersion was allowed to mix for 24 hours before film-casting. Glass plates were freshly cleaned by soaking in an isopropanol/sodium hydroxide solution, rinsed with deionized water, acetone, then dried under nitrogen. To cast free standing PBDT-LCGO nanocomposite films, ~3 g of the dispersion was deposited onto a glass plate. An automatic doctor blade set at 1 mm gap cast the dispersion at a constant linear velocity of 5 mm s^{-1}. The dispersions were placed into a leveled 60 °C oven in air and allowed to dry. The time for complete evaporation was approximately 2 hr. Release of the nanocomposite films was accomplished by soaking the film in acetone. The free standing PBDT-GO nanocomposite films were stored at room temperature for characterization. Concentrations of LCGO in the final films were calculated using a mass density of $\rho_{GO} = 1.8$ g mL^{-1} and $\rho_{PBDT} = 1.565$ g mL^{-1}.[62]

Tensile and Thermo-mechanical Characterization. Free-standing nanocomposite films were cut into rectangular strips of approximate cross-sectional area 1.5 × 0.03 mm^2 (width × thickness). A 10 mm gauge length was used for both stress-strain and dynamic mechanical thermal analysis (DMTA) measurements. All mechanical measurements were performed using

an RSA-G2 Solids Analyzer (TA Instruments) equipped with a 32 N load cell. Samples for tensile testing under dry conditions were treated at 200 °C for 20 minutes to eliminate water. Specimens were tested under dry conditions at 25 °C under a N_2 atmosphere. For all stress-strain measurements, a constant linear displacement rate of 0.1 mm min^{-1} was used. The Young's modulus was calculated by linear regression of the stress-strain curve between 0.15% and 0.3% strain, within the linear viscoelastic regime. Isochronal DMTA measurements used an oscillation frequency of 1 Hz over the temperature range of −150 to 500 °C at a heating rate of 2 °C min^{-1} was used. Arrhenius analysis of the β–relaxation was accomplished by performing frequency sweeps from 0.1 to 10 Hz over the range of −30 to 120 °C using 5 °C intervals. The sample was allowed to equilibrate for 3 minutes at each temperature prior to measurement. The temperature of the peak in the loss tangent was determined by differentiation of smooth curves fit to the raw loss tangent data. Loss modulus master curves were constructed by horizontally shifting isothermal frequency sweeps using shift factors obtained from the Arrhenius activation energy. The loss modulus master curves were fit with the imaginary component of the Havriliak-Negami equation[264] utilizing a baseline offset factor in Igor Pro.

X-ray Scattering. Nanocomposite films were thermally reduced at 200 °C for 20 min under an N_2 atmosphere to match conditions used for mechanical testing. Film strips of approximate dimensions of 60 × 2 × 0.03 mm^3 (length × width × thickness) were cut along the longitudinal direction and folded into eight layers. X-ray scattering (WAXS/SAXS) experiments were performed using a SAXSLab Ganesha equipped with a Cu 50kV Xenocs Genix ULD SL X-ray Source producing an incident x-ray beam of λ = 1.54 Å and a 2D detector. Sample to detector distances of 92, 432, and 1032 mm to cover a wide range of scattering vectors. The sample chamber was evacuated and kept at 10^{-2} mbar during measurement to avoid scattering from air.

The samples were affixed to a sample holder such that only the nanocomposite film was in the x-ray beam path. For measurement of the polymer alignment in the film plane and along the shear axis, the incident x-ray beam was parallel and orthogonal to the surface normal, respectively. Igor Pro using the Nika package[127] was used for 2D data reduction and analysis.

Characterization. Optical microscopy was carried out using a Nikon Microphot-FX microscope equipped with polarizing filters. Images were recorded using an OMAX 18 MP digital microscope camera and calibrated with a 0.01 mm calibration slide. All presented micrographs are from samples which have been loaded via capillary action into a 200 μm path length rectangular glass microscopy cell (Vitrotube®). Digital photographs were taken with an iPhone 8 Plus in photo mode. A Hitachi S-4700 Cold Cathode Field Emission Scanning Electron Microscope was used for film fracture surface analysis and flake size analysis of the GO. Film fracture surfaces were coated with 3 nm of Au prior to analysis. Local mechanical measurements were performed with an Asylum Research Cypher Atomic Force Microscope. Film cross-sectional surfaces for AFM analysis were prepared via cryotome at −55 °C. AFM tests were performed in amplitude modulation-frequency modulation (AM-FM) mode using Si probes with tip radius ~10 nm, cantilever stiffness ~ 4 N m^{-1}, and natural frequency ~75 KHz. The tips were calibrated on spin-coated polystyrene films; a Hertzian model was used to obtain elastic modulus. Dispersions of 0.1 wt.% were spun-cast onto hydrophilized (O_3 treated for 5 min) Si wafers for flake size analysis. A Kratos Axis Ultra DLD X-ray Photoelectron Spectrometer operating at 10^{-6} mbar was used for XPS measurements of as-synthesized (dried at 60 °C for 2 h) and thermally reduced (annealed at 200 °C for 2 h) GO films. The GO was deposited onto Au@Si substrates prior to analysis. A TGA 5500 (TA Instruments) was utilized for

thermogravimetric analysis (TGA) with a 100 μL Pt pan heating at a rate of 10 °C min^{-1} under a N_2 atmosphere.

5.3. RESULTS AND DISCUSSION

5.3.1. Wide- and Small-Angle X-ray Scattering: Solid-State Nanocomposites

We employed WAXS to study the influence of rGO concentration on the macroscopic alignment of PBDT in the nanocomposite films. In nematic PBDT films, the drying process causes polymer chains to orient parallel to the film plane (in-plane ordering) due to affine deformation after gelation of the polymer solution.[55, 65] Furthermore, the shear imposed during film casting can induce ordering of nematic domain directors, resulting in partial orientation along the shear direction. We analyzed the polymer orientation in PBDT-rGO films by using two scattering configurations, i.e., incident beam normal to the film surface (perpendicular configuration, **Figure 5.2a**) and parallel to the film surface (parallel configuration, **Figure 5.2c**). The polymer alignment with respect to the casting direction (z-axis) and in-plane polymer alignment are probed in the perpendicular and parallel configurations, respectively.[55]

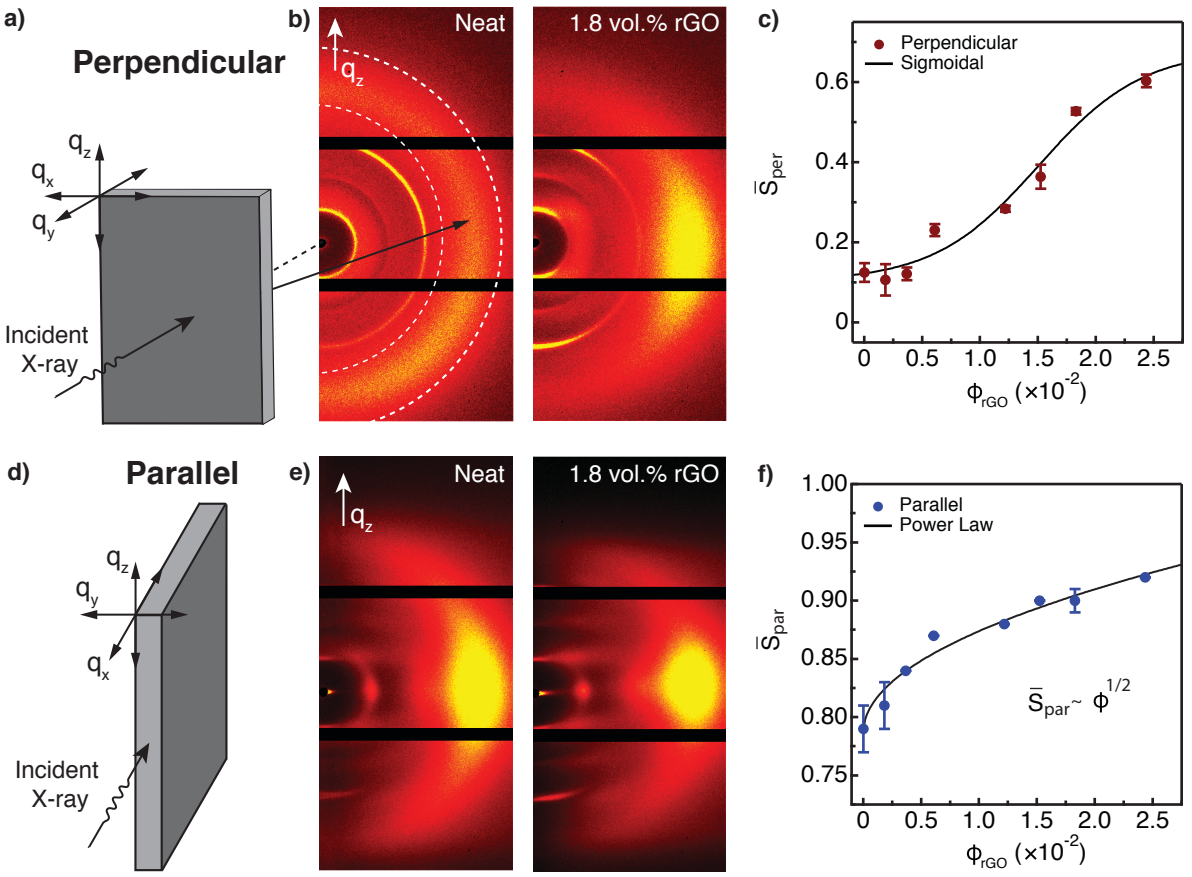

Figure 5.2. 2D wide-angle X-ray scattering (WAXS) of PBDT-rGO nanocomposite films. Depiction of the (a) perpendicular and (d) parallel configurations used for analysis of polymer alignment. The casting direction is along the z-axis, and the surface normal is parallel to the y-axis. 2D WAXS image of a neat PBDT and 1.8 vol.% rGO films in the (b) perpendicular and (e) parallel configuration, respectively. The interchain scattering peak at $q = 1.7$ Å^{-1} is indicated by the solid black arrow. The horizontal black lines are the seams of three individual detectors. (c) Perpendicular and (f) parallel order parameters determined from fitting of the azimuthal intensity profiles at $q = 1.7$ Å^{-1} (interchain distance) as a function of rGO concentration. Solid black lines are fits to the data with the indicated functional form.

A schematic representation of the perpendicular scattering configuration is shown in **Figure 5.2a**, where q_z is the shear casting direction and the incident X-ray beam is parallel to q_y. The 2D WAXS patterns in the $q_z - q_x$ scattering plane of a neat PBDT and a 1.8 vol.% rGO film in the perpendicular configuration are shown in **Figure 5.2b**. The white arrow represents the film-casting direction (z-axis) of the films. To quantify polymer alignment, we use the scattering

anisotropy of the intense diffraction ring at the widest angle (indicated by black arrow, $q = 1.7$ Å^{-1}, $d = 3.7$ Å) that corresponds to the nearest neighbor interchain π-π spacing.[55, 65] The interchain diffraction peak for PBDT is broad, illustrated in 1D lineouts of a neat film and 1.8 vol.% rGO nanocomposite shown in **Figure D.6**, consistent with amorphous packing of aromatic chains with a broad distribution of distances. Increasing concentration of rGO causes the scattering anisotropy to increase, i.e., we observe a stronger azimuthal scattering dependence. We quantified the polymer alignment by fitting the azimuthal scattering intensity distributions using a Maier-Saupe orientational distribution function, given by **Eqn. 5.4**:

$$I = I_0 + A\, exp[\alpha\, cos^2(\chi - \chi_0)] \qquad \textbf{(Eqn. 5.4)}$$

where I is the scattering intensity, I_0 is the baseline intensity, A is proportional to the scattering amplitude, α characterizes the width of the scattering peak, χ is the azimuthal angle and χ_0 is the azimuthal angle of peak intensity.[170] An example of the fitting function for a 0.4 vol.% and 1.8 vol.% rGO nanocomposite measured in the perpendicular configuration are shown in **Figure D.7**. Using the α values obtained from fitting the azimuthal intensity distribution, the macroscopic polymer alignment is quantified by the apparent order parameter, we define here as $\bar{S}$, given by numerical integration of **Eqn. 5.5**:

$$\bar{S} = \frac{\int_{-1}^{1} exp[\alpha\, cos^2(\beta)] P_2(cos\beta) dcos(\beta)}{\int_{-1}^{1} exp[\alpha\, cos^2(\beta)] dcos(\beta)} \qquad \textbf{(Eqn. 5.5)}$$

where $P_2(cos\beta) = \frac{1}{2}[3\, cos^2(\beta) - 1]$ is the second-order Legendre polynomial coefficient.[170] Note that due to the high defect density of lyotropic LCPs, $\bar{S}$ is proportional to both the microscopic (molecular) and mesoscopic (nematic domain) order parameters.[170]

The perpendicular order parameter as a function of rGO volume fraction is presented in **Figure 5.2c**. In neat PBDT, $\bar{S}_{per}$ is ~0.1, indicating relatively disordered polymer orientation

with respect to the shear axis. Above 0.4 vol.% rGO, $\bar{S}_{per}$ increases up to ~0.6 at 2.4 vol.% rGO. This value indicates a significant increase in polymer alignment along the casting (shear) direction in the nanocomposite films. We fit $\bar{S}_{per}$ with a sigmoid equation, characterized by a low concentration plateau (0.10 ± 0.06) and high concentration saturation (0.7 ± 0.2) of the order parameter. The saturation value of 0.7 is near the monodomain order parameter as measured by SAXS,[62] indicating our hybrid nematic nanocomposites possess high orientational order of individual nematic domains along the shear direction. For neat PBDT and at low LCGO concentrations, relaxation of the nematic PBDT directors towards global isotropy after cessation of shear following film casting explains the low order parameters.

The WAXS patterns for the parallel configuration of neat PBDT and a 1.8 vol.% rGO nanocomposite are shown in **Figure 5.2e**. In the neat polymer, we observe significant scattering anisotropy that indicates preferential polymer orientation in the film plane. Similar to the measurements in the perpendicular configuration, the scattering anisotropy increased with rGO concentration, confirming enhanced polymer alignment in the film plane. In the neat polymer, the $\bar{S}_{par}$ was ~0.79 and increased with rGO concentration up to 0.91 at 2.4 vol.% rGO. We fit the concentration dependence of $\bar{S}_{par}$ with a power law and baseline offset and find a concentration dependence of $\bar{S}_{par} \sim \varphi^{1/2}$. We do not find a saturation value of $\bar{S}_{par}$ over the concentration range investigated, indicating that the deformation process that induces in-plane orientation may be able to achieve order parameters near unity with higher LCGO concentration, leading to highly aligned nanocomposites.

To characterize the nanocomposite structure on supramolecular length scales, we performed SAXS on a 1.8 vol.% rGO nanocomposite in both the perpendicular and parallel scattering configurations, shown in **Figure 5.3a** and **Figure 5.3b**, respectively. The 2D SAXS patterns for

both configurations exhibit a sharp and anisotropic scattering peak corresponding to the 16.8 Å repeat unit along the q_z axis (along long axis of polymer chain). The 1D sector averages along q_z and q_x are shown in **Figure 5.3c** for the parallel (solid lines) and perpendicular (circles) scattering configurations. At low scattering angles, both scattering configurations exhibit an upturn in intensity related to the aligned fibrillar PBDT network, exhibiting a near ideal Porod intensity scaling exponent of −4.[265] The qualitative shape of the 1D scattering intensity for the parallel configuration indicates that the aligned fibrils are high aspect ratio and aligned in-plane; however, the utilized q-range precludes any quantitative length scale analysis.

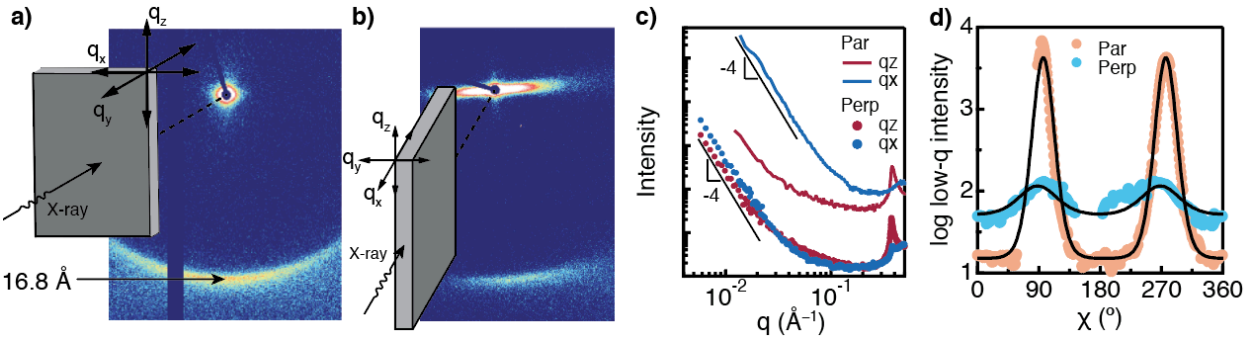

Figure 5.3. 2D small-angle X-ray scattering (SAXS) images of a 1.8 vol.% rGO nanocomposite in (a) perpendicular and (b) parallel scattering configuration. (c) Sector averaged 1D intensity as a function of q in the parallel (solid lines) and perpendicular (circles) scattering configurations. (d) Integrated azimuthal angular dependence of the low-q scattering intensity fit with a Maier-Saupe orientational distribution function (solid lines).

We analyzed the azimuthal dependence of the low-q scattering intensity, shown in **Figure 5.3d**, for both parallel and perpendicular configurations and fit the data using the previously described Maier-Saupe orientational distribution function. The low-q parallel anisotropy $\bar{S}_{par}$ = 0.837 ± 0.003 is significantly greater than in the perpendicular $\bar{S}_{per}$ = 0.41 ± 0.07 configuration, consistent with our WAXS measurements that utilized the scattering anisotropy from the local

interchain scattering reflection. Together, our analysis confirms an aligned network of polymer chains hierarchically assembled into high-aspect-ratio nanofibrils within the nanocomposite film.

5.3.2. Nanocomposite Cross-section: SEM and AFM Modulus Mapping

The enhanced macroscopic polymer alignment further manifests as a modification in the morphology and mechanical properties of the mesoscopic nanocomposite structure. To visualize the morphological change in the nanocomposite films, we utilized SEM to view the fracture surfaces of cryo-fractured films. Furthermore, we constructed modulus maps of cryo-microtomed cross-sections using the calibrated AFM response in elastic modulus mapping mode. Representative SEM and AFM images for neat PBDT (**Figure 5.4a** and **Figure 5.4b**) and a 1.8 vol.% rGO nanocomposite (**Figure 5.4c** and **Figure 5.4d**) demonstrate morphological differences between the neat polymer and hybrid liquid crystalline nanocomposite.

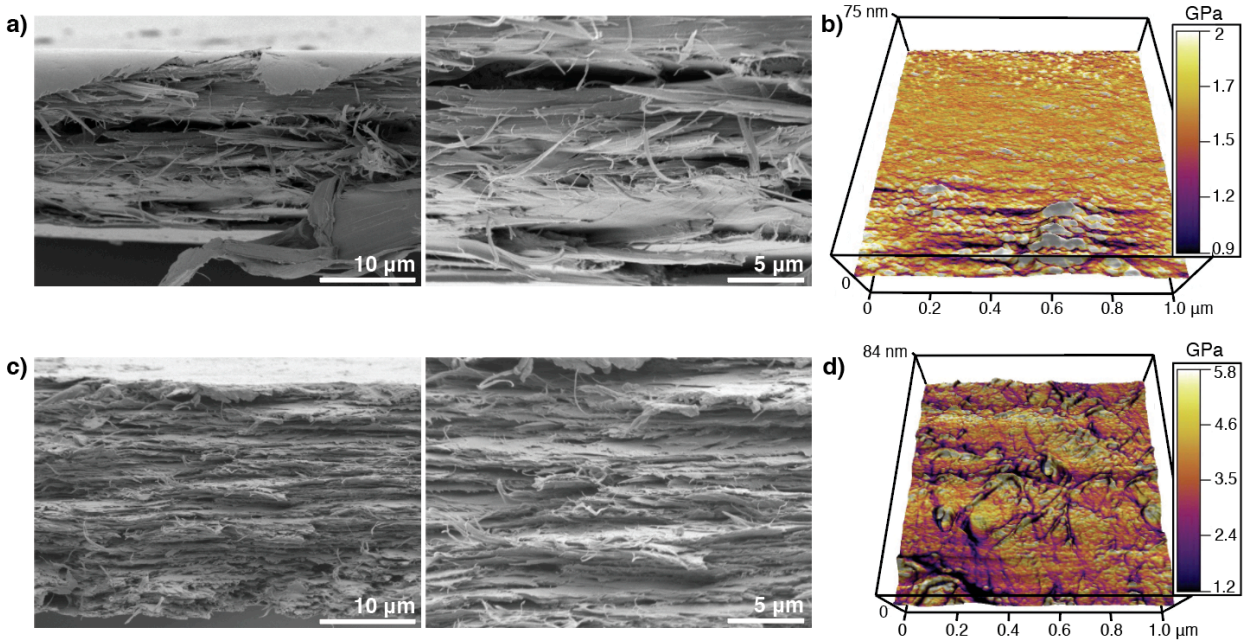

Figure 5.4. Morphological (a, c) SEM images and (b, d) AFM modulus-height maps of neat PBDT (*top*) and 1.8 vol.% rGO nanocomposite (*bottom*). The color scale indicates the elastic modulus map values from AFM measurements. An increase in the stratified morphology and modulus is observed due to the presence of LCGO within the nanocomposites. AFM measurements provided courtesy of Dr. Daniel P. Cole, Army Research Laboratory.

In the neat polymer, the morphology is fibrillar but appears to have some degree of preferred alignment within the film plane as evidenced by the partial vertical segregation in the direction normal to the film surface. In the PBDT-rGO nanocomposite at 1.8 vol.% rGO, we observe an increase in the layered morphology, reminiscent of morphology developed through the painstaking process of LBL assembly. Due to the lack of contrast between the polymer and GO, we cannot directly visualize the flakes within the fracture surface using SEM. However, AFM modulus mapping clearly demonstrates the increase in absolute stiffness and heterogeneity of stiffness spatial distribution. We speculate that the extended morphology of the LCGO platelets in the liquid crystal dispersion aids in the development of the polymer alignment and stiffens the interfacial polymer layers. These results suggest that the presence of an ordered and planar

surface extending over large length scales, such as LCGO, is critical for the formation of highly reinforced polymer NCs, achieved here using our hybrid liquid crystalline dispersions.

5.3.3. Stress-Strain Behavior

We investigated the stress-strain behavior with uniaxial tensile tests to characterize the tensile properties. In aligned polymeric fibers and uniaxial polymer-fiber composites, the alignment of reinforcing fibers results in unidirectional mechanical reinforcement.[266] The use of 2D rGO flakes should result in mechanical reinforcement when stress is applied along the rGO basal plane, i.e., both in the longitudinal and transverse directions of the nanocomposite film. The stress-strain curves of PBDT-rGO nanocomposites in both the longitudinal and transverse orientations to the casting direction, is presented in **Figure 5.5a** top and bottom, respectively.

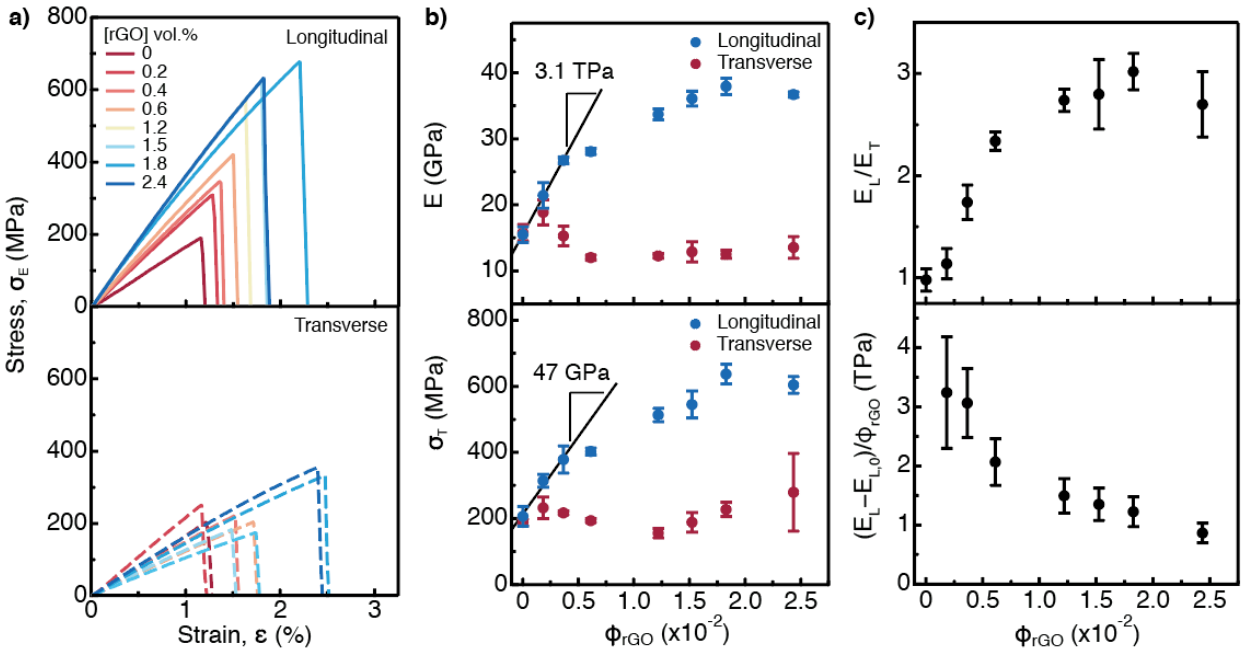

Figure 5.5. Stress-strain behavior of PBDT-rGO nanocomposites from uniaxial tension measurements at 25 °C under a N_2 atmosphere in the (a) longitudinal (*top*, solid lines) and transverse (*bottom*, dashed lines) direction. Samples with the highest strain at break values are presented. (b) Young's modulus (*top*) and tensile strength (*bottom*) in the longitudinal (blue) and transverse (red) directions as a function of rGO concentration. The straight lines are linear fits to the low concentration region of the data. The error bars indicate the standard error of six measurements for the Young's modulus and the standard error of the best three measurements for tensile strength. (c) Mechanical anisotropy of the Young's modulus (*top*) and reinforcement efficiency (*bottom*) in the longitudinal direction as a function of rGO concentration. Error bars indicate the propagated standard error of six modulus measurements.

Neat PBDT films exhibit low strains at break (~1.1–1.2%), and lack of a distinct yield stress suggesting little to no plastic deformation, consistent with the rigid structure of the polymer backbone. The neat PBDT film exhibits a Young's modulus of ~16 GPa and tensile strength of ~200 MPa. These values are considerably higher than isotropic glassy polymers due to its rigid backbone and high degree of polymer alignment. Incorporation of rGO causes substantial stress-strain improvements in the longitudinal direction, where the modulus, strain at break, and tensile strength all improve dramatically (**Figure 5.5b**). Incorporation of 1.8 vol.% rGO results in an impressive 678 MPa tensile strength and a ~37 GPa Young's modulus. Toughness, measured as

the area under the stress-strain curve, increases by nearly an order of magnitude from 1.1 to 8.2 MJ m^{-3} at 1.8 vol.% rGO. We note the obvious non-linear relationship between the longitudinal Young's modulus and tensile strength as a function of rGO concentration. However, to characterize the reinforcement efficiency, we fit straight lines to the low concentration regimes and obtained $dE/d\phi = 3100 \pm 100$ GPa and $d\sigma/d\phi = 47 \pm 7$ GPa. To the best of our knowledge, this modulus reinforcement value is the highest reported for graphene oxide polymer nanocomposite films that have not been drawn in post-processing.[251] Undoubtably, significant mechanical reinforcement of the nanocomposites originates from the enhancement of alignment of polymer. In general, for nanocomposites the observed strain at break tends to decrease with nanofiller loading. However, we observe an 83% increase in tensile ductility with incorporation of rGO; from 1.2% in neat PBDT to 2.2% at 1.8 vol.% rGO. Such increases in ductility have been observed in bicontinuous lamellar rGO composites and can be explained through a retardation in crack propagation due to the rGO sheets,[254] or enhanced polymer alignment.[267]

We have shown through perpendicular WAXS measurements that polymer alignment along the shear axis is modulated through the concentration of LCGO in the dispersion; thus, we expect anisotropic mechanical properties orthogonal to the direction of shear in the film plane. The concentration scaling of transverse Young's modulus and tensile strength are given in the bottom of **Figure 5.5b**. In the neat polymer, the transverse modulus and strength are the same as the longitudinal, consistent with the low order parameter measured in the perpendicular configuration from WAXS. Remarkably, despite the increased mechanical properties in the film-casting direction, we do not observe a significant reduction in transverse tensile properties in the nanocomposites as compared to the neat polymer. The transverse Young's modulus as a function of rGO concentration decreases from its' initial value of 16 GPa, but plateaus at ~12.5 GPa.

Enhanced ductility at rGO concentrations greater than 1.8 vol.% enabled transverse tensile strengths of over 300 MPa to be achieved. We postulate that these impressive mechanical properties in the transverse direction are made possible through the use of platelets as a reinforcing phase, which provide isotropic reinforcement along the basal plane of the rGO platelet.

The modulus anisotropy, defined as E_L/E_T, and the longitudinal modulus reinforcement efficiency, defined as $(E_L - E_{L,0})/\varphi_{rGO}$, as a function of rGO concentration are presented in **Figure 5.5c,** top and bottom, respectively. At low volume fractions of rGO, both the longitudinal and transverse moduli increase resulting in a small increase in the mechanical anisotropy. In this concentration regime, the reinforcement efficiency is maximum with a value of ~3 TPa. At higher rGO volume fractions, the mechanical anisotropy rapidly increases to between 2.75 and 3 and plateaus above 1.2 vol.%. This is concomitant with a monotonic decrease in the longitudinal modulus reinforcement efficiency. The simultaneous rise in the mechanical anisotropy and decay in reinforcement efficiency further confirms that polymer alignment with respect to the shear axis is a key mechanism responsible for the mechanical property improvements. Significantly, we observed reinforcement efficiencies ~1 TPa up to 2.4 vol.% rGO, which is drastically higher than what is typically used to calculate reinforcement (generally concentrations <1 vol.%).[251]

5.3.4. Thermomechanical Analysis

We used DMTA and TTS to investigate the thermomechanical properties of PBDT-rGO nanocomposites. Isochronal temperature ramps of the neat polymer and nanocomposite films (dT/dt = 2 °C min^{-1}, f = 1 Hz) are shown in **Figure 5.6a**.

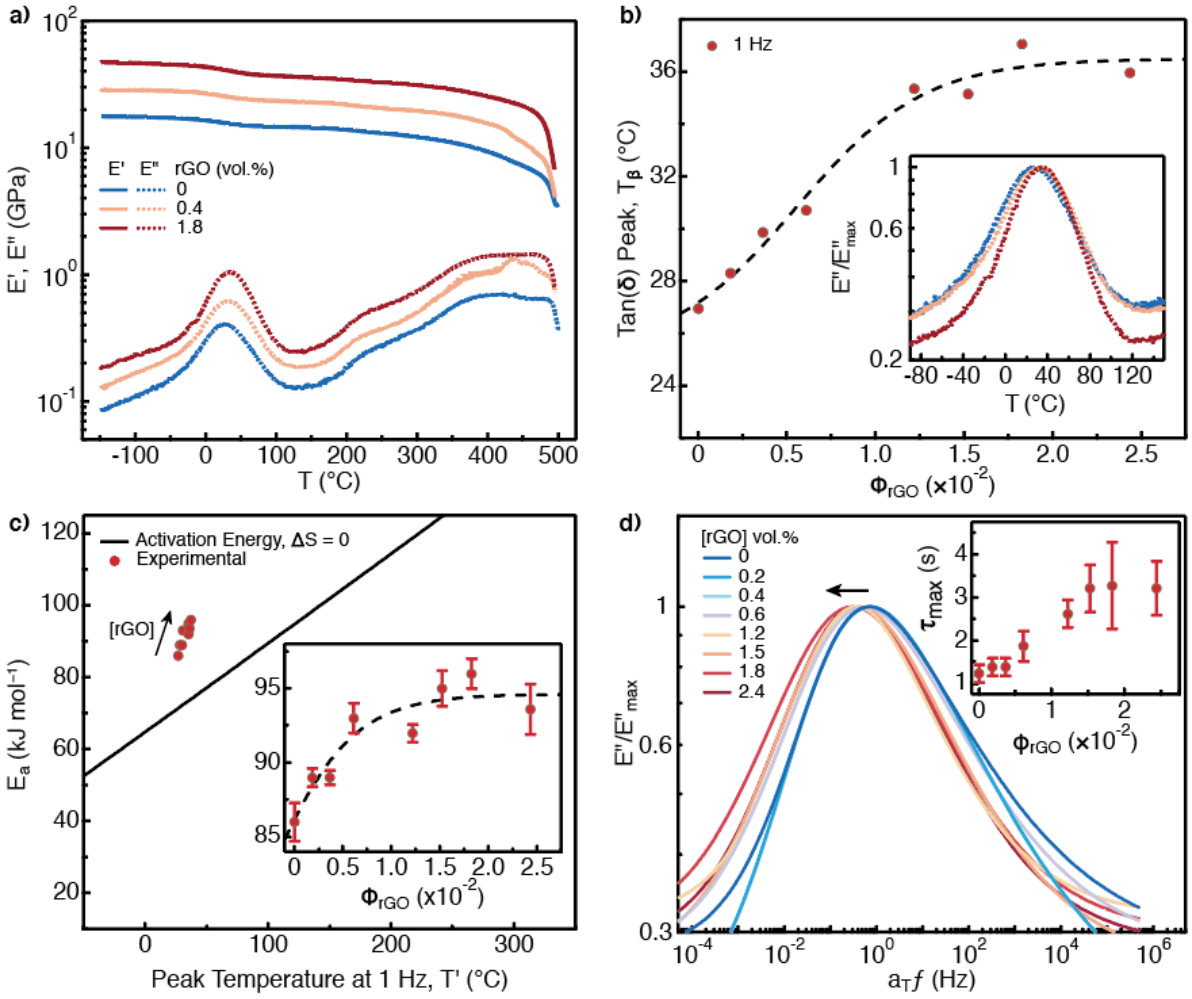

Figure 5.6. DMTA and time-temperature superposition (TTS) analysis of PBDT-rGO nanocomposites. (a) Storage (*E'*) and loss (*E"*) moduli as a function of temperature at 1 Hz measured using a heating rate of 2 °C min^{-1}. (b) β-relaxation temperature as measured by the temperature of the tan(δ) peak at 1 Hz. The dashed line is a guide to the eye. (*inset*) Normalized E" as a function of temperature over the β-relaxation temperature range. (c) Experimental activation energies of the PBDT-rGO nanocomposites compared to the zero-entropy activation energy (solid line). The deviation from the line indicates a complex and cooperative motional process is responsible for the relaxation. (d) Normalized Havriliak-Negami (H-N) fits to *E"* master curves of rGO-PBDT nanocomposites as a function of frequency (T_{ref} = 25 °C). A shift in the peak to lower frequency indicates a retardation of the β-relaxation process. (*inset*) Characteristic relaxation time as a function of rGO concentration, corresponding to the peak of the H-N curve.

The thermo-mechanical stability of the polymer and resulting nanocomposites is demonstrated by the absence of a glass transition (T_g), consistent with other high-performance *para*-aramids (e.g., PPTA).[268] The polymer and nanocomposite films maintain a significant fraction of their

room temperature modulus until approximately 400 °C, above which polymer decomposition begins to occur. The substantial mechanical reinforcement of the nanocomposites over the neat polymer, as previously shown in the stress-strain behavior, is evidenced by the significant increase in storage modulus of the nanocomposites over the neat polymer. At cryogenic temperatures, the storage modulus increased 178% from 17 GPa to nearly 45 GPa at 1.8 vol.% rGO. At 400 °C, the storage modulus increased 165% from 9 GPa to 26 GPa at 1.8 vol.% rGO. A well-resolved peak in the loss modulus, indicative of a β-relaxation, is observed at ~30 °C. This peak is present in neat PBDT and all nanocomposites, spanning the region between −30 °C and 120 °C. Upon inclusion of rGO, the magnitude of the β-relaxation increased in intensity as evidenced by the magnitude in storage modulus decrease and loss modulus peak intensity. The increased intensity is consistent with enhanced polymer alignment along the tension axis, similarly observed in PPTA fibers of varying alignment.[269] The peak temperature of the β-relaxation, as measured by the location of the loss tangent peak, increased by 33% from 27 °C in the neat polymer to a maximum of 37 °C at 1.8 vol.% rGO, shown in **Figure 5.6b**.

Thermo-mechanical measurements on PPTA filaments suggest that the low temperature β-relaxation has been attributed to local motions in the amorphous region, likely related to the amide group.[268-270] To gain a more detailed insight into the observed β-relaxation near room temperature in PBDT and the resulting nanocomposites, we interrogated the nanocomposites over two decades of frequency (0.1 to 10 Hz) through the temperature range of −30 to 120 °C in 5 °C intervals. The loss tangent at each discrete frequency as a function of temperature for all nanocomposites are given in **Figure D.8**. At higher mechanical oscillation frequency, the peak in the loss tangent was shifted to higher temperatures, consistent with the Arrhenius relationship. To extract the activation energy E_a of the relaxation from these data, the natural logarithm of

each frequency is plotted as a function of the inverse absolute peak temperature of the loss tangent maxima, shown in **Figure D.9.** These data fell on straight lines, indicating excellent agreement with an Arrhenius process. The experimental E_a for all rGO volume fractions is compared to the zero-entropy E_a, calculated by **Eqn. D.3**, in **Figure 5.6c** and as a function of rGO concentration in the inset. The E_a for the β-relaxation in neat PBDT is much higher than predicted by the zero-entropy E_a equation, suggesting a complex and cooperative relaxation process. With increasing rGO concentration, E_a deviates further from the zero-entropy line, suggesting the cooperativity of the β-relaxation increases. The activation energy increased ~12%, from ~86 kJ mol^{-1} in the neat polymer to ~96 kJ mol^{-1} at 1.8 vol.% rGO. As a result, the activation entropy of the β-relaxation as a function of rGO concentration increased ~34%, from ~50 to ~70 J mol^{-1} K^{-1}. The increased deviation of activation entropy with higher rGO loading suggests that the polymer chain's conformational entropy in the nanocomposites are increasingly restricted below the onset of the β-relaxation.

To further characterize the β-relaxation, we constructed master curves of the loss modulus over the β-relaxation region, shown in **Figure D.10**. The necessary shift factors were directly calculated from the E_a obtained from Arrhenius plots in **Figure D.9**. The master curves were fit using the Havriliak-Negami (H-N) relaxation model, given by **Eqn. 5.6**:

$$E^*(\omega) = E_\infty + \frac{\Delta E}{(1+[\omega\tau_{HN}]^\alpha)^\beta} \qquad \textbf{(Eqn. 5.6)}$$

where $E^*(\omega)$ is the complex modulus in the frequency domain, ΔE is the difference between the glassy and rubbery modulus, τ_{HN} is the Havriliak-Negami relaxation time, α and β are shape parameters which describe the broadness and asymmetry of the dispersion curve, respectively.[264] **Eqn. 5.6** can be decomposed into its real and imaginary components to fit the loss modulus data in the frequency domain. The model independent relaxation time, τ_{max}, corresponding to the

peak of the loss modulus master curve in the frequency domain was calculated from the H-N fit parameters using **Eqn. 5.7**:

$$\tau_{max} = \tau_{HN}\left[\frac{sin\left(\frac{\pi\alpha\beta}{2(\beta+1)}\right)}{sin\left(\frac{\pi\alpha}{2(\beta+1)}\right)}\right]^{\frac{1}{\alpha}} \quad \textbf{(Eqn. 5.7)}$$

where all other parameters are defined as previously.[264] The H-N model fits are shown in **Figure 5.6d**, which fit the experimental data satisfactorily. From the fitting parameters we calculate the τ_{max} in the inset of **Figure 5.6d**, which increased from 1.2 ± 0.2 s to 3.2 ± 0.6 s at 2.4 vol.% rGO. Increasing rGO concentration appears to hinder the molecular motion associated with the β-relaxation as compared to the neat polymer. We speculate that the changes observed in the β-relaxation with rGO concentration is due to a decrease in amide bond mobility, facilitated by the increased macroscopic polymer alignment due to the presence of aligned rGO platelets.

5.4. CONCLUSIONS

We have shown that hybrid nematic dispersions can be obtained by simple, facile solution mixing of a water-soluble liquid crystalline polyelectrolyte and LCGO. Film casting and thermal treatment of the nanocomposite films at 200 °C results in in-situ reduction of LCGO to rGO. Polymer alignment within the nanocomposite film can be modulated by the concentration of LCGO in the precursor hybrid liquid crystal. At 2.4 vol.% rGO, the polymer alignment is maximized; the order parameter along the casting direction increases to 0.6 and reaches 0.92 in the film plane. Driven by polymer alignment and a strong interface facilitated by myriad non-covalent interactions, the nanocomposite films exhibit dramatic increases in the longitudinal Young's modulus (16 to 37 GPa), ultimate strength (210 to ~680 MPa), strain at break (1.2 to 2.2%), and toughness (1.1 to 8.2 MJ m^{-3}). Despite increased polymer alignment along the casting direction (longitudinal direction), stress transfer from polymer to 2D rGO platelets results in

significant improvement of the transverse tensile strength (210 to 300 MPa) and strain at break (1.2 to 2.5%). SEM observations and AFM modulus mapping indicate the presence of a stratified morphology and enhanced stiffness near planar GO surfaces in the PBDT-rGO nanocomposite films. Dynamic thermo-mechanical measurements reveal a β-relaxation in PBDT attributed to the amide bond motion. Macroscopic polymer alignment and confinement between rGO platelets causes an increase in β-relaxation activation energy (86 to 96 kJ mol^{-1}) and retardation of the relaxation time (1.2 to 3.2 s). We have shown that rigid-rod, liquid-crystalline, high-performance polymers serve as ideal hosts for GO platelets. The results presented herein provide an understanding of hybrid liquid crystalline polymer nanocomposites, which overcome current challenges in nanocomposite preparation and processing.

CHAPTER 6: NANOFIBRILLAR IONIC POLYMER COMPOSITES ENABLE HIGH MODULUS ION-CONDUCTING MEMBRANES[3]

6.1. INTRODUCTION

A growing class of solid-state polymer electrolyte membranes (PEMs) consists of ionic liquid (IL) and a polymer, combining the desirable properties of high ionic conductivity and high elastic modulus. The polymer matrix provides mechanical integrity and can serve as a matrix to ion-conducting IL domains in the case of microphase-separated systems, i.e. block copolymers (BCPs). Such PEMs are employed in myriad applications, such as solid-state Li-metal battery (LMB) electrolytes,[271] fuel cells,[272] CO2 separation membranes,[273] electrochromic devices,[274] actuators,[275] and as gate insulators in organic thin-film transistors (OTFTs).[276] The versatility of the chosen IL, polymer, and processing strategy enable an unprecedented design space actively being explored.[277]

The potential to use PEMs in LMBs represents an enticing application that is poised to solve the issue of dendrite growth, which results in short-circuit failure and dangerous thermal runaways. Calculations and experiments show that stiff PEMs (shear modulus, G' > 1 GPa) inhibit dendrite growth, potentially enabling safe operation of LMBs.[271, 278, 279] Increasing the polymer concentration in PEMs improves the mechanical properties, but usually severely degrades the ionic conductivity due to coupling of ion transport with polymer segmental

[3]This chapter previously appeared as an article in *ACS Applied Materials & Interfaces*. The original citation is as follows: Fox, R. J.; Yu, D.; Hegde, M.; Kumbhar, A. S.; Madsen, L. A.; Dingemans, T. J., Nanofibrillar Ionic Polymer Composites Enable High-Modulus Ion-Conducting Membranes. *ACS Appl. Mater. Interfaces* **2019,** *11* (43), 40564-40574.

motion.[280] One of the primary design objectives for PEMs is to decouple high mechanical properties and ionic conductivity.[277] Towards this end, BCPs have been extensively investigated since they can be synthetically tailored to phase separate into ion-conducting and glassy domains.[277, 281-283] However, most PEMs based on BCPs exhibit low moduli as the glassy polymer domains are weakened due to plasticization by the IL, although cross-linking the polymer in the glassy phase can inhibit such effects.[282] This approach has received significant attention and can achieve moduli on the order of 108 Pa with ionic conductivities at room temperature in the range of 10^{-4}–10^{-3} S cm^{-1}.[282]

Recently, Wang et al. introduced a new class of potentially revolutionary polymer electrolytes utilizing the all-aromatic sulfonated polyamide (sulfo-aramid), poly(2,2'-disulfonyl-4,4'-benzidine terephthalamide) (PBDT) and a model IL composed of 1-ethyl-3-methyl imidazolium and trifluoromethanesulfonate [Emim][TfO].[68] These PBDT-IL composites exhibit an unprecedented combination of high ionic conductivity (4 mS cm^{-1}) and modulus (3 GPa) at extraordinarily low polymer concentrations (21 wt.%) with a wide electrochemical stability window (6.1 V).[68] Such a combination of high modulus and ionic conductivity for PEMs has not been achieved with any other strategy reported in the literature and may represent a class of next-generation, high-performance PEMs. These properties are enabled by a strong physical network of rigid sulfo-aramid chains self-assembled into high-aspect-ratio helical aggregates.[68] Moreover, recent molecular dynamics (MD) simulations suggest that a complex electrostatic network of highly structured IL exist within the PBDT-IL composites due to interactions with the rigid chains possessing a high density of discrete charges along the backbone.[69] However, the microstructure and nature of these materials is not fully resolved and detailed experimental investigations are needed to direct future simulation work and elucidate design rules.

Herein, we present a comprehensive investigation of the structure and thermo-mechanical properties of PBDT-IL composites utilizing polarized optical microscopy (POM), electron and atomic force microscopy (SEM/AFM), differential scanning calorimetry (DSC), small- and wide-angle X-ray scattering (SAXS/WAXS), dynamic mechanical thermal analysis (DMTA), time-temperature superposition (TTS), and tensile strength measurements. We conclusively demonstrate that PBDT-IL composites are composed of at least two phases consisting of domains with a high (PBDT-rich) and a low (PBDT-poor) polymer concentration. We directly observe through real-space AFM and reciprocal-space SAXS measurements that high-aspect-ratio polymer-rich fibrils form an aligned and physically cross-linked network. These fibrils form the basis of the load-bearing structure, while IL-rich domains of relatively low polymer concentration enable fast ion transport through the PBDT-IL composite. We propose that nanofibrillar self-assemblies of sulfo-aramids are key for designing PEMs with a high modulus and fast ion transport, that could lead to the design of next-generation gas separation membranes, fuel-cells, and LMBs.

6.2. EXPERIMENTAL

Chemicals. 1-Ethyl-3-methyl imidazolium triflate (Emim TfO) 99% was purchased from Iolitec and used as received. PBDT was synthesized with a Na^+ counterion according to previously reported literature procedures.[56, 65] A yellow beige fibrillar solid was obtained, and ^1H NMR (Bruker 400 NB, 400 MHz, 16 scans, 25 °C) confirmed the structure and purity (see **Figure E.1**). The viscosity average molecular weight was 14.7 kDa as determined by dilute solution viscometry using a suspended level viscometer in 96% sulfuric acid and using the Mark-Houwink constants for poly(*p*-phenylene terephthalamide) (PPTA).[284]

Membrane Preparation. PBDT-IL composite films were prepared by a solvent-casting method. Homogeneous solutions were prepared by dissolving dry PBDT and IL in deionized water and equilibrated at 85 °C. The mass ratio PBDT/(PBDT + IL) determines the polymer concentration in the final film. The total weight percent of PBDT and IL in the initial solution was kept constant at 4%. After complete dissolution of PBDT and IL, the homogenous clear solution was poured into a preheated flat glass dish and dried at 85 °C overnight in air. The film was further dried under vacuum at 85 °C and removed from the glass dish after 24 h.

Microscopy and Thermo-Mechanical Characterization. Optical micrographs were taken with a Nikon Microphot-FX microscope equipped with polarizing filters. Images were recorded using an OMAX 18 MP digital microscope camera and calibrated with a 0.01 mm calibration slide. Digital photographs with and without crossed polarizing film were taken with an iPhone 8 Plus. Scanning electron microscopy (SEM) was performed using a Hitachi S-4700 Cold Cathode Field Emission Scanning Electron Microscope operating at 20 kV and 11.4 mm working distance. Atomic force microscopy (AFM) topological and phase angle maps were obtained with an Asylum Research MFP3D Atomic Force Microscope. Differential scanning calorimetry (DSC) thermograms were measured with a TA Instruments DSC 2500 in aluminum pans. The samples were first heated to 200 °C to fully eliminate water and cooled at 10 °C min^{-1} until the onset of IL crystallization. The samples were held isothermally until IL crystallization was complete, to avoid cold crystallization during subsequent heating steps. The samples were then cooled to −150 °C at 10 °C min^{-1} before measuring the thermograms at a heating rate of 2 °C min^{-1}. The crystallinity of the IL in the PBDT-IL composites was calculated by the ratio of the composite melt enthalpy to the pure IL melt enthalpy, normalized to the mass of IL within each composite membrane. The glass transition temperature (T_g) is reported as the midpoint of the

transition in the heat flux vs. temperature thermograms. The T_g of PBDT-IL composites that exhibited crystallinity was measured by quenching from 200 °C to −150 °C at 200 °C min^{-1} to prevent crystallization before heating at 2 °C min^{-1}. Thermogravimetric analysis (TGA) of composite films was measured with a TA instruments TGA5500 utilizing Pt pans and a heating rate of 10 °C min^{-1} in a dry N_2 atmosphere. Dynamic mechanical thermal analysis (DMTA) was performed with a TA Instruments RSA-G2 Solids Analyzer equipped with a rectangular film clamp and forced convection oven controlled to within 0.1 °C. Dry liquid nitrogen was used as the atmosphere gas for all measurements. PBDT-IL composite films of approximate dimensions 2×0.2 mm^2 and a 15 mm gauge length were affixed into the sample clamps and dried at 200 °C for 10 min under an N_2 atmosphere. After drying, the samples were cooled down to −50 °C for a 30 min isothermal hold to allow the samples to crystallize. The samples were then cooled to −150 at 5 °C min^{-1} and equilibrated for 15 min. The isochronal temperature ramps were measured at an oscillation frequency of 1 Hz and heating rate of 2 °C min^{-1}. A strain amplitude of either 0.02 or 0.1% was used below and above the T_g or T_m of the IL, respectively, both within the linear viscoelastic regime. The RSA-G2 was also used for stress-strain measurements in axial control mode at 25 °C and a Hencky strain rate of 1% min^{-1}.

X-Ray Characterization. SAXS/WAXS measurements were taken with a SAXSLab Ganesha equipped with a Cu 50 kV Xenocs Genix ULD SL X-ray Source producing an incident X-ray beam of λ = 1.54 Å and a 2D detector. Three sample to detector distances (1031, 431, and 92 mm) were used to cover the scattering vector range of $q = 4\times10^{-3}$ to 2.75 Å^{-1}. The total counts for each configuration was kept constant at 5×10^4, 10^6, and 2×10^7, respectively, to ensure consistency between different samples. The sample chamber was evacuated and kept at 10^{-2} mbar during measurements to avoid scattering from air. The samples were affixed to a sample

holder such that only the membrane was in the X-ray beam path, thus no background subtraction was performed. For scattering measurements in the parallel configuration, the incident X-ray beam was oriented nearly parallel to the film edge. To produce 1D scattering spectra, the raw 2D scattering data were corrected for instrumental sensitivity and azimuthally averaged using software provided by SAXSLab. SasView was used to fit the 1D SAXS data using the shape-independent model function 'Correlation Length' and plotted using Igor Pro 8. The anisotropic 2D scattering patterns collected using a sample-to-detector distance of 431 mm were analyzed using the Nika package for Igor Pro 8.[127] The polar transform of the 2D scattering data was used to plot the integrated scattering intensity over the q range 0.02 to 0.1 $Å^{-1}$ as a function of the azimuthal angle.

6.3. RESULTS AND DISCUSSION

6.3.1. Polymer Electrolyte Membranes from PBDT and IL

PBDT is a water-soluble, sulfonated, all-aromatic polyamide (sulfo-aramid) that forms high-aspect-ratio helical supramolecular structures in aqueous solution.[62, 65, 67] These helical structures form rigid rodlike aggregates of ~0.8 nm in diameter with a persistence length of several hundred nanometers.[67] These high aspect ratio rodlike aggregates result in a lyotropic nematic liquid crystal phase at relatively low concentrations (~1 wt.%) in water,[57, 62, 65, 67] similar to other sulfo-aramids.[52, 53, 55] The chemical structures for PBDT and the IL used in this work are shown in **Figure 6.1A**, as in our previous publication.[68]

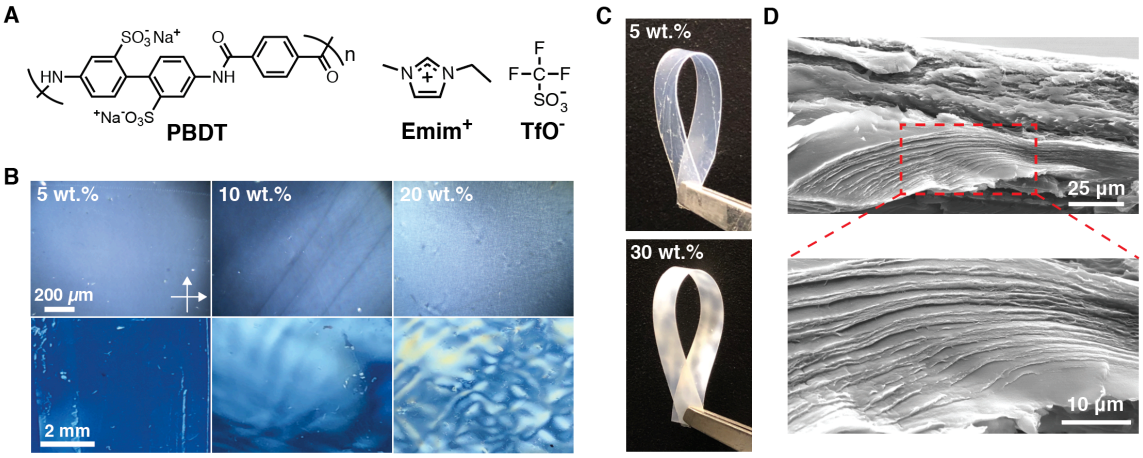

Figure 6.1. PBDT-IL composite membranes fabricated from the sulfonated all-aromatic polyamide, PBDT, and the IL [Emim][TfO]. (A) Molecular structures of PBDT and [Emim][TfO]. (B) Optical micrographs (*top*) and digital photographs (*bottom*) of PBDT-IL composites between crossed polarizers. The light transmittance indicates birefringence of the membranes and confirms nematic orientational order. (C) Digital photographs of 5 and 30 wt.% PBDT-IL composites demonstrating the flexibility of our membranes. Multiple bending/straightening cycles can be performed manually with no apparent structural degradation. (D) SEM micrographs of a 30 wt.% PBDT-IL composite cross section after freeze-fracturing. The layered morphology at this composition evidences a high degree of in-plane orientation within the membranes.

Co-dissolution of PBDT and IL in aqueous solution is readily achieved with moderate heating, and the mass ratio between PBDT and IL is varied to fabricate PBDT-IL composites with different polymer concentrations. After drop-casting and water evaporation, the obtained PBDT-IL composites exhibit nematic liquid-crystalline textures, shown in **Figure 6.1B**, confirming liquid crystalline (nematic) orientational order of PBDT rodlike aggregates. We obtained free-standing, robust, and flexible membranes with as low as 5 wt.% PBDT that can be handled easily, demonstrated in **Figure 6.1C**. The PBDT-IL composites can be bent and/or twisted repeatedly without any apparent degradation in the structural integrity, suggesting strong non-covalent interactions between the PBDT and IL. Furthermore, the thermal stability of PBDT ($T_{d,95\%}$ ≈ 500 °C) and resulting PBDT-IL composites ($T_{d,95\%}$ ≈ 350 °C) are superior to any

polymer-based material that is currently in use (see thermogravimetric analysis of PBDT-IL composites in **Figure E.2**).

Depending on the polymer concentration used, the PBDT-IL composites are either translucent (low PBDT concentration) or semi-opaque (high PBDT concentration). This optical effect arises from the spatial heterogeneity of PBDT that exists in domains of different concentrations and the domain sizes are on the order of the wavelength of light (shown by AFM measurements in **Figure 6.3**). However, as we did not apply an external field (i.e. shear or magnetic field) during fabrication, there is no preferred global orientational order along any axis parallel to the film plane (see SAXS measurements below in **Figure 6.5**).

The film-drying process, where water is removed and the membrane experiences a large uniaxial dimensional change (i.e., effective compression), can however induce significant in-plane alignment of semi-rigid polymers.[55, 285] The layered and hierarchical polymer morphology observed by SEM, shown in **Figure 6.1D** of a 30 wt.% PBDT-IL composite cross-section, suggests a high degree of in-plane orientation of PBDT within the composite membrane. The presence of IL obscures more detailed morphological observations by SEM, which would require extraction of IL with a solvent prior to imaging.[273, 286, 287] Nonetheless, the clearly observable layered morphology is related to the strong local polymer orientational order and can be expected to enhance the mechanical properties of PBDT-IL composites. Moreover, this enhanced layering presents the possibility for controlled assembly of polymeric layers for separations or optical applications.

To motivate the detailed structure-property analysis in this work, we compare the mechanical properties of our PBDT-IL composites obtained at 25 °C with a compilation of the existing

literature,[273, 279, 282, 283, 286, 288-302] by plotting the storage modulus (E' or $3G'$) for a collection of PEMs/ion gels as a function of polymer concentration, as shown in **Figure 6.2A**.

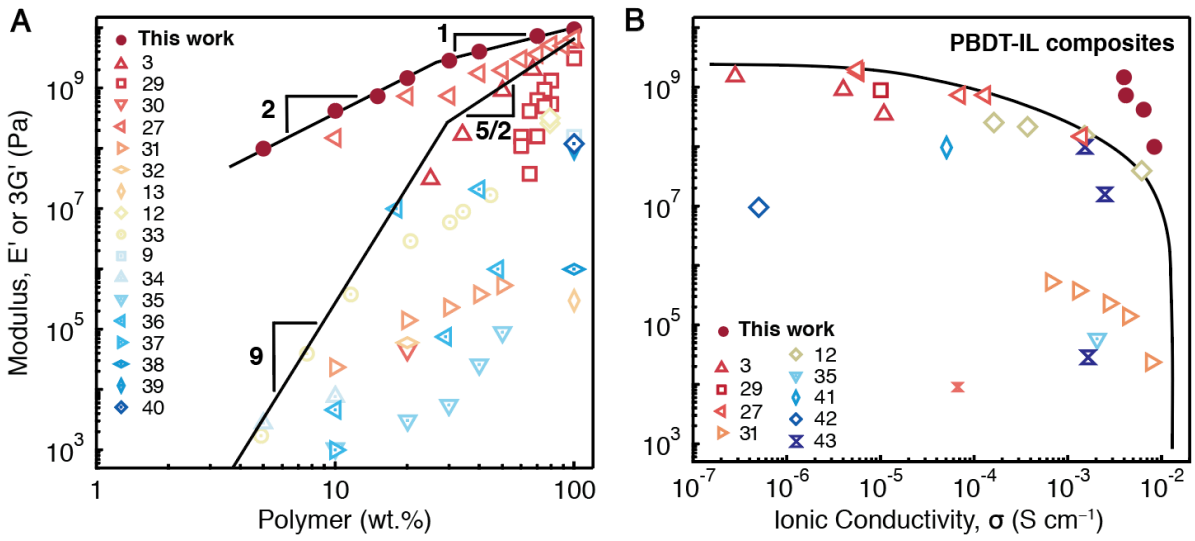

Figure 6.2. Comparison of PBDT-IL composites to a comprehensive literature compilation of PEMs and ion gels. The storage moduli (E' or $3G'$) of the PEMs/ion gels are plotted as a function of (A) polymer concentration and (B) ionic conductivity. Reference numbers are given in the figure legend. PBDT-IL composites exhibit a weak dependence (lower power law slope) of the modulus as a function of polymer concentration, enabling high stiffness at low PBDT concentration. Simultaneously, PBDT-IL composites boast high ionic conductivity combined with high moduli and outperforms all literature reports to date.

Two power laws with slopes of 5/2 and 9 represent an empirical upper bound for the majority of PEMs/ion gels reported to date, to the best of our knowledge. The strong concentration dependence of the modulus for these materials conclusively demonstrates that ILs have a strong plasticizing effect on the polymeric load-bearing components (e.g., the glassy blocks in BCPs) for PEMs reported in the literature. This results in the unfavorable requirement to use high polymer concentrations (ca. 50–80 wt.%) to obtain moduli on the order of 100 MPa or higher, which in turn reduces ionic conductivity substantially. Only two PEMs utilizing fibrillar-based polymers (i.e., this work (sulfo-aramid) and Mantravadi et al. using methyl cellulose), report a weaker dependence of the PEM modulus on polymer concentration (data above solid black line),

scaling as 2 and 1 at low and high concentrations, respectively.[286] This demonstrates an important reinforcement mechanism that polymer fibril formation hinders the plasticizing effects of IL on the glassy, load-bearing network. However, our PBDT-IL composites outperform the ionic conductivity of cellulose-based membranes by over 2 decades in ionic conductivity at similar modulus values.

We further demonstrate the exceptional combination of mechanical and ion transport properties of PBDT-IL composites by plotting *E'* as a function of ionic conductivity in **Figure 6.2B**. In our previous report, the conductivity values for PBDT-IL composites were measured at 22 °C.[68] We found the ionic conductivity along the polymer alignment direction (shown in **Figure 6.2B**) to be larger than the conductivity in the direction perpendicular to polymer orientation, and this anisotropy increases as the polymer concentration increases (from 1 to 3.5). For the present materials, we measured the conductivity of for a few representative films in the through-thickness direction using the same apparatus and procedure as our previous report, and the conductivity values are consistent with each other. For example, the ionic conductivity of the 10 wt.% PBDT-IL composite is 4.3 mS cm^{-1} at room temperature. We will report more detailed conductivity measurements of these films in a separate paper. The data included in **Figure 6.2B** from the wider literature range in temperature (with the lowest being room temperature and up to 150 °C for some materials) and polymer concentration. We plot the highest values reported from each reference, so the comparisons with our 22 °C measurements are overly favorable for many of the prior literature cases. Again, here the solid line designates an empirical upper bound for inaccessible combinations of modulus and ion conductivity based on the current literature. The upper right corner of the graph represents an unprecedented combination of stiffness and ion transport, which is achieved alone by PBDT-IL composites. Such results strongly motivate more

detailed structure-property analysis of PBDT-IL composites undertaken in the current work and represent an alternative to the current design paradigm dominated by BCP-type PEMs.

6.3.2. Morphological Observations

AFM has been utilized to observe the morphology of PEMs, revealing complex microphase-separated structures. Watanabe and coworkers identified microphase-separated domains of ionic and non-ionic polyimide blocks through analysis of the surface topology (height) and phase angle (relative stiffness).[273] Similarly, we investigated the morphology of PBDT-IL composites using tapping-mode AFM, shown in **Figure 6.3**. The topological images, where bright and dark areas correspond to higher and lower heights, respectively, are shown in **Figure 6.3** (*top*). The PBDT concentration and scale bars are in the topological images. Due to changes in height differences between samples with various polymer concentrations, the height maps are not on the same absolute scale. We present the corresponding phase maps, where higher and lower phase angles are brighter and darker regions, in **Figure 6.3** (*bottom*). A lower phase angle corresponds to regions of higher stiffness,[303] which likely correlates with domains of higher polymer concentration.

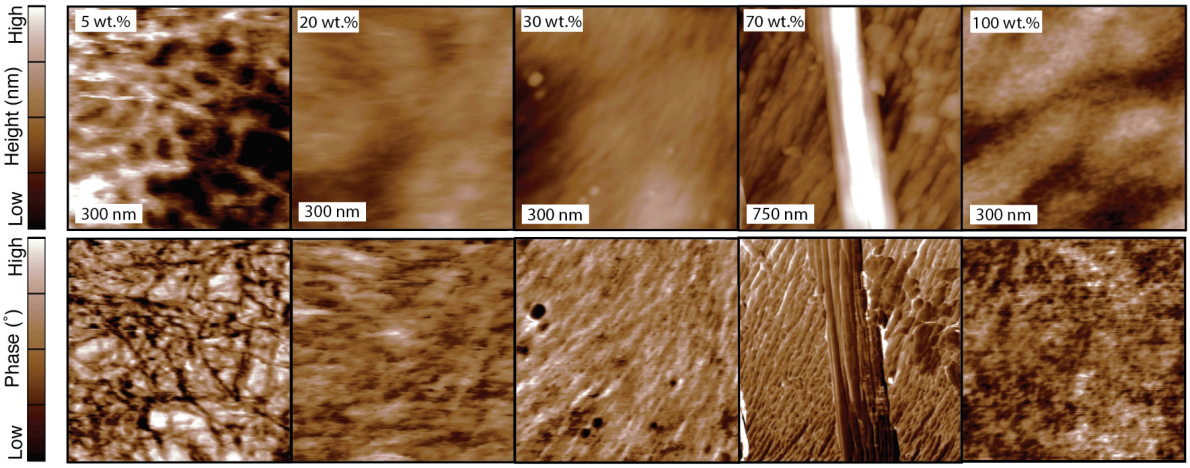

Figure 6.3. AFM of the PBDT-IL composite morphology. The height (*top*) and phase angle (*bottom*) maps are shown stacked for ease of comparison. The polymer concentration and scale bar are given in the topological image for each concentration. Domains of high stiffness (low phase angle) and low stiffness (high phase angle) suggest two distinct phases with different local polymer concentrations.

All of the PBDT-IL composites we investigated exhibit a heterogeneous morphology consistent with a phase-separated microstructure. At 5 wt.% PBDT, anisotropic domains with high stiffness form an interconnected network that span the observable sample. These high-stiffness domains likely contain higher PBDT concentrations than the nominal bulk concentration, i.e. local domains consisting of greater than 5 wt.% PBDT. Co-existing with these high stiffness anisotropic domains are domains of poorly defined morphology and lower stiffness, likely IL-rich domains. The observable morphology for the 5 wt.% PBDT-IL composite strongly suggests at least two distinct local environments within the composite material.

At intermediate concentrations (20 and 30 wt.%), domains of high and low stiffness are also observed, similar to the 5 wt.% PBDT-IL composite. However, the texture at 20 and 30 wt.% appears to have a distinct direction of alignment that is not readily observable at the lower concentration. This orientational order is consistent with the nematic phase behavior observed

under crossed polarizers at the micro- and macroscopic scale (see **Figure 6.1B).** Moreover, the domain boundaries between regions of high and low stiffness appear much more diffuse and less well-defined. These diffuse domain boundaries would suggest a decrease in polymer concentration heterogeneity.

Increasing the polymer content (70 wt.% PBDT) reveals higher-order fibrillar structures with lateral dimensions of ca. 1 um and axial lengths that traverse the entire scanned area. Upon closer inspection, these structures are composed of smaller fibrillar structures, similar to the anisotropic domains observed at lower concentrations (20-30 wt.%), on the order of 10–100 nm that evidences a complex hierarchical assembly of nanofibrillar polymer rodlike aggregates. Topological images in 3D reveal more explicitly the exquisite structure of these hierarchical fibrils (see **Figure E.3**). These fibrillar structures cannot be resolved in the neat PBDT material, as there is very little stiffness contrast, and we observe a relatively uniform surface.

Our understanding of the phase morphology is represented in **Figure 6.4**, which depicts PBDT-rich fibrils forming a macroscopic network surrounded by PBDT-poor domains strongly coordinating with IL. To clarify, the terms 'rich' and 'poor' are relative with respect to the average value for the composite of interest, i.e., we are referring to local heterogeneities in the polymer concentration. The spatial arrangement of IL in the vicinity of PBDT chains is complex; however, we depict the positively charged [Emim] moieties strongly localized near the negatively charged sulfonic groups and the anion [TfO] localized near the hydrophobic terephthalic acid residue.[69] The transformed binary image and its corresponding 1D fast Fourier transform (FFT) intensity indicates a characteristic length scale of heterogeneous domains on the order of 100 nm. Thus, this two-phase structural model, which is phase-separated at the ~130 nm

length scale, informs our understanding towards interpreting the following thermal, scattering and thermo-mechanical results.

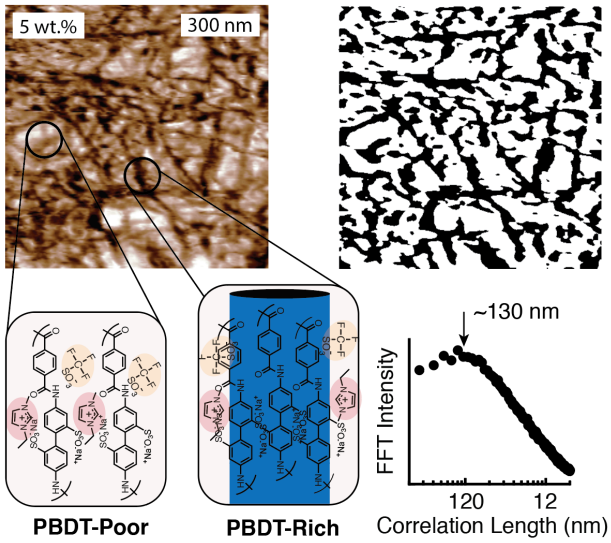

Figure 6.4. AFM phase angle map of a 5 wt.% PBDT-IL composite and idealized representation of the two-phase morphology, characterized by a PBDT-rich and PBDT-poor phase. The transformed binary image and corresponding 1D fast Fourier transform (FFT) intensity indicates a correlation length of ~130 nm.

6.3.3. Thermal Behavior

We investigated the thermal behavior of PBDT-IL composites with DSC to confirm the two-phase morphology observed via AFM. Thus, after complete elimination of water and cooling down to −150 °C, we show the heating thermograms (2 °C min^{-1}) for neat IL and PBDT-IL composites in **Figure 6.4A**. To investigate the crystallization of IL within the PBDT-IL composites, samples were allowed to fully crystallize during the cooling step prior to measurements.

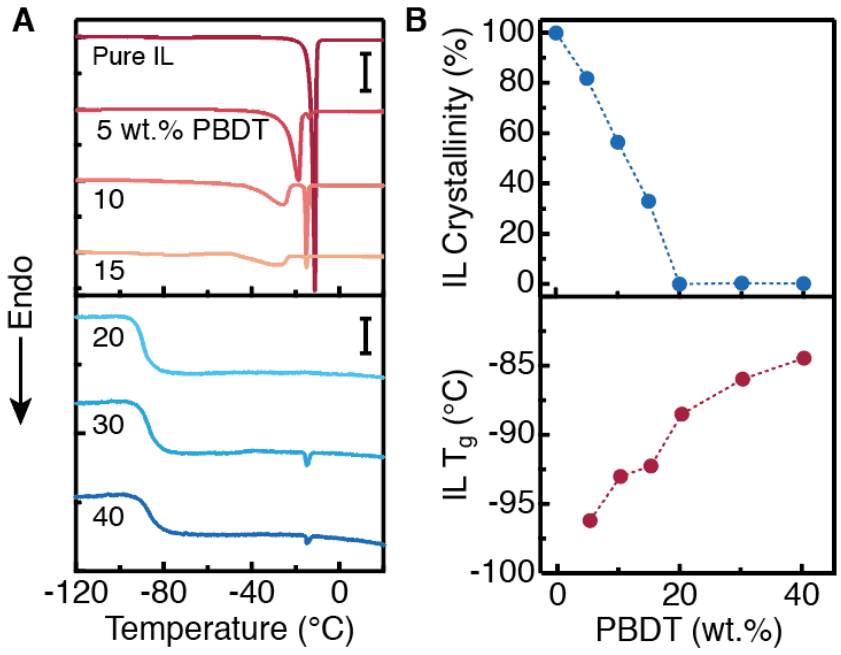

Figure 6.4. DSC characterization of PBDT-IL composites. (A) Thermograms of the 2nd heat measured for neat IL (i.e., 0 wt.% PBDT) and PBDT-IL composites with up to 40 wt.% PBDT. The heat flux vertical scale bars are 50 mW g^{-1} (*top*) and 5 mW g^{-1} (*bottom*) given in the figure. The melt endotherm peak splitting observed at 5, 10, and 15 wt.% PBDT indicates the coexistence of two local environments for the IL. (B) (*top*) Calculation of the IL crystallinity from total melt enthalpy for the PBDT-IL composites as a function of PBDT concentration, assuming the neat IL is 100% crystalline. The IL crystallinity is eliminated at 20 wt.% PBDT, while higher PBDT concentrations result in composites with negligible crystallinity. (*bottom*) T_g measured on the 2nd heat of samples after quenching to –150 °C at a cooling rate of 200 °C min^{-1}. The glass transition increases nearly linearly with PBDT concentration, before beginning to plateau.

The neat polymer does not exhibit any measurable thermal transitions, i.e., T_g or T_m, as detectable by DSC up to its degradation temperature. However, the morphology of PBDT-IL composites can be elucidated by analysis of the changes in phase transitions related to the IL in the presence of PBDT. The IL melt endotherms in PBDT-IL composites containing between 5–20 wt.% PBDT is shifted to temperatures below the T_m of the pure IL and splits into two distinct endotherms, shown in **Figure 6.4A**. The two peak temperatures and shapes are sensitive to the concentration of PBDT, and strongly suggests that the IL experiences two distinct local

environments. As a means of comparison, water within a hydrophilic polymer matrix exhibits multiple melt peaks depending on the degree of confinement and the strength of its interaction with the polymer.[304-306] The assignment of melt peaks is made more complicated by the fact that cation exchange of Na^+ with $Emim^+$ can occur between PBDT and IL.[68, 69] We doped small amounts of [Na][TfO] into [Emim][TfO] and observed that the resulting crystal melt endotherms were of lower melt enthalpy and shifted to slightly lower temperatures compared to the pristine IL (see **Figure E.4**).

We approximate the degree of IL crystallinity in the PBDT-IL composites by taking the ratio of the melt endotherms of the composites to the neat IL (assuming 100% crystallinity of the neat IL), shown in **Figure 6.4B** (*top*). The decrease in crystallinity with PBDT concentration is nearly linear, with a ~5% crystallinity decrease per wt.% PBDT added. Above 20 wt.% PBDT, we observe only a small degree of crystallinity (<1%) and a prominent T_g associated with the IL near –90 °C. These results demonstrate the ability of PBDT to inhibit IL crystallization, suggesting a significant reduction in IL mobility.

To confirm the synergistic interactions between PBDT and IL on the IL dynamics within the composite, we measured the IL T_g of wholly amorphous (non-crystallized) composites obtained by quenching the samples from 200 °C to –150 °C at 200 °C min^{-1}, which prevented IL crystallization (see **Figure E.5**). We show the T_g as a function of PBDT concentration in **Figure 6.4B** (*bottom*), which increases monotonically with PBDT concentration from –97 to –83 °C. This increase in T_g demonstrates compatibility between the charged PBDT and IL that restricts the mobility of the IL and is consistent with recent MD simulations.[69]

6.3.4. SAXS/WAXS Characterization

We employed SAXS to characterize the polymer structure within the PBDT-IL composites to complement our surface-based AFM measurements. The orthorhombic membrane geometry dictates that two scattering configurations are used to fully characterize the polymer structure and orientational distribution.[10] First, we orient the incident X-ray beam parallel to the surface normal, depicted in **Figure 6.5A**, which causes the scattering vector (q) to be located within the x-y plane.

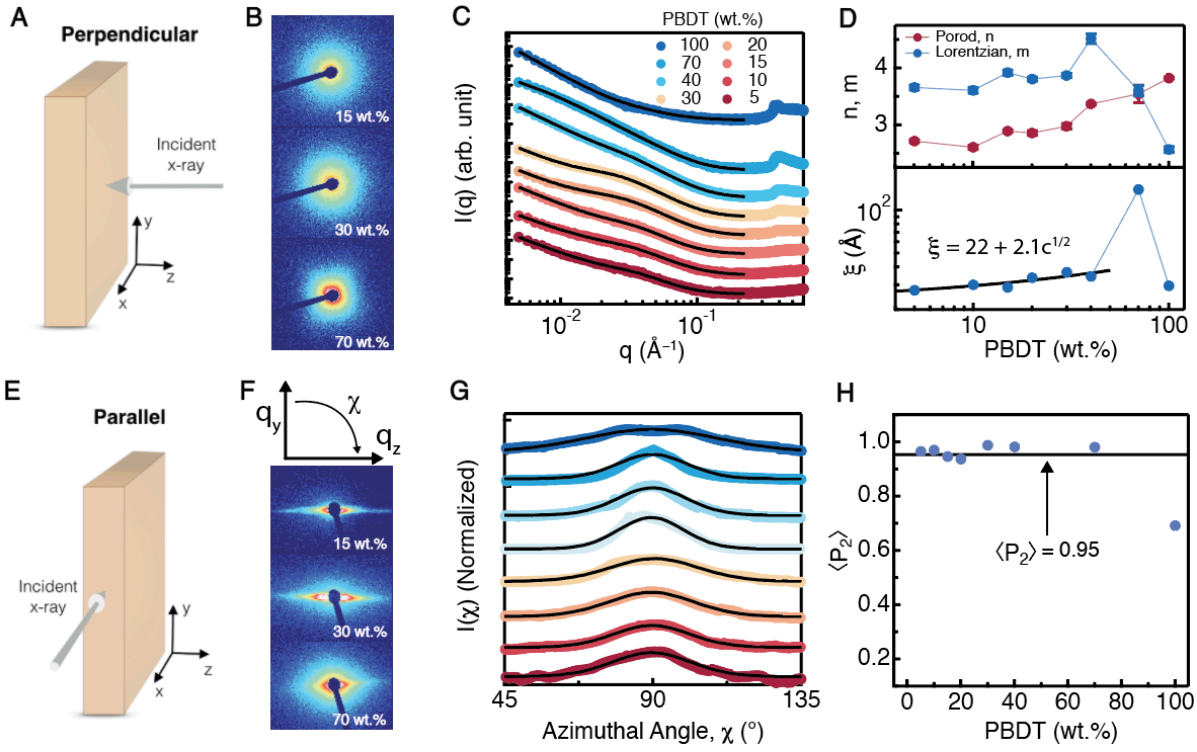

Figure 6.5. SAXS analysis of PBDT-IL composites. (A) The perpendicular scattering configuration, where the incident X-ray is parallel to the film normal, probes spatial correlations in the x-y plane. (B) Representative 2D SAXS patterns of the low-q region for 15, 30, and 70 wt.% PBDT-IL composites. The isotropic scattering intensity distribution confirms that the nematic domain directors have no significant macroscopic orientation with respect to the x- or y-axis. (C) 1D SAXS intensity as a function of q for the PBDT-IL composites with 5 to 100 wt.% polymer (bottom to top). The intensity spectra have been vertically offset for clarity. Solid lines are fits with a correlation length model given by **Eqn. 6.1**. (D) Concentration dependence of the Porod exponent (n), Lorentzian exponent (m), and correlation length (ξ) obtained from fitting the 1D SAXS data. (E) The parallel scattering configuration, where the incident X-

ray is parallel to the film surface, probes spatial correlations in the y-z plane. (F) 2D SAXS patterns for PBDT-IL composites in the parallel configuration and schematic illustrating the azimuthal intensity dependence. Strongly anisotropic scattering is observed for all PBDT-IL composites, indicating a high degree of in-plane polymer nanofibril orientational order. (G) Scattered intensity distribution along the azimuthal angle (χ) over the q range of 0.01 to 0.08 Å^{-1}. The solid lines are fits to the data using a Maier-Saupe type distribution given by **Eqn. 6.2**. Colors and concentrations are the same as in (C). (H) Order parameter $\langle P_2 \rangle$ calculated from numerical integration of **Eqn. 6.3** as a function of PBDT concentration. The average order parameter for all composites is 0.95 ± 0.03, indicating high orientational order of PBDT fibrils. Error bars for individual values are smaller than the markers.

The 2D intensity pattern from SAXS measurements in the perpendicular scattering configuration are shown in **Figure 6.5B** for a select set of PBDT-IL composites. The scattered intensity is isotropic at all PBDT concentrations, indicating a random orientational distribution of polymer chains in the x-y plane averaged over the illuminated volume from the X-ray beam diameter (~1 mm) and sample thickness. We emphasize that the observed isotropy here does not conflict with the aligned texture observed in AFM images presented earlier, as SAXS is a bulk-averaged technique and AFM is inherently microscopic and surface level. The azimuthally averaged 1D intensity as a function of q is given in **Figure 6.5C** and vertically offset for visual clarity. We fit the 1D SAXS intensity for the PBDT-IL composites with a shape independent correlation length model in SasView over the q range 0.004 to 0.2 Å^{-1}, given by **Eqn. 6.1**:

$$I(q) = \frac{A}{q^n} + \frac{B}{1+(q\xi)^m} + I_{inc} \qquad \textbf{(Eqn. 6.1)}$$

where the first term describes a Porod law with amplitude A and exponent n, and the second term is a Lorentzian correlation decay with amplitude B, correlation length ξ, and exponent m. The additive parameter I_{inc} accounts for the incoherent background scattering. The fits are shown as the solid lines in **Figure 6.5C** and the model agreement with the data is excellent. The corresponding fitting parameters of n, m, and ξ are shown in **Figure 6.5D** as a function of polymer concentration. With increasing polymer concentration, n increases from 2.7 at 5 wt.% to

3.8 at 100 wt.% PBDT. Using a mass fractal theoretical framework, the increasing power law exponent suggests a denser network structure of polymer chains with higher polymer content.[307] We interpret the Lorentzian feature as arising from the cross-section of rodlike aggregates within higher order PBDT-rich fibrillar structures. The Lorentzian exponent m is weakly dependent on the polymer concentration, with values fluctuating between 3.5 and 4.5 for all materials except the pure polymer. These values are close to 4, which would suggest that the nanofibrillar aggregates have a well-defined interface, irrespective of the IL concentration.[265] We fit the concentration dependence of the correlation length ξ of the PBDT-IL composites, below 70 wt.% PBDT, with a power law and baseline offset, giving an extrapolated zero-concentration correlation length of ~22 Å. We speculate that this represents the limiting value of the nanofibril lateral dimension after mixing IL with an aqueous PBDT solution. The correlation length increases weakly with polymer concentration over this concentration range scaling as $\xi \sim c^{1/2}$. This result suggests that the constituent nanofibrils within the PBDT-IL composites increase in diameter with higher PBDT concentration and are highly resistant to complete solubilization by IL.

The uniaxial deformation experienced by the polymer fibrils during the drying process induces a significant amount of in-plane orientation producing a highly layered structure (**Figure 6.1D**). The parallel scattering configuration, also referred to as 'edge-on', probes this alignment by placing the incident X-ray beam nearly parallel to the film surface, as illustrated in **Figure 6.5E**. The anisotropic azimuthal angular dependence of the scattered intensity projected on the y-z plane in reciprocal-space, shown in **Figure 6.5F**, is related to the in-plane orientational distribution of PBDT fibrils. We quantify the orientational order by fitting the azimuthal intensity distribution with a Maier-Saupe type distribution, given by **Eqn. 6.2**:

$$I(\chi) = I_0 + A\, exp[\alpha\, cos^2(\chi - \chi_0)] \qquad \textbf{(Eqn. 6.2)}$$

where I_0 is the isotropic baseline, A is the scattering amplitude, α is an anisotropy factor related to the width of the intensity distribution, and χ_0 is the azimuthal angle of the peak.[170] The azimuthal intensity distributions, normalized and vertically offset for visual clarity, and corresponding fits using **Eqn. 6.2** is shown in **Figure 6.5G** for all PBDT-IL composites studied here. Using the α values obtained from fitting the azimuthal intensity distributions, the fibril alignment is calculated through the order parameter, $\langle P_2 \rangle$, via numerical integration of **Eqn. 6.3**:

$$\langle P_2 \rangle = \frac{\int_{-1}^{1} exp[\alpha\, cos^2(\beta)]\, P_2(cos\beta)\, dcos(\beta)}{\int_{-1}^{1} exp[\alpha\, cos^2(\beta)]\, dcos(\beta)} \qquad \textbf{(Eqn. 6.3)}$$

where $P_2(cos\beta) = \frac{1}{2}[3\, cos^2(\beta) - 1]$ is the second-order Legendre polynomial coefficient (also known as the Hermann's orientation function). A $\langle P_2 \rangle$ value of unity indicates perfect orientation, while a value of zero corresponds to an isotropic orientational distribution. The calculated $\langle P_2 \rangle$ values for the PBDT-IL composites is given as a function of polymer concentration in **Figure 6.5H**. A $\langle P_2 \rangle$ value near 0.7 is calculated for neat PBDT, in agreement with previous studies of supramolecular sulfo-aramids.[55] The alignment for PBDT-IL composites appears to be invariant with concentration, with an average $\langle P_2 \rangle$ of 0.95 ± 0.03, indicating near perfect orientation of PBDT fibrils in-plane of the film. This value is in agreement with the expected orientational order calculated using an affine deformation model under uniaxial deformation (analogous to the film-drying process), which asymptotically approaches 1 at large strains.[170] Clearly, by the high value of $\langle P_2 \rangle$ and its concentration independence, the orientational order of PBDT fibrils within the composites is close to the maximum attainable using a solution-casting method.

Further structural details, reporting on both polymer and IL spatial correlations, can be elucidated by analysis of the high-q scattering of PBDT-IL composites using WAXS. We show the 1D scattering intensity in the perpendicular configuration, arbitrarily vertically offset for visual clarity, in **Figure 6.6** for the neat IL, neat PBDT, and resulting PBDT-IL composites and the scattering features are summarized in **Table 6.1**.

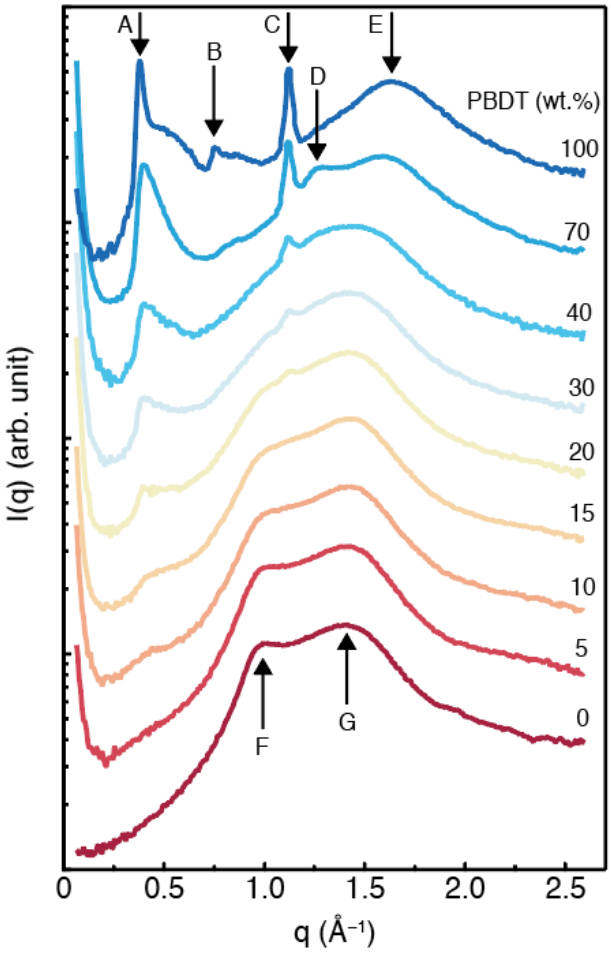

Figure 6.6. WAXS spectra of neat PBDT, PBDT-IL composites, and neat IL measured in the perpendicular configuration. The ordinate is log-scale and the intensity spectra have been arbitrarily vertically offset for clarity. The scattering features are marked with arrows in the figure and are tabulated in **Table 6.1**. Features originating from the polymer increase in intensity with polymer concentration. The pure IL has a double-topped feature that dominates the scattering below 20 wt.% PBDT.

Table 6.1. Tabulated peak positions of WAXS analysis, corresponding d-spacings from Bragg's Law, and assignment of their structural origin. The scattering feature that is not common to either the neat polymer or neat IL is shaded in grey.

Peak	q* (Å^{-1})	2π/q* (Å)	Assignment
A	0.38	16.5	PBDT 001
B	0.75	8.4	PBDT 002
C	1.12	5.6	PBDT 003
D	1.29	4.9	PBDT-IL-PBDT
E	1.64	3.8	PBDT-PBDT
F	1.00	6.3	IL Correlation
G	1.41	4.5	IL Correlation

The X-ray diffraction peaks for neat PBDT have been assigned previously[62, 65, 67, 68] and are summarized here. Peaks located at q = 0.38 Å^{-1} (**A:** 16.5 Å), 0.75 Å^{-1} (**B:** 8.3 Å) and 1.12 Å^{-1} (**C:** 5.6 Å) correspond to the polymer repeat unit 001, 002, and 003 reflections, characteristic of nematically aligned sulfo-aramids.[55] Local π-π packing of amorphous all-aromatic PBDT chains yields a broad peak centered at q = 1.64 Å^{-1} (**E**: 3.8 Å). As the polymer concentration increases within the PBDT-IL composite, the features associated with the polymer increase in intensity, and vice-versa.

The neat IL displays two prominent correlation peaks, which present as a double-topped feature with maxima at q = 1.00 Å^{-1} (**F:** 6.3 Å) and 1.41 Å^{-1} (**G:** 4.5 Å). The double-topped feature builds in as the concentration of polymer is reduced and dominates the scattering spectra for composites with less than 20 wt.% PBDT. We assign peak F as [Emim]-[Emim] correlations by measuring IL samples doped with [Na][TfO], which reduces the intensity of peak F (**Figure E.6**). More detailed analysis of the local structure of the IL is out of the scope of the current work.

The only peak that is observed in the PBDT-IL composites WAXS spectra which is not common to either neat PBDT or IL is peak D, at q = 1.29 $Å^{-1}$ (**D:** 4.9 Å), see **Table 6.1**. Only two PBDT-IL composites, 70 and 40 wt.%, exhibit this scattering feature as a small, broad peak. We propose that this scattering peak corresponds to a population of PBDT chains with an expanded π-π distance due to coordination with the IL. Direct insertion of an imidazolium ring between two benzene rings in mixtures of 1-dodecyl-3-methylimidazolium bis(trifluoromethanesulfonyl)amide ([$C_{12}mim^+$][$TFSA^-$]) and benzene causes an increase in the π-π distance from 3.3 to 7.5 Å.[308] In PBDT-IL composites, the coordination of the imidazolium cation with the PBDT chains may not be a direct insertion between the aromatic rings of PBDT. Instead, we speculate that the coordination and partial insertion of [Emim] with PBDT expands the inter-aromatic distance of PBDT from 3.8 to 4.9 Å. For the 70 wt.% PBDT-IL composite, both the 4.9 and 3.8 Å correlation distances are clearly observed. This confirms that there are two distinct local environments within the PBDT-IL composites, consisting of either strongly coordinated or uncoordinated PBDT chains with IL. This peak, which may be present at lower PBDT content but obscured by the pure IL peaks, likely reports on local IL-polymer interactions that could contribute to the formation of a collective electrostatic network proposed to be important for PBDT-IL composites.[68, 69]

6.3.5. Thermo-Mechanical Characterization

The mechanical properties of PEMs are of utmost importance for their envisioned use as gas separation membranes or solid-state battery electrolytes. Moreover, detailed analysis of the thermo-mechanical response of polymer PEMs can provide information on their local- and long-range dynamics and phase behavior. We used DMTA to characterize the mechanical properties

of PBDT-IL composite films as a function of temperature. The storage (E') and loss (E'') moduli, measured isochronally at 1 Hz from –150 to 350 °C, is given in **Figure 6.7A** for four PBDT concentrations.

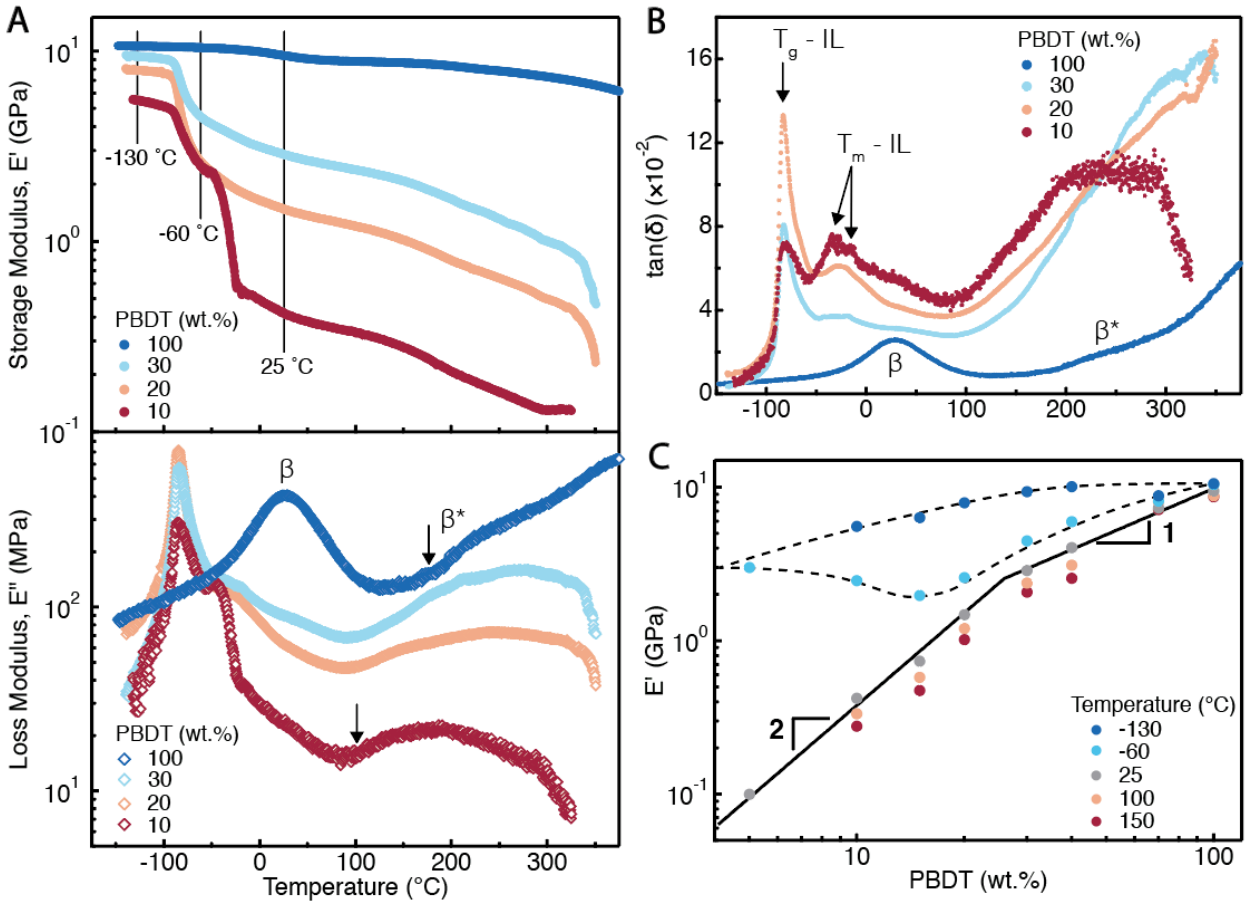

Figure 6.7. Isochronal DMTA results of PBDT-IL composites. (A) Storage (E', *top*) and loss (E'', *bottom*) moduli as a function of temperature measured at 1 Hz with a heating rate of 2 °C min^{-1}. Temperatures are indicated in the figure by vertical lines where storage modulus scaling relationships are extracted. Dispersion peaks arising from secondary polymer relaxations, designated as β and β*, are labeled on the E'' curve. The onset of the β^* relaxation is shifted to lower temperatures with higher IL concentration, indicated by the arrows. (B) Isochronal loss tangent as a function of temperature for PBDT-IL composites. The IL T_g is evident as a sharp, prominent peak near –90 °C. Dispersion peaks due to the dual IL crystal melting event for 10 wt.% PBDT are marked with arrows. (C) Storage modulus as a function of PBDT concentration at –130, –60, 25, 100, and 150 °C. Solid lines are power law fits to the data and dashed lines are guides to the eye. A transition in power law scaling from 2 to 1 occurs between 20 and 30 wt.% PBDT. The extrapolated modulus to zero PBDT concentration at –130 and –60 °C is 2–3 GPa.

The neat polymer exhibits a E' of ~10 GPa at cryogenic temperatures, and maintains its high stiffness up to extreme temperatures of >350 °C. These exceptional thermo-mechanical properties, characteristic of aramids, bestows PBDT with ideal characteristics as a matrix material for fabrication of high-performance PEMs. Two main relaxation processes are evident in the neat polymer by inspection of E", with a β-relaxation centered near 25 °C and a β^*-relaxation appearing as a broad shoulder with an onset temperature near 200 °C. The β- and β^*-relaxations have been attributed to complex motions of the amide bond and ring flips from the main-chain aromatic groups, respectively, and are characteristic of aramid secondary thermal relaxations.[268]

The PBDT-IL composites between 10 and 30 wt.% PBDT possess E' values between 5–10 GPa at −130 °C, but experience a significant drop in their stiffness over the range of −130 to −60 °C. This decrease in stiffness is primarily due to the T_g of IL as evidenced previously via DSC measurements. The observed loss peak associated with this transition is intense and narrow. Inspection of the loss tangent, presented in **Figure 6.7B**, indicates that the most intense IL transition is observed at 20 wt.% PBDT. Thus, the 20 wt.% PBDT-IL composite has the highest concentration of amorphous, glassy IL that results in the most significant mechanical decrease over the T_g of the IL.

At temperatures higher than the IL T_g, the E' for 20 and 30 wt.% PBDT-IL composites maintain a relatively constant value over the temperature range of −60 to 150 °C. This behavior is consistent with a physical network of glassy polymer chains providing mechanical integrity to the composite. At higher temperatures, the onset of the β*-relaxation causes a slight decrease in the stiffness. The β^*-relaxation precedes complete decomposition of the IL above ~300 °C, resulting in mechanical failure of the PBDT-IL composites. In contrast, the 10 wt.% PBDT-IL

composite experiences a significant and sudden drop in E' from −50 to −10 °C arising from the melting of IL crystals. The IL crystal dual-melting endotherm, observed in DSC experiments, can also be confirmed by inspection of the loss tangent of the 10 wt.% PBDT-IL composite, indicated by the two arrows (**Figure 6.7B**).

To determine the effective modulus of crystalline IL, we plot the decrease in E' from −50 to −10 °C as a function of IL crystallinity (**Figure E.7**). The linear slope, 2.0 ± 0.6 GPa, extracted from fitting these data is an estimate of the effective modulus of IL crystallites. This value is in agreement with recent rheological measurements of imidazolium-based ionic liquids, which reports a glassy modulus of ~1 GPa.[309-311] This is the first measured value of the modulus of crystalline IL within a PEM and suggests that IL-rich regions form a percolated network throughout the material.

We analyze the role of PBDT in the reinforcement of the composite by plotting E' as a function of PBDT concentration at various temperatures corresponding to different IL structures within the material (**Figure 6.7C**). At −130 °C, the IL is glassy and/or semi-crystalline, depending on the specific polymer concentration as shown by DSC (**Figure 5**). At −60 °C, the amorphous IL is above its T_g and bestowing liquid-like mobility but is still below the T_m of the IL crystal, resulting in the small decrease in E' up to 20 wt.%. The two trends in E' at −130 and −60 °C, when extrapolated to zero polymer concentration, converge on a value of ~2 GPa (dashed lines in **Figure 6.7C**) representing the effective modulus of the crystalline IL, as shown above. Finally, at 25 °C the IL is above both the T_g and T_m, exhibiting liquid-like behavior at all concentrations. At 25 °C, the IL appears to have a negligible individual contribution to the mechanical properties of the composite; thus, the E' scaling at 25 °C reports on the morphology and structure of the PBDT network alone.

The E' concentration scaling of the PBDT-IL composites at 25 °C follows two power law regimes, which intersect between 20 and 30 wt.% PBDT. At low concentrations, E' follows a power law of exponent 2, while at high concentrations the E' scaling is linear. Below 30 wt.% PBDT, the modulus power law scaling exponent 2 is consistent with the expected value from considerations of polymer interactions mediated through chain entanglements.[240] In contrast, the linear scaling of E' at high polymer concentrations is consistent with the expected trend of continuous fiber reinforced composites as described by the linear rule of mixtures.[10] Here, mesoscopic percolated PBDT-rich fibrils may act as a self-reinforcing network that mechanically supports the IL-rich domains. Our SAXS data indicates a smooth transition in structural characteristics at the length scales of <50 nm over this concentration range. Thus, we speculate that the cross-over in E' scaling likely corresponds to a critical mesoscopic network connectivity which enables rule of mixtures type behavior (linear E' scaling).

We have shown through DSC and AFM analysis that PBDT-IL composites consist of a structure with at least two microphase-separated domains, one PBDT-poor (IL-rich) and another PBDT-rich (IL-poor). With this model of the PBDT-IL composite morphology, we show in **Figure 6.8A** an idealized isochronal E'' temperature scan with decomposed contributions from PBDT-rich and PBDT-poor domains arising from secondary polymer relaxations with the IL T_g superimposed near –85 °C. Experimentally, we find evidence for this structural model through analysis of the E" temperature dependence, where all concentrations are shown, vertically offset for visual clarity, in **Figure 6.8B**.

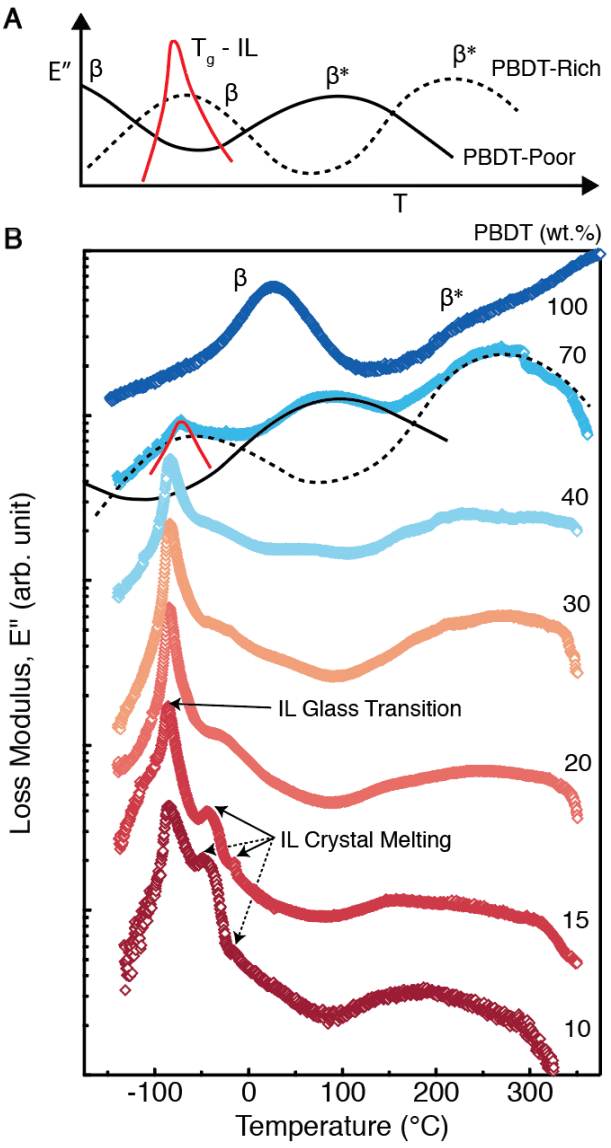

Figure 6.8. Analysis of the thermo-mechanical relaxations of neat PBDT and PBDT-IL composites. (A) Idealized isochronal E" as a function of temperature at 1 Hz for PBDT-IL composites decomposed into contributions from the amorphous IL, PBDT-rich, and PBDT-poor domains. (B) Experimental E" temperature dependence at 1 Hz for neat PBDT (dark blue) and PBDT-IL composites (concentrations given in figure) vertically offset for visual clarity. Black solid and dashed lines on the 70 wt.% sample represent the relaxation features originating from PBDT-poor and PBDT-rich domains, respectively. The red line and arrows indicate features originating from the crystal melting and glass transition of IL.

Due to the presence of two distinct polymer phases (PBDT-poor and PBDT-rich), we observe a superposition of polymer secondary relaxations, illustrated by the solid and dashed lines in

Figure 6.8B. Such a superposition of two secondary loss peaks has been observed previously in microphase-separated sulfonated polyimide PEMs.[273] The polymer contained in the PBDT-poor phase is highly plasticized through coordination with IL, shifting the entire relaxation temperature profile to lower temperatures and broadening the E'' dispersion peaks.

The superposition of secondary relaxations is most evident in the 70 wt.% PBDT-IL composite. The broad E'' peak between 0 and 150 °C for the 70 wt.% PBDT sample arises from the β^*-relaxation process occurring in the PBDT-poor domains. This feature can be seen to systematically grow in intensity with increasing PBDT concentration in the composites and is absent in the neat polymer. We do not observe an E" feature associated with the β-relaxation of the PBDT-poor, suggesting that this relaxation is below the accessible experimental temperature range.

The PBDT-rich secondary relaxations are more prominent in the E'' signal because these polymer-rich domains constitute the primary load-bearing structure in the PBDT-IL composites. We observe a clear shift in the 'β^* - PBDT-rich' relaxation to lower temperatures as the polymer concentration is reduced. This trend indicates that increasing the IL concentration plasticizes the local dynamics of the PBDT chains to some extent. The low-temperature 'β - PBDT-rich' relaxation is similarly shifted to lower temperatures when compared to the β-relaxation of the neat PBDT. However, this relaxation is dominated by the T_g of the IL and is strongly obscured. From these data, we conclude that there exists a broad relaxation feature in all composites near the IL T_g, likely originating from the β-relaxation within the PBDT-rich domain.

6.3.6. Time-Temperature Superposition

To further probe the secondary polymer relaxations and IL glass transition observed in isochronal DMTA measurements, we utilize time-temperature superposition (TTS) to construct master curves for the neat polymer and PBDT-IL composites with 20, 30 and 40 wt.% PBDT at a reference temperature T_{ref} = –90 °C, shown in **Figure 6.9A**. Over the temperature range used for the master curve construction, we successfully applied TTS and no vertical shift factors were used. For the PBDT-IL composites, temperatures higher than –50 °C resulted in a breakdown in TTS, and we omitted those data in our analysis. We observed high frequency tails to the E" data, likely due to the very high material stiffness and small amplitude strains used (<0.1%).

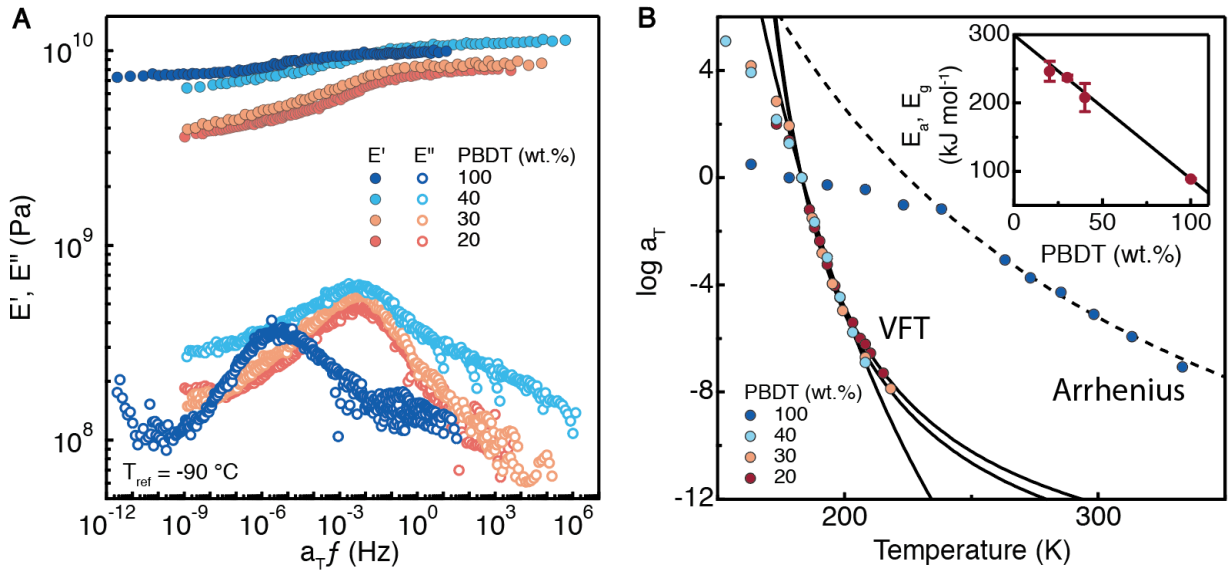

Figure 6.9. TTS analysis of PBDT-IL composites. (A) Master curves of *E'* (filled symbols) and *E"* (open symbols) at T_{ref} = –90 °C. (B) Logarithm of shift factors used in TTS as a function of absolute temperature. Dashed line is a fit to the Arrhenius equation (**Eqn. 6.4**) for the neat PBDT and solid lines are fits to the VFT law (**Eqn. 6.5**) for the PBDT-IL composites. (*Inset*) Arrhenius activation energy (E_a) and VFT apparent activation energy (E_g) for neat PBDT and PBDT-IL composites, respectively. Solid line is a linear fit to the data.

For neat PBDT, the main transition we observe is the β-relaxation centered at 25 °C (see **Figure 6.7**). Thus, when plotted using a T_{ref} = –90 °C, the E'' peak is shifted to a low frequency of ~5×10^{-6} Hz. As expected, the local motions associated with the β-relaxation dynamics are effectively frozen out at –90 °C and require long times for thermal activation. We plot the master curve shift factors (a_T) in **Figure 6.9B** and fit the PBDT β-relaxation shift factors with an Arrhenius equation, given as

$$log\ a_T = \frac{E_a}{2.303R}\left(\frac{1}{T} - \frac{1}{T_{ref}}\right) \qquad \textbf{(Eqn. 6.4)}$$

and shown as the dotted line in **Figure 6.9B**. The activation energy of the β-relaxation is E_a ~89 kJ mol^{-1}, significantly higher than typically found for simple non-cooperative β-relaxations (~40 kJ mol^{-1}), indicating a complex and cooperative relaxation process. This value is in agreement with prior studies investigating the β-relaxation of all-aromatic polyamides.[268]

The master curves for PBDT-IL composites with 20–40 wt.% PBDT are qualitatively similar to the pure polymer. However, *a priori* we know that the major component of the PBDT-IL composites is IL (60–80 wt.%) and IL dominates the thermo-mechanical response in the vicinity of the IL T_g. Thus, we assign the broad relaxation feature of the PBDT-IL composites to be a signature of the IL T_g. The intensity of the relaxation increases with decreasing polymer concentration, confirming that we are probing the IL dynamics in this range. We fit the shift factors using the so-called Vogel-Fulcher-Tammann (VFT) law that relates the thermal dependence of the relaxation time $\tau(T)$ in the vicinity of the glass transition temperature as

$$\tau(T) = \tau_0 \exp\left(\frac{B}{T - T_\infty}\right) \qquad \textbf{(Eqn. 6.5)}$$

where τ_0 is the infinite temperature relaxation time, T_∞ is the VFT divergence temperature, and B is a material specific parameter. We use an equation for fitting the a_T from TTS by taking the

logarithm of the quotient $\tau(T)/\tau(T_{ref})$ and using B and T_∞ as fitting parameters. Within the framework of the VFT model, the apparent activation energy (E_g) and fragility index (m) is calculated from

$$E_g = \frac{RB}{(1-T_\infty/T_g)} \quad \textbf{(Eqn. 6.6)}$$

$$m = \frac{B/T_g}{\ln 10(1-T_\infty/T_g)^2} \quad \textbf{(Eqn. 6.7)}$$

where R is the gas constant and the T_g is determined from DSC measurements. The fragility index is related to the rate of change of transport properties at temperatures close to, but above, the T_g.[311] Within this context, high and low m values indicate a fragile and strong glass former, respectively. Imidazolium-based ILs have m values in the range of 60-80, indicative of a fragile glass, i.e. the viscosity drops by many orders of magnitude as the temperature is raised through the T_g.[311] We plot the calculated E_g values in the inset of **Figure 6.9B** in addition to the Arrhenius E_a value of neat PBDT. We find a linear relationship between the activation energies and PBDT concentration, which suggests that the measured activation energy is a simple composite average of the IL T_g and PBDT-rich β-relaxation. The intercept value, corresponding to the E_g of pure IL, is 300 ± 5 kJ mol^{-1}, in agreement with the E_g values reported by rheometry studies on imidazolium-based ILs.[311] The calculated values of m for our PBDT-IL composites lie in the range of 0.1-10, indicating a very strong glass former. However, these calculated values are merely an apparent fragility, as the mechanical properties of the PBDT-IL composite are dominated by the glassy polymer network at temperatures above the IL T_g.

6.3.7. Stress-Strain Behavior

To withstand the stresses likely to be imposed upon PEMs for use as solid-state battery electrolytes or gas separation membranes, the material should possess sufficient stiffness. In general, the addition of ILs to glassy polymer matrices results in significant plasticization and causes the tensile failure behavior to change from brittle to ductile.[288, 312] This plasticization reduces the stiffness and ultimate strength considerably, negatively impacting material properties. To investigate the effects of IL on the tensile behavior of PBDT-IL composites, we performed stress-strain measurements at 25 °C in dry conditions as shown in **Figure 6.10**.

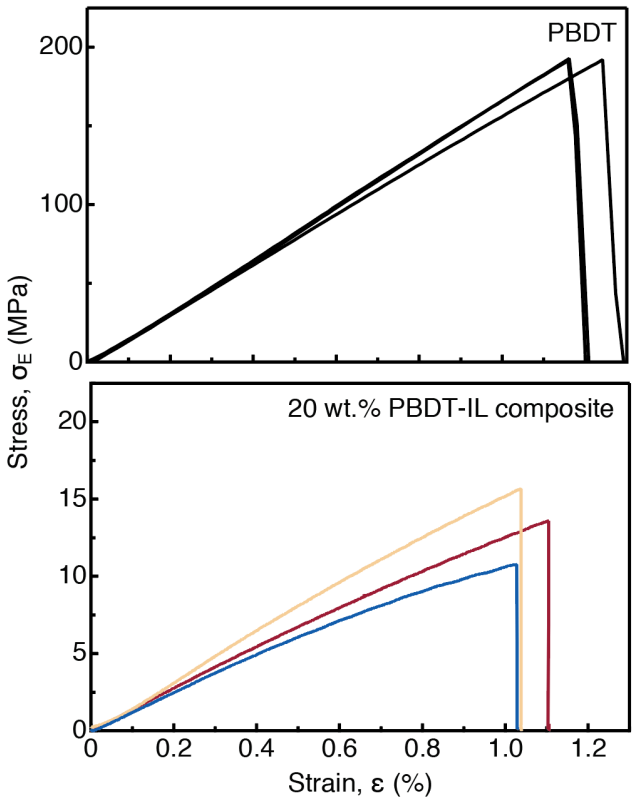

Figure 6.10. Stress-strain measurement in uniaxial tension for three samples of neat PBDT (*top*) and 20 wt.% PBDT-IL composite (*bottom*) at a strain rate of 1% min^{-1}. The same qualitative brittle stress-strain behavior is observed for the PBDT-IL composites as is found for neat PBDT.

Interestingly, the stress-strain behavior of the composites qualitatively matches that of the neat polymer and exhibits brittle behavior with a strain at break of ~1.1%. The ultimate strength is reduced from ~200 MPa in the neat polymer to ~13 MPa for the 20 wt.% PBDT-IL composite. This result strongly suggests that the load-bearing network structure in PBDT-IL composites remains glassy in the presence of IL and is strongly resistant to plasticization.

6.4. CONCLUSIONS

In summary, we have prepared PBDT-IL composites from a sulfo-aramid and a model IL that forms supramolecular fibrillar networks across the entire compositional range. We compared the mechanical properties and ionic conductivity of PBDT-IL composites to an exhaustive literature compilation that unambiguously demonstrates the advantage of our approach. Morphological observations utilizing optical, electron, and atomic force microscopy in conjunction with SAXS and thermo-mechanical analysis revealed a liquid crystalline, self-assembled two-phase morphology consisting of ion-conducting domains and load-bearing polymer-rich fibrils. Through SAXS, we demonstrated that the size and density of constituent fibrils within higher-order structures are modulated as a function of IL concentration with a diameter of 20–40 Å. These fibrils are highly aligned in the film plane, with an order parameter near 0.95, due to affine deformation during the membrane drying process. Thermo-mechanical measurements highlighted the best combination of room temperature modulus (0.1–2 GPa) and ion conductivity (8–4 mS cm^{-1}) of any PEM reported to date, to the best of our knowledge. Careful analysis of the thermo-mechanical data revealed a superposition of a PBDT-rich and PBDT-poor phase contributing to the mechanical relaxation spectrum, convoluted with the thermal transitions related to the pure IL. Using TTS, we extensively characterized the secondary relaxation

dynamics of the PBDT-IL composites and elucidated the linear contributions of both the polymer β-relaxation and the IL glass transition to the relaxation activation energy. These new insights will guide future material design and enable the application of high-modulus and high-ion-conductivity PEMs in a variety of high-performance electrochemical and gas separation applications.

APPENDIX A: CHAPTER 2 SUPPORTING INFORMATION

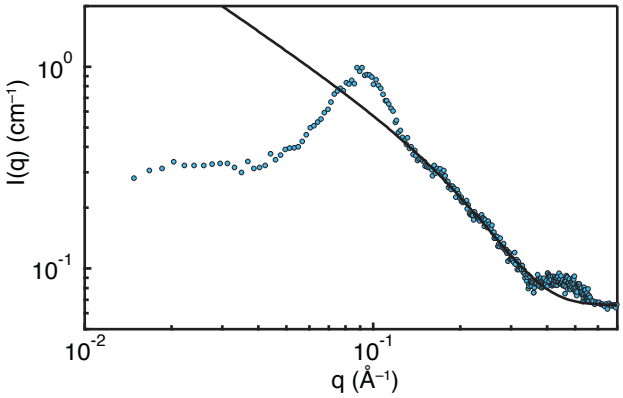

Figure A.1. 1D radially averaged SAXS intensity as a function of q for $c = 2.8$ wt.% fit in the high-q region with the form factor of a rigid rod with a Gaussian radial distribution function.[313] The position of the structure factor peak provides the correlation length between negatively charged PBDT rods, $\xi = 2\pi/q^* = 6.7$ nm. Fitting of the 1D SAXS intensity in the region given by $q > 1.5q^*$ yields a cross-sectional diameter of 0.778±0.008 nm. The deviation from the fit near $q \approx 0.4$ Å^{-1} is due to the intramolecular scattering from the PBDT repeat unit length.[67]

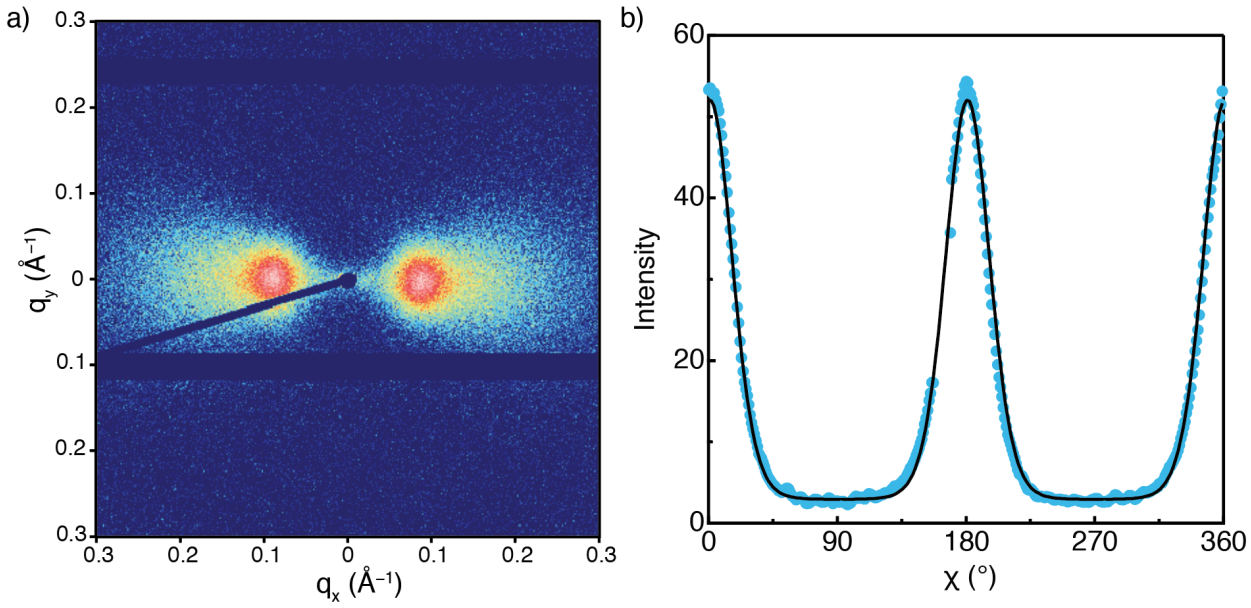

Figure A.2. (a) 2D SAXS pattern of an aligned 2.8 wt.% PBDT solution and (b) 1D azimuthal intensity integrated over the q-range between q = 0.05 – 0.13 Å^{-1} and fit with the Maier-Saupe orientation distribution function.[170] The monodomain was prepared by alignment within a magnetic field, and after removal from the field, the monodomain alignment remained due to confinement within the narrow, cylindrical capillary.[62] The calculated order parameter is $S_{eq} = 0.886 \pm 0.002$.

APPENDIX B: CHAPTER 3 SUPPORTING INFORMATION

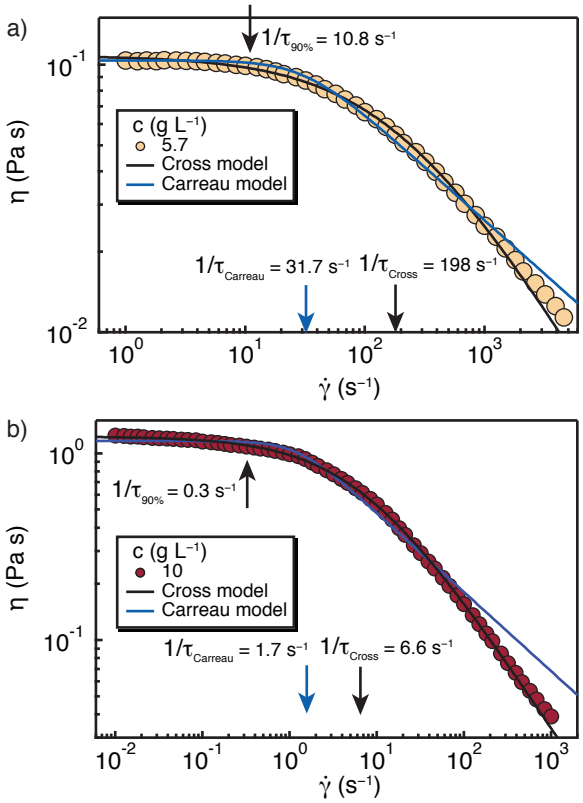

Figure B.1. Determination of the relaxation time by fitting the steady-state flow curve using the Cross model, Carreau model, or a model-independent method using the 90% value of the viscosity for determination of the critical shear rate, and thus the longest relaxation time.

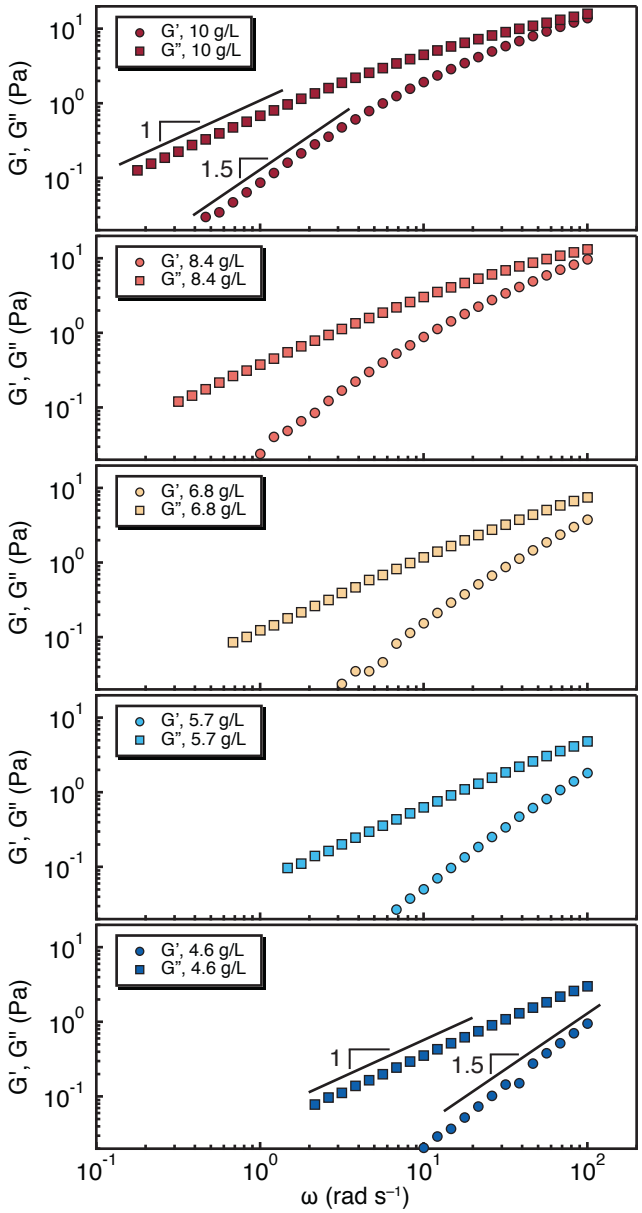

Figure B.2. Linear oscillatory rheology frequency sweeps of G' and G'' within the linear viscoelastic regime (strain amplitude = 10%) at 25 °C. Limiting slopes of G' and G'' are shown in the figure.

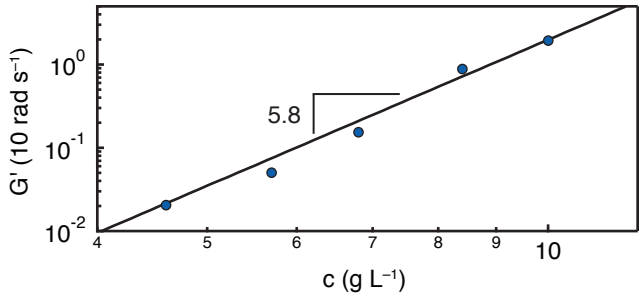

Figure B.3. Concentration scaling of G' at 10 rad s^{-1} of quiescently isotropic PBDT solutions. A power law exponent of 5.8 ± 0.7 is found when fitting the data, shown in the figure.

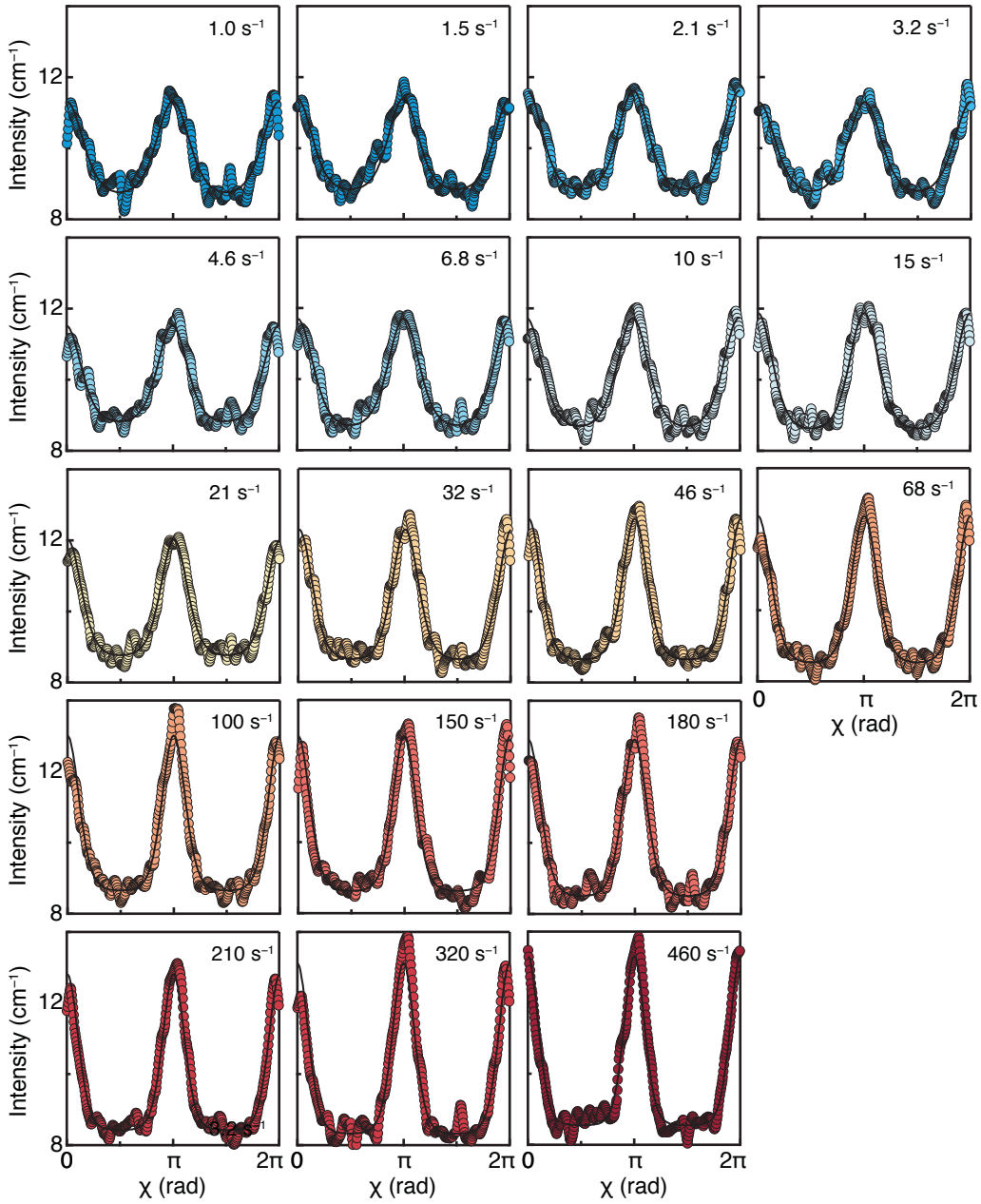

Figure B.4. Intensity as a function of azimuthal angle for the scattering from the rod-rod structure factor peak at various shear rates (listed in the figures) for $c = 21$ g L^{-1} PBDT solution. Solid lines are fits with a Maier-Saupe orientational distribution function.[170]

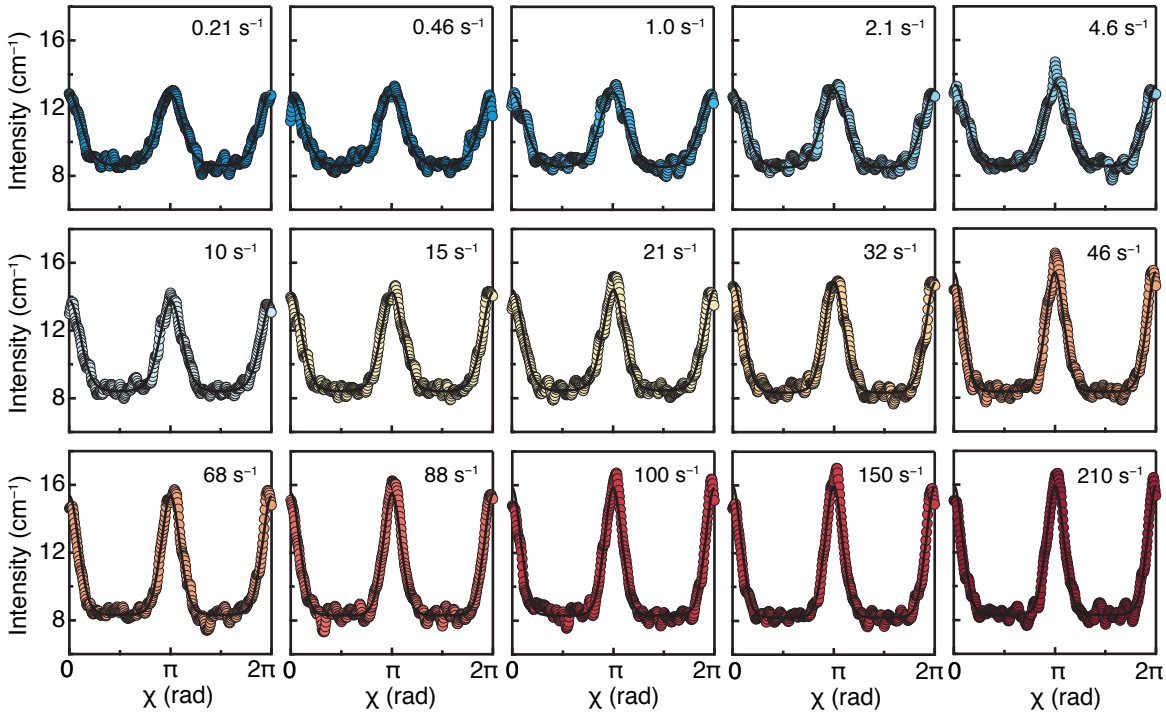

Figure B.5. Intensity as a function of azimuthal angle for the scattering from the rod-rod structure factor peak at various shear rates (listed in the figures) for $c = 30$ g L^{-1} PBDT solution. Solid lines are fits with a Maier-Saupe orientational distribution function.[170]

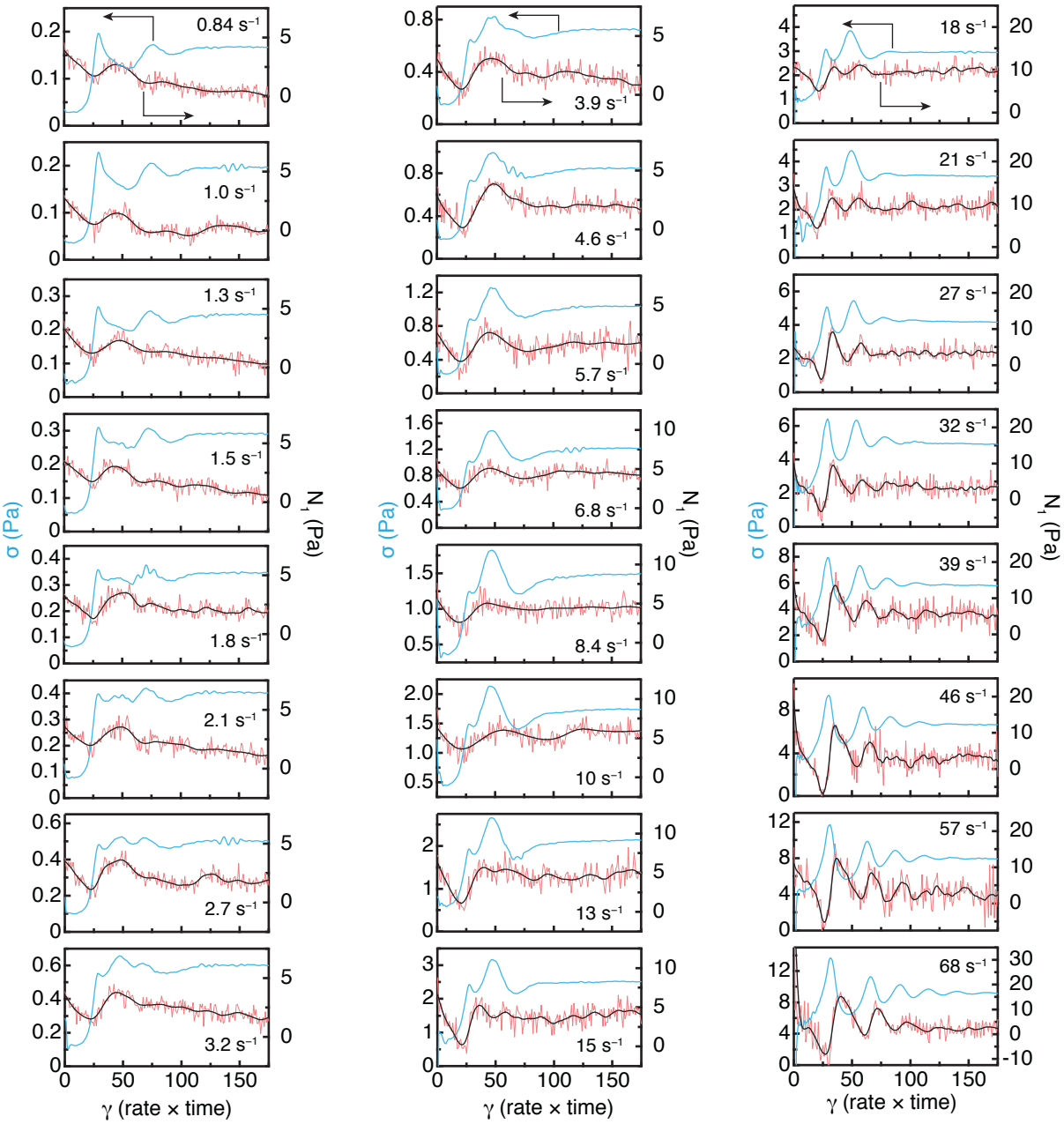

Figure B.6. Transient shear stress (left axes, blue) and N_1 (right axes, red) following step-down from a flow aligned state to shear rates ranging from 0.84 to 68 s^{-1} for a fully nematic $c = 21$ g L^{-1} PBDT solution. Final shear rates are given in the figures. The initial shear rate for all figures is 570 s^{-1}. The N_1 is smoothed and shown as the black lines overlaying the raw N_1 data.

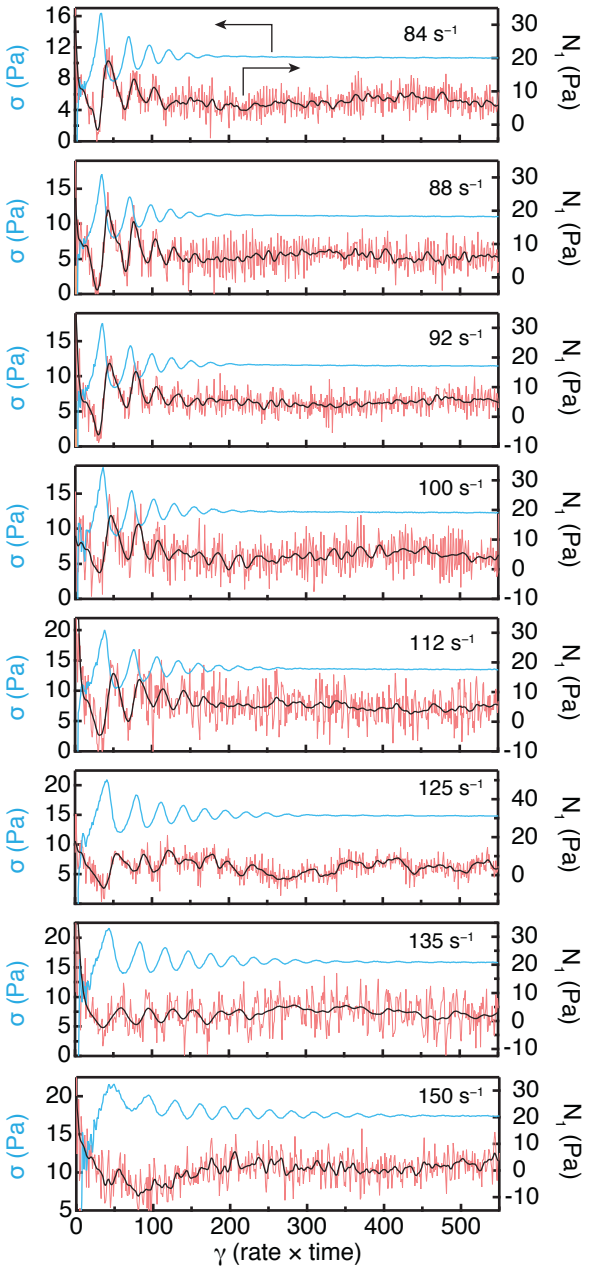

Figure B.7. Transient shear stress (left axes, blue) and N_1 (right axes, red) following step-down from a flow aligned state to shear rates ranging from 84 to 150 s^{-1} for a fully nematic $c = 21$ g L^{-1} PBDT solution. Final shear rates are given in the figures. The initial shear rate for all figures is 570 s^{-1}. The N_1 is smoothed and shown as the black lines overlaying the raw N_1 data.

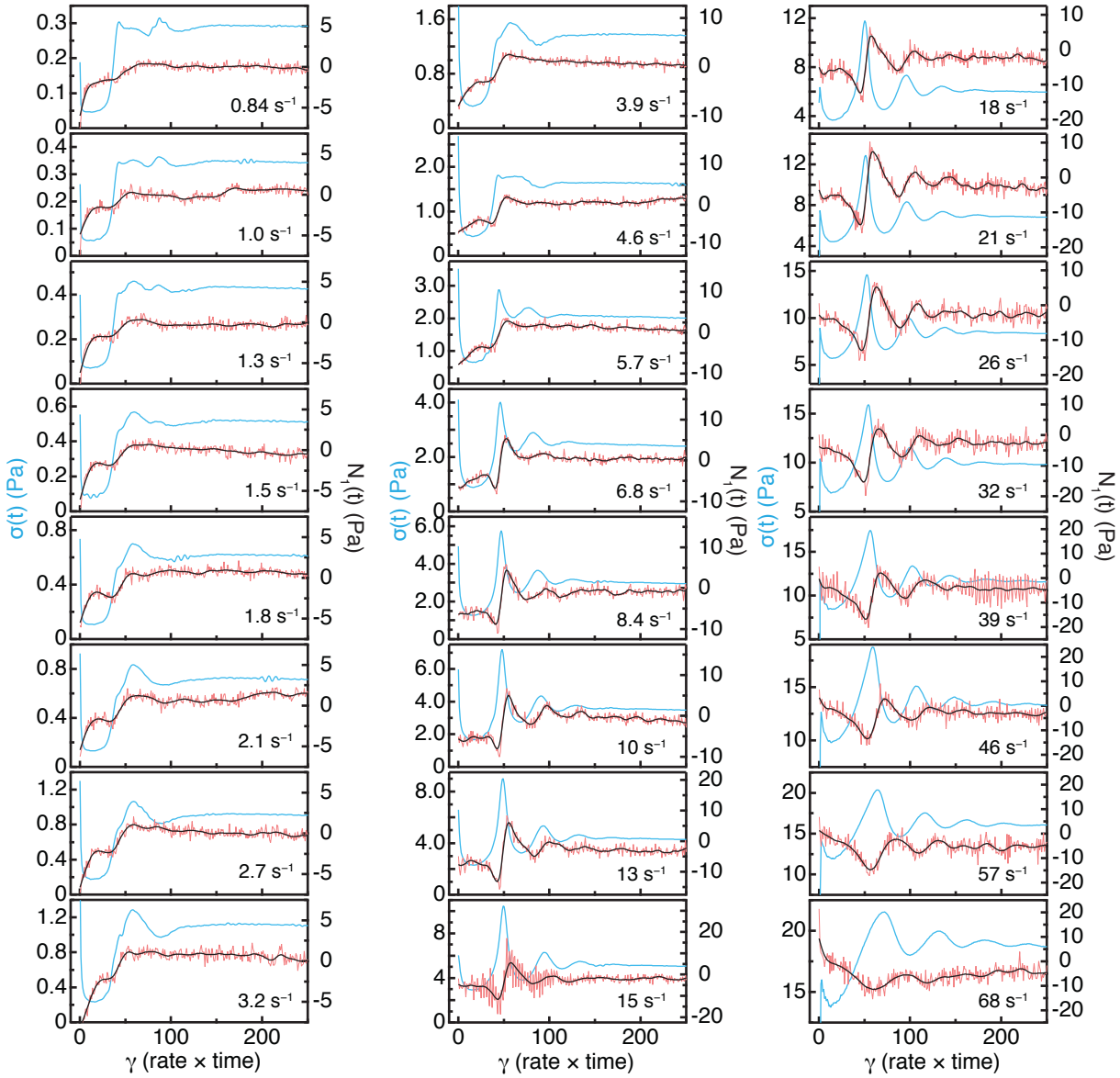

Figure B.8. Transient shear stress (left axes, blue) and N_1 (right axes, red) following shear step-down for $c = 30$ g L^{-1} as a function of strain. The N_1 is smoothed and shown as the black lines overlaying the raw N_1 data.

APPENDIX C: CHAPTER 4 SUPPORTING INFORMATION

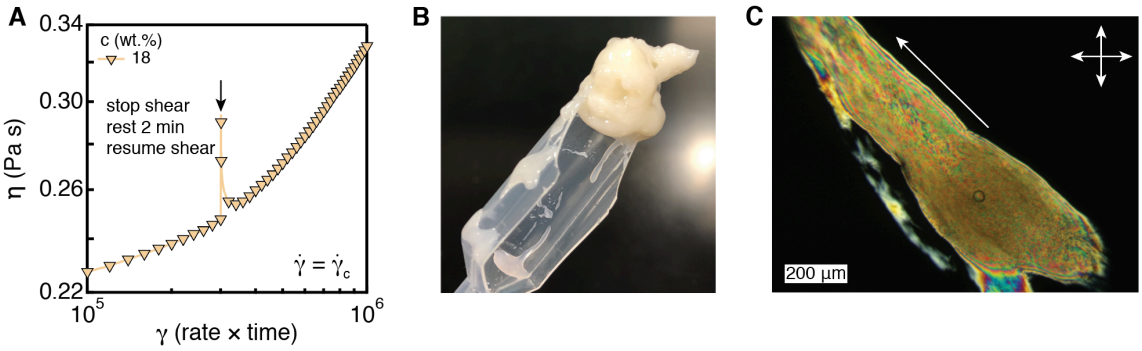

Figure C.1. (A) Transient viscosity of an 18 wt.% PBDT solution at the critical shear rate (1000 s^{-1}) over the strain range of 10^5–10^6. At the point indicated by the arrow, the shear flow was stopped, the solution was allowed to rest for 2 minutes, and then the experiment was resumed. The stress followed the same trend before and after the short rest period, indicating the structure did not relax significantly. Note that the data point density of the transient viscosity is reduced by a factor of 200 for visual clarity. (B) Digital photograph of the 18 wt.% gel as removed from the rheometer after shear-induced gelation. The gel does not flow and can easily be handled, indicating an irreversible structure that does not relax after flow cessation. (C) Polarized optical micrograph of a highly birefringent chaotic multidomain texture microfibril isolated from the shear-induced gel.

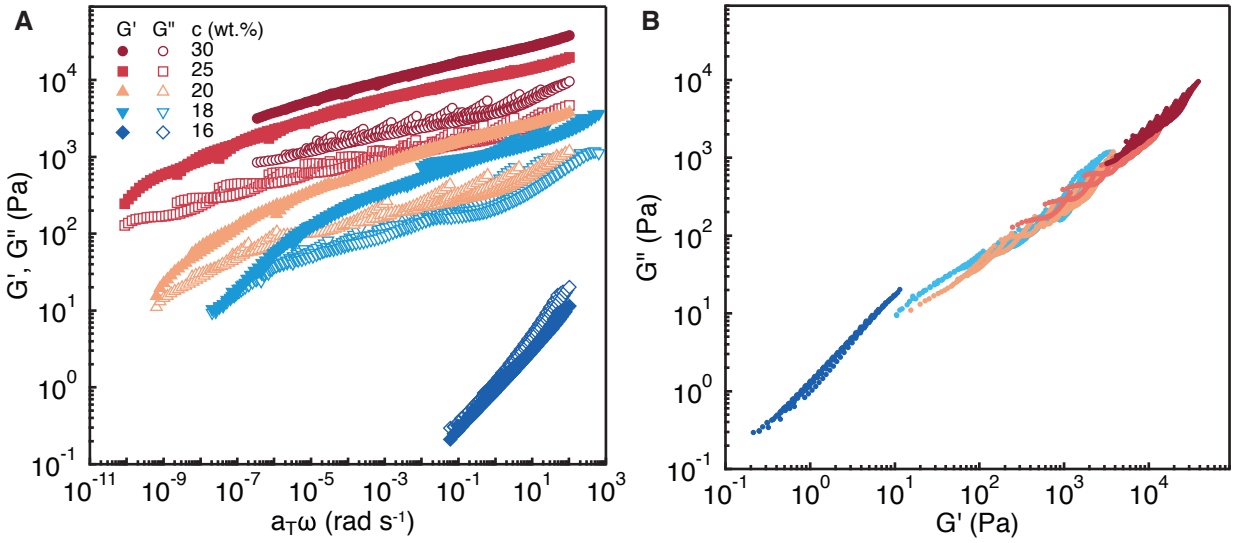

Figure C.2. (A) Master curves from time-temperature superposition (TTS) of shear-induced PBDT hydrogels. (B) Cole-Cole representation of the imaginary (G'') vs real (G') components of the shear

modulus. A semi-circular shape, as expected for a Maxwell fluid with a single relaxation time, is not observed indicating the presence of a spectrum of relaxation times.

Small-Angle X-Ray Scattering. We characterized the solution structure before and after shear-induced gelation using small-angle X-ray scattering (SAXS). The 1D scattering intensity as a function of scattering vector (q) for low viscosity PBDT solutions (pre-shear) and after shear-induced gelation (post-shear) between 14–20 wt.% is given in **Figure C.3**. Qualitatively, the scattering spectra are typical of polyelectrolytes, which exhibit a low-q upturn originating from long wavelength concentration fluctuations, and a broad mid-q structure factor peak (q*) related to the inter-aggregate lateral correlation distance (ξ) through Bragg's law $q^* = 2\pi/\xi$. At higher scattering vector, a sharp peak at q = 0.375 $Å^{-1}$, which is invariant with concentration, corresponds to the 001 reflection of the repeat unit (16.8 Å) is shown in the inset for each concentration.

The correlation length ξ decreases with concentration scaling as $\xi \sim c^{-0.43}$, consistent with prior literature and scaling predictions (**Figure C.4**). The ξ for flexible polyelectrolytes scales as $c^{-0.5}$, and the observed deviation from theoretical predictions may be related to clustering effects.[60] The shape and position of the structure factor is independent of shear history, indicating the local spatial correlations and lateral dimensions of rodlike aggregates do not change upon shear-activated gelation. However, we observe two distinct changes in the scattering spectra after gelation: (i) the low-q intensity increases, and (ii) the 001 reflection is suppressed and broadened. The increase in low-q scattering intensity is rationalized by an increase in the spatial heterogeneity of polymer concentration due to non-spatially uniform growth of PBDT rodlike assemblies.

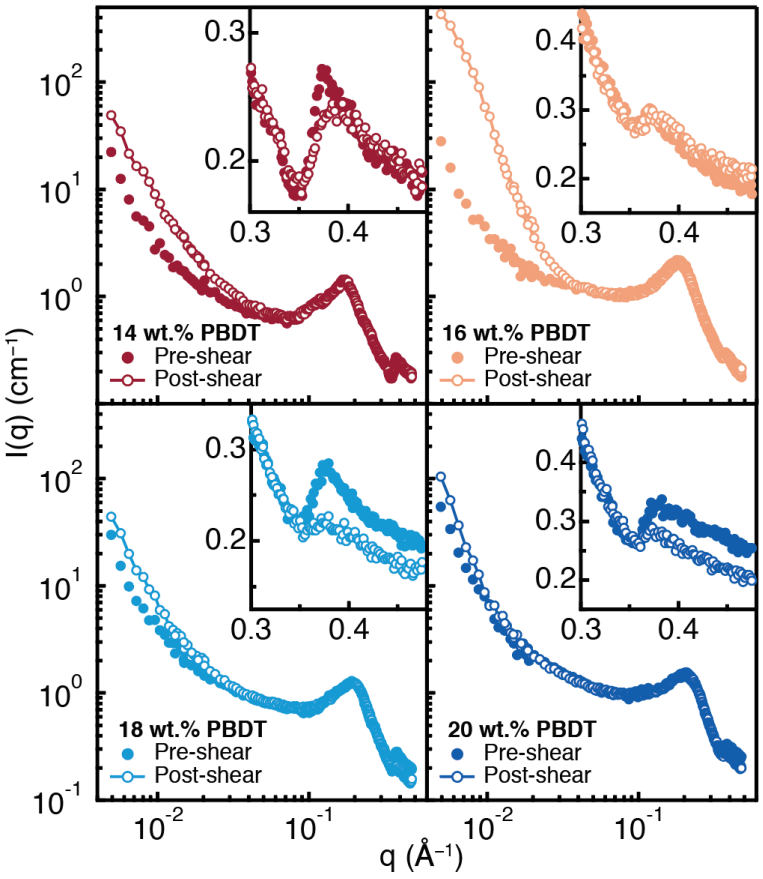

Figure C.3. Small-angle X-ray scattering (SAXS) intensity as a function of scattering vector (q) of PBDT low-viscosity solutions (pre-shear, filled circles) and shear-induced gels (post-shear, open circles) for various PBDT concentrations spanning the onset of shear-induced gelation. The 001 reflection of the repeat unit is given in the insets for each concentration.

The 001 reflection, shown in the inset for each concentration in **Figure C.3**, is present due to the linear regularity of electron density along the polymer backbone from the stiffness of sulfonated all-aromatic LCPs in water.[55] The sharpness of the 001 reflection and relative intensity is suppressed and broadened after shear-induced gelation. We interpret this result to be due to a decrease in the local linearity of PBDT chains after shear-induced gelation. The increased conformational flexibility may enable an increase in inter-aggregate connectivity, promoting a macroscopic gel network. However, conclusive determination regarding local

polymer structure and conformation before and after shear-induced gelation will require more detailed investigation.

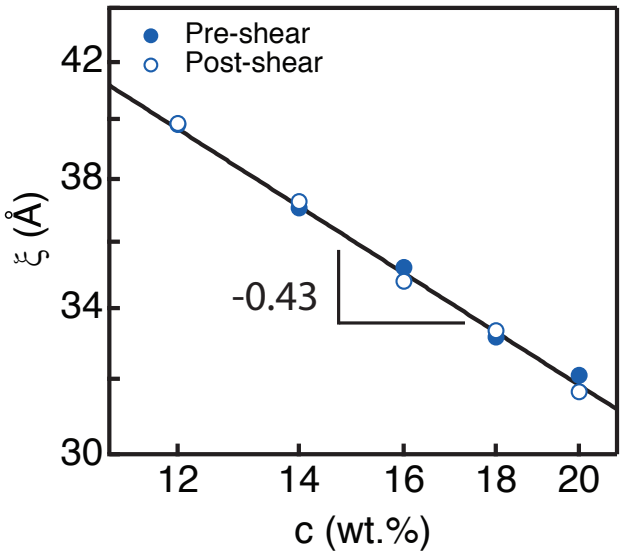

Figure C.4. Correlation length for PBDT solutions and shear-induced gels as a function of concentration pre-shear (*filled circles*) and post-shear (*open circles*). The lack of change after shear-induced gelation indicates the diameter of the PBDT-RAs do not change. A power law with an exponent of –0.43 fits the data in agreement with prior literature, slightly less than the scaling prediction of –0.5.[43]

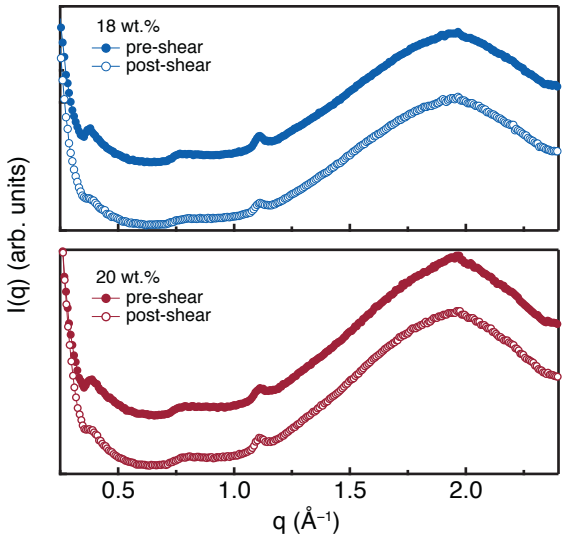

Figure C.5. Wide-angle X-ray scattering spectra of PBDT solutions pre-shear (*filled circles*) and post-shear (*open circles*) at 18 wt.% (*top*) and 20 wt.% (*bottom*). The curves have been shifted by an arbitrary scale factor to ease comparison. The scattering peak at large q related to the $\pi - \pi$ distance of PBDT chains is unchanged and no evidence of shear-induced crystallization is observed. The scattering peaks associated with the 001, 002, and 003 reflections of the PBDT repeat unit are suppressed in the post-shear gels, suggesting a decrease in linearity of the chain.

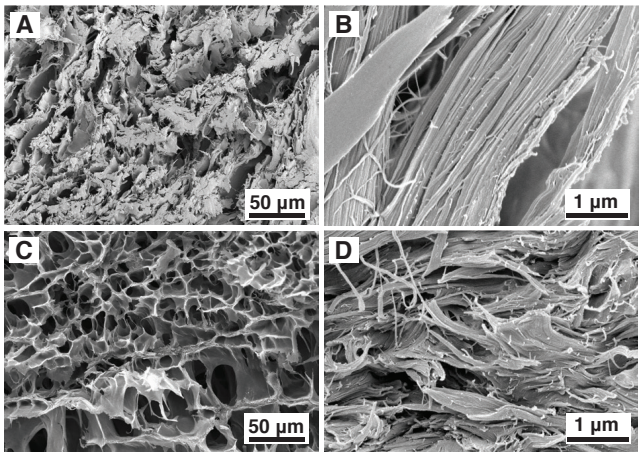

Figure C.6. Scanning electron microscopy (SEM) images of the cross-section surface of a freeze-fractured 16 wt.% PBDT sample **(A, B)** pre- and **(C, D)** post-shear. An open-cell structure consistent with network formation is observed in the post-shear gels. The local fibrillar structure appears more disordered in the post-shear gels.

Effect of Monovalent Salt. We investigated the role of electrostatics on the solution structure and rheological properties of PBDT rods through addition of monovalent salt. The rods are characterized by a hard-core diameter $d \approx 0.8$ nm and effective diameter d_{eff} due to the electrostatic repulsions between rod segments, depicted in **Figure C.7a**, found as $d_{eff} = 2\pi/q^*$, where q^* is the location of the scattering peak.[314] Upon addition of monovalent electrolyte (NaCl) reduces d_{eff} and suppresses the rod-rod positional correlation through charge screening.[315] Salt addition also likely increases the contour length of the rods in dynamic equilibrium,[235, 316] and reduces the total persistence length l_p through a reduction in the electrostatic persistence length.[317-318] A reduction in l_p for PBDT rods is consistent with our observation that birefringence is eliminated at an equimolar salt-to-sulfonate concentration for initially biphasic 3 wt.% solution, consistent with prior literature.[58]

We present small-angle X-ray scattering (SAXS) spectra of a 3 wt.% PBDT solution in **Figure C.7b**. In salt-free conditions, the structure factor peak is present that is progressively suppressed with increasing molar ratio of NaCl to monomeric sulfonates. The solid lines are fits to the high-q region of the spectra with the form factor of a rigid-rod with infinite length and finite d, and Gaussian monomer radial distribution function.[313] We find that d increases from 8.36 ± 0.09 Å in salt-free solution to 9.11 ± 0.07 Å at molar ratios of salt greater than 0.1, likely from increasing tendency of counterions to condense along the backbone.[319]

The flow curves for these solutions with added salt, i.e., viscosity versus shear rate, evidence a physically entangled network that exhibits high viscosity and strong shear thinning (slope −0.77), but without a yield stress (slope −1) in **Figure C.7c**. In contrast, salt-free PBDT solutions exhibit low viscosity and a nearly Newtonian viscoelastic response. No hysteresis occurs when the shear rate was increased or decreased, in contrast to the irreversible gelation due to shear at high PBDT concentrations.

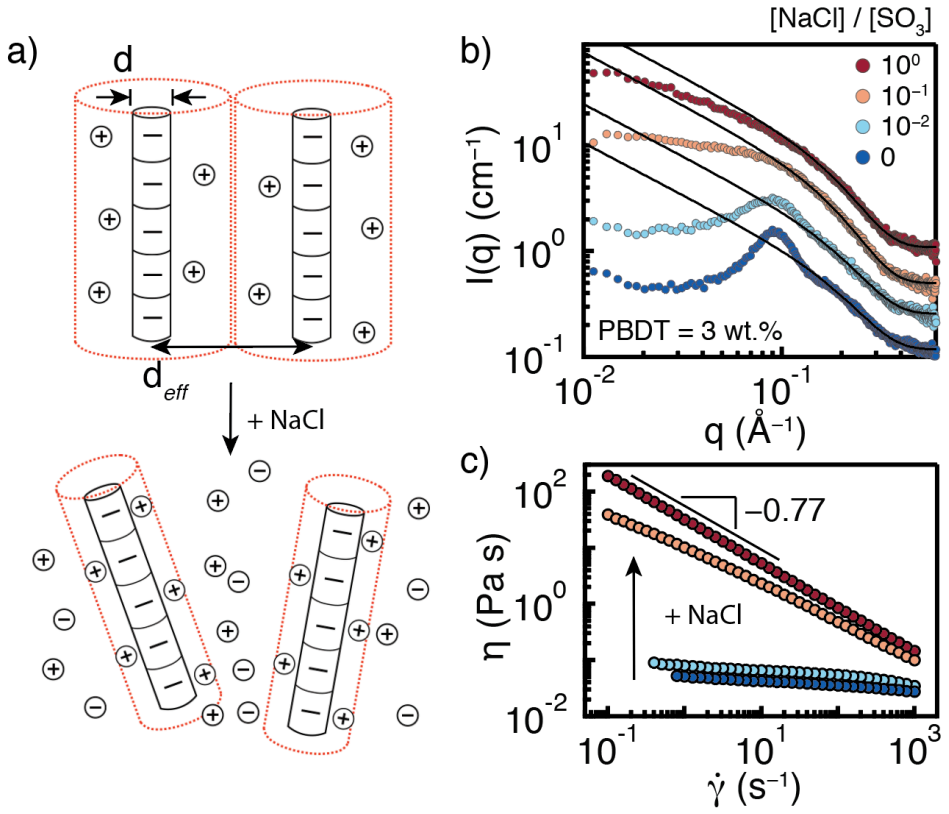

Figure C.7. Effect of salt on the structure and nonlinear rheology of PBDT solutions. (a) Depiction of the intermolecular electrostatic interactions that exist between salt-free, semidilute PBDT rods. Addition of a monovalent salt, NaCl, screens the rod-rod electrostatic interactions. (b) 1D SAXS intensity and (c) steady-state viscosity as a function of shear rate for 3 wt.% PBDT solutions in salt-free water and increasing amounts of NaCl. The molar ratio of NaCl to sulfonic acid groups is given in the legend of (b). 1D SAXS intensity curves were offset by a factor of 3, 6, and 10 for [NaCl]/[SO_3] ratios of 10^{-2}, 10^{-1}, and 10^{0}, respectively.

APPENDIX D: CHAPTER 5 SUPPORTING INFORMATION

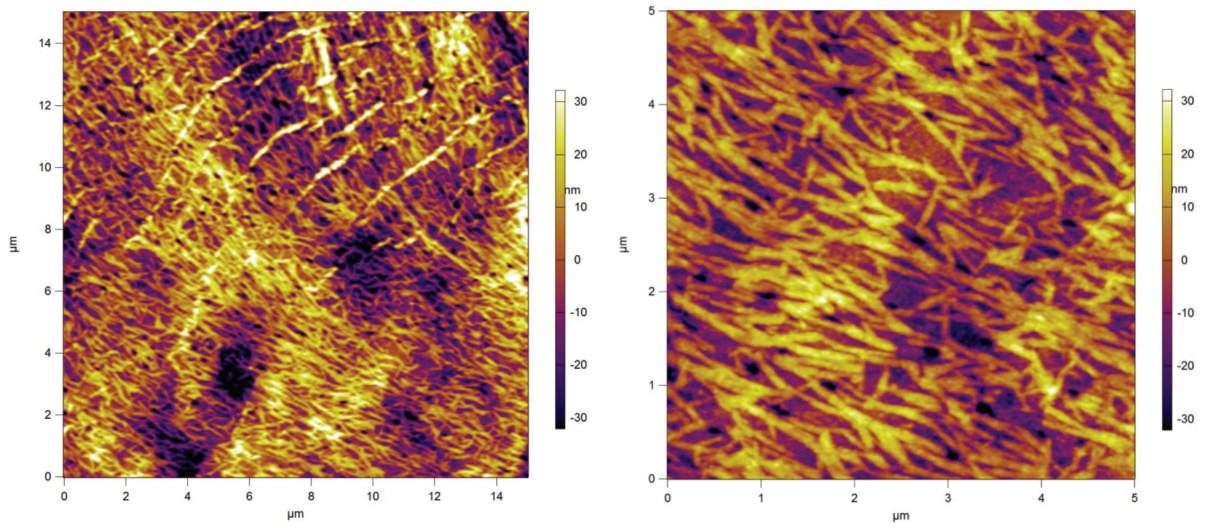

Figure D.1. Tapping mode atomic force microscopy (AFM) of neat PBDT film revealing slender nanofibers with cross-sectional dimension between 50 and 200 nm. Measurement provided courtesy of Dr. Daniel P. Cole, Army Research Laboratory.

Reduction of Graphene Oxide *Ex-Situ*. Thermogravimetric analysis (TGA) was used to determine the thermal stability and amount of labile oxygen functionality of the as-synthesized LCGO. A scanning TGA at 10 °C min^{-1} of the as-prepared graphene oxide is shown in **Figure D.2A**. Below 150 °C, the weight loss observed is primarily residual water evaporation. Between approximately 180 °C and 250 °C, a sharp reduction in weight (~30%) was observed corresponding to a partial reduction of GO to rGO. To investigate the kinetics of the main reduction event occurring around 200 °C, we first dried a sample of GO at 120 °C until weight stabilization, eliminating most of the residual water. The sample was brought to 200 °C, held for 2 h isothermally and the weight was recorded as a function of time. As seen in **Figure D.2B**, within 20 min at 200 °C the weight loss was approximately 30% and did not significantly reduce at longer times. X-ray photoelectron spectroscopy (XPS) of the as-synthesized and thermally

reduced GO films confirmed the partial reduction of GO to reduced GO (rGO), increasing the C/O ratio from approximately 2.6 to 6.5, respectively.

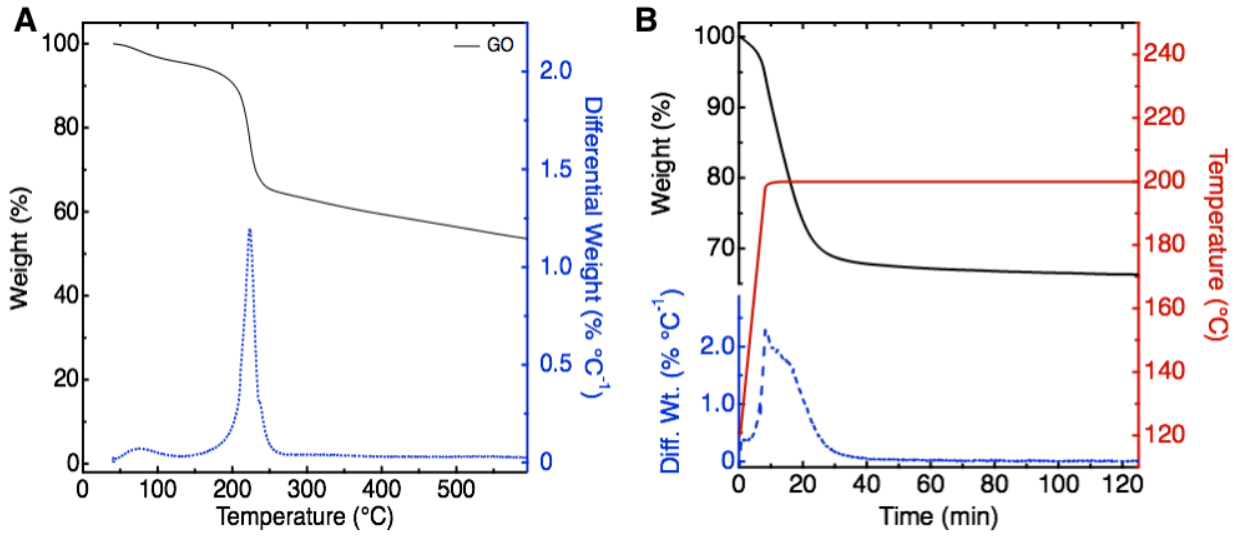

Figure D.2. Thermogravimetric analysis of GO used in this study. (A) Scanning TGA at a heating rate of 10 °C min^{-1} under N_2 atmosphere. (B) Isothermal hold at 200 °C after being dried at 120 °C.

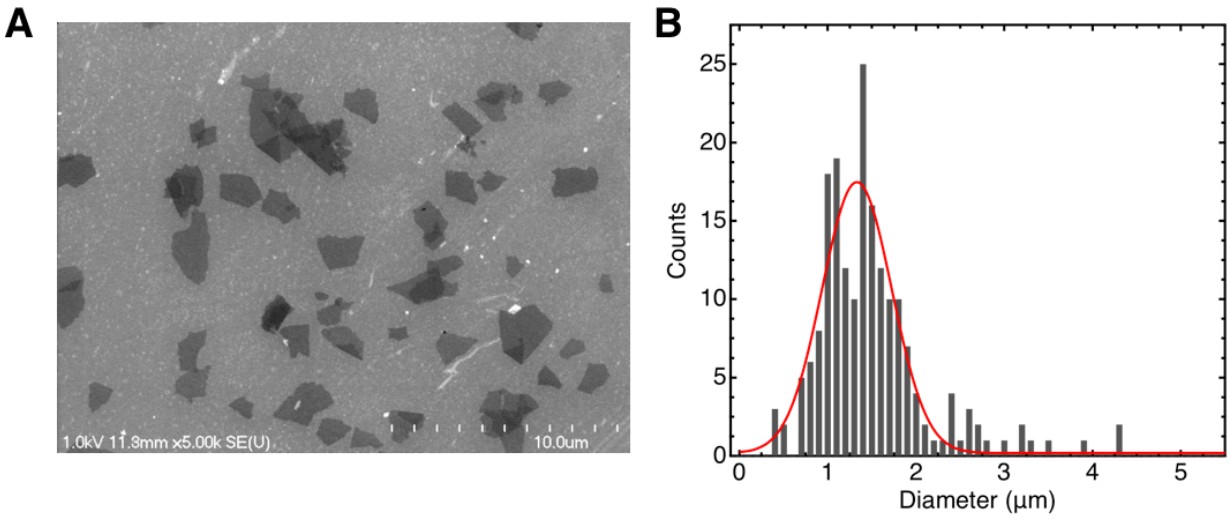

Figure D.3. (A) Representative SEM image of GO flakes deposited onto a Si wafer, and (B) equivalent diameter flake size distribution for 196 individual flakes LCGO after centrifugation purification.

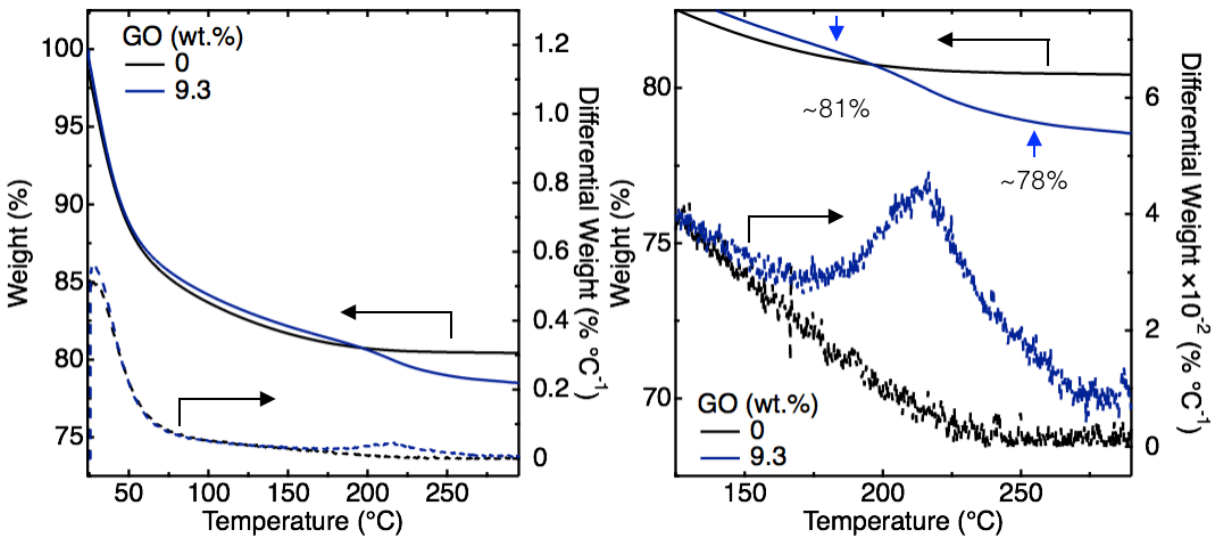

Figure D.4. Scanning thermogravimetric analysis (TGA) at 10 °C min^{-1} of PBDT-LCGO nanocomposite films after drying at 60 °C in air. Below ~180 °C, water is expelled from the sample due to the hydrophilic nature of PBDT and GO. Examination of the weight loss from 180 to 250 °C of a 9.3 wt.% PBDT-GO film shows a ~30% weight loss due to GO reduction, in agreement with *ex-situ* measurements and confirming *in-situ* reduction of GO to rGO.

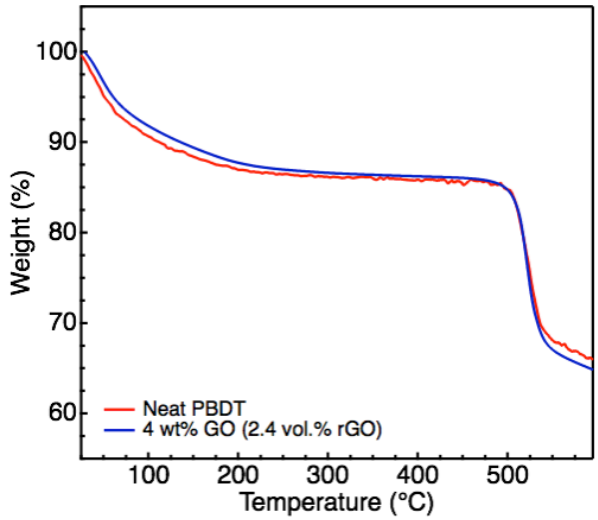

Figure D.5. Scanning TGA of a neat PBDT and 4 wt.% GO (2.4 vol.% rGO) nanocomposite film at 10 °C min^{-1}. The maximum degradation temperature is unchanged for the nanocomposite as compared to the neat polymer.

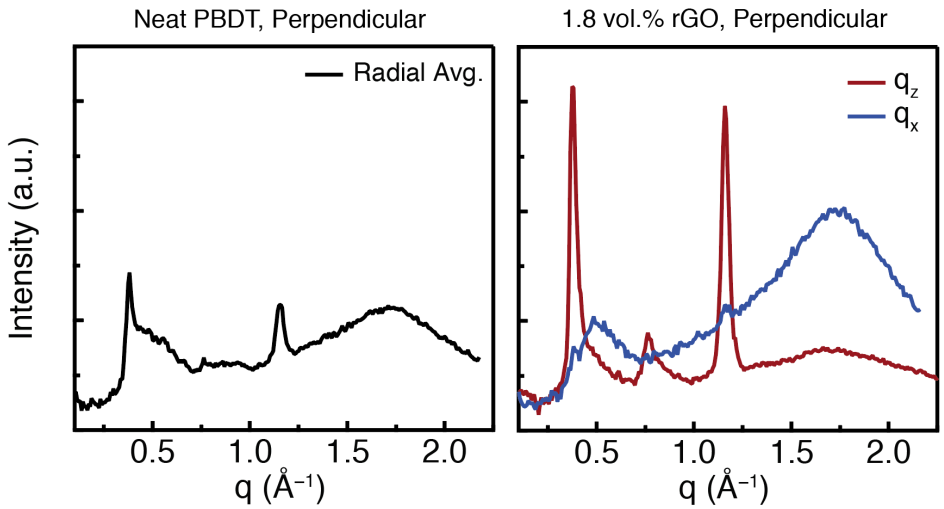

Figure D.6. 1D WAXS lineouts of a neat PBDT film (radially averaged, *left*) and a 1.8 vol.% rGO nanocomposite film with 30° sector averages along the q_z and q_x directions (*right*). Both figures have the same axes scaling.

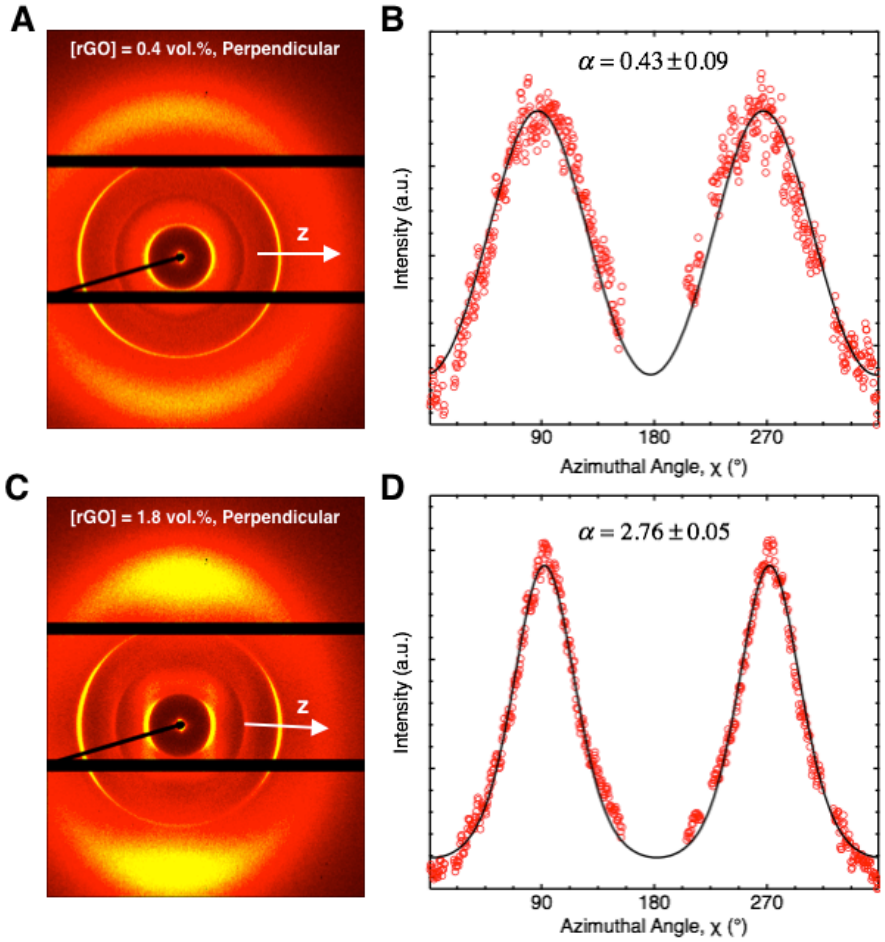

Figure D.7. Representative 2D WAXS patterns of PBDT-rGO nanocomposite films in the perpendicular configuration. The film's z-axis (along direction of shear casting) is indicated by the arrow. The scattering intensity is shown on a linear scale. **(A, C)** WAXS pattern and **(B, D)** azimuthal fitting using for a 0.4 vol.% and 1.8 vol.% PBDT-rGO nanocomposite film, respectively. The alpha parameter is a measure of the width of the intensity distribution as a function of azimuthal angle and is used to calculate the experimental order parameter. Integration around the azimuthal begins at the black line and rotates clockwise in the 2D scattering patterns.

Arrhenius Analysis of β-Relaxation

Following the treatment by Starkweather,[320-322] the frequency of a secondary polymer relaxation event (f) can be described by an Arrhenius law, given as

$$f = A \exp\left(\frac{-E_a}{RT}\right) \qquad \textbf{(Eqn. D.1)}$$

where A is a pre-exponential factor, E_a is the activation energy of the transition, R is the gas constant, and T is the absolute temperature. Linearization of **Equation D.1** allows determination of the relaxation activation energy by plotting natural logarithm of the mechanical oscillation frequency as a function of the inverse temperature at the loss peak maximum. Alternatively, a relationship derived from the theory of absolute reaction rates can be used

$$f = \frac{k_B T}{2\pi h} \exp\left(\frac{-\Delta H^*}{RT}\right) \exp\left(\frac{-\Delta S^*}{R}\right) \qquad \textbf{(Eqn. D.2)}$$

where k_B is the Boltzmann constant, h is Planck's constant, ΔH^* and ΔS^* are the activation enthalpy and entropy, respectively. The relationship between the activation energy and activation enthalpy is given by $E_a = \Delta H^* + RT$, which allows the activation energy for a secondary relaxation to be expressed as

$$E_a = RT'\left[1 + ln\left(\frac{k_B T}{2\pi h f}\right)\right] + T\Delta S^* \qquad \textbf{(Eqn. D.3)}$$

with all variables as defined previously. For simple and non-cooperative secondary thermal relaxations, $\Delta S^* = 0$, and the relationship between the activation energy and transition temperature is nearly a linear function.[322] The difference between the calculated zero entropy activation energy from **Eqn. D.3** and experimentally measured activation energy yields $T\Delta S^*$. Simple and non-cooperative relaxations are characterized by low (<30 J mol^{-1} K^{-1}) activation entropy, and complex and cooperative secondary relaxations yield high (>80 J mol^{-1} K^{-1}) values of activation entropy.

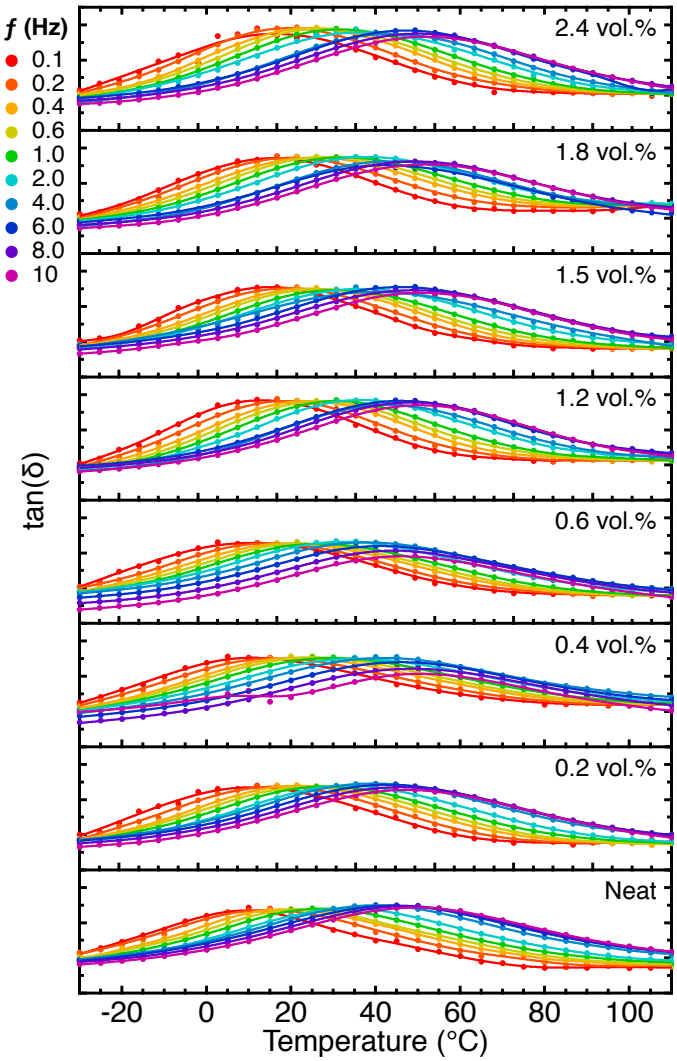

Figure D.8. Loss tangent over the temperature range of –30 to 110 °C in 5 °C intervals from 0.1 to 10 Hz. The solid lines are smoothing interpolation curves used for determination the peak loci by linear regression of the zero intercept of the derivatives. All vertical axes in each figure are scaled from 0 to 0.035. The concentration of rGO is given in each figure.

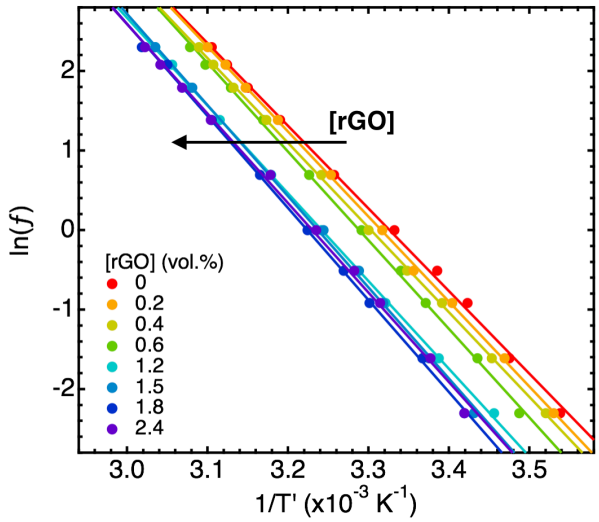

Figure D.9. Arrhenius plots of the natural logarithm of mechanical oscillation frequency as a function of inverse absolute temperature of the maximum loss tangent loci over the β-relaxation temperature range. Linear fits indicate agreement with the Arrhenius function for this thermal relaxation. The peak loss tangent temperature is shifted to higher temperatures with increasing rGO concentration.

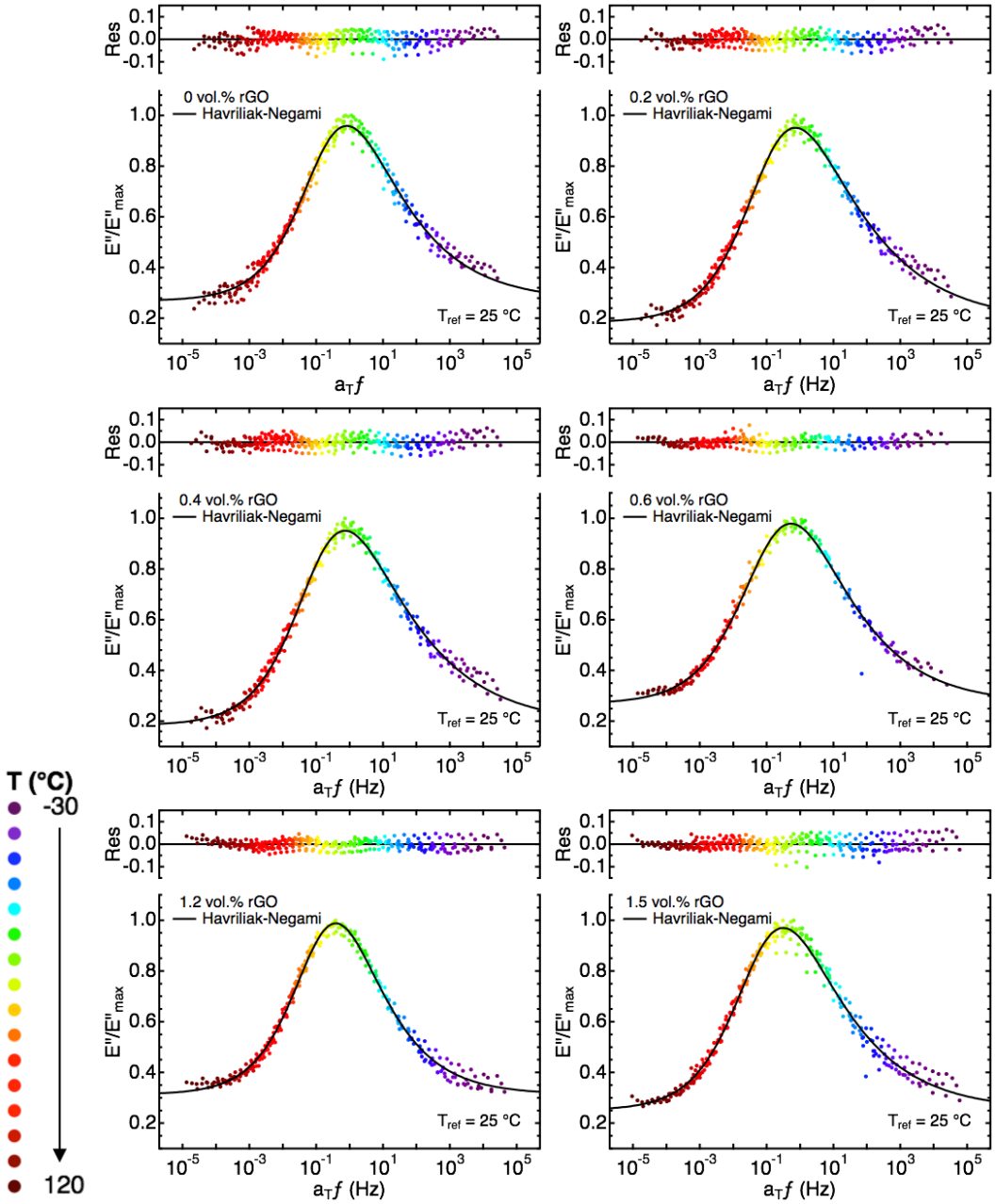

Figure D.10. Fitting and residuals of the β-relaxation using the Havriliak-Negami function for the loss modulus master curves obtained by horizontal shifting. The colors correspond to the measurement temperature used. No vertical shift factor was used for master curve construction. The horizontal shift factor was calculated using the activation energy obtained from slopes of the Arrhenius analysis.

Dilute Solution Viscometry

Molecular weight characterization of charged polymers is complicated by the polyelectrolyte effect, which causes chain expansion in dilute solution.[323] We used 96% sulfuric acid as a solvent to molecularly dissolve PBDT, as done for intrinsic viscosity determination of PPTA.[324] The reduced viscosity as a function of concentration for PBDT and a commercial sample of PPTA (Teijin Aramid, η_{inh} = 5.1), shown for comparison, is presented in **Figure D.11**, and summarized in **Table D.1**. We measured a commercially available PPTA sample to confirm validity of the Mark-Houwink parameters used in calculation of viscosity average molecular weight for PBDT. The reduced viscosity of both polymers was well described by the Huggin's Equation, given by

$$\eta_{red} = \eta_{sp}\, c^{-1} = [\eta] + K_H[\eta]^2 c \qquad \textbf{(Eqn. D.4)}$$

where η_{red} is the reduced viscosity, $\eta_{sp} = \frac{t-t_o}{t_o}$ is the specific viscosity, where t and t_0 are the solution and solvent flow time, respectively, c is the mass concentration, $[\eta]$ is the intrinsic viscosity, and K_H is the Huggin's coefficient.[323] Extrapolation to zero concentration yields the intrinsic viscosity and the slope allows determination of the Huggin's coefficient. The measured intrinsic viscosity for PBDT was 3.0 ± 0.1 dL g^{-1}, as compared to 6.1 ± 0.1 dL g^{-1} for the commercial PPTA sample. Using Mark-Houwink parameters for PPTA in 96% sulfuric acid,[261] a viscosity average molecular weight of approximately 19 kg mol^{-1} and 34 kg mol^{-1} is estimated for the PBDT and PPTA samples measured, respectively. These values are consistent with our previous publication for the molecular weight of PBDT[65] and that reported for PPTA[324] ($\eta_{inh} \approx$ 5.1) which were both characterized by size exclusion chromatography in 100% sulfuric acid.

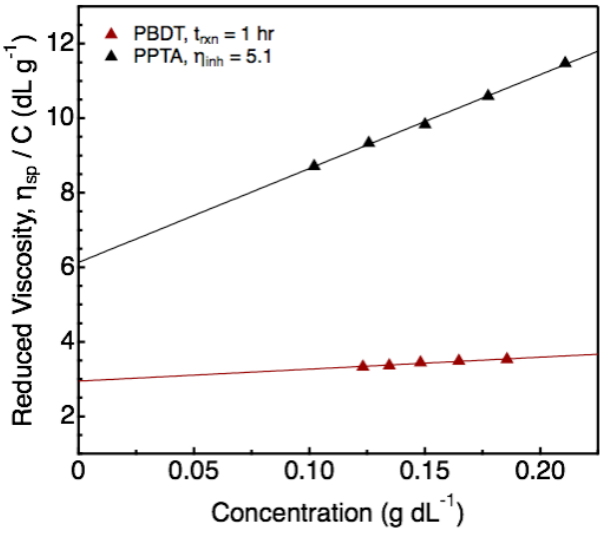

Figure D.11. Dilute solution viscometry of PBDT and PPTA in 96% sulfuric acid at 25 °C. The reduced viscosity as a function of mass concentration is fit to the Huggin's equation, and extrapolation to the y-intercept yields the intrinsic viscosity.

Table D.1. Properties of commercially available PPTA and the PBDT used in this study obtained by dilute solution viscometry in concentrated (96%) sulfuric acid. [a]Provided by Teijin Aramid. [b]Estimated using the Mark-Houwink equation parameters for PPTA (K = 2.14 x 10^{-5}, a = 1.203).[261]

Polymer	η_{inh} (dL g^{-1})[a]	[η] (dL g^{-1})	K_H	M_v (kg mol^{-1})[b]
PPTA	5.1	6.1±0.1	0.67±0.04	34.4±0.5
PBDT	-	3.0±0.1	0.37±0.06	19.0±0.5

APPENDIX E: CHAPTER 6 SUPPORTING INFORMATION

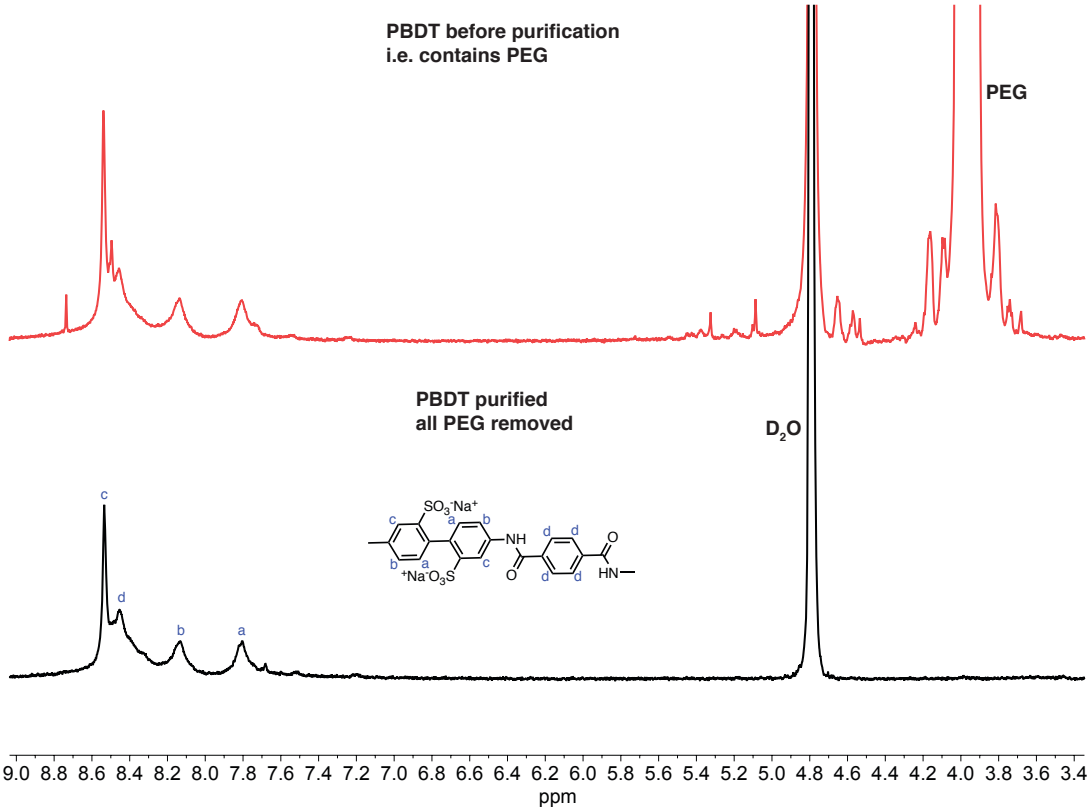

Figure E.1. ^{1}H NMR spectra of 0.1 wt.% PBDT in D_2O directly after synthesis (*top*) and after purification by washing with water/acetone (*bottom*), confirming the removal of PEG300 used during synthesis. The aromatic protons observed are assigned to the chemical repeat unit of PBDT.

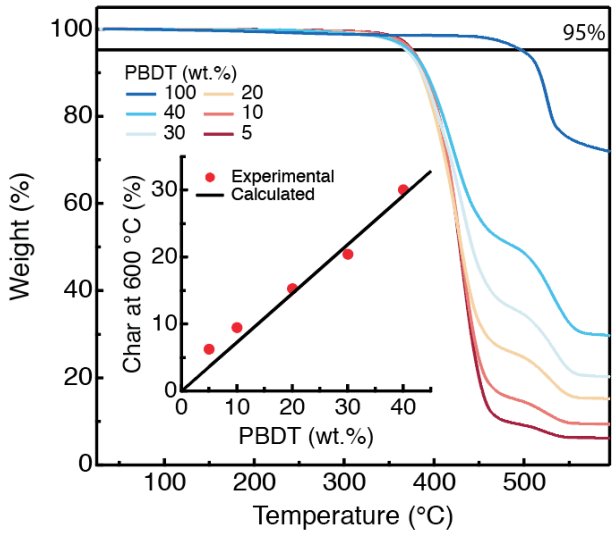

Figure E.2. TGA of neat PBDT and corresponding composites, exhibiting superior thermal stability. The horizontal line indicates the 5% mass loss temperature, which is >350 °C for all composites. The inset shows the calculated and experimental char weight at 600 °C assuming a 27 wt.% loss of PBDT at 600 °C.

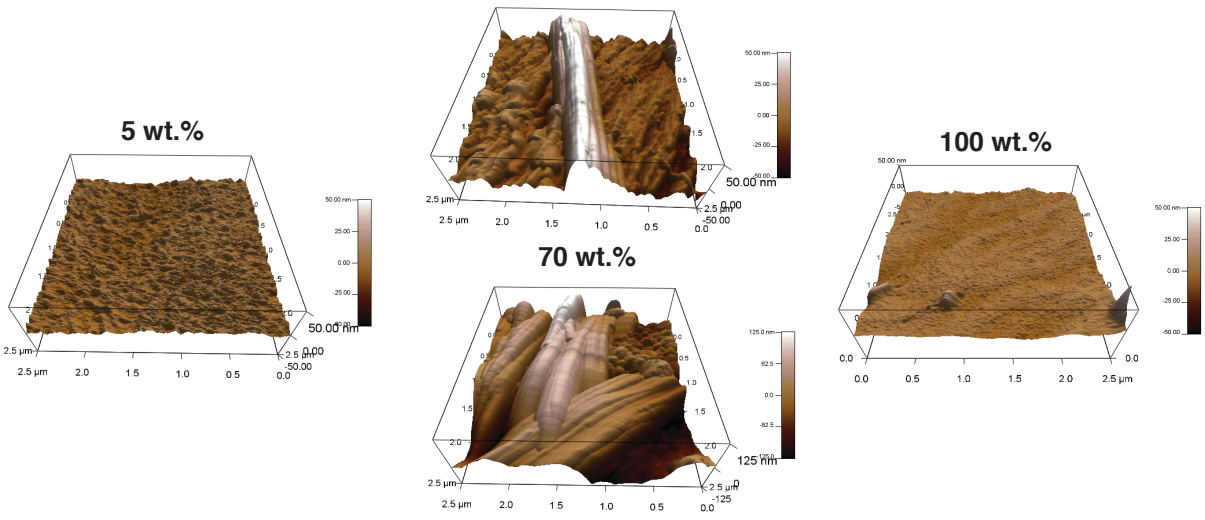

Figure E.3. AFM 3D topological scans of a 5 (left) and 70 (middle) wt.% PBDT-IL composite compared to the 100 wt.% PBDT material (right).

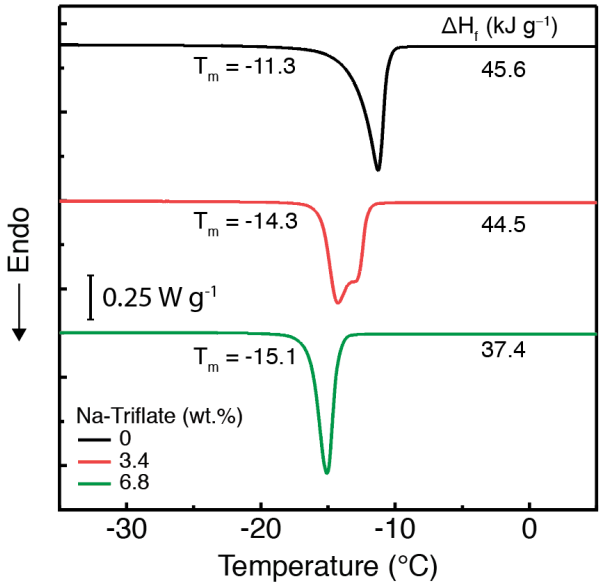

Figure E.4. DSC 2nd heat thermograms at a rate of 2 °C min^{-1} for neat [Emim][TfO] and with 3.4 and 6.8 wt.% of [Na][TfO]. The sample has been heated to 200 °C to fully eliminate water and erase the thermal history. The melt peak temperature shifts to lower temperatures with increasing Na^+ concentration. The melt endotherm does not exhibit significant peak splitting and broadening, as observed in microphase separated PBDT-IL composites, consistent with single phase behavior.

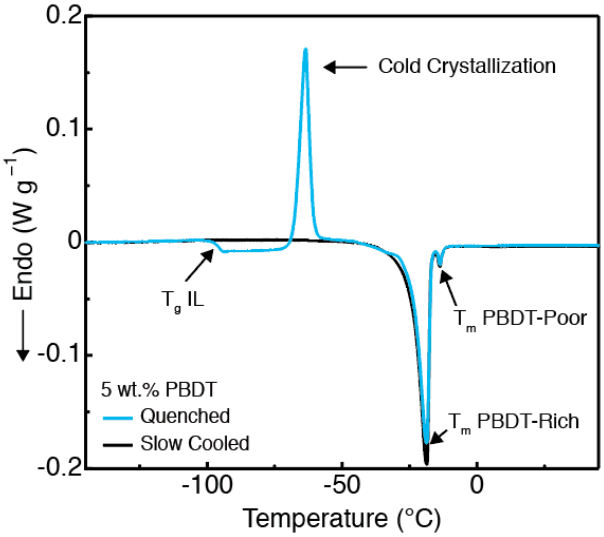

Figure E.5. DSC thermograms of a 5 wt.% PBDT-IL composite at a heating rate of 2 °C min^{-1}. The sample has been heated to 200 °C to fully eliminate water and erase thermal history. The blue curve has

been quenched rapidly to prevent IL crystallization in order to observe amorphous IL behavior. The T_g, cold crystallization, and subsequent melt endotherms can be clearly observed. The black curve has been slow cooled to allow the IL to crystallize (~82% at 5 wt.% PBDT) and has no measurable T_g. The double melt endotherm behavior and total melt enthalpy for both heating ramps are the same, indicating we are observing near-equilibrium thermal behavior.

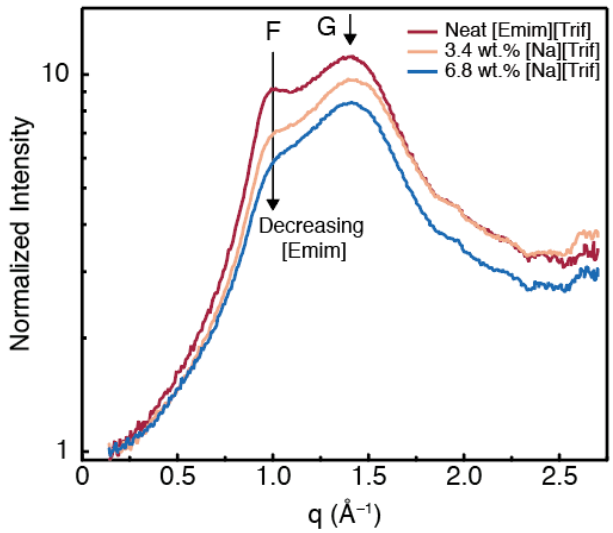

Figure E.6. WAXS of neat [Emim][TfO] and with the addition of 3.4 and 6.8 wt.% [Na][TfO]. The spectra of the neat IL is characterized by a double topped feature composed of a main peak (peak G in main text) at 1.41 $Å^{-1}$ and a minor peak (peak **F** in main text) at 1.00 $Å^{-1}$. The minor peak corresponds to [Emim]-[Emim] spatial correlations, and replacement of [Emim] with small amounts of Na^+ ions reduces its' relative intensity.

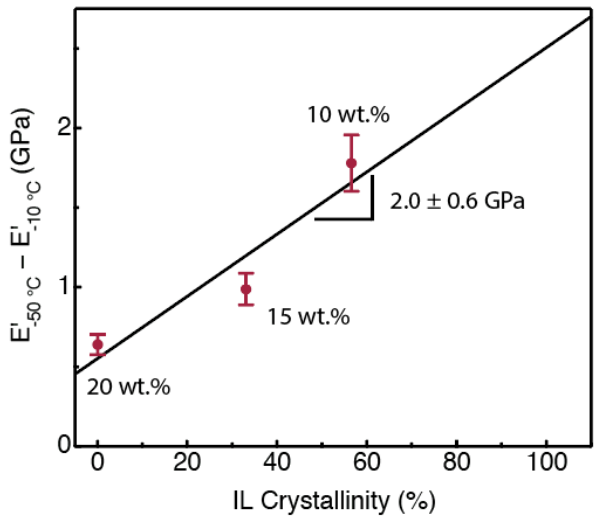

Figure E.7. Decrease in E' from −50 to −10 °C as a function of IL crystallinity. The concentrations for each data point correspond to the PBDT mass loading. The slope of the linear fit is the effective modulus the IL crystal. Error bars are shown as 10% of measured E' value.

REFERENCES

1. Liu, Y.; Chen, W. R.; Chen, S. H., Cluster formation in two-Yukawa fluids. *J Chem Phys* **2005,** *122* (4), 44507.

2. Chandler, D.; Weeks, J. D., Equilibrium Structure of Simple Liquids. *Phy. Rev. Lett.* **1970,** *25* (3), 149-152.

3. Stewart, G. T., Liquid Crystals in Biological Systems. *Molecular Crystals* **1966,** *1* (4), 563-580.

4. Stewart, G. T., Liquid Crystals of Lipid in Normal and Atheromatous Tissue. *Nature* **1959,** *183*, 873-875.

5. Gennes, P. G. d.; Prost, J., *The Physics of Liquid Crystals*. 2nd ed.; Oxford University Press: 1978.

6. Doi, M.; Edwards, S. F., *The Theory of Polymer Dynamics*. Oxford University Press: 1986.

7. Dingemans, T. J.; Murthy, N. S.; Samulski, E. T., Javelin-, Hockey Stick-, and Boomerang-Shaped Liquid Crystals. Structural Variations on p-Quinquephenyl. *J. Phys. Chem. B* **2001,** *105*, 8845-8860.

8. Andrienko, D., Introduction to liquid crystals. *J. Mol.* **2018,** *267*, 520-541.

9. Burghardt, W. R., Molecular orientation and rheology in sheared lyotropic liquid crystalline polymers. *Macromol. Chem. Phys.* **1998,** *199*, 471-488.

10. Ward, I. M.; Sweeney, J., *An Introduction to the Mechanical Properties of Solid Polymers, 2nd Ed*. John Wiley & Sons, Ltd: 2004.

11. Picken, S. J.; Zwaag, S. v. d.; Northolt, M. G., Molecular and macroscopic orientational order in aramid solutions- a model to explain the influence of some spinning parameters on the modulus of aramid yarns. *Polymer* **1992,** *33* (14), 2998-3006.

12. Sawyer, L. C.; Chen, R. T.; Jamieson, M. G.; Musselman, I. H.; Russell, P. E., The fibrillar hierarchy in liquid crystalline polymers. *J. Mater. Sci.* **1993,** *28*, 225-238.

13. Rubinstein, M.; Colby, R. H., *Polymer Physics*. Oxford University Press: 2003.

14. Lang, C.; Kohlbrecher, J.; Porcar, L.; Radulescu, A.; Sellinghoff, K.; Dhont, J. K. G.; Lettinga, M. P., Microstructural Understanding of the Length- and Stiffness-Dependent Shear Thinning in Semidilute Colloidal Rods. *Macromolecules* **2019,** *52* (24), 9604-9612.

15. Onsager, L., The effects of shape on the interaction of colloidal particles. *Annals New York Academy of Sciences* **1949,** *51*, 627-659.

16. Kayser, R. F.; Raveché, H. J., Bifurcation in Onsager's model of the isotropic-nematic transition. *Phys. Rev. A* **1978,** *17* (6), 2067-2072.

17. Stroobants, A.; Lekkerkerker, H. N. W.; Odijk, T., Effect of Electrostatic Interaction on the Liquid Crystal Phase Transition in Solutions of Rodlike Polyelectrolytes. *Macromolecules* **1986,** *19*, 2232-2238.

18. Odijk, T.; Lekkerkerker, H. N. W., Theory of the isotropic-liquid crystal phase separation for a solution of bidisperse rodlike macromolecules. *J. Phys. Chem.* **1985,** *89*, 2090-2096.

19. Vroege, G. J.; Lekkerkerker, H. N. W., Theory of phase separation for a solution of tridisperse rod-like particles. *Colloids and Surf. A: Physicochem. Eng. Asp.* **1997,** *129-130*, 405-413.

20. Vroege, G. J.; Lekkerkerker, H. N. W., Theory of the isotropic-nematic-nematic phase separation for a solution of bidisperse rodlike particles. *J. Phys. Chem.* **1993,** *97*, 3601-1605.

21. Vroege, G. J.; Lekkerkerker, H. N. W., Phase transitions in lyotropic colloidal and polymer liquid crystals. *Rep. Prog. Phys.* **1992,** *55*, 1241-1309.

22. Flory, P. J., Phase Equilibria in Solutions of Rod-Like Particles. *Proceedings of the Royal Society of London. Series A. Mathematical and Physical Sciences* **1956,** *234*, 73-89.

23. Narayan, R.; Kim, J. E.; Kim, J. Y.; Lee, K. E.; Kim, S. O., Graphene Oxide Liquid Crystals: Discovery, Evolution and Applications. *Adv. Mater.* **2016,** *28*, 3045-68.

24. Papkov, S. P.; Kulichikhin, V. G.; Kalmykova, V. D.; Malkin, A. Y., Rheological Properties of Anisotropic Poly(para-Benzamide) Solutions. *J. Polym. Sci.: Polym. Phys. Ed.* **1974,** *12*, 1753-1770.

25. Marrucci, G.; Maffettone, P. L., Nematic phase of rodlike polymers. II. Polydomain predictions in the tumbling regime. *J. Rheol.* **1990,** *34* (8), 1231-1244.

26. Marrucci, G.; Maffettone, P. L., Nematic phase of rodlike polymers. I. Prediction of transient behavior at high shear rates. *J. Rheol.* **1990,** *34* (8), 1217-1230.

27. Larson, R. G., Arrested tumbling in shearing flows of liquid-crystal polymers. *Macromolecules* **1990,** *23* (17), 3983-3992.

28. Doi, M.; Larson, R., The effect of steady flow fields on the isotropic–nematic phase transition of rigid rod-like polymers. *J. Chem. Phys.* **1990,** *92*, 792-800.

29. Marrucci, G.; Maffettone, P. L., Description of the Liquid-Crystalline Phase of Rodlike Polymers at High Shear Rates. *Macromolecules* **1989,** *22*, 4076-4082.

30. Marrucci, G., Rheology of liquid crystalline polymers. *Pure & Appl. Chem.* **1985,** *57*, 1545-1552.

31. Kuzuu, N.; Doi, M., Constitutive Equation for Nematic Liquid Crystals under Weak Velocity Gradient Derived from a Molecular Kinetic Equation. II. Leslie Coefficients for Rodlike Polymers. *J. Phys. Soc. Jpn.* **1984,** *53* (3), 1031-1040.

32. Doi, M., Molecular Dynamics and Rheological Properties of Concentrated Solutions of Rodlike Polymers in Isotropic and Liquid Crystalline Phases. *J. Polymer Sci. Phys.* **1981,** *19*, 229-243.

33. Hess, S., Pre- and Post-Transitional Behavior of the Flow Alignment and Flow-Induced Phase Transition in Liquid Crystals. *Z. Naturforsch.* **1976,** *31 a*, 1507-1513.

34. Greco, F.; Marrucci, G., The Slightly-Bending-Rod Model of Nematic Polymers. *Mol. Cryst. Liq. Cryst.* **1995,** *266* (1), 1-8.

35. Chaubal, C. V.; Leal, L. G., Effects of Flexibility on Liquid Crystalline Polymer Behavior: The Nematic Broken Rod. *J. Polym. Sci.: Polym. Phys. Ed.* **1999,** *37*, 281-300.

36. Greco, F.; Marrucci, G., The tumbling or flow-aligning nature of nematics as predicted from the Slightly Bending Rod molecular model. *Liq. Cryst.* **1997,** *22* (1), 11-16.

37. Odijk, T., Theory of lyotropic polymer liquid crystals. *Macromolecules* **1986,** *19*, 2313-2329.

38. Odijk, T., The statistics and dynamics of confined or entangled stiff polymers. *Macromolecules* **1983,** *16*, 1340-1344.

39. Picken, S. J.; Noirez, L.; Luckhurst, G. R., Molecular conformation of a polyaramid in nematic solution from small angle neutron scattering and comparison with theory. *J. Chem. Phys.* **1998,** *109* (17), 7612-7617.

40. Westerhof, H. P. On the Structure and Dissolution Properties of Poly(p-phenylene terephthalamide). Delft University of Technology, The Netherlands, 2009.

41. Tzoupanos, N. D.; Zouboulis, A. I., Preparation, characterisation and application of novel composite coagulants for surface water treatment. *Water. Res.* **2011,** *45* (12), 3614-26.

42. Rubinstein, M.; Colby, R. H.; Dobrynin, A. V.; Joanny, J.-F., Elastic Modulus and Equilibrium Swelling of Polyelectrolyte Gels. *Macromolecules* **1996,** *29*, 398-406.

43. Dobrynin, A. V.; Colby, R. H.; Rubinstein, M., Scaling Theory of Polyelectrolyte Solutions. *Macromolecules* **1995,** *28*, 1859-1871.

44. Rubinstein, M.; Colby, R. H.; Dobrynin, A. V., Dynamics of semidilute polyelectrolyte solutions. *Phys. Rev. Lett.* **1994,** *73* (20), 2776-2779.

45. Colby, R. H., Structure and linear viscoelasticity of flexible polymer solutions: comparison of polyelectrolyte and neutral polymer solutions. *Rheol. Acta* **2010,** *49* (5), 425-442.

46. Dou, S.; Colby, R. H., Solution Rheology of a Strongly Charged Polyelectrolyte in Good Solvent. *Macromolecules* **2008,** *41*, 6505-6510.

47. Wang, L.; Bloomfield, V. A., Small-angle x-ray scattering of semidilute rodlike DNA solutions- polyelectrolyte behavior. *Macromolecules* **1991,** *24*, 5791-5795.

48. Purdy, K. R.; Dogic, Z.; Fraden, S.; Ruhm, A.; Lurio, L.; Mochrie, S. G., Measuring the nematic order of suspensions of colloidal fd virus by x-ray diffraction and optical birefringence. *Phys. Rev. E* **2003,** *67*, 031708.

49. Rulkens, R.; Schulze, M.; Wegner, G., Rigid-rod polyelectrolytes- synthesis of sulfonated poly(p-phenylene)s. *Macoromol. Rapid Commun.* **1994,** *15*, 669-676.

50. Viale, S.; Jager, W. F.; Picken, S. J., Synthesis and characterization of a water-soluble rigid-rod polymer. *Polymer* **2003,** *44* (26), 7843-7850.

51. Mendes, E.; Viale, S.; Santin, O.; Heinrich, M.; Picken, S. J., A small-angle neutron scattering investigation of rigid polyelectrolytes under shear. *J. Appl. Cryst.* **2003,** *36*, 1000-1005.

52. Viale, S.; Mendes, E.; Picken, S.; Santin, O., Water Soluble Rigid Rod Polymers: A SANS Study of Shear-Induced Alignment and Relaxation. *Mol. Cryst. Liq. Cryst.* **2004,** *411* (1), 525-535.

53. Viale, S.; Best, A. S.; Mendes, E.; Jager, W. F.; Picken, S. J., A supramolecular nematic phase in sulfonated polyaramides. *Chem. Commun.* **2004,** *14*, 1596-1597.

54. Viale, S.; Best, A. S.; Mendes, E.; Picken, S. J., Formation of aqueous molecular nematic liquid crystal phase in poly(p-sulfophenylene sulfoterephthalamide). *Chem. Commun.* **2005,** (12), 1528-1530.

55. Every, H. A.; Mendes, E.; Picken, S. J., Ordered Structures in Proton Conducting Membranes from Supramolecular Liquid Crystal Polymers. *J. Phys. Chem. B* **2006,** *110*, 23729-23735.

56. Sarkar, N.; Kershner, D., Rigid rod water-soluble polymers. *J. Appl. Polym. Sci.* **1996,** *62*, 393-408.

57. Funaki, T.; Kaneko, T.; Yamaoka, K.; Ohsedo, Y.; Gong, J. P.; Osada, Y.; Shibasaki, Y.; Ueda, M., Shear-Induced Mesophase Organization of Polyanionic Rigid Rods in Aqueous Solution. *Langmuir* **2004,** *20*, 6518-6520.

58. Yang, W.; Furukawa, H.; Shigekura, Y.; Shikinaka, K.; Osada, Y.; Gong, J. P., Self-Assembling Structure in Solution of a Semirigid Polyelectrolyte. *Macromolecules* **2008,** *41*, 1791-1799.

59. Wu, Z. L.; Arifuzzaman, M.; Kurokawa, T.; Le, K.; Hu, J.; Sun, T. L.; Furukawa, H.; Masunaga, H.; Gong, J. P., Supramolecular Assemblies of a Semirigid Polyanion in Aqueous Solutions. *Macromolecules* **2013,** *46* (9), 3581-3586.

60. Chremos, A.; Douglas, J. F., Communication: Counter-ion solvation and anomalous low-angle scattering in salt-free polyelectrolyte solutions. *J. Chem. Phys.* **2017,** *147* (24), 241103.

61. De Gennes, P. G.; Pincus, P.; Velasco, R. M.; Brochard, F., Remarks on polyelectrolyte conformation. *J. Phys. I.* **1976,** *37* (12), 1461-1473.

62. Wang, Y.; Gao, J.; Dingemans, T. J.; Madsen, L. A., Molecular Alignment and Ion Transport in Rigid Rod Polyelectrolyte Solutions. *Macromolecules* **2014,** *47* (9), 2984-2992.

63. Manning, G. S., Limiting Laws and Counterion Condensation in Polyelectrolyte Solutions II. Self-Diffusion of the Small Ions. *J. Chem. Phys.* **1969,** *51* (3), 934-938.

64. Ha, B.-Y.; Liu, A. J., Counterion-Mediated Attraction between Two Like-Charged Rods. *Phys. Rev. Lett.* **1997,** *79* (7), 1289-1292.

65. Gao, J.; Wang, Y.; Norder, B.; Garcia, S. J.; Picken, S. J.; Madsen, L. A.; Dingemans, T. J., Water and sodium transport and liquid crystalline alignment in a sulfonated aramid membrane. *J. Membr. Sci.* **2015,** *489*, 194-203.

66. Hegde, M.; Yang, L.; Vita, F.; Fox, R. J.; Watering, R. v. d.; Norder, B.; Lafont, U.; Francescangeli, O.; Madsen, L. A.; Picken, S. J.; Samulski, E. T.; Dingemans, T. J., Strong Graphene Oxide Nanocomposites from Aqueous Hybrid Liquid Crystals *Nat. Commun.* **2020,** *11*, 830.

67. Wang, Y.; He, Y.; Yu, Z.; Gao, J.; Ten Brinck, S.; Slebodnick, C.; Fahs, G. B.; Zanelotti, C. J.; Hegde, M.; Moore, R. B.; Ensing, B.; Dingemans, T. J.; Qiao, R.; Madsen, L. A., Double helical conformation and extreme rigidity in a rodlike polyelectrolyte. *Nat. Commun.* **2019,** *10* (1), 801.

68. Wang, Y.; Chen, Y.; Gao, J.; Yoon, H. G.; Jin, L.; Forsyth, M.; Dingemans, T. J.; Madsen, L. A., Highly Conductive and Thermally Stable Ion Gels with Tunable Anisotropy and Modulus. *Adv. Mater.* **2016,** *28*, 2571-8.

69. Yu, Z.; He, Y.; Wang, Y.; Madsen, L. A.; Qiao, R., Molecular Structure and Dynamics of Ionic Liquids in a Rigid-Rod Polyanion-Based Ion Gel. *Langmuir* **2017,** *33* (1), 322-331.

70. Yu, Z.; Wu, H.; Qiao, R., Electrical Double Layers near Charged Nanorods in Mixture Electrolytes. *J. Phys. Chem. C* **2017,** *121* (17), 9454-9461.

71. Lee, C.; Wei, X.; Kysar, J. W.; Hone, J., Measurement of the elastic properties and intrinsic strength of monolayer graphene. *Science* **2008,** *321* (5887), 385-8.

72. Johnson, D. W.; Dobson, B. P.; Coleman, K. S., A manufacturing perspective on graphene dispersions. *Curr. Opin. Colloid Interface Sci.* **2015,** *20* (5-6), 367-382.

73. Pardes, J. I.; Villar-Rodil, S.; Martinez-Alonso, A.; Tascon, J. M. D., Graphene Oxide Dispersions in Organic Solvents. *Langmuir* **2008,** *24*, 10560-10564.

74. Li, Z.; Kinloch, I. A.; Young, R. J., The role of interlayer adhesion in graphene oxide upon its reinforcement of nanocomposites. *Philos. Trans. R. Soc. A* **2016,** *374* (2071), 20150283.

75. Suk, J. W.; Piner, R. D.; An, J.; Ruoff, R. S., Mechanical Properties of Monolayer Graphene Oxide. *ACS Nano* **2010,** *11*, 6557-6564.

76. Zandiatashbar, A.; Lee, G. H.; An, S. J.; Lee, S.; Mathew, N.; Terrones, M.; Hayashi, T.; Picu, C. R.; Hone, J.; Koratkar, N., Effect of defects on the intrinsic strength and stiffness of graphene. *Nat. Commun.* **2014,** *5*, 3186.

77. Xu, Z.; Gao, C., Aqueous Liquid Crystals of Graphene Oxide. *ACS Nano* **2011,** *4*, 2908-2915.

78. Xu, Z.; Gao, C., Graphene chiral liquid crystals and macroscopic assembled fibres. *Nat. Commun.* **2011,** *2*, 571.

79. Kim, J. E.; Han, T. H.; Lee, S. H.; Kim, J. Y.; Ahn, C. W.; Yun, J. M.; Kim, S. O., Graphene oxide liquid crystals. *Angew. Chem. Int. Ed.* **2011,** *50*, 3043-3047.

80. Guo, F.; Kim, F.; Han, T. H.; Shenoy, V. B.; Huang, J.; Hurt, R. H., Hydration-responsive folding and unfolding in graphene oxide liquid crystal phases. *ACS Nano* **2011,** *5* (10), 8019-25.

81. Dan, B.; Behabtu, N.; Martinez, A.; Evans, J. S.; Kosynkin, D. V.; Tour, J. M.; Pasquali, M.; Smalyukh, I. I., Liquid crystals of aqueous, giant graphene oxide flakes. *Soft Matter* **2011,** *7* (23).

82. Aboutalebi, S. H.; Gudarzi, M. M.; Zheng, Q. B.; Kim, J.-K., Spontaneous Formation of Liquid Crystals in Ultralarge Graphene Oxide Dispersions. *Adv. Funct. Mater.* **2011,** *21*, 2978-2988.

83. Hu, X.; Xu, Z.; Gao, C., Multifunctional, supramolecular, continuous artificial nacre fibres. *Sci. Rep.* **2012,** *2*, 767.

84. Hu, X.; Xu, Z.; Liu, Z.; Gao, C., Liquid crystal self-templating approach to ultrastrong and tough biomimic composites. *Sci. Rep.* **2013,** *3*, 2374.

85. Kou, L.; Gao, C., Bioinspired design and macroscopic assembly of poly(vinyl alcohol)-coated graphene into kilometers-long fibers. *Nanoscale* **2013,** *5* (10), 4370-8.

86. Liu, Z.; Xu, Z.; Hu, X.; Gao, C., Lyotropic Liquid Crystal of Polyacrylonitrile-Grafted Graphene Oxide and Its Assembled Continuous Strong Nacre-Mimetic Fibers. *Macromolecules* **2013,** *46* (17), 6931-6941.

87. Kim, H.; Jalili, R.; Spinks, G. M.; Wallace, G. G.; Kim, S. J., High-strength graphene and polyacrylonitrile composite fiber enhanced by surface coating with polydopamine. *Comp. Sci. Technol.* **2017,** *149*, 280-285.

88. Seyedin, M. Z.; Razal, J. M.; Innis, P. C.; Jalili, R.; Wallace, G. G., Achieving Outstanding Mechanical Performance in Reinforced Elastomeric Composite Fibers Using Large Sheets of Graphene Oxide. *Adv. Funct. Mater.* **2015,** *25*, 94-104.

89. Seyedin, S.; Razal, J. M.; Innis, P. C.; Jalili, R.; Wallace, G. G., Compositional Effects of Large Graphene Oxide Sheets on the Spinnability and Properties of Polyurethane Composite Fibers. *Adv. Mater. Interfaces* **2016,** *3* (5).

90. Yousefi, N.; Gudarzi, M. M.; Zheng, Q.; Aboutalebi, S. H.; Sharif, F.; Kim, J.-K., Self-alignment and high electrical conductivity of ultralarge graphene oxide–polyurethane nanocomposites. *J. Mater. Chem.* **2012,** *22* (25).

91. Yousefi, N.; Lin, X.; Zheng, Q.; Shen, X.; Pothnis, J. R.; Jia, J.; Zussman, E.; Kim, J.-K., Simultaneous in situ reduction, self-alignment and covalent bonding in graphene oxide/epoxy composites. *Carbon* **2013,** *59*, 406-417.

92. Yousefi, N.; Sun, X.; Lin, X.; Shen, X.; Jia, J.; Zhang, B.; Tang, B.; Chan, M.; Kim, J. K., Highly aligned graphene/polymer nanocomposites with excellent dielectric properties for high-performance electromagnetic interference shielding. *Adv. Mater.* **2014,** *26*, 5480-7.

93. Yuan, J.; Luna, A.; Neri, W.; Zakri, C.; Schilling, T.; Colin, A.; Poulin, P., Graphene liquid crystal retarded percolation for new high-k materials. *Nat. Commun.* **2015,** *6*, 8700.

94. Lee, K. E.; Oh, J. J.; Yun, T.; Kim, S. O., Liquid crystallinity driven highly aligned large graphene oxide composites. *J. Solid State Chem.* **2015,** *224*, 115-119.

95. Stroobants, A.; Lekkerkerker, H. N. W., Liquid crystal phase transitions in a solution of rodlike and disklike particles. *J. Phys. Chem.* **1984,** *88*, 3669-3674.

96. Wensink, H. H.; Vroege, G. J.; Lekkerkerker, H. N., Biaxial versus uniaxial nematic stability in asymmetric rod-plate mixtures. *Phys. Rev. E* **2002,** *66* (4 Pt 1), 041704.

97. Forest, M. G.; Wang, Q.; Zhou, R., The weak shear kinetic phase diagram for nematic polymers. *Rheol. Acta* **2004,** *43* (1), 17-37.

98. Forest, M. G.; Wang, Q.; Zhou, R., The flow-phase diagram of Doi-Hess theory for sheared nematic polymers II: finite shear rates. *Rheol. Acta* **2004,** *44* (1), 80-93.

99. Ugaz, V. M.; Burghardt, W. R.; Zhou, W.; Kornfield, J. A., Transient molecular orientation and rheology in flow aligning thermotropic liquid crystalline polymers. *J. Rheol.* **2001,** *45* (5), 1029-1063.

100. Mortier, M.; Moldenaers, P.; Mewis, J., Transient rheological behaviour of poly-para-phenylenetherephthalamide (PpPTA) in sulphuric acid. *Rheol. Acta*. **1996,** *35*, 57-68.

101. Moldenaers, P.; Mortier, M.; Mewis, J., Transient Normal Stresses in Lyotropic Liquid Crystalline Polymers. *Chem. Eng. Sci*. **1994,** *49* (5), 699-707.

102. Hongladarom, K.; Burghardt, W. R., Molecular Alignment of Polymer Liquid Crystals in Shear Flows. 2. Transient Flow Behavior in Poly(benzyl glutamate) Solutions. *Macromolecules* **1993,** *26*, 785-794.

103. Picken, S. J.; Aerts, J.; Doppert, H. L.; Reuvers, A. J.; Northolt, M. G., Structure and rheology of aramid solutions- transient rheological and rheooptical measurements. *Macromolecules* **1991,** *24*, 1366-1375.

104. Guskey, S. M.; Winter, H. H., Transient shear behavior of a thermotropic liquid crystalline polymer in the nematic state. *J. Rheol*. **1991,** *35* (6), 1191-1207.

105. Grizzuti, N.; Cavella, S.; Cicarelli, P., Transient and steady-state rheology of a liquid crystalline hydroxypropylcellulose solution. *J. Rheol*. **1990,** *34* (8), 1293-1310.

106. Mewis, J.; Moldenaers, P., Transient Rheological Behaviour of A Lyotropic Polymeric Liquid Crystal. *Mol. Cryst. Liq. Cryst*. **1987,** *153* (1), 291-300.

107. Viola, G. G.; Baird, D. G., Studies on the Transient Shear Flow Behavior of Liquid Crystalline Polymers. *J. Rheol*. **1986,** *30* (3), 601-628.

108. Farhoudi, Y.; Rey, A. D., Shear flows of nematic polymers. I. Orienting modes, bifurcations, and steady state rheological predictions. *J. Rheol*. **1993,** *37* (2), 289-314.

109. Larson, R. G.; Ottinger, H. C., Effect of Molecular Elasticity on Out-of-Plane Orientations in Shearing Flows of Liquid-Crystalline Polymers. *Macromolecules* **1991,** *24*, 6270-6282.

110. Forest, M. G.; Wang, Q., Monodomain response of finite-aspect-ratio macromolecules in shear and related linear flows. *Rheol. Acta* **2003,** *42* (1-2), 20-46.

111. Hess, S.; Kröger, M., Regular and chaotic orientational and rheological behaviour of liquid crystals. *J. Phys. Condens. Matter* **2004,** *16* (38), S3835-S3859.

112. Grosso, M.; Crescitelli, S.; Somma, E.; Vermant, J.; Moldenaers, P.; Maffettone, P. L., Prediction and observation of sustained oscillations in a sheared liquid crystalline polymer. *Phys. Rev. Lett*. **2003,** *90* (9), 098304.

113. Rienacker, G.; Kroger, M.; Hess, S., Chaotic orientational behavior of a nematic liquid crystal subjected to a steady shear flow. *Phys. Rev. E* **2002,** *66* (4 Pt 1), 040702.

114. Rienacker, G.; Kroger, M.; Hess, S., Chaotic and regular shear-induced orientational dynamics of nematic liquid crystals. *Physica A* **2002,** *315*, 537-568.

115. Grosso, M.; Keunings, R.; Crescitelli, S.; Maffettone, P. L., Prediction of chaotic dynamics in sheared liquid crystalline polymers. *Phys. Rev. Lett.* **2001,** *86* (14), 3184-7.

116. Greco, F.; Minale, M.; Marrucci, G., Dynamics of stiff polymers with the slightly-bending-rod model. *J. Non-Newtonian Fluid Mech.* **1998,** *76*, 351-362.

117. Mewis, J.; Mortier, M.; Vermant, J.; Moldenaers, P., Experimental Evidence for the Existence of a Wagging Regime in Polymeric Liquid Crystals. *Macromolecules* **1997,** *30*, 1323-1328.

118. Lettinga, M. P.; Dogic, Z.; Wang, H.; Vermant, J., Flow Behavior of Colloidal Rodlike Viruses in the Nematic Phase. *Langmuir* **2005,** *21*, 8048-8057.

119. Lettinga, M. P.; Dhont, J. K. G., Non-equilibrium phase behaviour of rod-like viruses under shear flow. *J. Phys. Condens. Matter* **2004,** *16* (38), S3929-S3939.

120. Tao, Y. G.; den Otter, W. K.; Briels, W. J., Kayaking and wagging of liquid crystals under shear: Comparing director and mesogen motions. *Europhys. Lett.* **2009,** *86*, 56005.

121. Tao, Y. G.; den Otter, W. K.; Briels, W. J., Periodic orientational motions of rigid liquid-crystalline polymers in shear flow. *J. Chem. Phys.* **2006,** *124* (20), 204902.

122. Tao, Y. G.; den Otter, W. K.; Briels, W. J., Kayaking and wagging of rods in shear flow. *Phys. Rev. Lett.* **2005,** *95* (23), 237802.

123. Tsuji, T.; Rey, A. D., Effect of long range order on sheared liquid crystalline materials Part 1: compatibility between tumbling behavior and fixed anchoring. *J. Non-Newtonian Fluid Mech.* **1997,** *73* (1-2), 127-152.

124. Rey, A. D.; Denn, M. M., Dynamical Phenomena In Liquid-Crystalline Materials. *Annu. Rev. Fluid Mech.* **2002,** *34*, 233-266.

125. Fox, R. J.; Yu, D.; Hegde, M.; Kumbhar, A. S.; Madsen, L. A.; Dingemans, T. J., Nanofibrillar Ionic Polymer Composites Enable High-Modulus Ion-Conducting Membranes. *ACS Appl. Mater. Interfaces* **2019,** *11* (43), 40564-40574.

126. Kulicke, W. M.; Kiss, G.; Porter, R. S., Inertial normal-force corrections in rotational rheometry. *Rheol. Acta* **1977,** *16*, 568-572.

127. Ilavsky, J., Nika: software for two-dimensional data reduction. *J. Appl. Cryst.* **2012,** *45*, 324-328.

128. Bostwick, J. E.; Zanelotti, C. J.; Iacob, C.; Korovich, A. G.; Madsen, L. A.; Colby, R. H., Ion Transport and Mechanical Properties of Non-Crystallizable Molecular Ionic Composite Electrolytes. *Macromolecules* **2020,** *53* (4), 1405-1414.

129. Larson, R. G., On the relative magnitudes of viscous, elastic and texture stresses in liquid crystalline PBG solutions. *Rheol. Acta* **1996,** *35*, 150-159.

130. Rey, A. D., Analysis of Shear Flow Effects on Liquid Crystalline Textures. *Mol. Cryst. Liq. Cryst.* **1993,** *225* (1), 313-335.

131. Alderman, N. J.; Mackley, M. R., Optical Textures Observed during the Shearing of Thermotropic Liquid-crystal Polymers. *Faraday Discuss. Chem. Soc.* **1985,** *79*, 149-160.

132. Larson, R. G.; Mead, D. W., Development of orientation and texture during shearing of liquid-crystalline polymers. *Liq. Cryst.* **1992,** *12* (5), 751-768.

133. Onogi, S.; Asada, T., *Rheology and Rheo-Optics of Polymer Liquid Crystals*. 1980.

134. Walker, L.; Wagner, N., Rheology of region I flow in a lyotropic liquid-crystal polymer: The effects of defect texture. *J. Rheol.* **1994,** *38* (5), 1525-1547.

135. Walker, L. M.; Kernick, W. A.; Wagner, N. J., In Situ Analysis of the Defect Texture in Liquid Crystal Polymer Solutions under Shear. *Macromolecules* **1997,** *30*, 508-514.

136. Ugaz, V. M.; D. K. Cinader, J.; Burghardt, W. R., Origins of Region I Shear Thinning in Model Lyotropic Liquid Crystalline Polymers. *Macromolecules* **1997,** *30*, 1527-1530.

137. Walker, L. M.; Mortier, M.; Moldenaers, P., Concentration effects on the rheology and texture of PBG/m-cresol solutions. *J. Rheol.* **1996,** *40* (5), 967-981.

138. Walker, L. M.; Wagner, N. J.; Larson, R. G.; Mirau, P. A.; Moldenaers, P., The rheology of highly concentrated PBLG solutions. *J. Rheol.* **1995,** *39* (5), 925-952.

139. Moldenaers, P.; Fuller, G.; Mewis, J., Mechanical and optical rheometry of polymer liquid-crystal domain structure. *Macromolecules* **1989,** *22* (2), 960-965.

140. Burghardt, W. R.; Fuller, G. G., Role of Director Tumbling in the Rheology of Polymer Liquid Crystal Solutions. *Macromolecules* **1991,** *24*, 2546-2555.

141. Larson, R. G.; Doi, M., Mesoscopic domain theory for textured liquid crystalline polymers. *J. Rheol.* **1991,** *35* (4), 539-563.

142. Larson, R. G., Arrested Tumbling in Shearing Flows of Liquid Crystal Polymers. *Macromolecules* **1990,** *23*, 3983-3992.

143. Kiss, G.; Porter, R. S., Rheology of Concentrated Solutions of Helical Polypeptides. *J. Polymer Sci. Phys.* **1980,** *18*, 361-388.

144. Kiss, G.; Porter, R. S., Rheology of Concentrated Solutions of Poly(y-Benzyl-Glutamate). *J. Polym. Sci.* **1978,** *65*, 193-211.

145. Vasudevan, M.; Buse, E.; Lu, D.; Krishna, H.; Kalyanaraman, R.; Shen, A. Q.; Khomami, B.; Sureshkumar, R., Irreversible nanogel formation in surfactant solutions by microporous flow. *Nat. Mater.* **2010,** *9* (5), 436-41.

146. Liu, C.-H.; Pine, D. J., Shear-Induced Gelation and Fracture in Micellar Solutions. *Phys. Rev. Lett.* **1996,** *77* (10), 2121-2124.

147. Perazzo, A.; Nunes, J. K.; Guido, S.; Stone, H. A., Flow-induced gelation of microfiber suspensions. *Proc. Natl. Acad. Sci. U.S.A.* **2017,** *114* (41), E8557-E8564.

148. Rendon, S.; Burghardt, W. R.; Bubeck, R. A., Orientation dynamics in commercial thermotropic liquid crystalline polymers in transient shear flows. *Rheol. Acta* **2007,** *46* (7), 945-956.

149. Pakdel, P.; McKinley, G. H., Elastic Instability and Curved Streamlines. *Phys. Rev. Lett.* **1996,** *77* (12), 2459-2462.

150. Magda, J. J.; Larson, R. G., A transition occurring in ideal elastic liquids during shear flow. *J. Non-Newtonian Fluid Mech.* **1988,** *30*, 1-19.

151. Magda, J. J.; Baek, S. G.; DeVris, K. L.; Larson, R. G., Unusual pressure profiles and fluctuations during shear flows of liquid crystal polymers. *Polymer* **1991,** *32* (10), 1794-1796.

152. Magda, J. J.; Baek, S.-G.; DeVries, K. L.; Larson, R. G., Shear Flows of Liquid Crystal Polymers: Measurements of the Second Normal Stress Difference and the Doi Molecular Theory. *Macromolecules* **1991,** *24*, 4460-4468.

153. Baek, S. G.; Magda, J. J.; Larson, R. G.; Hudson, S. D., Rheological differences among liquid-crystalline polymers. II. Disappearance of negative N1 in densely packed lyotropes and thermotropes. *J. Rheol.* **1994,** *38* (5), 1473-1503.

154. Faraoni, V.; Grosso, M.; Crescitelli, S.; Maffettone, P. L., The rigid-rod model for nematic polymers: An analysis of the shear flow problem. *J. Rheol.* **1999,** *43* (3), 829-843.

155. Cocchini, F.; Nobile, M. R.; Acierno, D., Letter: About negative first normal stress differences in a thermotropic liquid crystalline polymer. *J. Rheol.* **1992,** *36* (7), 1307-1311.

156. Baek, S. G.; Magda, J. J.; Larson, R. G., Rheological differences among liquid-crystalline polymers. I. The first and second normal stress differences of PBG solutions. *J. Rheol.* **1993,** *37* (6), 1201-1224.

157. Baek, S. G.; Magda, J. J.; Cementwala, S., Normal stress differences in liquid crystalline hydroxypropylcellulose solutions. *J. Rheol.* **1993,** *37* (5), 935-945.

158. Zhou, W.-J.; Kornfield, J. A.; Ugaz, V. M.; Burghardt, W. R.; Link, D. R.; Clark, N. A., Dynamics and Shear Orientation Behavior of a Main-Chain Thermotropic Liquid Crystalline Polymer. *Macromolecules* **1999,** *32*, 5581-5593.

159. Cocchini, F.; Nobile, M. R.; Acierno, D., Transient and steady rheological behavior of the thermotropic liquid crystal copolymer 73/27 HBA/HNA. *J. Rheol.* **1991,** *35* (6), 1171-1189.

160. Romo-Uribe, A.; Windle, A. H., A Flow-Orientation Transition in a Thermotropic Random Copolyester. *Macromolecules* **1993,** *36*, 7100-7102.

161. Brigham, E. O., *The Fast Fourier Transform and Its Applications*. Prentice-Hall, Inc: 1988.

162. Caputo, F. E.; Burghardt, W. R., Real-Time 1-2 Plane SAXS Measurements of Molecular Orientation in Sheared Liquid Crystalline Polymers. *Macromolecules* **2001,** *34*, 6684-6694.

163. Caputo, F. E.; Ugaz, V. M.; Burghardt, W. R.; Berret, J.-F., Transient 1–2 plane small-angle x-ray scattering measurements of micellar orientation in aligning and tumbling nematic surfactant solutions. *J. Rheol.* **2002,** *46*, 927-946.

164. Picken, S. J., Clearing temperatures of aramid solutions in sulfuric acid. *Macromolecules* **1989,** *22*, 1766-1771.

165. Noel, C.; Navard, P., Liquid Crystal Polymers. *Prog. Polym. Sci.* **1991,** *16*, 55-110.

166. Wissbrun, K. F., Rheology of Rod-like Polymers in the Liquid Crystalline State. *J. Rheol.* **1981,** *25* (6), 619-662.

167. Taeger, A.; Vogel, C.; Lehmann, D.; Jehnichen, D.; Komber, H.; Meier-Haack, J.; Ochoa, N. A.; Nunes, S. P.; Peinemann, K. V., Ion exchange membranes derived from sulfonated polyaramides. *React. Funct. Polym.* **2003,** *57* (2-3), 77-92.

168. Every, H. A.; Janssen, G. J. M.; Sitters, E. F.; Mendes, E.; Picken, S. J., Performance analysis of sulfonated PPTA polymers as potential fuel cell membranes. *J. Power Sources* **2006,** *162* (1), 380-387.

169. Wu, Z. L.; Kurokawa, T.; Liang, S.; Gong, J. P., Dual Network Formation in Polyelectrolyte Hydrogel via Viscoelastic Phase Separation: Role of Ionic Strength and Polymerization Kinetics. *Macromolecules* **2010,** *43* (19), 8202-8208.

170. Picken, S. J.; Aerts, J.; Visser, R.; Northolt, M. G., Structure and rheology of aramid solutions- X-ray scattering measurements. *Macromolecules* **1990,** *23*, 3849-3854.

171. Fox, R. J.; Forest, M. G.; Picken, S. J.; Dingemans, T. J., Observation of Transition Cascades in Sheared Liquid Crystalline Polymers. *Soft Matter* **2020,** *16, 3891-3901*

172. Moldenaers, P.; Mewis, J., Transient Behavior of Liquid Crystalline Solutions of Poly(benzylglutamate). *J. Rheol.* **1986,** *30* (3), 567-584.

173. Maffettone, P. L.; Marrucci, G.; Mortier, M.; Moldenaers, P.; Mewis, J., Dynamic characterization of liquid crystalline polymers under flow-aligning shear conditions. *J. Chem. Phys.* **1994,** *100* (10), 7736-7743.

174. Doi, M.; Edwards, S. F., Dynamics of Rod-like Macromolecules in Concentrated Solution. Part 1. *J. Chem. Soc., Faraday Trans. 2*, **1978**, 74, 560-570.

175. Doi, M.; Edwards, S. F., Dynamics of Rod-Like Macromolecules in Concentrated Solution. Part 2. *J. Chem. Soc., Faraday Trans. 2*, **1978**, 74, 918-932.

176. Baird, D. G.; Ballman, R. L., Comparison of the Rheological Properties of Concentrated Solutions of a Rodlike and a Flexible Chain Polyamide. *J. Rheol.* **1979,** *23* (4), 505-524.

177. Edwards, S. F.; Evans, K. E., Dynamics of Highly Entangled Rod-like Molecules. *J. Chem. Soc., Faraday Trans. 2* **1982,** *78*, 113-121.

178. Lopez, C. G.; Rogers, S. E.; Colby, R. H.; Graham, P.; Cabral, J. T., Structure of Sodium Carboxymethyl Cellulose Aqueous Solutions: A SANS and Rheology Study. *J. Polym. Sci. B Polym. Phys.* **2015,** *53* (7), 492-501.

179. Dou, S.; Colby, R. H., Charge density effects in salt-free polyelectrolyte solution rheology. *J. Polym. Sci. B Polym. Phys.* **2006,** *44* (14), 2001-2013.

180. Ferry, J. D., *Viscoelastic Properties of Polymers*. 3rd ed.; John Wiley & Sons: 1980.

181. Moldenaers, P.; Fuller, G.; Mewis, J., Mechanical and optical rheometry of polymer liquid-crystal domain structure. *Macromolecules* **1989,** *22*, 960-965.

182. Hongladarom, K.; Burghardt, W. R., Molecular orientation, "Region I" shear thinning and the cholesteric phase in aqueous hydroxypropylcellulose under shear. *Rheol. Acta* **1998,** *37*, 46-53.

183. López-Barrón, C. R.; Wagner, N. J., Solvent isotope effect on the microstructure and rheology of cationic worm-like micelles near the isotropic-nematic transition. *Soft Matter* **2011,** *7* (22), 10856-10863.

184. Jones, G.; Fornwalt, H. J., The Viscosity of Deuterium Oxide and Its Mixtures with Water at 25°C. *J. Chem. Phys.* **1936,** *4* (1), 30-33.

185. Huang, G.-R.; Wang, Y.; Do, C.; Shinohara, Y.; Egami, T.; Porcar, L.; Liu, Y.; Chen, W.-R., Orientational Distribution Function of Aligned Elongated Molecules and Particulates Determined from Their Scattering Signature. *ACS Macro Lett.* **2019,** *8* (10), 1257-1262.

186. Walker, L. M.; Wagner, N. J., SANS Analysis of the Molecular Order in Poly(g-benzyl L-glutamate):Deuterated Dimethylformamide (PBLG:d-DMF) under Shear and During Relaxation. *Macromolecules* **1996,** *29*, 2298-2301.

187. Keates, P.; Mitchell, G. R.; Pauvrel-Disdier, E.; Navard, P., In situ X-ray scattering study of anisotropic solutions of hydroxypropylcellulose subjected to shear flow. *Polymer* **1993,** *34*, 1316-1319.

188. Greger, M.; Kollar, M.; Vollhardt, D., Isosbestic points: How a narrow crossing region of curves determines their leading parameter dependence. *Physical Review B* **2013,** *87* (19).

189. Ballard, M. J.; Buscall, R.; Waite, F. A., The theory of shear-thickening polymer solutions. *Polymer* **1987,** *29*, 1287-1293.

190. Leibler, L.; Rubinstein, M.; Colby, R. H., Dynamics of reversible networks. *Macromolecules* **1991,** *24*, 4701-4707.

191. Rubinstein, M.; Semenov, A. N., Dynamics of Entangled Solutions of Associating Polymers. *Macromolecules* **2001,** *34*, 1058-1068.

192. Chowdhury, A. H.; Russo, P. S., Late stages of phase separation/gelation of isotropic solutions of rod-like polymers by video microscopy. *J. Chem. Phys.* **1990,** *92* (9), 5744-5750.

193. Schmidtke, S.; Russo, P.; Nakamatsu, J.; Buyuktanir, E.; Turfan, B.; Temyanko, E.; Negulescu, I., Thermoreversible Gelation of Isotropic and Liquid Crystalline Solutions of a "Sticky" Rodlike Polymer. *Macromolecules* **2000,** *33*, 4427-4432.

194. Tipton, D. L.; Russo, P. S., Thermoreversible Gelation of a Rodlike Polymer. *Macromolecules* **1996,** *29*, 7402-7411.

195. Lott, J. R.; McAllister, J. W.; Wasbrough, M.; Sammler, R. L.; Bates, F. S.; Lodge, T. P., Fibrillar Structure in Aqueous Methylcellulose Solutions and Gels. *Macromolecules* **2013,** *46* (24), 9760-9771.

196. Arvidson, S. A.; Lott, J. R.; McAllister, J. W.; Zhang, J.; Bates, F. S.; Lodge, T. P.; Sammler, R. L.; Li, Y.; Brackhagen, M., Interplay of Phase Separation and Thermoreversible Gelation in Aqueous Methylcellulose Solutions. *Macromolecules* **2012,** *46* (1), 300-309.

197. Kobayashi, K.; Huang, C.-i.; Lodge, T. P., Thermoreversible Gelation of Aqueous Methylcellulose Solutions. *Macromolecules* **1999,** *32*, 7070-7077.

198. Bertula, K.; Martikainen, L.; Munne, P.; Hietala, S.; Klefström, J.; Ikkala, O.; Nonappa, Strain-Stiffening of Agarose Gels. *ACS Macro Lett.* **2019,** *8* (6), 670-675.

199. Krishna Reddy, N.; Zhang, Z.; Paul Lettinga, M.; Dhont, J. K. G.; Vermant, J., Probing structure in colloidal gels of thermoreversible rodlike virus particles: Rheology and scattering. *J. Rheol.* **2012,** *56* (5), 1153-1174.

200. Zhang, Z.; Krishna, N.; Lettinga, M. P.; Vermant, J.; Grelet, E., Reversible Gelation of Rod-Like Viruses Grafted with Thermoresponsive Polymers. *Langmuir* **2009,** *25*, 2437-2442.

201. Rammensee, S.; Slotta, U.; Scheibel, T.; Bausch, A. R., Assembly mechanism of recombinant spider silk proteins. *Proc. Natl. Acad. Sci. U.S.A* **2008,** *105* (18), 6590-6595.

202. Jin, H.-J.; Kaplan, D. L., Mechanism of silk processing in insects and spiders. *Nature* **2003,** *424*, 1057-1061.

203. Oates, K. M. N.; Krause, W. E.; Jones, R. L.; Colby, R. H., Rheopexy of synovial fluid and protein aggregation. *J. R. Soc. Interface*. **2006,** *3* (6), 167-174.

204. Keller, S. L.; Boltenhagen, P.; Pine, D. J.; Zasadzinksi, J. A., Direct Observation of Shear-Induced Structures in Wormlike Micellar Solutions by Freeze-Fracture Electron Microscopy. *Phys. Rev. Lett*. **1998,** *80* (12), 2725-2728.

205. Boltenhagen, P.; Hu, Y.; Matthys, E. F.; Pine, D. J., Observation of Bulk Phase Separation and Coexistence in a Sheared Micellar Solution. *Phys. Rev. Lett*. **1997,** *79* (12), 2359-2362.

206. Wunderlich, I.; Hoffmann, H.; Rehage, H., Flow birefringence and rheological measurements on shear induced micellar structures. *Rheol. Acta* **1987,** *26*, 532-542.

207. Vasudevan, M.; Shen, A.; Khomami, B.; Sureshkumar, R., Self-similar shear thickening behavior in CTAB/NaSal surfactant solutions. *J. Rheol*. **2008,** *52* (2), 527-550.

208. Hofmann, S.; Rauscher, A.; Hoffmann, H., Shear Induced Micellar Structures. *Ber. Bunsenges. Phys. Chem*. **1991,** *95*, 153-164.

209. Hu, Y. T.; Boltenhagen, P.; Matthys, E.; Pine, D. J., Shear thickening in low-concentration solutions of wormlike micelles. II. Slip, fracture, and stability of the shear-induced phase. *J. Rheol*. **1998,** *42* (5), 1209-1226.

210. Hu, Y. T.; Boltenhagen, P.; Pine, D. J., Shear thickening in low-concentration solutions of wormlike micelles. I. Direct visualization of transient behavior and phase transitions. *J. Rheol*. **1998,** *42* (5), 1185-1208.

211. Hu, Y.; Wang, S. Q.; Jamieson, A. M., Rheological and flow birefringence studies of a shear-thickening complex fluid—A surfactant model system. *J. Rheol*. **1993,** *37* (3), 531-546.

212. Cardiel, J. J.; Dohnalkova, A. C.; Dubash, N.; Zhao, Y.; Cheung, P.; Shen, A. Q., Microstructure and rheology of a flow-induced structured phase in wormlike micellar solutions. *Proc. Natl. Acad. Sci. U.S.A*. **2013,** *110* (18), E1653-60.

213. Cates, M. E.; Turner, M. S., Flow-Induced Gelation of Rodlike Micelles. *Europhys. Lett*. **1990,** *11* (7), 681-686.

214. Bruinsma, R.; Gelbart, W. M.; Ben-Shaul, A., Flow-induced gelation of living (micellar) polymers. *J. Chem. Phys.* **1992,** *96* (10), 7710-7727.

215. Salmon, J. B.; Colin, A.; Manneville, S.; Molino, F., Velocity profiles in shear-banding wormlike micelles. *Phys. Rev. Lett.* **2003,** *90* (22), 228303.

216. Sprakel, J.; Spruijt, E.; Cohen Stuart, M. A.; Besseling, N. A. M.; Lettinga, M. P.; van der Gucht, J., Shear banding and rheochaos in associative polymer networks. *Soft Matter* **2008,** *4* (8).

217. Billen, J.; Wilson, M.; Baljon, A. R. C., Shear banding in simulated telechelic polymers. *Chem. Phys.* **2015,** *446*, 7-12.

218. Boukany, P. E.; Wang, S. Q.; Ravindranath, S.; Lee, L. J., Shear banding in entangled polymers in the micron scale gap: a confocal-rheoscopic study. *Soft Matter* **2015,** *11* (41), 8058-68.

219. Castillo-Tejas, J.; Carro, S.; Manero, O., Shear Banding in Telechelic Associative Polymers by Molecular Dynamics. *ACS Macro Lett.* **2017,** *6* (3), 190-193.

220. Sprakel, J.; Spruijt, E.; van der Gucht, J.; Padding, J. T.; Briels, W. J., Failure-mode transition in transient polymer networks with particle-based simulations. *Soft Matter* **2009,** *5* (23).

221. Fardin, M. A.; Lasne, B.; Cardoso, O.; Gregoire, G.; Argentina, M.; Decruppe, J. P.; Lerouge, S., Taylor-like vortices in Shear-Banding Flow of Giant Micelles. *Phys. Rev. Lett.* **2009,** *103* (2), 028302.

222. Fardin, M. A.; Lopez, D.; Croso, J.; Grégoire, G.; Cardoso, O.; McKinley, G. H.; Lerouge, S., Elastic Turbulence in Shear Banding Wormlike Micelles. *Phys. Rev. Lett.* **2010,** *104* (17).

223. Omar, A. K.; Wang, Z. G., Shear-Induced Heterogeneity in Associating Polymer Gels: Role of Network Structure and Dilatancy. *Phys. Rev. Lett.* **2017,** *119* (11), 117801.

224. Grønbech-Jensen, N.; Mashl, R. J.; Bruinsma, R. F.; Gelbart, W. M., Counterion-Induced Attraction between Rigid Polyelectrolytes. *Phys. Rev. Lett.* **1997,** *78* (12), 2477-2480.

225. Angelini, T. E.; Liang, H.; Wriggers, W.; Wong, G. C., Like-charge attraction between polyelectrolytes induced by counterion charge density waves. *Proc. Natl. Acad. Sci. U.S.A.* **2003,** *100* (15), 8634-7.

226. Kroeger, A.; Deimede, V.; Belack, J.; Lieberwirth, I.; Fytas, G.; Wegner, G., Equilibrium length and shape of rodlike polyelectrolyte micelles in dilute aqueous solutions. *Macromolecules* **2007,** *40* (1), 105-115.

227. Bockstaller, M.; Köhler, W.; Wegner, G.; Vlassopoulos, D.; Fytas, G., Levels of Structure Formation in Aqueous Solutions of Anisotropic Association Colloids Consisting of Rodlike Polyelectrolytes. *Macromolecules* **2001,** *34*, 6359-6366.

228. Bockstaller, M.; Köhler, W.; Wegner, G.; Fytas, G., Characterization of Association Colloids of Amphiphilic Poly(p-phenylene)sulfonates in Aqueous Solution. *Macromolecules* **2001,** *34*, 6353-6358.

229. Bockstaller, M.; Köhler, W.; Wegner, G.; Vlassopoulos, D.; Fytas, G., Hierarchical Structures of a Synthetic Rodlike Polyelectrolyte in Water. *Macromolecules* **2000,** *33* (11), 3951-3953.

230. Rulkens, R.; Wegner, G.; Thurn-Albrecht, T., Cylindrical Micelles of Wormlike Polyelectrolytes. *Langmuir* **1999,** *15*, 4022-4025.

231. Every, H. A.; Ham, L. V. v. d.; Picken, S. J.; Mendes, E., Physical Properties of Oriented Thin Films Formed by the Electrostatic Complexation of Sulfonated Polyaramid. *J. Phys. Chem. B* **2008,** *112*, 16403-16408.

232. Cates, M. E., Reptation of living polymers- dynamics of entangled polymers in the presence of reversible chain-scission reactions. *Macromolecules* **1987,** *20* (9), 2289-2296.

233. Lekkerkerker, H. N. W.; Coulon, P.; Van Der Haegen, R.; Deblieck, R., On the isotropic-liquid crystal phase separation in a solution of rodlike particles of different lengths. *J. Chem. Phys.* **1984,** *80* (7), 3427-3433.

234. Cates, M. E.; Fielding, S. M., Rheology of giant micelles. *Adv. Phys.* **2006,** *55* (7-8), 799-879.

235. Safran, S. A.; Pincus, P. A.; Cates, M. E.; MacKintosh, F. C., Growth of Charged Micelles. *J. Phys. France* **1990,** *51* (6), 503-510.

236. McAllister, J. W.; Lott, J. R.; Schmidt, P. W.; Sammler, R. L.; Bates, F. S.; Lodge, T. P., Linear and Nonlinear Rheological Behavior of Fibrillar Methylcellulose Hydrogels. *ACS Macro Lett.* **2015,** *4* (5), 538-542.

237. Broedersz, C. P.; Depken, M.; Yao, N. Y.; Pollak, M. R.; Weitz, D. A.; MacKintosh, F. C., Cross-link-governed dynamics of biopolymer networks. *Phys. Rev. Lett.* **2010,** *105* (23), 238101.

238. MacKintosh, F. C.; Kas, J.; Janmey, P. A., Elasticity of semiflexible biopolymer networks. *Phys. Rev. Lett.* **1995,** *75* (24), 4425-4428.

239. Gardel, M. L.; Shin, J. H.; MacKintosh, F. C.; Mahadevan, L.; Matsudaira, P.; Weitz, D. A., Elastic Behavior of Cross-Linked and Bundled Actin Networks. *Science* **2004,** *304*, 1301-1305.

240. Graessley, W. W.; Edwards, S. F., Entanglement interactions in polymers and the chain contour concentration. *Polymer* **1981,** *22*, 1329-1334.

241. Yao, N. Y.; Broedersz, C. P.; Lin, Y. C.; Kasza, K. E.; Mackintosh, F. C.; Weitz, D. A., Elasticity in ionically cross-linked neurofilament networks. *Biophys. J.* **2010,** *98* (10), 2147-53.

242. Tadmor, R.; Khalfin, R. L.; Cohen, Y., Reversible Gelation in Isotropic Solutions of the Helical Polypeptide Poly(γ-benzyl-l-glutamate)- Kinetics and Formation Mechanism of the Fibrillar Network. *Langmuir* **2002,** *18*, 7146-7150.

243. Guery, J.; Bertrand, E.; Rouzeau, C.; Levitz, P.; Weitz, D. A.; Bibette, J., Irreversible shear-activated aggregation in non-Brownian suspensions. *Phys. Rev. Lett.* **2006,** *96* (19), 198301.

244. Zaccone, A.; Wu, H.; Gentili, D.; Morbidelli, M., Theory of activated-rate processes under shear with application to shear-induced aggregation of colloids. *Phys. Rev. E* **2009,** *80* (5 Pt 1), 051404.

245. Lattuada, M.; Zaccone, A.; Wu, H.; Morbidelli, M., Population-balance description of shear-induced clustering, gelation and suspension viscosity in sheared DLVO colloids. *Soft Matter* **2016,** *12* (24), 5313-24.

246. Koumakis, N.; Moghimi, E.; Besseling, R.; Poon, W. C.; Brady, J. F.; Petekidis, G., Tuning colloidal gels by shear. *Soft Matter* **2015,** *11* (23), 4640-4648.

247. Lazzari, S.; Maggioni, G. M.; Soos, M.; Wu, H.; Morbidelli, M., Shear-stability and gelation of inverse latexes. *Soft Matter* **2013,** *9* (45), 10866-10876.

248. Zaccone, A.; Gentili, D.; Wu, H.; Morbidelli, M.; Del Gado, E., Shear-driven solidification of dilute colloidal suspensions. *Phys. Rev. Lett.* **2011,** *106* (13), 138301.

249. Zaccone, A.; Gentili, D.; Wu, H.; Morbidelli, M., Shear-induced reaction-limited aggregation kinetics of brownian particles at arbitrary concentrations. *J. Chem. Phys.* **2010,** *132* (13), 134903.

250. Thivilliers-Arvis, F.; Laurichesse, E.; Schmitt, V.; Leal-Calderon, F., Shear-induced instabilities in oil-in-water emulsions comprising partially crystallized droplets. *Langmuir* **2010,** *26* (22), 16782-90.

251. Papageorgiou, D. G.; Kinloch, I. A.; Young, R. J., Mechanical properties of graphene and graphene-based nanocomposites. *Prog. Mater. Sci.* **2017,** *90*, 75-127.

252. Kinloch, I. A.; Suhr, J.; Lou, J.; Young, R. J.; Ajayan, P. M., Composites with carbon nanotubes and graphene: An outlook. *Science* **2018,** *362*, 547-553.

253. Rouhollah Jalili; Seyed Hamed Aboutalebi; Dorna Esrafilzadeh; Roderick L. Shepherd; Jun Chen; Sima Aminorroaya-Yamini; Konstantin Konstantinov; Andrew I. Minett; Joselito M. Razal; Wallace, G. G., Scalable One-Step Wet-Spinning of Graphene Fibers and Yarns from Liquid Crystalline Dispersions of Graphene Oxide: Towards Multifunctional Textiles. *Adv. Funct. Mater.* **2013,** *23*, 5345-5354.

254. Liu, S.; Liu, J.; Xu, Z.; Liu, Y.; Li, P.; Guo, F.; Wang, F.; Liu, Y.; Yang, M.; Gao, W.; Gao, C., Artificial Bicontinuous Laminate Synergistically Reinforces and Toughens Dilute Graphene Composites. *ACS Nano* **2018,** *12* (11), 11236-11243.

255. Gong, L.; Kinloch, I. A.; Young, R. J.; Riaz, I.; Jalil, R.; Novoselov, K. S., Interfacial Stress Transfer in a Graphene Monolayer Nanocomposite. *Adv. Mater.* **2010,** *22*, 2694-2697.

256. Young, R. J.; Gong, L.; Kinloch, I. A.; Riaz, I.; Jalil, R.; Novoselov, K. S., Strain Mapping in a Graphene Monolayer Nanocomposite. *ACS Nano* **2011,** *4*, 3079-3084.

257. Gong, L.; Young, R. J.; Kinloch, I. A.; Riaz, I.; Jalil, R.; Novoselov, K. S., Optimizing the Reinforcement of Polymer-Based Nanocomposites by Graphene. *ACS Nano* **2012,** *3*, 2086-2095.

258. Pang, Y.; Yang, J.; Curtis, T. E.; Luo, S.; Huang, D.; Feng, Z.; Morales-Ferreiro, J. O.; Sapkota, P.; Lei, F.; Zhang, J.; Zhang, Q.; Lee, E.; Huang, Y.; Guo, R.; Ptasinska, S.; Roeder, R. K.; Luo, T., Exfoliated Graphene Leads to Exceptional Mechanical Properties of Polymer Composite Films. *ACS Nano* **2019,** *13* (2), 1097-1106.

259. May, P.; Khan, U.; O'Neill, A.; Coleman, J. N., Approaching the theoretical limit for reinforcing polymers with graphene. *J. Mater. Chem.* **2012,** *22* (4), 1278-1282.

260. Tayal, A.; Khan, S. A., Degradation of a Water-Soluble Polymer: Molecular Weight Changes and Chain Scission Characteristics. *Macromolecules* **2000,** *33* (26), 9488-9493.

261. Zero, K.; Aharoni, S. M., Depolarization ratios and rigidity of aromatic polyamides. *Macromolecules* **1987,** *20*, 1957-1960.

262. William S. Hummers, J.; Offeman, R. E., Preparation of Graphitic Oxide. *J. Am. Chem. Soc.* **1958,** *80* (6), 1339.

263. Dreyer, D. R.; Park, S.; Bielawski, C. W.; Ruoff, R. S., The chemistry of graphene oxide. *Chem. Soc. Rev.* **2010,** *39*, 228-40.

264. Kremer, F.; Schönhals, A., *Broadband Dielectric Spectroscopy*. Springer-Verlag Berlin Heidelberg: 2003.

265. Zhang, F.; Ilavsky, J., Ultra-Small-Angle X-ray Scattering of Polymers. *Polym. Rev.* **2010,** *50* (1), 59-90.

266. Rexer, J.; Anderson, E., Composites with Planar Reinforcements (Flakes, Ribbons) - A Review. *Polym. Eng. Sci.* **1979,** *19*, 1-11.

267. Rao, Y.; Waddon, A. J.; Farris, R. J., The evolution of structure and properties in poly(p-phenylene terephthalamide) fbers. *Polymer* **2001,** *42*, 5925-5935.

268. Frosini, V.; Butta, E., Some Remarks on the Mechanical Relaxations in Aliphatic, Partially Aromatic, and Wholly Aromatic Polyamides. *Polym. Lett.* **1971,** *9*, 253-260.

269. Kunugi, T.; Watanabe, H.; Hashimoto, M., Dynamic Mechanical Properties of Poly(p-phenylene terephthalamide) Fiber. *J. Appl. Polym. Sci.* **1979,** *24*, 1039-1051.

270. Haraguchi, K.; Kajiyama, T.; Takayanagi, M., Dynamic Mechanical Property of Poly(p-Phenylene Terephthalamide) Fiber. *Sen-I Gakkaishi* **1977,** *33*, 41-46.

271. Shauser, N. S.; Harry, K. J.; Parkinson, D. Y.; Watanabe, H.; Balsara, N. P., Lithium Dendrite Growth in Glassy and Rubbery Nanostructured Block Copolymer Electrolytes. *J. Electrochem. Soc.* **2015,** *162* (3), A398-A405.

272. Lee, S.-Y.; Ogawa, A.; Kanno, M.; Nakamoto, H.; Yasuda, T.; Watanabe, M., Nonhumidified Intermediate Temperature Fuel Cells Using Protic Ionic Liquids. *J. Am. Chem. Soc.* **2010,** *132*, 9764-9773.

273. Ito, A.; Yasuda, T.; Yoshioka, T.; Yoshida, A.; Li, X.; Hashimoto, K.; Nagai, K.; Shibayama, M.; Watanabe, M., Sulfonated Polyimide/Ionic Liquid Composite Membranes for CO2 Separation: Transport Properties in Relation to Their Nanostructures. *Macromolecules* **2018,** *51* (18), 7112-7120.

274. Thakur, V. K.; Ding, G.; Ma, J.; Lee, P. S.; Lu, X., Hybrid materials and polymer electrolytes for electrochromic device applications. *Adv. Mater.* **2012,** *24* (30), 4071-4096.

275. Kikuchi, K.; Tsuchitani, S., Nafion®-based polymer actuators with ionic liquids as solvent incorporated at room temperature. *J. Appl. Phys.* **2009,** *106* (5), 053519.

276. Cho, J. H.; Lee, J.; He, Y.; Kim, B.; Lodge, T. P.; Frisbie, C. D., High-Capacitance Ion Gel Gate Dielectrics with Faster Polarization Response Times for Organic Thin Film Transistors. *Adv. Mater.* **2008,** *20*, 686-690.

277. Lodge, T. P., A Unique Platform for Materials Design. *Science* **2008,** *321*, 50-51.

278. Monroe, C.; Newman, J., The Impact of Elastic Deformation on Deposition Kinetics at Lithium/Polymer Interfaces. *J. Electrochem. Soc.* **2005,** *152* (2), A396-A404.

279. Stone, G. M.; Mullin, S. A.; Teran, A. A.; Jr., D. T. H.; Minor, A. M.; Hexemer, A.; Balsara, N. P., Resolution of the Modulus versus Adhesion Dilemma in Solid Polymer Electrolytes for Rechargeable Lithium Metal Batteries. *J. Electrochem. Soc.* **2012,** *159* (3), A222-A227.

280. Teran, A. A.; Tang, M. H.; Mullin, S. A.; Balsara, N. P., Effect of molecular weight on conductivity of polymer electrolytes. *Solid State Ionics* **2011,** *203*, 18-21.

281. Chopade, S. A.; Au, J. G.; Li, Z.; Schmidt, P. W.; Hillmyer, M. A.; Lodge, T. P., Robust Polymer Electrolyte Membranes with High Ambient-Temperature Lithium-Ion Conductivity via Polymerization-Induced Microphase Separation. *ACS Appl. Mater. Interfaces* **2017,** *9* (17), 14561-14565.

282. Schulze, M. W.; McIntosh, L. D.; Hillmyer, M. A.; Lodge, T. P., High-modulus, high-conductivity nanostructured polymer electrolyte membranes via polymerization-induced phase separation. *Nano Lett.* **2014,** *14* (1), 122-126.

283. Khurana, R.; Schaefer, J. L.; Archer, L. A.; Coates, G. W., Suppression of lithium dendrite growth using cross-linked polyethylene/poly(ethylene oxide) electrolytes: a new approach for practical lithium-metal polymer batteries. *J. Am. Chem. Soc.* **2014,** *136* (20), 7395-7402.

284. Lavrenko, P. N.; Okatova, O. V., Diffusion of poly(p-phenylene terephthalamide) in concentrated sulfuric acid. *Polym. Sci. U.S.S.R.* **1979,** *21*, 406-412.

285. Russell, H. G.; Swalen, J. D., In-plane orientation of polyimide. *J. Polym. Sci.: Polym. Phys. Ed.* **1983,** *21*, 1745-1756.

286. Mantravadi, R.; Chinnam, P. R.; Dikin, D. A.; Wunder, S. L., High Conductivity, High Strength Solid Electrolytes Formed by in Situ Encapsulation of Ionic Liquids in Nanofibrillar Methyl Cellulose Networks. *ACS Appl. Mater. Interfaces* **2016,** *8* (21), 13426-13436.

287. Yasuda, T.; Nakamura, S.-i.; Honda, Y.; Kinugawa, K.; Lee, S.-Y.; Watanabe, M., Effects of Polymer Structure on Properties of Sulfonated Polyimide/Protic Ionic Liquid Composite Membranes for Nonhumidified Fuel Cell Applications. *ACS Appl. Mater. Interfaces* **2012,** *4* (3), 1783-1790.

288. Smith, D. M.; Pan, Q.; Cheng, S.; Wang, W.; Bunning, T. J.; Li, C. Y., Nanostructured, Highly Anisotropic, and Mechanically Robust Polymer Electrolyte Membranes via Holographic Polymerization. *Adv. Mater. Interfaces* **2018,** *5* (1), 1700861.

289. Kamio, E.; Yasui, T.; Iida, Y.; Gong, J. P.; Matsuyama, H., Inorganic/Organic Double-Network Gels Containing Ionic Liquids. *Adv. Mater.* **2017,** *29* (47), 1704118.

290. Tang, B.; White, S. P.; Frisbie, C. D.; Lodge, T. P., Synergistic Increase in Ionic Conductivity and Modulus of Triblock Copolymer Ion Gels. *Macromolecules* **2015,** *48*, 4942-4950.

291. Horowitz, A. I.; Panzer, M. J., Poly(dimethylsiloxane)-supported ionogels with a high ionic liquid loading. *Angew. Chem. Int. Ed.* **2014,** *53* (37), 9780-9783.

292. Visentin, A. F.; Panzer, M. J., Poly(Ethylene Glycol) Diacrylate-Supported Ionogels with Consistent Capacitive Behavior and Tunable Elastic Response. *ACS Appl. Mater. Interfaces* **2012,** *4*, 2836-2839.

293. Fujii, K.; Asai, H.; Ueki, T.; Sakai, T.; Imaizumi, S.; Chung, U.-i.; Watanabe, M.; Shibayama, M., High-performance ion gel with tetra-PEG network. *Soft Matter* **2012,** *8*, 1756-1759.

294. Zhang, S.; Lee, K. H.; Frisbie, C. D.; Lodge, T. P., Ionic Conductivity, Capacitance, and Viscoelastic Properties of Block Copolymer-Based Ion Gels. *Macromolecules* **2011,** *44*, 940-949.

295. Henderson, K. J.; Zhou, T. C.; Otim, K. J.; Shull, K. R., Ionically Cross-Linked Triblock Copolymer Hydrogels with High Strength. *Macromolecules* **2010,** *43*, 6193-6201.

296. He, Y.; Boswell, P. G.; Buhlmann, P.; Lodge, T. P., Ion Gels by Self-Assembly of a Triblock Copolymer in an Ionic Liquid. *J. Phys. Chem. B* **2007,** *111*, 4645-4652.

297. Cho, B.-K.; Jain, A.; Gruner, S. M.; Wiesner, U., Mesophase Structure-Mechanical and Ionic Transport Correlations in Extended Amphiphilic Dendrons. *Science* **2004,** *305*, 1598-1601.

298. Wang, C.; Sakai, T.; Watanabe, O.; Hirahara, K.; Nakanishi, T., All Solid-State Lithium-Polymer Battery Using a Self-Cross-Linking Polymer Electrolyte. *J. Electrochem. Soc.* **2003,** *150* (9), A1166-A1170.

299. Lauter, U.; Meyer, W. H.; Enkelmann, V.; Wegner, G., Supramolecular structures of poly(*p*-phenylenes) with oxyethylene side chains and their mixtures with lithium salts. *Macromol. Chem. Phys.* **1998,** *199*, 2129-2140.

300. Singh, M.; Odusanya, O.; Wilmes, G. M.; Eitouni, H. B.; Gomez, E. D.; Patel, A. J.; Chen, V. L.; Park, M. J.; Fragouli, P.; Iatrou, H.; Hadjichristidis, N.; Cookson, D.; Balsara, N. P., Effect of Molecular Weight on the Mechanical and Electrical Properties of Block Copolymer Electrolytes. *Macromolecules* **2007,** *40*, 4578-4585.

301. Susan, M. A. B. H.; Kaneko, T.; Noda, A.; Watanabe, M., Ion Gels Prepared by in Situ Radical Polymerization of Vinyl Monomers in an Ionic Liquid and Their Characterization as Polymer Electrolytes. *J. Am. Chem. Soc.* **2005,** *127*, 4976-4983.

302. Glynos, E.; Papoutsakis, L.; Pan, W.; Giannelis, E. P.; Nega, A. D.; Mygiakis, E.; Sakellariou, G.; Anastasiadis, S. H., Nanostructured Polymer Particles as Additives for High Conductivity, High Modulus Solid Polymer Electrolytes. *Macromolecules* **2017,** *50* (12), 4699-4706.

303. DeVecchio, D.; Bhushan, B., Localized surface elasticity measurements using an atomic force microscope. *Rev. Sci. Instrum.* **1997,** *68* (12), 4498-4505.

304. Chang, K.; Luo, H.; Geise, G. M., Water content, relative permittivity, and ion sorption properties of polymers for membrane desalination. *J. Membr. Sci.* **2019,** *574*, 24-32.

305. Solveyra, E. G.; de la Llave, E.; Scherlis, D. A.; Molinero, V., Melting and crystallization of ice in partially filled nanopores. *J. Phys. Chem. B* **2011,** *115* (48), 14196-204.

306. Higuchi, A.; Iijima, T., D.s.c investigation of the states of water in poly(vinyl alcohol-co-itaconic acid) membranes. *Polymer* **1985,** *26*, 1833-1837.

307. Teixeira, J., Small-Angle Scattering by Fractal Systems. *J. Appl. Cryst.* **1988,** *21*, 781-785.

308. Shimomura, T.; Takamuku, T.; Yamaguchi, T., Clusters of imidazolium-based ionic liquid in benzene solutions. *J. Phys. Chem. B* **2011,** *115* (26), 8518-27.

309. Tao, R.; Simon, S. L., Rheology of Imidazolium-Based Ionic Liquids with Aromatic Functionality. *J. Phys. Chem. B* **2015,** *119*, 11953-11959.

310. Pogodina, N. V.; Nowak, M.; Läuger, J.; Klein, C. O.; Wilhelm, M.; Friedrich, C., Molecular Dynamics of Ionic Liquids as Probed by Rheology. *J. Rheol.* **2011,** *55* (241), 241-255.

311. Shamim, N.; McKenna, G. B., Glass Dynamics and Anomalous Aging in a Family of Ionic Liquids above the Glass Transition Temperature. *J. Phys. Chem. B* **2010,** *114*, 15742-15752.

312. Xu, D.; Wang, B.; Wang, Q.; Gu, S.; Li, W.; Jin, J.; Chen, C.; Wen, Z., High-Strength Internal Cross-Linking Bacterial Cellulose-Network-Based Gel Polymer Electrolyte for Dendrite-Suppressing and High-Rate Lithium Batteries. *ACS Appl. Mater. Interfaces* **2018,** *10* (21), 17809-17819.

313. Kassapidou, K.; Jesse, W.; Kuil, M. E.; Lapp, A.; Egelhaaf, S.; Maarel, J. R. C. v. d., Structure and Charge Distribution in DNA and Poly(styrenesulfonate) Aqueous Solutions. *Macromolecules* **1997,** *30*, 2671-2684.

314. Orts, W. J.; Godbout, L.; Marchessault, R. H.; Revol, J.-F., Enhanced Ordering of Liquid Crystalline Suspensions of Cellulose Microfibrils- A Small Angle Neutron Scattering Study. *Macromolecules* **1998,** *31*, 5717-5725.

315. Nierlich, M.; Williams, C. E.; Boué, F.; Cotton, J. P.; Daoud, M.; Famoux, B.; Jannink, G.; Picot, C.; Moan, M.; Wolff, C.; Rinaudo, M.; de Gennes, P. G., Small angle neutron scattering by semi-dilute solutions of polyelectrolyte. *J. Phys. I* **1979,** *40* (7), 701-704.

316. Mackintosh, F. C.; Safran, S. A.; Pincus, P. A., Self-Assembly of Linear Aggregates: the Effect of Electrostatics on Growth. *Europhys. Lett.* **1990,** *12*, 697-702.

317. Odijk, T., Polyelectrolytes near the rod limit. *J. Polym. Sci.: Polym. Phys. Ed.* **1977,** *15*, 477-483.

318. Buhler, E.; Boue, F., Persistence length for a model semirigid polyelectrolyte as seen by small angle neutron scattering: a relevant variation of the lower bound with ionic strength. *Eur. Phys. J. E Soft Matter* **2003,** *10* (2), 89-92.

319. Dobrynin, A. V.; Rubinstein, M., Counterion Condensation and Phase Separation in Solutions of Hydrophobic Polyelectrolytes. *Macromolecules* **2001,** *34*, 1964-1972.

320. Starkweather, H. W., Aspects of simple, non-cooperative relaxations. *Polymer* **1991,** *32* (13), 2443-2448.

321. Starkweather, H. W., Noncooperative Relaxations. *Macromolecules* **1988,** *21*, 1798-1802.

322. Starkweather, H. W., Simple and Complex Relaxations. *Macromolecules* **1991,** *14* (1277-1281).

323. Kulicke, W.-M.; Clasen, C., *Viscosimetry of Polymers and Polyelectrolytes*. Springer-Verlag Berline Heidelberg New York: 2004.

324. Arpin, M.; Strazielle, C., Characterization and conformation of aromatic polyamides. Poly(1,4-phenylene terephthalamide) and poly(p-benzamide) in sulfuric acid. *Polymer* **1977,** *18*, 591-596.